Development of a prototype camera and Monte Carlo studies for the optimisation of the CBM-RICH detector

Dissertation

zur Erlangung des Doktorgrades
der Naturwissenschaften (Dr. rer. nat.)

BERGISCHE
UNIVERSITÄT
WUPPERTAL

Fachbereich C - Mathematik und Naturwissenschaften

Der Fachgruppe Physik vorgelegt von

Jan Martin Kopfer

Februar 2014

Die Dissertation kann wie folgt zitiert werden:
urn:nbn:de:hbz:468-20140515-122625-5
[http://nbn-resolving.de/urn/resolver.pl?urn=urn%3Anbn%3Ade%3Ahbz%3A468-20140515-122625-5]

Von der Fachgruppe Physik der Bergischen Universität Wuppertal als Dissertation angenommen.
Tag der mündlichen Prüfung: 14.04.2014

1. Gutachter	2. Gutachter
Prof. Dr. Karl-Heinz Kampert	Prof. Dr. Claudia Höhne
Bergische Universität Wuppertal	Justus-Liebig-Universität Gießen

Contents

Chapter 1

Introduction

1.1 Motivation

The Standard Model of Particle Physics describes electromagnetic, weak, and strong interactions between the elementary constituents of matter. It groups particles into quarks and leptons as the building blocks of matter and gauge bosons as the force carriers. Furthermore, particles, irrespective of being elementary or composite, are classified as fermions and bosons according to their half-integer respectively integer spin. As of 2013, the existence of all particles predicted by the Standard Model has been proven experimentally: The observation of a new boson, announced in July 2012 [1, 2] and confirmed one year later to be the (or at least one) Standard Model Higgs boson after measuring parity and spin [3], is experimental evidence for the Brout-Englert-Higgs mechanism, that, within the Standard Model, gives mass to the massive elementary particles, while not explaining the hadron masses.

Despite the experimental success of the Standard Model, it is known to be incomplete. For example, it fails to include general relativity as the theory of gravitation and describes solely ordinary matter which makes up only $4.9\,\%$ of the mass of the known universe [4], lacking an answer to the origin of dark matter and dark energy.

Within the Standard Model, the interaction between quarks and the gauge bosons of strong interaction, the gluons, is described by Quantum Chromodynamics (QCD). QCD is a very well established theory but some phenomena have not been fully understood and are subject of investigation. Fundamental questions of QCD Physics are [5]: Why are quarks confined? What is the origin of the hadron masses which is larger than the Higgs mass of their constituents? What are the properties and degrees of freedom of nuclear matter at high temperature and high pressure? In other words, what are the properties of compressed baryonic matter, which existed in the early universe a few microseconds after the big bang and still exists in compact stars as well as in the core of supernova explosions?

The answers to these questions are believed to be related to phase transitions in strongly interacting matter. The study of these phases and transitions is thus an important field of physics with a high discovery potential. Starting from cold nuclear matter composed of protons and neutrons, different phases of matter can be reached by heating and/or compression. In this regard, there are four approaches [6]: analytical theory, astrophysical observations, numerical experiments on the lattice, and laboratory experiments.

The construction of the Facility for Antiproton and Ion Research (FAIR) at Darmstadt and the Compressed Baryonic Matter (CBM) experiment [7] will provide the opportunity to study the QCD phase diagram in the region of high baryon densities and moderate temperatures with unprecedented statistical precision using ultrarelativistic nucleus-nucleus collisions. An important part of the CBM experiment is a Ring Imaging Cherenkov (RICH) detector because it is designed for the identification of electrons among the abundance of collision products. Electrons are ideal probes of the early, high-density phase of the collision process due to their lack of strong interactions with the hot and dense medium.

The aim of the work presented in this thesis is to contribute to the development of the CBM-RICH detector, in particular to the construction of its photon camera. The work comprises three parts: the experimental characterisation of appropriate photon sensors in the laboratory, data analysis from beam tests with a prototype, and detector performance studies using Monte Carlo simulations.

1.2 Thesis outline

This thesis comprises seven chapters, the first two being of introductory character. Experimental results are presented in the three following chapters. Performance studies based on Monte Carlo methods are explained in the last chapter before the summary. Chapters 3 to 6, those which contain new results, are preceded by an overview and concluded by a summary, respectively.

Chapter 2 introduces the physics motivation of the CBM experiment and exposes the CBM detector design. The phase diagram of nuclear matter is discussed and the connection to observables measured with CBM is drawn. Because the RICH detector will be used for electron identification, the physics case of di-electrons from the decay of low mass vector mesons is outlined. After a brief overview of the CBM subdetectors, the CBM-RICH detector is discussed in more detail including a summary of the fundamentals and the operating principle of RICH detectors. The ring finding and fitting algorithms used in the CBM-RICH detector are explained. In the last section, the background rejection strategy and the status of feasibility studies for physics measurements are discussed.

Chapter 3 addresses the evaluation of multianode photomultiplier tubes (MAPMTs). In two introductory sections, basic characteristics of PMTs and MAPMTs are discussed. They are followed by a description of the experimental methods and the test stand set up for device characterisation. Measurement results in terms of spectral sensitivity and single photon detection capabilities are presented and discussed.

Chapter 4 is dedicated to wavelength shifting (WLS) films used to enhance the sensor sensitivity in the ultraviolet region of the electromagnetic spectrum. After an introduction to the method of wavelength shifting, an overview of various application techniques and the description of a dip-coating process, specifically developed for the coating of MAPMTs, is given. The chapter focuses on measurements of quantum efficiency, homogeneity, and crosstalk of coated MAPMTs.

Chapter 5 covers the presentation of a real-size CBM-RICH prototype detector, its operation, and performance in beam. The contribution of the Wuppertal group was the development of the photon camera, which is described in detail together with the readout concept. A complete description of the experimental setup during two beam test campaigns is given. The main sections of chapter 5 are dedicated to the data analysis as well as to the presentation and discussion of the results. It is shown that important quantities like ring parameters, the effect of WLS films and radiator conditions on the detector performance, and the electron pion separation could be measured accurately with the prototpye.

Chapter 6 identifies the implications from laboratory and beam test results for Monte Carlo simulations of the RICH performance. The first section introduces the simulation tool. In the second section, it is updated with results obtained over the course of this thesis. With that, the simulations are verified through comparison with beam test results and adapted to a more realistic detector description by implementing supplementary parameters.

Finally, the most important results are summarised in **chapter 7**.

Chapter 2

CBM physics motivation and the CBM experiment

2.1 Exploring the phase diagram of nuclear matter

The phase diagram of nuclear matter
Cold nuclear matter in form of normal nuclei is composed of protons and neutrons at a net baryon density $\rho_B = 1$ and low temperature. With increasing temperature and density, nucleons are excited to baryonic resonances, i.e. short lived states which decay by the emission of mesons into pions and nucleons. At higher temperatures, also baryon-antibaryon pairs are created. The mixture of nucleons, baryonic resonances and baryon-antibaryon pairs is referred to as hadronic phase. At very high temperatures or densities, hadrons are no longer confined and dissolve into their partons, namely quarks and gluons. This partonic phase is denoted as Quark-Gluon-Plasma (QGP). The phases of nuclear matter can be illustrated in a diagram of temperature T versus ρ_B or baryon chemical potential μ_B as shown in Fig. 2.1. μ_B is a thermodynamic quantity and can be understood as energy which is needed to add a particle to given system. μ_B and ρ_B are related via temperature and particle mass.

Of particular interest are transitions between the phases. The transition between the hadronic phase and the QGP at zero net baryon density is a crossover [8]. Lattice calculations predict this transition at temperatures in the range from $150\,\mathrm{MeV}$ to $170\,\mathrm{MeV}$ [9, 10] corresponding to more than $100\,000$ times the temperature of the interior of our sun. An important prediction from theory is the existence of a critical endpoint [11]. At this point, the phase transition is expected to change its character. While being a crossover at low μ_B, the phase transition is of first order at larger μ_B.

More structures in the phase diagram have been predicted, e.g. a quarkyonic phase beyond the first order phase transition and a triple point where hadronic matter, quarkyonic matter, and the QGP coexist [12]. While chiral symmetry is spontaneously broken in the hadronic phase due to the non-zero quark masses, it is believed to be restored in the QGP. Whether it is also restored in quarkyonic matter is not clear [12]. At very high densities, correlated quark-quark pairs are expected to form a colour superconductor.

Apart from these predictons, mainly from lattice QCD and from measurements at large T and low ρ_B, the nature of the phase diagram of nuclear matter is hardly known. A discussion on the current status of theoretical approaches to the phase diagram can be found e.g in [13]. Especially the access to the diagram at non-zero net baryon density is very difficult. The success of lattice methods at zero and small net baryon densities e.g. is hampered by the so-called sign problem [14]. The experimental discovery of the landmarks of the phase diagram, the critical point, the first order phase transition, and the chiral phase transition would be a major step in understanding nuclear matter.

Probing the phase diagram in heavy ion collisions

Super-dense nuclear matter can be produced in the laboratory in the reaction volume of a relativistic heavy ion collision. According to the current understanding, in the initial phase of such a collision, the two colliding ions are strongly compressed and heated forming a so-called fireball. If the energy density is sufficiently high, the system reaches thermal equilibrium within a very short time of 1 fm/c [15], and forms a QGP phase. While expanding, the system cools down. Around the critical temperature T_C, hadrons form from quarks and gluons, denoted as hadronisation. The hadrons interact inelastically during the hadronisation until the chemical freeze-out sets in. After the chemical freeze-out, number and type of particles are fixed. The system cools down further and after the kinetic freeze-out, also particle momenta do not change any more.

Experimental findings obtained so far can be summarised in three basic items [16]: First, particle abundancies and particle ratios can be predicted by the thermal model, T and μ_B being the only free parameters in the fits. The success of this model to describe the experimental data shows that thermal equilibrium is approximately reached in heavy ion collisions at high energies [17]. The freeze-out conditions for hadrons, extracted from thermal fits to beam data taken at different colliding energies and with different systems, line up on a freeze-out curve. Second, the freeze-out temperature at zero μ_B is around $160\,\mathrm{MeV}$ which is in agreement with T_C from lattice calculations. This, in turn, is an indication for the creation of a QGP at very high temperatures. Third, the properties of the QGP in the range of very high temperature and low μ_B are characterised in-depth at RHIC and LHC [18].

Depending on the beam energy, different net baryon densities and temperatures can be reached. By varying the beam energy, it is therefore possible to create different states and phases of nuclear matter within certain limits. Figure 2.2 shows the dynamical trajectories for central Au+Au collisions in the plane of T versus μ_B for incident energies from 5 AGeV to 158 AGeV. Depending on the energy, the trajectories cross different regions of the phase diagram. While at high energies extremely large values of T and μ_B are reached and the system returns to the freeze-out within a very short time, the situation is different at lower energies where the system is expected to remain beyond the transition line in the QPG phase for longer time. This and the fact that in heavy ion collisions the largest possible values for ρ_B at freeze-out are reached at $\sqrt{s_{NN}} = 8$ AGeV [19] is the motivation to conduct experiments at lower energies like in the RHIC energy scan [20, 21], at low SPS energies, and at FAIR.

Experimental approaches to the phase diagram of nuclear matter are or will be conducted with heavy ion collisions at LHC, RHIC, SPS, NICA, and FAIR[1]. The LHC experiments study the QGP at very high temperatures and almost zero net-baryon densities using the data from the heavy ion runs. Experiments at the other facilities look for the landmarks of the phase diagram at high net-baryon densities. The STAR experiment at RHIC [22] as well as NA61/SHINE at SPS [23] are searching for the critical point and the MPD detector at NICA for a mixed phase of nuclear matter [24]. These experiments measure bulk observables and cannot make use of rare probes because of luminosity or detector limitations.

The situation will be different with CBM at FAIR. The CBM detector is designed for the measurement of observables with very low production cross section. The SIS100/300 accelerators at FAIR will provide beams with sufficient energy to produce high net baryon densities [25] and sufficient intensity for the measurement of rare probes.

---

[1] The abbreviations signify Large Hadron Collider (LHC) at CERN, Geneva; Relativistic Heavy Ion Collider (RHIC) at BNL, Brookhaven; Super Proton Synchrotron (SPS) at CERN; Nuclotron-based Ion Collider Facility (NICA) at JINR, Dubna; Facility for Antiproton and Ion Research (FAIR), Darmstadt.

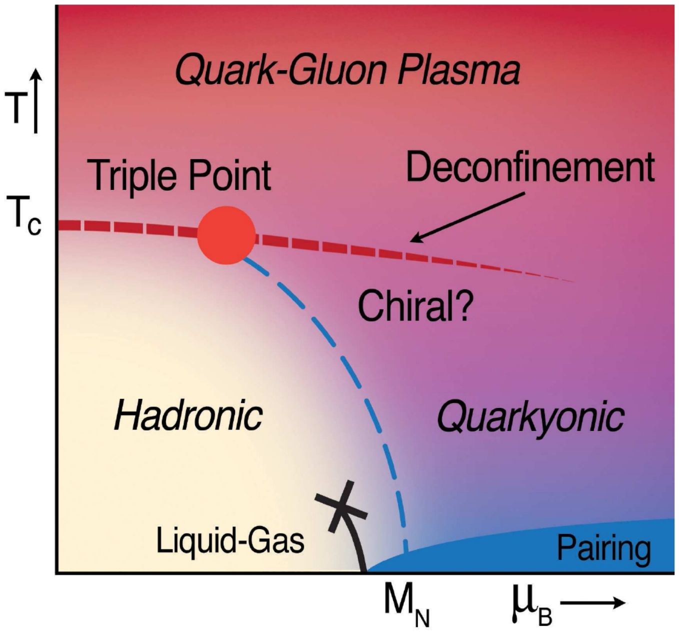

Figure 2.1 – One of many phase diagrams of nuclear matter which can be found in literature. The schematic phase diagram shown here illustrates the possible existence of hadronic, quarkyonic, and quark-gluon phases as well as a triple point where all three phases coexist. Figure taken from [12].

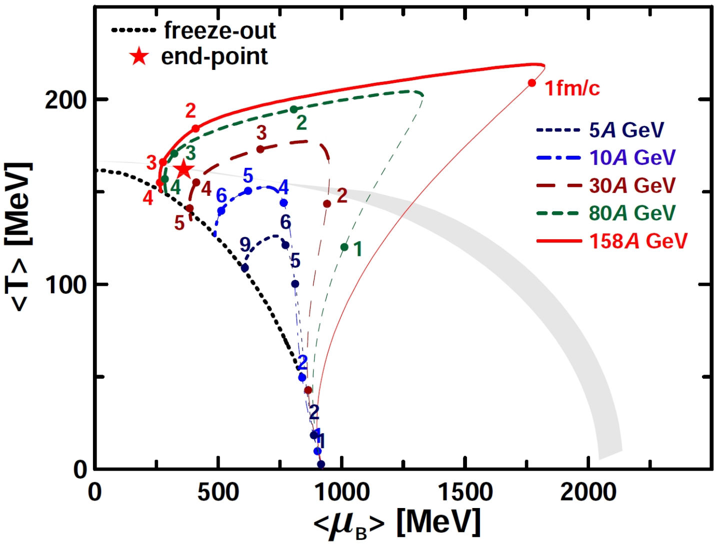

Figure 2.2 – Dynamical trajectories that a system of two centrally colliding Au ions undergoes in the plane of temperature versus baryon chemical potential as calculated with a 3-fluid hydrodynamic model for incident energies from 5 AGeV to 158 AGeV. It can be seen that the trajectories cover different areas depending on the energy. Numbers next to the trajectories indicate time steps in fm/c in the centre of mass frame of the colliding ions. At very high energies, the system enters very rapidly regions of extremely high μ_B but also reaches the freeze-out in very short time at relatively low μ_B. At lower energies, on the other hand, the system remains longer in the region beyond the phase transition to the QGP indicated by the grey belt and freezes out at larger μ_B. The star marks the critical point predicted in [11]. Figure taken from [26].

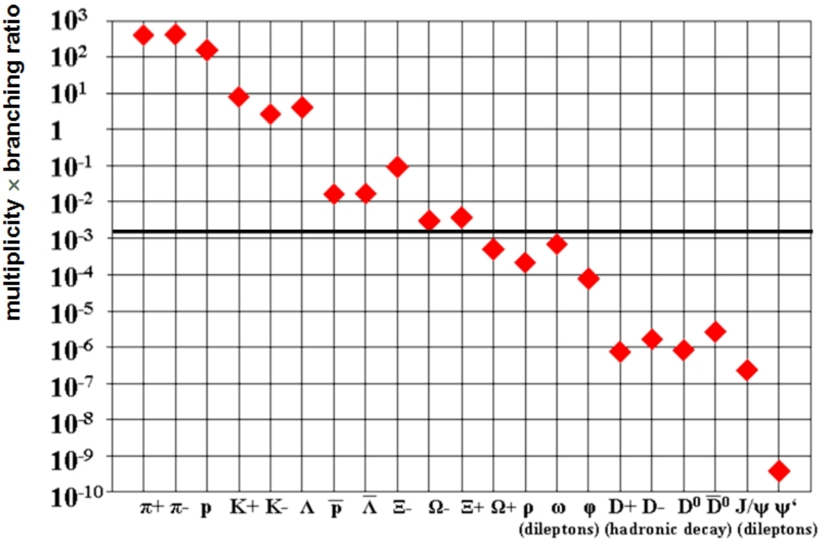

Figure 2.3 – Product of particle multiplicity and branching ratio for central Au+Au collisions at 25 AGeV calculated with the HSD transport code [29] and the statistical model [30]. For ρ^0, ω, ϕ, J/ψ, J/ψ', a decay into lepton pairs is assumed, for D mesons the decay into kaons and pions. Probes above the horizontal line have already been measured at beam energies around 25 AGeV corresponding to the maximum freeze-out densities. Figure taken from [31].

2.2 CBM observables

In a Au+Au collision at a laboratory beam energy of 25 AGeV, which is in the scope of SIS300, approximately 1000 charged particles are produced, mostly pions, protons, and kaons ($400\,\pi^-$, $400\,\pi^+$, $160\,p$, $44\,K^+$, and $13\,K^-$ according to the UrQMD model [27, 28]). The interesting particles carrying information from the hot and dense phase of the collision are produced less abundantly. Figure 2.3 shows the product of particle multiplicity and branching ratio for varius particles created in a central Au+Au collision at 25 AGeV. The rare probes below the horizontal line have not been measured yet at energies corresponding to maximum ρ_B and drive the requirements in precision and data rate of the CBM experiment.

The variety of CBM physics cases and observables is discussed in detail in the CBM Physics Book [14]. The main questions addressed by the experiment are the phase transition between hadronic and partonic matter, the QCD critical endpoint, new forms of strange matter, i.e. objects along the third dimension of the chart of nuclei, in-medium modifications of hadrons, and the chiral phase transition which is related to the origin of hadron masses.

The CBM experiment is one of the four scientific pillars and part of the modularised start version of FAIR [7]. While the SIS300 accelarator provides the long term perspective, the SIS100 accelerator of the start version will deliver beams of heavy ions up to 11 AGeV ($\sqrt{s_{NN}} = 4.7\,\mathrm{GeV}$) for Au, 14 AGeV ($\sqrt{s_{NN}} = 5.3\,\mathrm{GeV}$) for Ca and 29 GeV ($\sqrt{s_{NN}} = 7.5\,\mathrm{GeV}$) for protons. In the following, the physics cases of CBM at SIS100 as outlined in [32] will be listed in brief.

Properties of dense nuclear matter

In heavy ion collisions at SIS100 energies, net-baryon densities of up to seven times the saturation density ($\rho_0 \approx 0.15\,\mathrm{fm}^{-3}$) can be reached according to transport calculations [25]. At these densities and low temperatures, the existence of a possible quarkyonic phase is predicted [12]. This phase is therefore subject to investigation of CBM at SIS100. It is predicted that crossing the transition line from the quarkyonic to the hadronic phase acts as thermalizer. Because of that, the experimental approach will focus on fitting the particle yields according to the statistical model.

Another probe for the possible transition to quarkyonic matter and the degrees of freedom of QCD matter at supra-nuclear densities are multi-strange hyperons, i.e. baryons with more than one strange quark, in particular Ξ and Ω. In contrast to p+p collisions, Ξ and Ω can be produced in nuclear collisions below threshold beam energies due to doubly strange cascade reactions which has been observed for Ξ^- in Ar+KCl reactions [33]. In general, measurements of multi-strange hyperons are very rare. Below $40\,\mathrm{AGeV}$ ($\sqrt{s_{NN}} = 8.8\,\mathrm{GeV}$) e.g. no data on Ω production exists [34].

Equation of state

The measurement of the Fourier expansion of the azimuthal distribution of final state hadrons, the so-called flow, on event-by-event basis has been proposed in [35] where also the connection between the Fourier coefficients corresponding to different harmonics and their physical meaning is established. Since the collective flow of nucleons is driven by the pressure in the reaction volume of a heavy ion collision, it is sensitive to the equation of state of nuclear matter [14]. The disappearance of flow e.g. has been discussed as signature for a first order phase transition [36]. In addition, the flow of strange particles is related to the restoration of chiral symmetry.

In-medium properties of vector mesons and onset of chiral symmetry restoration

A consequence of the expected restoration of chiral symmetry in the QGP phase is a modification of the properties of hadrons such as mass, width or more generally the hadron spectral function [37]. Experimentally, the light vector mesons ρ^0, ω, ϕ are accessible via their decays into lepton pairs. A more detailed discussion of the low mass vector meson physics case is presented in section 2.3.

Charm production and propagation in nuclear matter at threshold energies

A classical, yet promising and debated probe of hot and dense nuclear matter are hadrons containing charm quarks. Because of their large mass, $c\bar{c}$ pairs are essentially produced in hard processes in the very early stage of a heavy ion collision and subsequently propagate through the dense medium. If this medium is partonic, the formation rate of bound $c\bar{c}$ states, so-called charmonium, will be reduced because abundantly produced gluons will screen c and $\bar{c}$ quarks. This effect is referred to as Debye or colour screening. The individual charm quarks will finally coalesce with light quarks to hadrons with non-zero charm quantum number, denoted as open charm. In particular, the ratio of the charmonium ground state J/ψ to $D + \bar{D}$ is expected to be very sensitive to the medium. Within the statistical hadronisation model (SHM [38]), which assumes a complete dissociation of charmonium in the QGP, the J/ψ to $D + \bar{D}$ ratio depends only on T and μ_B and is in first order independent of the total abundance of c and $\bar{c}$ quarks. In a hadronic scenario (hadronic string dynamics, HSD [39]), on the other hand, the J/ψ to $D+\bar{D}$ ratio is significantly larger [14]. The measurement of the J/ψ to $D + \bar{D}$ ratio is therefore a good quantity to distinguish between a partonic (SHM) and hadronic (HSD) fireball.

The suppression of J/ψ was already predicted in the year 1986 in a more than thousandfold cited article [40]. Since J/ψ is detected via its decay into lepton pairs ($\approx 6\,\%$ of total decay branching ratio), its suppression has to be given relative to the dilepton yield from Drell-Yan processes, i.e. the formation of a lepton pair via a virtual photon or Z boson from the annihilation of a quark and an antiquark in hadron scattering processes. The discrepancy between the magnitude of J/ψ suppression as measured by the NA50 [41] and the NA60 [42] experiments, where different beam energies for the cold nuclear matter reference (p+A) were used, showed that high-precision multidifferential data on charmonium and open charm production in both A+A and p+A collisions are indispensable. At SIS100, charm production close to threshold and the propagation of charm in cold nuclear matter will be studied, the latter being essential for the further charm measurements at SIS300.

Double hypernuclei

The question how far the chart of nuclei can be extended towards the third dimension corresponding to strangeness, is subject to the measurement of hypernuclei, i.e. nuclei with at least one hyperon in addition to neutrons and protons. Extracted information on hyperon-nucleon and hyperon-hyperon interactions are important for neutron star models. Traditionally, hypernuclei are produced in collisions of K^- with light nuclei. At SIS100, hypernuclei will be produced via coalescence of Λ baryons, i.e. a baryon containing one u, one d and one heavier quark. According to the thermal model, the yield of hypernuclei peaks at beam energies of 7 AGeV to 11 AGeV [43]. Experimentally, hypernuclei are accessible by the reconstruction of their decay chains.

Meta-stable multi-strange objects

In a high energy heavy ion collision, strangeness is abundantly produced in form of K mesons and Λ baryons. Therefore, composite states with multiple units of strangeness, so-called multi-strange objects, like di-baryons, strangelets, or kaonic clusters could be created at SIS100.

2.3 Electron pairs from low mass vector meson decays

The measurement of electromagnetic radiation in the form of photons or leptons has been already suggested in 1987 [44] in order to extract information about the evolution of a heavy ion collision. These probes are very well suited because they do not interact strongly with the medium. They interact only electromagnetically and therefore have a long mean free path compared to the size of the hot and dense collision zone leaving the region basically undistorted. Thus, photons and leptons carry information on the medium where they were produced.

In the CBM experiment, the RICH detector will be used for the measurement of di-electrons from different sources like charmonium and low mass vector mesons and from γ-conversion processes of direct photons. As shown in Fig. 2.3, di-electron probes are rare signals because the branching ratios are low, as it is the case for low mass vector mesons, or the production probability is small as in the case of charmonium. In order to obtain significant results, high statistics runs are essential as well as purely identified electrons, and a well controlled background. Systematic studies at various energies and for different system sizes in proton+proton (p+p), proton+nucleus (p+A), and nucleus+nucleus (A+A) collisions are needed.

Direct photons are predicted to be produced mainly thermally in the medium and can be used as thermometer for the medium. Direct photons will be detected via electron positron pairs from γ-conversion ($\gamma \rightarrow \mathrm{e}^+ + \mathrm{e}^-$) in the detector material which is the dominant process for the interaction of photons with matter at energies exceeding several MeV. As mentioned in section 2.2, di-electrons from charmonium decays, especially the measurement of the J/ψ to $D + \bar{D}$ ratio, will allow to draw conclusions on whether the created medium has a partonic or hadronic character.

At lower energy, di-electron measurements from low mass vector meson decays are a key signature of CBM measurements at SIS100 and SIS300. Of particular interest is the ρ^0 meson which is abundantly produced by pion annihilation. Its lifetime in the vacuum is only 1.3 fm/c and thus less than the typical lifetime of the fireball of approx. 10 fm/c. Di-leptons from the ρ^0 meson decay can therefore provide information about the in-medium mass and width of the ρ^0 meson, which are expected to be modified in dense baryonic matter. The ω and ϕ mesons, in contrast, have larger lifetimes of 23 fm/c and 44 fm/c respectively, so most of them decay outside the fireball after regaining their vacuum properties.

The invariant mass spectrum of low mass vector mesons

In 1997, the DLS collaboration published results on the di-electron production cross section measured in light collisions systems at 1 AGeV [45]. The observation of an enhancement in the low-mass region of the di-electron spectrum with respect to the expectation remained the unexplained “DLS puzzle” until the HADES detector was built and confirmed the result [46], this time with better statistics and mass resolution. Based on this measurements, the puzzle seems to be solved by new transport model calculations revealing baryonic resonances and bremsstrahlung contributions as source of the di-electron enhancement [47].

An excess in the di-electron and in the di-muon invariant mass spectra in the range from $0.2\,\mathrm{GeV/c}$ to $0.7\,\mathrm{GeV/c}$ was also measured by the CERES and NA60 collaborations, respectively. These data, however, cannot be explained without strong in-medium modifications of the ρ^0 mesons [48, 49].

Figure 2.4 shows the invariant mass spectrum of di-electrons measured by the CERES experiment in the range from $0\,\mathrm{GeV/c^2}$ to $1.6\,\mathrm{GeV/c^2}$ in Pb+Au collisions at the energy of 158 AGeV. On the left panel, the measured di-electron yield is shown with black dots. The black line indicates the expected di-electron yield from meson decays, denoted as hadronic cocktail. It can be seen that for the lowest momenta, π^0 and also η Dalitz decays are the dominant source of di-electrons. Towards higher momenta, also contributions from ω, ρ^0, and ϕ appear. The above mentioned excess of the di-electron yield over the hadronic cocktail can be clearly observed. The right panel of Fig. 2.4 shows the same data compared to calculations taking into account either a dropping ρ^0 mass or a broadened spectral function of the ρ^0 meson. In conclusion, the data favor models including a strong broadening of the ρ^0 spectral function in a hot and dense hadronic medium over a density dependent ρ^0 mass shift.

Similarly to the measurements from CERES and NA60 at top SPS energies at CERN, the HADES collaboration measured an excess in the di-electron invariant mass spectrum from $0.2\,\mathrm{GeV/c^2}$ to $0.7\,\mathrm{GeV/c^2}$ in Ar+KCl collisions at the much lower energy of 1.76 AGeV [50] which cannot be seen in C+C collisions (see Fig. 2.5). In conclusion, Ar+KCl, in contrast to the lighter C+C system, cannot anymore be seen as a superposition of independent nucleon+nucleon collisions.

However, those measurements are strongly limited in precision and statistics. In the case of CERES, ρ^0 and ω could not be disentangled and the ω peak in the HADES data contains only 40 reconstructed electron pairs. In addition, no data are available up to now in the range between 2 AGeV (HADES) and 40 AGeV (CERES). HADES and CBM at SIS100 will continue and extend the di-electron programme. It is planned to measure di-electrons in a common overlap of beam energies. While HADES, limited by detector granularity, will focus on collision systems up to Ni+Ni, the measurement of the invariant di-electron and di-muon spectra in heavier systems is a central part of the CBM physics programme at SIS100.

Electron identification with the RICH detector

As shown in Fig. 2.6, the momentum distribution for electrons from the decay of low mass vector mesons and J/ψ produced in heavy ion collisions at a beam energy of 25 AGeV is in the range from $0\,\mathrm{GeV/c}$ to $15\,\mathrm{GeV/c}$. It is therefore necessary to design the detector with an electron identification capability in this momentum range. The identification of electrons and positrons in the CBM experiment will be done with a RICH detector for momenta below $8\,\mathrm{GeV/c}$ to $10\,\mathrm{GeV/c}$. A transition radiation detector (TRD) complementing the RICH detector will be effective at higher momenta.

Clean identification of electrons below $10\,\mathrm{GeV/c}$ can be done efficiently with a gaseous RICH detector. The design of the CBM-RICH will be discussed in detail in section 2.5.

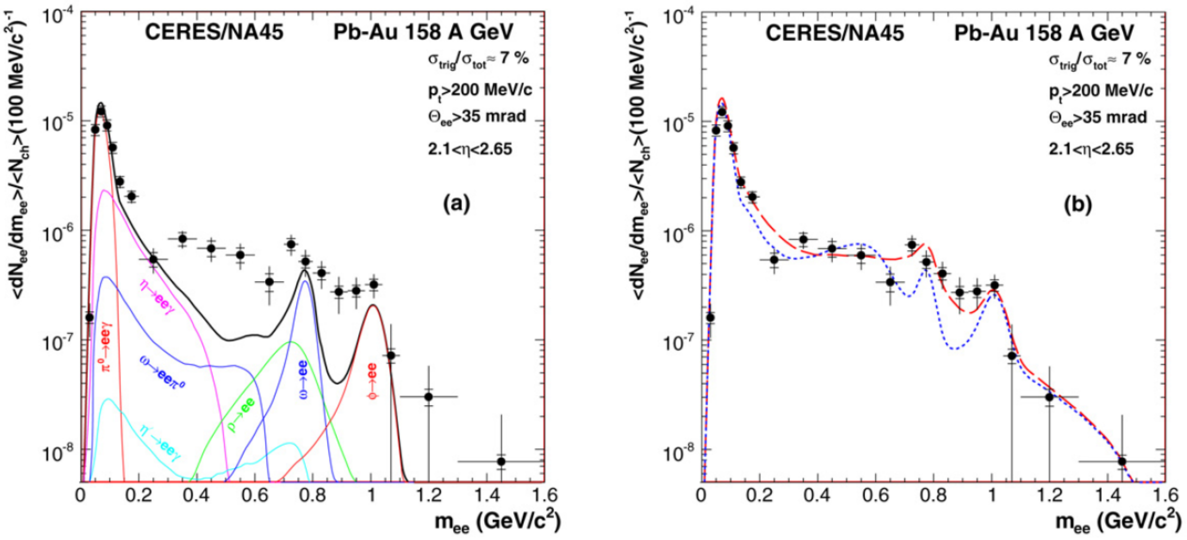

Figure 2.4 – Invariant mass spectrum of di-electrons measured by the CERES experiment in the range from 0 GeV/c^2 to 1.6 GeV/c^2 for Pb+Au collisions at the energy of 158 AGeV. Left: Comparison of the measured di-electron yield to the hadronic cocktail (solid line). An excess in the data over the cocktail can be observed in the range from 0.2 GeV/c^2 to 0.7 GeV/c^2. Right: Comparison of data with calculations including a dropping ρ^0 mass (dotted line) and a broadening of the ρ^0 spectral function (dashed line). It can be seen that the latter is in better agreement with the data. Figure taken from [48].

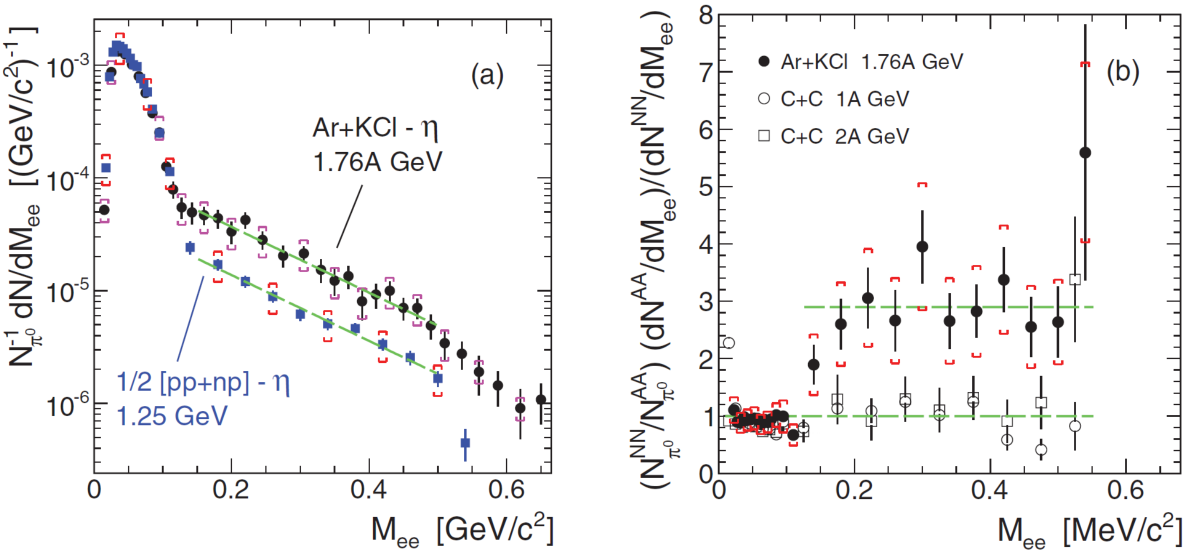

Figure 2.5 – Left: Invariant mass spectrum of di-electrons measured by the HADES experiment in the range from 0 GeV/c^2 to 0.65 GeV/c^2 for Ar+KCl collisions at the energy of 1.76 AGeV. An excess in the di-electron yield compared to the averaged [pp+np] reference can be observed. Right: Di-electron mass spectra measured in Ar+KCl and C+C collisions normalised to the [pp+np] reference. It can be seen that a qualitative change occurs when going from the relatively light C+C to the heavier Ar+KCl system. The data in the left and right plots are normalised to their respective pion multiplicity. The yield from η Dalitz decays is subtracted. Figure taken from [50].

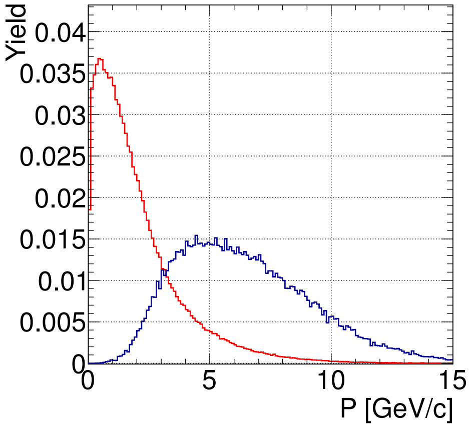

Figure 2.6 – Momentum distribution of electrons from the decay of ρ^0 (red) and J/ψ mesons (blue) in the laboratory system calculated for collisions at a beam energy of 25 AGeV. The mesons were generated with the PLUTO event generator [51] with a thermal p_t-distribution, transverse flow and a Gaussian rapidity distribution in the centre-of-mass frame. The corresponding parameters are $T = 130\,\mathrm{MeV}$, $\beta = 0.3\,\mathrm{c}$, $\sigma_y = 0.41$ for the ρ^0 meson and $T = 170\,\mathrm{MeV}$, $\beta = 0\,\mathrm{c}$, $\sigma_y = 0.23$ for the J/ψ. Figure taken from [6].

2.4 The CBM detector

The CBM experiment will operate at FAIR using heavy ion beams from the SIS100 and SIS300 accelerators in fixed target mode. It is designed to explore the phase diagram of nuclear matter in the region of high net-baryon densities and moderate temperatures. The focus will be on the measurement of rare probes requiring very high interaction rates of up to 10 MHz.

The CBM detector comprises a superconducting dipole spectrometer magnet and various subdetectors, each designed to cope with such high interaction rates, and briefly described in the following. Figure 2.7 depicts the CBM detector in electron and muon configuration. The electron setup comprises the RICH and the TRD detectors for electron identification. In the muon setup, the RICH detector is replaced by an instrumented hadron absorber for muon identification. It is planned to perform electron and muon measurements consecutively. For the measurements, the RICH or the muon detector are lifted into the acceptance by crane.

2.4.1 Subsystems

Superconducting dipole magnet

The target, typically a thin gold foil of $\approx 100\,\mu\mathrm{m}$, is positioned inside the gap of a superconducting dipole magnet which is used to bend the trajectories of charged particles in order to allow the measurement of particle momenta. The CBM magnet has a large aperture of $\pm 25°$ polar angle. The gap height of 140 cm and the gap width of 260 cm are large enough to host the Silicon Tracking System (see below). The magnet is an H-type magnet with two superconducting circular coils in separate cryostats and provides a magnetic field integral of 1 T m. The Technical Design Report for the CBM dipole magnet has been approved by FAIR in January 2014.

Micro-vertex detector

For the determination of the secondary decay vertices of open charm particles ($c\tau = 123\,\mu\mathrm{m}$ for D^0 mesons and $c\tau = 314\,\mu\mathrm{m}$ for $D^\pm$ mesons), a detector with excellent spatial resolution is needed. In addition, a very low material budget in order to minimise multiple scattering and radiation hardness due to the harsh environment in the region close to the target are required. A silicon pixel detector based on ultra-thin Monolithic Active Pixel Sensors (MAPS) will meet these requirements and is foreseen to be used as Micro-Vertex Detector (MVD) for CBM.

The MVD in its present design consists of 3 MAPS layers located at 5 cm, 10 cm and 15 cm downstream of the target in the vacuum with only 300 µm to 500 µm silicon equivalent for sensors and support structures. It will allow to determine the secondary decay vertex of a D-meson with a resolution of 50 µm to 100 µm along the beam axis.

Silicon tracking system

In order to provide information for track reconstruction and to determine the momenta of all charged particles produced in the heavy ion collision, a Silicon Tracking System (STS) as the CBM core detector will be placed inside the dipole magnet. It consists of 8 detector layers placed 30 cm to 100 cm downstream of the target. Double-sided micro-strip sensors with outer dimensions of 6.2×2.2 mm^2, 6.2×4.2 mm^2, and 6.2×6.2 mm^2 and a strip pitch of 58 µm, strip lengths from 20 mm to 60 mm, and a thickness of 300 µm of silicon will be used.

The required momentum resolution $\Delta p/p = 1\,\%$ necessitates an ultra-low material budget. The need to operate the STS in a thermal enclosure at $\approx -10\,°\mathrm{C}$ imposes strong restrictions on the cooling of the power-dissipating front-end electronics for the readout of 2.1 million channels. The STS Technical Design Report has been approved by FAIR in August and published in October 2013 [52].

Ring Imaging Cherenkov detector

The Ring Imaging Cherenkov (RICH) detector will be used for electron identification up to momenta of 8 GeV/c to 10 GeV/c.

An important quantity is the pion suppression factor π_{suppr} defined as number of pions which are reconstructed in the STS and have a track projection lying in the RICH acceptance divided by the number of such pions which are misidentified as electrons

$$\pi_{\text{suppr}} = \frac{\text{no. of pions reconstructed in STS with track in RICH acceptance}}{\text{no. of pions misidentified as electrons}}. \tag{2.1}$$

A pion suppression factor of the RICH of at least 100 is required in order to get a combined pion suppression with the Transition Radiation Detector of 10^4 needed for the di-lepton spectra at SIS300. For SIS100 the background is already dominated by physical sources like γ-conversion in the target or π^0-Dalitz decays at a pion suppression factor of 10^3 (see section 2.6). The electron identification covers the full angular acceptance of the CBM detector, i.e. from 2.5° to 25° in polar angle and full azimuthal coverage. In order to accommodate the bending of tracks in the dipole magnet, all detectors behind the magnetic field will be wider by a factor 1.5 compared to the height [6].

The design of the CBM-RICH detector will be discussed in detail in section 2.5. The RICH Technical Design Report has been approved by FAIR in February 2014.

Muon detection system

The CBM experiment will measure di-leptons from vector meson decays by detecting both $e^\pm$ and $\mu^\pm$ pairs. While electrons are measured by using the RICH detector, muons are measured by a Muon Detection System (MUCH). The measurements will be conducted subsequently and both detectors are designed to be craned out of the acceptance and replaced by each other.

The Muon Detection System is an instrumented hadron absorber. It consists of 6 absorber layers made of iron plates with increasing thickness from 20 cm to 100 cm and 18 gaseous tracking chambers located in triplets behind each iron slab.

Behind the first and the second absorber, where a high hit rate density of up to 2 MHz/cm^2 will be present, Gas Electron Multiplier (GEM) detectors will be used. In the environment with lower hit occupancy further downstream, straw-tubes will be used. The total active area of the muon chambers will add up to 70 m^2.

For J/ψ measurements at SIS100, a MUCH start version with 3 tracking chamber triplets will be sufficient. Prototype GEM detectors and full-size straw-tube detectors have been built and tested. The Technical Design Report for the Muon Detection System has been submitted to FAIR in December 2013.

Transition radiation detector

For particle tracking and for electron and positron identification at momenta $p > 1.5\,$GeV/c, a Transition Radiation Detector (TRD) is being developed. It will be built from 9 to 10 detector layers in three stations located $4\,$m to $9\,$m downstream of the target with a total active area of $\approx 600\,\text{m}^2$. Particle rate densities of the order of $100\,\text{kHz/cm}^2$ for $10\,$MHz minimum bias Au$+$Au collisions at $25\,$AGeV are expected. In order to keep the occupancy sufficiently low, the minimum size of a single cell will not exceed $1\,\text{cm}^2$. Rotating every second TRD layer by $90°$ and using rectangular pads of $0.3\,$mm to $0.5\,$mm times $3\,$mm to $30\,$mm will provide a sufficient spatial resolution.

For the TRD detector, a pion suppression factor of 100 for particles with $p > 1.5\,$GeV/c at an electron efficiency of $90\,\%$ is required and will be reached with 9 layers. For measurements at SIS100, only one station with 2 to 4 detector layers will be used as an intermediate tracker between the STS and the TOF wall. Prototype detectors based on multi-wire proportional chambers (MWPC) have been built and tested with particle rates of up to $400\,\text{kHz/cm}^2$ without performance loss.

Time of flight detector

Hadrons will be identified by an array of Multi-gap Resistive Plate Chambers (MRPCs) via time-of-flight (TOF) measurements. The required time resolution is in the order of $80\,$ps. Being installed $6\,$m downstream of the target in the case of measurements at SIS100 and $10\,$m at SIS300, the TOF wall covers an area of $\approx 120\,\text{m}^2$. The rate density in the central part of the detector will reach $20\,\text{kHz/cm}^2$ for $10\,$MHz minimum bias Au$+$Au collisions at $25\,$AGeV. For this scenario, the occupancy can be kept below $5\,\%$ when using pads of $5\,\text{cm}^2$. Special low-resistivity glass will be used to cope with the high particle rates. In the outer region, at larger polar angles, the hit rate density is in the order of $1\,\text{kHz/cm}^2$ and conventional MRPCs with standard float glass can be used.

Prototype MRPCs for both the outer TOF wall built with standard glass and the inner part built with low-resistivity glass have been tested. For the latter, a time resolution of $40\,$ps to $60\,$ps at $20\,\text{kHz/cm}^2$ was achieved. The TOF Technical Design Report has been submitted to FAIR in December 2013.

Electromagnetic calorimeter

For the measurement of direct photons and neutral mesons like π^0 and η decaying into photons, a “shashlik” type electromagnetic calorimeter (ECAL) will be built. It will be composed of modules consisting of $140\,$layers of $1\,$mm lead and $1\,$mm scintillator, with cell sizes of $3{\times}3\ \text{cm}^2$, $6{\times}6\ \text{cm}^2$, and $12{\times}12\ \text{cm}^2$. The shashlik modules can be arranged either as a wall or in a tower geometry in a variable distance from the target.

Projectile spectator detector

The Projectile Spectator Detector (PSD) as the most downstream subdetector will be used for the determination of the collision centrality and the orientation of the reaction plane. Both quantities are of major importance for the analysis of event-by-event observables. Also for the quantification of collective flow, the determination of the reaction plane is essential. It is done by measuring the particles not participating in the collision, the so-called spectators. Therefore, the PSD is designed to measure the number of spectators from the projectile nucleus.

The PSD is a modular lead-glass calorimeter providing a very precise and uniform energy resolution. It consists of 44 individual modules with 60 lead/scintillator layers each and a front surface of $20\times20\,\mathrm{cm}^2$. The scintillator readout is performed via wavelength shifting (WLS) fibres by Multi-Avalanche Photo-Diodes (MAPDs) with an active area of $3\times3\,\mathrm{mm}^2$ and a pixel density of 10^4 per mm^2.

2.4.2 Data acquisition and first level event selector

Due to the focus of the CBM experiment on the measurement of rare probes and the required enormous event rates of up to 10 MHz [14] together with high multiplicities of charged tracks in heavy ion collisions, classical trigger concepts, e.g. based on hit multiplicities or energy deposit in certain detector components, are not suitable. The CBM experiment will therefore be operated in a so-called data-driven mode. That means that all data which is generated by the various subdetectors is transmitted to a large computing farm (GSI GreenIT cube) where event reconstruction and event selection, the so-called first-level event selection (FLES) takes place. The former is based on fast online event reconstruction which, as its most time consuming step, includes a track reconstruction using the Cellular Automaton [53] and Kalmann Filter [54] methods.

Triggering on certain events requires partial event reconstruction before the selection of events which are considered to be interesting enough to be stored for analysis. The need for an online event selection becomes clear when assuming an archiving rate of 1 GB/s and an event volume of about 10 kB for minimum bias Au+Au collisions which results in a maximum event rate of 100 kHz that can be accepted by the data acquisition. Therefore, measurements with event rates of 10 MHz require online event selection algorithms which reject the background events containing uninteresting event signatures by a factor of 100 at least.

For open charm production the trigger will be based on an online search for secondary vertices, which requires high speed tracking and event reconstruction in the STS and MVD. The highest suppression factor has to be achieved for J/ψ mesons where a high-energetic pair of electrons or muons is required in the TRD or in the MUCH and provides a fairly unique trigger signature. For low mass electron pairs, no online selection is possible due to the large number of rings/event in the RICH caused by the material budget of the STS. In the case of low mass muon pairs, some background rejection might be feasible.

On the detector side, the FEE will run in a self-triggered mode in which all hits passing a threshold are digitised and provided with a time stamp. The asynchronously time-stamped data messages will be shipped through fast optical links to a readout buffer into a high-throughput event building network. The decision whether data is stored or refused will be obtained after the FLES. Since no hardware triggers are used, the system will not be limited by latency but only by throughput [55].

It should be emphasised that online event reconstruction and event selection require a fundamental redesign of traditional approaches to data processing. Fast and parallel reconstruction algorithms on the software side and massive parallelisation on the hardware side are essential. In addition, a system with self-triggered FEE is very sensitive to noise which has to be minimised in order not to saturate the data links.

2.5 The CBM-RICH subdetector

As motivated in section 2.3, a RICH detector will be used in the CBM experiment to identify electrons and positrons at momenta below 10 GeV/c. Due to the huge abundance of pions produced in a heavy ion collision (see section 2.2), the separation of electrons and positrons from pions is the main task of the RICH detector. This section exposes the basics of RICH detectors and the design of the CBM-RICH detector.

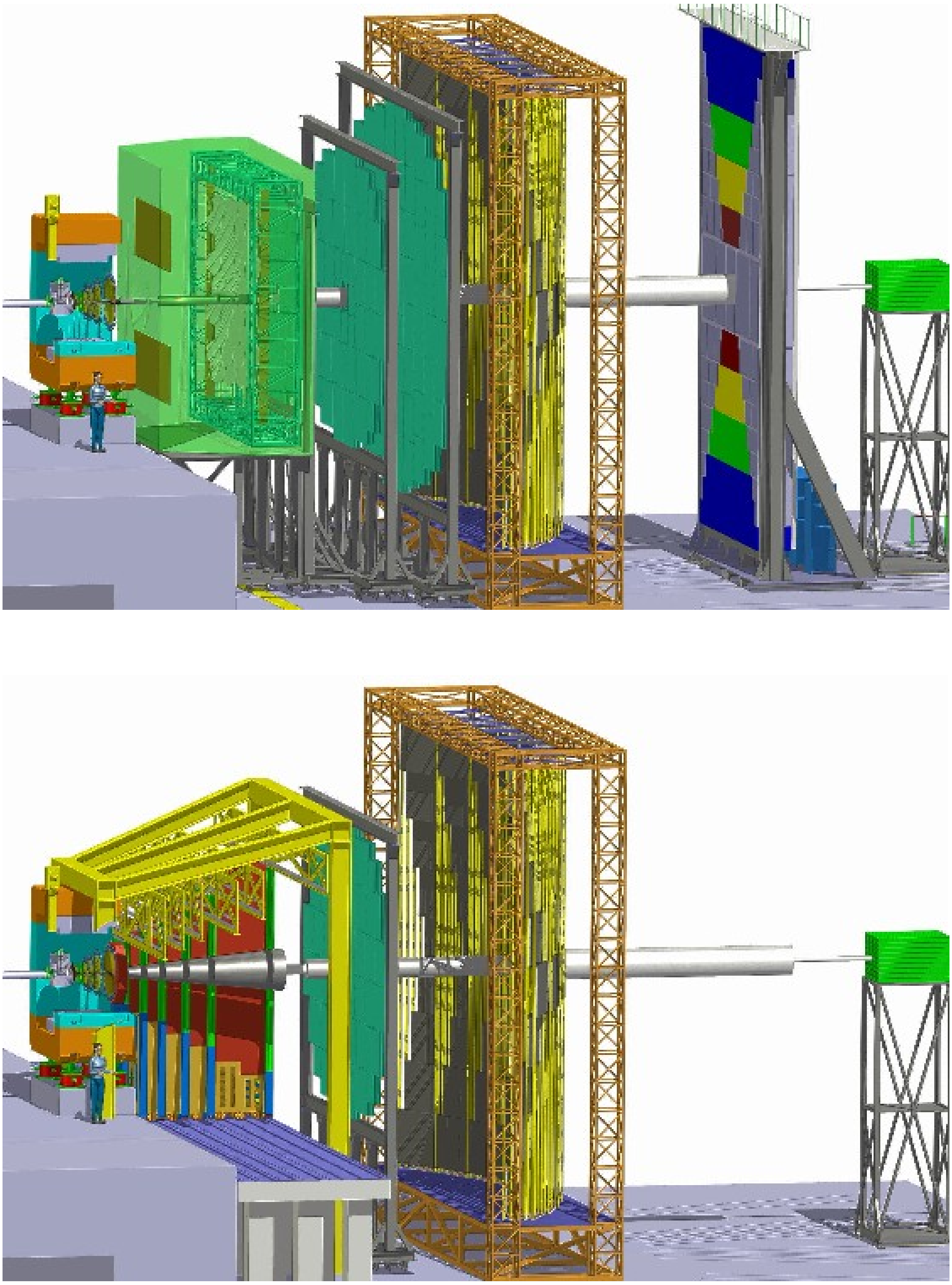

Figure 2.7 – The CBM experiment in electron (top) and muon configuration (bottom). The electron setup comprises the RICH and the TRD detectors for electron identification, the muon setup an instrumented hadron absorber for muon identification. The subdetectors in the top figure are from left to right: STS inside the dipole magnet, RICH, TRD, TOF, ECAL, PSD. In the bottom figure, STS, MUCH, TRD, TOF, PSD are sketched. Figures taken from [6].

2.5.1 Fundamentals of RICH detectors

The Cherenkov effect
A charged particle traversing a transparent medium with refractive index n at a velocity v faster than the speed of light in that medium emits continuous electromagnetic radiation in the visible and UV wavelength region (see [56] and references therein). The threshold velocity is given by

$$\beta = \frac{v}{c} \geq \frac{1}{n}. \tag{2.2}$$

This type of radiation is referred to as Cherenkov radiation according to Pavel Alekseyevich Cherenkov, who, together with Il'ja Mikhailovich Frank, and Igor Yevgenyevich Tamm, was awarded the Nobel Prize in Physics in 1958 "for the discovery and the interpretation of the Cherenkov effect" published in the years 1934 to 1937 although it was observed before by other scientists. M. Curie observed a blue light from radium solutions already in 1920 and L. Mallet made observations from which he deduced that the spectrum is continuous [57, 58, 59] in contrast to fluorescence light which was extensively studied at that time [60]. But it was P. Cherenkov who observed the angular distribution of the radiation, its dependence on n and β and who measured the spectral distribution and total intensity which was the experimental basis to test the theory of Frank and Tamm [61].

The occurrence of Cherenkov radiation can be explained by the polarisation of the molecules of the medium that a charged particle passes through. If the speed of the charged particle is below the medium speed of light, the medium is polarised in all directions in a solid angle of 4π. In this case, radiation from the polarised molecules cancels due to destructive interference. In the case of a charged particle exceeding the medium speed of light, however, only those molecules within the distance $c/n \cdot t$ are polarised. Due to this asymmetry, a conical wavefront of Cherenkov photons propagates through the medium. From geometrical considerations, it can be deduced that the angle θ between the path of the charged particle and the Cherenkov cone is determined by

$$\cos\theta = \frac{1}{\beta n}. \tag{2.3}$$

The azimuthal emission angle ϕ has a rotationally symmetric distribution. The intensity and the spectrum of Cherenkov radiation is given by the Frank-Tamm relation [61]

$$\frac{d^2N}{dE\,dl} = \frac{\alpha z^2}{\hbar c}\left(1 - \frac{1}{(\beta n)^2}\right) = \frac{\alpha z^2}{\hbar c}\sin^2\theta = \frac{\alpha z^2}{\hbar c}\sin^2\theta \tag{2.4}$$

with N being the number of photons emitted with energy between E and dE, the length l of the particle path through the medium, the electromagnetic fine structure constant α, and the electric charge z of the particle in units of the elementary charge. Using the relation $E = \frac{hc}{\lambda}$, one obtains the dependence of the Cherenkov spectrum on the wavelength λ

$$\frac{d^2N}{d\lambda\,dl} = \frac{2\pi\alpha z^2}{\lambda^2}\sin^2\theta \tag{2.5}$$

which shows that the number of photons emitted per interval of wavelength and radiator length is proportional to λ^{-2} and most of the radiation is emitted in the UV range.

Operating principle of RICH detectors
Like all Cherenkov detectors, the first being proposed and demonstrated in practice in 1977 [62], the CBM-RICH detector makes use of the Cherenkov effect. Using a photon detector, projections of the Cherenkov

cone can be measured in form of rings. Apart from relatively new developments where complicated patterns are registered on the photon detector plane [63, 64], it can be distinguished between *proximity focusing RICH detectors*[2] (e.g. the RICH detector of the Alpha Magnetic Spectrometer (AMS) installed on the International Space Station [65]) and *projective RICH detectors*. While a proximity focusing RICH detector consists of two basic components, a fairly thin radiator and a photon detection system, a projective RICH detector makes use of a focusing optic like a lens or a mirror in combination with a long radiator, usually a gas volume. The CBM-RICH detector is designed as projective detector with focusing mirror. Its operating principle will be described in the following.

Cherenkov photons are emitted along the particle trajectory through the radiator with an angle θ. They are then reflected by a spherical mirror with radius of curvature R onto a photon detector located in the focal plane of the mirror at a distance equal to the mirror focal length $f = R/2$. With this geometry, all Cherenkov photons emitted along a straight track, independently of their origin on that track, are focused on the detection plane where they form a ring.

In a RICH detector with spherical mirror, parallel particles with the same momentum cause the same ring image, i.e. rings with the same radius and the same centre coordinates. Inclined particles with same momentum cause rings with the same radius and shifted centre coordinates.

The ring radius is given by the Cherenkov angle and the focal length of the mirror

$$r = f \cdot \tan\theta = \frac{R}{2} \cdot \tan\theta. \tag{2.6}$$

Since the focal length is a detector constant, r depends only on the Cherenkov angle and is therefore a unique function of β. For small angles, equation (2.6) can be approximated as function of mass m and momentum p of the Cherenkov light producing particle [66]

$$r \approx f\sqrt{2 - \frac{2}{n}\sqrt{1 + (\frac{mc}{p})^2}}. \tag{2.7}$$

Knowing p which is measured in the case of CBM by the STS, the particle can be identified by determination of m via measurement of r in the RICH detector.

Integrating equation (2.5) over λ and l, merging all constants, and assuming a constant refractive index yields

$$N = N_0 \cdot L \cdot \sin^2\theta \tag{2.8}$$

with L being the radiator length and N_0 the *figure of merit* of a RICH detector describing the detector quality in terms of the photon yield. For the comparison of RICH detectors however, the figure of merit has to be set in relation to the refractive index of the radiator due to the strong dependence of the number of Cherenkov photons on n (see equation (2.4).

Chromatic dispersion

In reality, the refractive index is a function of wavelength, $n = n(\lambda)$, which is referred to as *chromatic dispersion*. For the choice of the radiator material, chromatic dispersion has to be considered because of the dependence of the Cherenkov ring radius on n according to equation (2.7). In practise, a trade-off has to be made between the selection of radiator, mirror, and photon detector for a high UV-sensitivity leading to a large photon yield one the one hand and the loss of radius resolution due to chromatic dispersion on the other hand, which, for common radiators, increases towards the UV region.

---

[2] A proximity focusing RICH detector is restricted to a thin radiator in order to have a sharp ring image on the photon detection plane. This, in turn, requires a high refractive index of the radiator to produce enough photons. Since the CBM-RICH detector needs a low refractive index for electron identification (cf. section 2.3), a proximity focusing RICH is no option for CBM.

2.5.2 The RICH detector for the CBM experiment

The CBM-RICH detector will operate in an environment that is characterised by [6]

- interaction rates of up to 10 MHz,
- track densities of approximately 1000 charged particles in central Au+Au collisions,
- rather high radiation level,
- large number of secondary electrons produced in the material in front of the RICH detector, thus high ring densities in the RICH detector,
- magnetic stray field due to the close vicinity of the CBM dipole magnet,
- possibility to exchange RICH detector and Muon Detection System in order to allow independent measurements of the di-lepton signals at low and high masses,
- beam pipe with low material budget and beam pipe access.

In order to meet both the physics requirements presented in section 2.4.1 and a good performance in the demanding environmental conditions listed above, the CBM-RICH detector is designed as presented in the following. The detector design is foreseen to rely on a large extend on commercially available parts from industry. It consists of a gaseous radiator volume, a focusing spherical mirror, and a photon camera. It can be considered as new development of a “standard RICH” [67] detector. The mechanical design of the CBM-RICH detector is shown in Fig. 2.8. Details on the technical design of the detector can be found in [6]. The main parameters and dimensions are summarised in Tab 2.1.

Concept	focusing gas RICH detector
Dimensions	2 m × 5.14 m × 3.93 m (length × height × width)
Acceptance	0° to 35° (horizontal) / 0° to 25° (vertical)
Radiator	CO_2 gas, atmospheric pressure (+2 mbar)
Radiator volume	$\approx 35\,\mathrm{m}^3$
Radiator length	1.7 m
Focusing mirror	glass mirror, Al+MgF_2 coating, 6 mm thick
Mirror size	$13\,\mathrm{m}^2$
Focal length	1.5 m (radius 3 m)
Photon sensor	Multianode or Micro Channel Plate photomultiplier tubes
Active camera area	$2.4\,\mathrm{m}^2$
Overall channel no.	$\approx$ 55 000 channels

Table 2.1 – Summary of the main CBM-RICH design parameters and dimensions. Table adapted from [6].

Radiator
The separation of electrons and pions at momenta below 10 GeV/c requires a low refractive index of the radiator and therefore determines the radiator to be a gas. A CO_2 radiator is foreseen which has a threshold Lorentz factor of $\gamma_{\mathrm{th}} = 1/\sqrt{1 - 1/n^2} = 33.3$, given a refractive index of $n = 1.00045$ at a temperature of

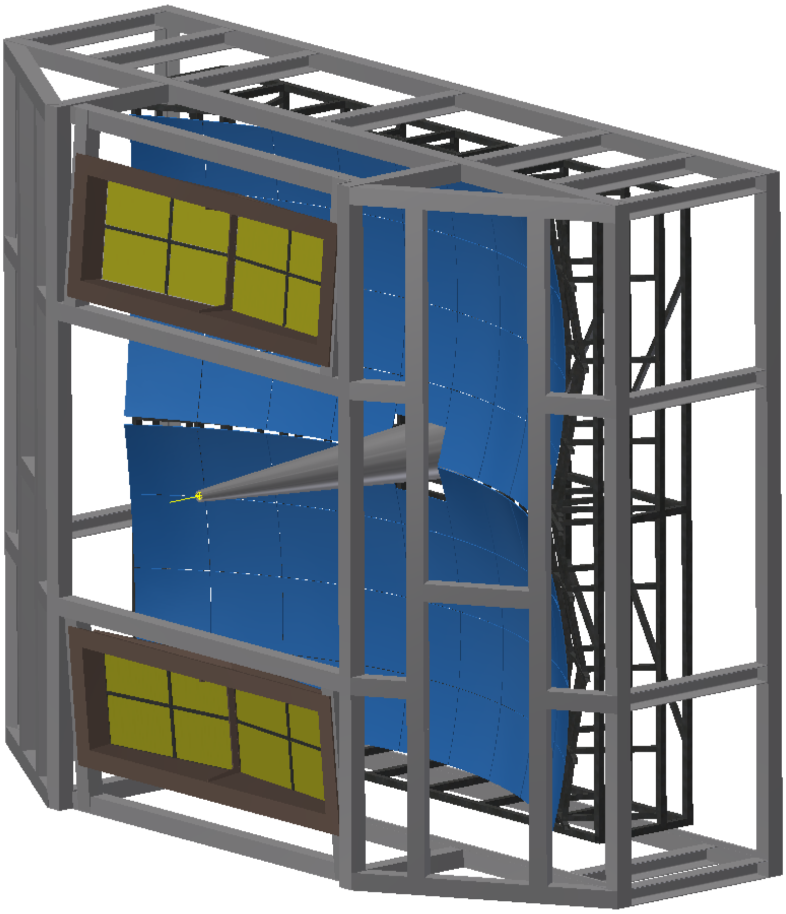

Figure 2.8 – Mechanical design of the CBM-RICH detector. Charged particles enter the detector from the left and create Cherenkov photons in the radiator volume which are reflected by spherical mirrors (blue) onto the upper and lower camera modules (yellow). The light-weight mirror support structure is shown in black. The grey cone indicates the beam pipe and grey bars the outer support structure. Figure taken from [6].

0 °C, a pressure of 1000 mbar, and a wavelength of 600 nm [68]. The Cherenkov threshold is $p = 4.65$ GeV/c for charged pions and $p = 0.03$ GeV/c for electrons and positrons. The threshold for kaons is $\approx$ 16 GeV/c. The saturated Cherenkov angle for ultrarelativistic particles is $1.72°$. Assuming that pions can be separated from electrons up to 90 % of the maximum Cherenkov opening angle $\theta = \arccos(1/n)$, electrons and pions can be separated up to $\approx$ 10 GeV/c with CO_2 as radiator gas.

The radiator length is 1.7 m and the volume $\approx 35\,\mathrm{m}^3$. Since the RICH detector will be placed between the STS in the dipole magnet and the TRD detector, its overall length is constrained by the distance between the magnet and its shielding yokes at about 1.6 m from target and the first TRD station. On the one hand, a long radiator is favourable due to the proportionality between photon yield and radiator length according to equation (2.8). On the other hand, a short gap between the tracking detectors STS and TRD is advantageous for tracking which requires a short RICH detector in between. In consequence, the overall length of the RICH detector including radiator, mirror, and support structure is foreseen to be $\approx$ 2 m.

When designing a RICH detector “one has to be extremely careful in matching the choice of (gas-)radiator with the sensitive wavelength range of the photon detection system” [66]. In the case of the CBM-RICH, the low wavelength limit of the photomultiplier sensitivity (see section 3.4) coincides well with the absorption edge of CO_2 at $\approx$ 185 nm (see section 6.2.1).

For CO_2, chromatic absorption becomes sizeable only in the region below 200 nm (see section 6.2.1) and does not deteriorate the Cherenkov ring resolution significantly as shown below.

Due to the fact that CO_2 does not exhibit a high level of scintillation, it is often added to other radiator gases as quenching gas. Approximately 5 photons/MeV, mostly in the blue wavelength range, are expected [69]. An energy deposit in the radiator of $\approx$ 1 GeV is expected for a central Au+Au collision with $\approx$

1000 minimum ionizing particles [6] leading to 5000 scintillation photons emitted isotropically along the particle tracks. This leads to ≈ 250 measured additional photons distributed homogeneously over the photon detector plane when conservatively assuming that $20\,\%$ of the photons reach the photon camera with $25\,\%$ of them being detected. Given the total of $55\,000$ channels, noise from scintillation will add up to $0.45\,\%$ of all channels. This is well within the noise level that the CBM-RICH detector can tolerate without performance loss [6].

Mirror

The mirror of the CBM-RICH detector is split into two parts above and below the beam pipe. Each mirror half is oriented towards a photon detection plane and part of a sphere with $R = 3.00\,\mathrm{m}$. The total area of the two mirror halves is $12.96\,\mathrm{m}^2$. The mirror halves consist of 36 mirror tiles each arranged in four rows of nine tiles. The tiles themselves have a slightly trapezoidal shape in order to minimise gaps in between to $3\,\mathrm{mm}$ to $4\,\mathrm{mm}$. Two different tile sizes are foreseen, 430/425.6 mm × 425 mm for the inner two rows and 425.5/412.5 mm × 425 mm for the outer rows.

The mirror tiles are made of a $6\,\mathrm{mm}$ thick SIMAX glass substrate front-coated with Al+MgF_2. Aluminium provides a good reflectivity in both the visible and the UV wavelength region down to below $200\,\mathrm{nm}$. The MgF_2 layer is used as protective layer in order to prevent the formation of UV absorbing aluminium oxide. Mirror tiles from JLO Olomuc were successfully tested in a prototype (see section 5.1), characterised in terms of homogeneity [70] and reflectivity [71], and chosen to be used for the CBM-RICH detector.

A tripod concept is foreseen for mounting the mirror tiles on an aluminum frame. Each mirror tile is glued to three actuators allowing for the precise alignment of the tiles in a sphere.

In order to reduce the production of secondary particles, the material budget of the RICH detector has to be kept low. The mirror support structure is therefore designed as a compromise between stability and light weight.

Camera

Task of the CBM-RICH photon camera is the detection of Cherenkov photons produced by charged particles in the gas radiator and reflected by the focusing mirror. The camera is developed for the detection of single photons with high efficiency. A precise measurement of position and time of arrival of each photon is required as input for the ring reconstruction algorithm discussed in section 2.5.3.

The photon camera of the CBM-RICH detector consists of two parts, one above and one below the beam pipe in the focal plane of the spherical mirrors. The two photon detector planes are located in front of the CBM dipole magnet shielded by the magnet yokes. The Cherenkov rings from the upper mirror half will be projected onto the upper photon detector, rings from the lower mirror half onto the lower photon detector. Each of the two photon detector planes is divided into two parts in order to optimise the angle towards the mirror. Thus, the camera consists of four separated areas, so-called camera modules. Each module covers an area of $0.6\,\mathrm{m} \times 1.0\,\mathrm{m}$ (height × width). The total active camera area is $2.4\,\mathrm{m}^2$.

The CBM-RICH design foresees the usage of commercially available multianode photomultiplier tubes (MAPMTs) as photon sensors. The use of Micro Channel Plate (MCP) sensors is considered as alternative [6]. Due to the good geometrical coverage of these sensor types, no focusing elements like lenses or Winston cones are envisaged.

Magnetic stray field in the camera region

According to TOSCA[3] calculations, the photon camera is exposed to significant magnetic stray fields in the order of $10\,\mathrm{mT}$ to $50\,\mathrm{mT}$. Measurements show that the single photon detection efficiency of the foreseen MAPMTs drops significantly for values exceeding $1\,\mathrm{mT}$ to $2\,\mathrm{mT}$ especially in the edge and corner pixels [6]. Therefore, the magnetic field strength in the region of the photon sensors has to be kept below this value.

In order to cope with the magnetic stray field in the region of the photon camera, two design options are considered and currently studied. The first option is to rotate the two mirror planes and to move the camera modules further away from the beam axis where the magnetic stray field is lower. In addition, a shielding box enfolding the camera modules can reduce the magnetic field strength in the region of the photocathodes significantly. The second option is the use of a second mirror reflecting the Cherenkov photons to the camera positioned farther away from the magnet. This option, however, requires a larger camera surface due to an increased focal length. Details on all design options can be found in [6].

Cherenkov angle resolution

A good Cherenkov angle resolution is required for an efficient and clean particle identification with the CBM-RICH detector. A good resolution leads first to a high reconstruction efficiency, and second to a good electron pion separation capability, especially at high momenta.

Several sources limit the Cherenkov angle resolution in the RICH detector: granularity of the photon sensors, mirror quality, chromatic dispersion in the radiator gas, multiple scattering, and the magnetic stray field [60, 72]. Their contribution to the Cherenkov angle resolution is estimated as follows [6].

- **Photon sensor granularity**
  The effective pixel size of the anticipated photon sensor H8500D-03 is $6.125\ \mathrm{mm}\times 6.125\ \mathrm{mm}$ resulting in a measurement error of $6.125\,\mathrm{mm}/\sqrt{12} = 1.8\,\mathrm{mm}$ which corresponds to an error in the Cherenkov angle resolution of $\sigma_{\mathrm{pixel}} \approx 1\,\mathrm{mrad}$.
- **Mirror quality**
  The errors from mirror inhomogeneities and angular deviations of the mirror are neglected.
- **Chromatic dispersion**
  The error from chromatic dispersion of the $\mathrm{CO_2}$ radiator can be estimated to be $\sigma_{\mathrm{disp}} \approx 1\,\mathrm{mrad}$ [6].
- **Multiple scattering**
  The error from multiple scattering (MS) of the Cherenkov light emitting particles in the radiator gas is inversely proportional to the momentum p. With the radiator length $L = 1.7\,\mathrm{m}$ and the $\mathrm{CO_2}$ radiation length $X_0 = 183.1\,\mathrm{m}$, the error in mrad is given by [60]

  $$\sigma_{\mathrm{MS}} = \frac{2}{3} \cdot 13.6\,\mathrm{MeV/c} \cdot \sqrt{\frac{L}{X_0}} \cdot \frac{1}{p} = 0.874\,\mathrm{MeV/c} \cdot \frac{1}{p}. \tag{2.9}$$

  Thus, the Cherenkov angle resolution due to multiple scattering is $\sigma_{\mathrm{MS}} = 2.2\,\mathrm{mrad}$ for $p = 0.4\,\mathrm{GeV/c}$, $\sigma_{\mathrm{MS}} = 0.9\,\mathrm{mrad}$ for $p = 1\,\mathrm{GeV/c}$, and $\sigma_{\mathrm{MS}} = 0.1\,\mathrm{mrad}$ for $p = 8\,\mathrm{GeV/c}$.

  $0.4\,\mathrm{GeV/c}$ is the lower momentum cut-off in the CBM-RICH due to the bending power of the magnetic field for the full field strength. For a reduced field strength of $70\,\%$ of the nominal value, which may be planned for special di-electron runs, the cut-off is at $0.3\,\mathrm{GeV/c}$, and at $0.2\,\mathrm{GeV/c}$ for $50\,\%$ of the nominal magnetic field strength. In these cases, the Cherenkov angle resolution decreases to $\sigma_{\mathrm{MS}} = 2.9\,\mathrm{mrad}$ and $\sigma_{\mathrm{MS}} = 4.4\,\mathrm{mrad}$, respectively.

---

[3] The TOSCA software package is a module of OPERA-3d, a general-purpose finite element software for the simulation of electromagnetic devices. http://www.himarcsimulations.com/wp-content/Tosca_data_sheet.pdf

- **Magnetic stray field**
  The error on the Cherenkov angle resolution due to the bending of the Cherenkov light emitting charged particles in the radiator volume is estimated to be [60]

  $$\sigma_{\mathrm{B}} = 55.1 \frac{\mathrm{MeV}}{\mathrm{T\,m}} \cdot \frac{L B_{\mathrm{T}}}{p} \tag{2.10}$$

  with the radiator length L in m, the magnetic field strength B in T, and its transverse component B_{T} relative to the particle momentum p.

  In the current design of the CBM-RICH detector, the magnetic transverse field strength B_{T} integrated along the beam axis adds up to $\approx 0.077\,\mathrm{T\,m}$ leading to $\sigma_{\mathrm{B}} = 18\,\mathrm{mrad}$ for $p = 0.4\,\mathrm{GeV/c}$, $\sigma_{\mathrm{B}} = 7.2\,\mathrm{mrad}$ for $p = 1\,\mathrm{GeV/c}$, and $\sigma_{\mathrm{B}} = 0.9\,\mathrm{mrad}$ for $p = 8\,\mathrm{GeV/c}$. Especially for low momentum particles, the magnetic stray field is the dominating error source and the main reason for a reduced reconstruction efficiency at lowest momenta [6].

  However, the CBM dipole magnet has been redesigned causing a shift of the RICH detector by $\approx 20\,\mathrm{cm}$ compared to the current position which would lower the integrated magnetic field along the beam axis to $\approx 0.04\,\mathrm{T\,m}$. In this case, no significant loss in ring reconstruction is expected anymore [6]. Moreover, a shift of the RICH detector allows for larger field clamps in order to further reduce the magnetic stray field in the region of the RICH detector.

The above listed errors correspond to the Cherenkov ring resolution of single photons. Since all errors are independent, they can be added quadratically. According to [72], the overall error σ for N_{det} detected Cherenkov photons per ring is scaled[4] with $1/\sqrt{N_{\mathrm{det}}}$ and reads

$$\sigma = \frac{\sqrt{\sigma^2_{\mathrm{pixel}} + \sigma^2_{\mathrm{mirror}} + \sigma^2_{\mathrm{disp}} + \sigma^2_{\mathrm{MS}} + \sigma^2_{\mathrm{B}}}}{\sqrt{N_{\mathrm{det}}}}. \tag{2.11}$$

Due to the $1/p$-dependence of σ_{MS} and σ_{B}, the overall error σ becomes large for low-momentum particles. Since the pion threshold is at $p = 4.65\,\mathrm{GeV/c}$, this does not affect the electron pion separation capabilities. The ring reconstruction at low momenta, however, suffers from the decreasing Cherenkov angle resolution towards low p.

For 20 detected photons per Cherenkov ring and neglecting errors from the mirror quality, the overall error is calculated according to equation (2.11) to be $\sigma = 0.38\,\mathrm{mrad}$ for $p = 8\,\mathrm{GeV/c}$ corresponding to $1.3\,\%$ of the saturated Cherenkov opening angle for ultrarelativistic particles of $1.72° = 30.02\,\mathrm{mrad}$.

For an overall Cherenkov angle resolution of $0.57\,\mathrm{mrad}$ ($1.9\,\%$ resolution), pions and electrons are separated by 5 sigma up to about $11\,\mathrm{GeV/c}$ [6].

2.5.3 Ring reconstruction and particle identification

The ring reconstruction and electron identification routines, being the basis of physics feasibility and detector performance studies, are implemented in the CbmRoot framework [74].

Challenges for the ring reconstruction
The main challenge for the ring reconstruction is the high hit multiplicity in heavy ion collisions. For central Au+Au collisions at 25 AGeV, around 1000 charged particles are produced in the RICH acceptance,

---

[4] The scaling of σ_{MS} (multiple scattering) and σ_{B} (track bending in the magnetic field) with $1/\sqrt{N_{\mathrm{det}}}$ is under debate [73] although simulations are in agreement with equation (2.11) [6].

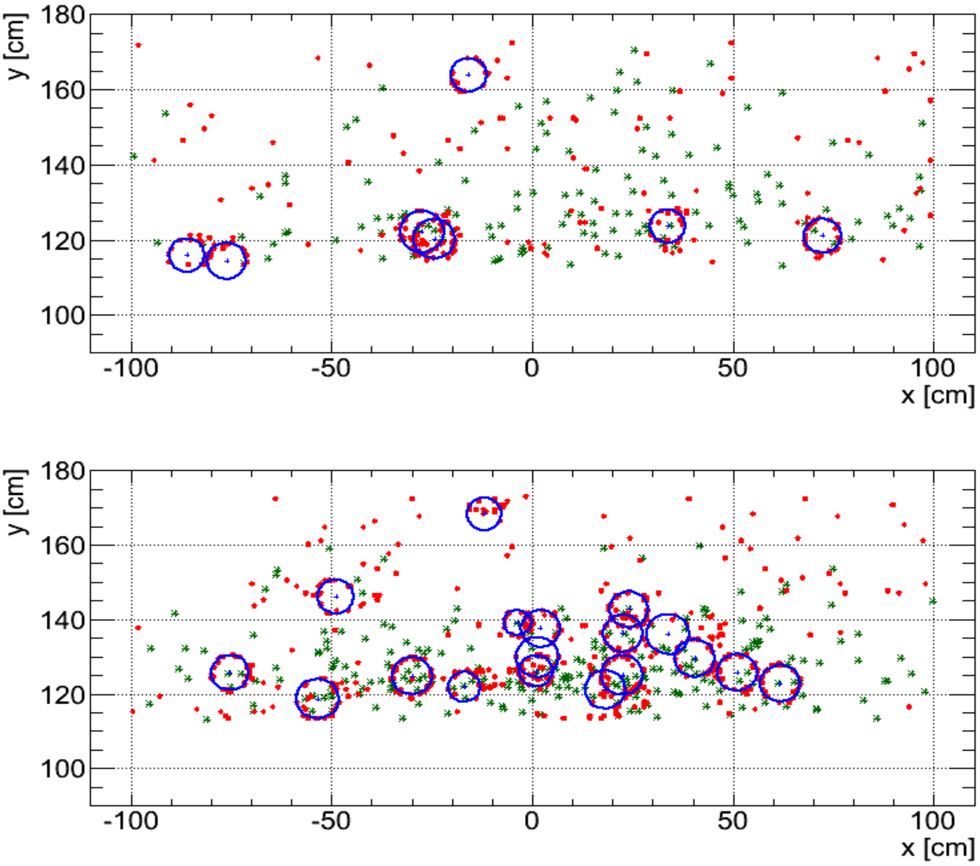

Figure 2.9 – Typical response of the upper two camera modules of the CBM-RICH detector to an event with a central Au+Au collision at 8 AGeV (top) and 25 AGeV beam energies (bottom). Blue circles: reconstructed rings; red points: RICH hits including noisy channels ($0.35\,\%$); green markers: reconstructed track projections onto the photon detector plane. Figures taken from [6].

many of them being charged pions with high momenta. In addition, photon generated in the interaction are converted to $e^{\pm}$ pairs by conversion processes in the detector material or even in the target. This results in ≈ 65 rings per event on the RICH camera. Figure 2.9 shows the response of the upper two camera modules to Au+Au collisions at 8 AGeV and 25 AGeV. The maximum hit density is ≈ 0.5 hits/cm^2/event.

Other challenges are the high interaction rate of up to $10\,$MHz requiring fast reconstruction algorithms, the varying number of hits per ring from 5 to 40, and the elliptic shape of the rings in the outer regions of the camera (see below).

Event reconstruction scheme

The event reconstruction in the CBM-RICH detector consists of several steps schematically shown in Fig. 2.10. In the first step, tracks reconstructed in the STS are extrapolated to the mirror. The tracks are then reflected onto the camera plane. The second step is the search and grouping of hits belonging to a ring, and the ring or ellipse fitting as described below. The ring finding and fitting is stand-alone, i.e. independent of extrapolated STS tracks. The fit provides radius and centre coordinates for each ring. In the third and final step, found rings are matched with the extrapolated STS tracks and particle identification is done using the ring radius information from the RICH and the momentum information from the STS.

For the CBM-RICH detector, this way of ring search reveals a superior performance compared to a track-

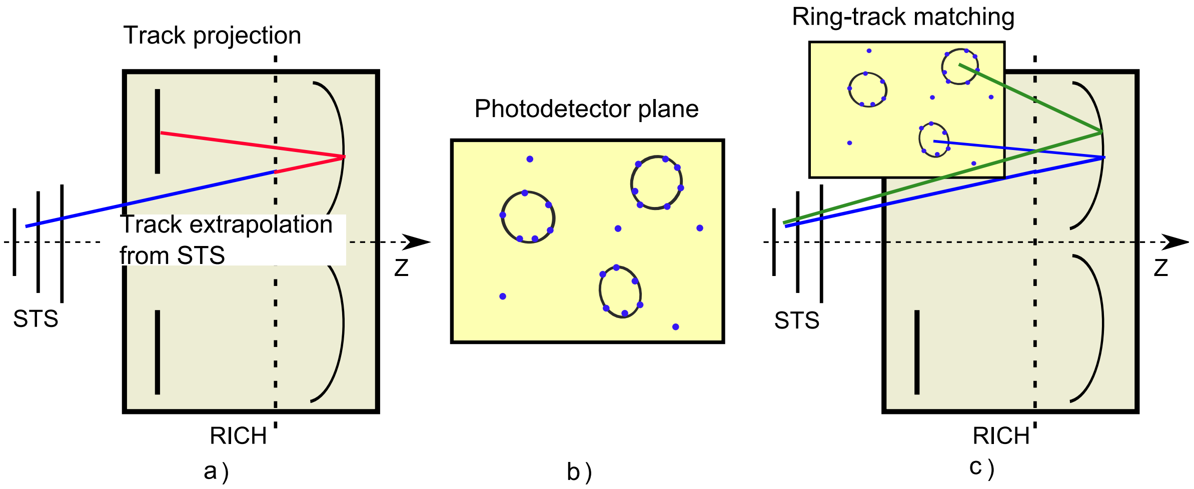

Figure 2.10 – Steps of the event reconstruction in the CBM-RICH detector. a) Schematic view of the STS and RICH detectors, STS track extrapolation and projection onto the photon detector plane; b) photon detector plane with hits and reconstructed rings; c) RICH ring and STS track matching. Figure taken from [6].

based ring search, where hits within a certain distance around a track projection are searched for. The reason is the high hit density on the camera plane [75].

Ring recognition algorithm

The ring recognition algorithm comprises three stages: ring-candidate finding, ring fitting, and ring selection.

1. **Ring-candidate finding**
   The search for ring-candidates is based on the Hough Transform method [76], a standard method for curve recognition in digital images. For the ring search, hit triplets, which unambiguously define a ring, are combined. Then, centre x_c, y_c and radius r of these rings are calculated from every hit triplet using Hough Transform equations [77]. With these parameters, a 2D histogram for x_c and y_c and a 1D histogram for r are filled. Maxima in these histograms correspond to the centre coordinates and radii of the Cherenkov rings. If the maxima exceed a certain height, the parameter set is considered as ring-candidate.

   The main disadvantage of the Hough Transform method is that it requires very large combinatorics making the algorithm intrinsically slow. Thus, instead of combining all possible hit triplets in the whole camera plane, only hits within a distance corresponding to a maximum ring radius are combined. This localised Hough Transform method decreases the computing time significantly [6].

2. **Ring fitting**
   In order to estimate the ring parameters of ring-candidates precisely, a ring fitting algorithm is applied. Due to the high interaction rate and the large number of rings in the CBM-RICH detector, the main requirement for the ring fitting algorithm is a high computational speed while keeping a reasonable accuracy. Therefore, a circle fitting procedure is used due to its simplicity and very high computational speed.

   The implemented Chernov-Ososkov-Pratt (COP) algorithm [78] minimises the functional

$$\bar{M}(a,b,r) = \sum_{i=1}^{N} \left[\left((x_i - x_\mathrm{c})^2 + (y_i - y_\mathrm{c})^2 - r^2 \right)^2 / 4 \cdot r^2 \right] \tag{2.12}$$

where (x_i, y_i) are the coordinates of the hits belonging to the ring and x_c, y_c the center coordinates of the ring. For the minimisation of the functional, the Newton method for non-linear equations with one variable is used. The algorithm converges for 3 to 4 iterations and is very robust to the initial parameters [77].

Since the Cherenkov rings projected on the photon camera have a slightly elliptic shape, the ring fitting algorithm is succeeded by an ellipse fitting algorithm which further improves the parameter determination[5]. The implemented ellipse fitting algorithm is based on the Taubin method [79]. The functional to be minimised is the squared sum of the distance between the hits belonging to the ring and the ellipse described by $P(x) = Ax^2 + Bxy + Cy^2 + Dx + Ey + F$ with the minimising parameters A, B, C, D, E, F. Using the Tailor expansion of the functional, the algorithm is very fast, non-iterative and does not need starting parameters [77].

3. **Ring selection**
The array of ring-candidates, obtained from the localised Hough Transform, does not only include true Cherenkov rings but also rings from random combinations of hits. The latter are referred to as *fake rings*[6]. In order to reject fake rings, a ring quality estimation based on six parameters is done. These parameters are the number of hits in the ring, the ring radius, the χ^2 of the ring fit, the position of the ring on the camera plane, the uniformity of the hit distribution on the ring and the number of hits in a small corridor around the ring. For the estimation of the ring quality, an artificial neural network (ANN) with six input neurons corresponding to the six quality parameters is used. The ANN contains 12 neurons in the hidden layer. The output value of the ANN determines the ring quality. In the ANN training, the output value for fake rings was set to -1 and $+1$ for correctly found rings. For real events, the output value of the ANN is not binary and values only concentrate around ± 1. One therefore gets a ring quality measure or probability, whether a ring-candidate was correctly found or not.

The ring quality is used for the selection of good rings from the array of found ring-candidates. In a first step, the array of rings is sorted by the ring quality starting with rings with highest quality. In a second step, the algorithm checks each ring-candidate for shared hits with all other ring-candidates. If the candidate shares more than 25 % of its hits with better quality rings, it is rejected.

2.6 Feasibility studies

Ring quality parameters

A detailed study of fit parameters from rings reconstructed in response to electrons and positrons generated at the primary vertex, so-called *primary electrons*, tracked through the CBM-RICH detector and projected on the $2.4\,\mathrm{m}^2$ camera plane is presented in [6]. The main results shall be mentioned here.

The number of hits in the ring after ring finding (*hit multiplicity*) follows a gaussian distribution with a mean of 26.1 hits and a width of 4.4 hits per electron induced Cherenkov ring.

Since the camera modules are plane and follow only approximately the spherical focal plane of the mirror, the ring radius varies in dependence of the ring position on the camera. The mean value of the radius varies from 4.3 cm at the edges in the outer part to 5.2 cm in the inner part. Similarly, the radius resolution of the rings varies as function of the position on the camera. The local radius resolution is about a factor 2 better than the integrated one and adds up to 1 % to 2 % which is well in agreement with the expectation presented in section 2.5.2.

---

[5] In fact, the ellipse fitting is only applied after ring selection in step three in order to save computing time.

[6] In the context of ring reconstruction, it is distinguished between *fake rings* which are formed by random combinations of hits and *clone rings* which are repeatedly found rings.

Since it is difficult to define a ring resolution, a ring thickness respectively ring sharpness, quantified by the parameter *dR*, is used. *dR* is defined as RMS of the distribution of the distance between each hit and the circular ring fit. Depending on the momentum, *dR* increases from $0.3\,\text{cm}$ for $p > 1\,\text{GeV/c}$ to $0.43\,\text{cm}$ for $p = 0.5\,\text{GeV/c}$, mainly due to the magnetic stray field in the RICH.

The ellipticity of the rings is quantified by the ratio between minor (B) and major (A) half-axes of the fitted ellipse. The mean value on the whole camera is $B/A = 0.92$. Rings in the centre of the camera have a more circular shape.

RICH reconstruction performance

Apart from the pion suppression factor, defined in equation (2.1), important quantities related to the RICH detector are the *ring reconstruction efficiency* and the *electron identification efficiency*.

The ring reconstruction efficiency is the number of correctly found rings after reconstruction divided by the number of reconstructable rings in the RICH acceptance, i.e. rings with at least 7 detected hits in the RICH.

The electron identification efficiency is defined as the number of correctly reconstructed electrons, matched and identified in the STS+RICH(+TRD)+TOF detectors divided by the number of electrons in the STS+RICH +(TRD)+TOF detector acceptance. The acceptance, in turn, is defined by requiring at least 4 consecutive STS points, at least 7 RICH hits, at least 8 TRD points and one TOF hit[7].

In order to study the reconstruction performance and the pion suppression capability of the CBM-RICH detector, central Au+Au collisions at beam energies of 8 AGeV and 25 AGeV were simulated.

Figure 2.11 shows the ring reconstruction efficiency for primary electrons in dependence of the number of hits per ring. The ring reconstruction efficiency is very low for less than 10 hits and rises rapidly with increasing number of hits. In the case of 8 AGeV beam energy, the ring reconstruction efficiency is close to $100\,\%$ for > 18 hits and in the case of 25 AGeV for > 20 hits.

In Figures 2.12 and 2.13, the electron identification efficiencies and pion suppression factors are shown for 8 AGeV and 25 AGeV beam energy, respectively. The momentum integrated electron identification efficiency is $\approx 85\,\%$ in both cases. The momentum integrated pion suppression factors for the RICH detector add up to $\pi_{\text{suppr}} = 1435$ for 8 AGeV and $\pi_{\text{suppr}} = 360$ for 25 AGeV. This numbers fulfill the requirement of $\pi_{\text{suppr}} > 100$ mentioned in section 2.4.1.

Background rejection strategy

A possible source of background, i.e. electron positron pairs other than those stemming from leptonic low mass vector meson decays, are pions which are misidentified as electrons. With a pion suppression factor combining all PID detectors (RICH, TRD and TOF) of the order of 10^4, misidentified pions are a minor background source only [6].

It was pointed out in section 2.3 that di-electrons from low mass vector mesons are rare probes due to low branching ratios of the leptonic decay channels. The fact that a huge background has to be under control when studying di-electrons in heavy ion collisions is a major challenge for di-lepton measurements.

In the case of di-electrons, the main background stems from random combinations of e^+ and e^- from

1. hadron decays after freeze-out, mostly π^0 Dalitz decay ($\pi^0 \rightarrow \gamma + e^+ + e^-$),
2. γ-conversion ($\gamma \rightarrow e^+ + e^-$) in the detector material in front of the RICH.

---

[7] In the simulation, it is distinguished between *point* (pure Monte Carlo information of a particle passing the detector) and *hit* (information of a particle passing the detector taking into account the detector granularity and efficiency). For 8 AGeV, the simulation does not include the TRD detector.

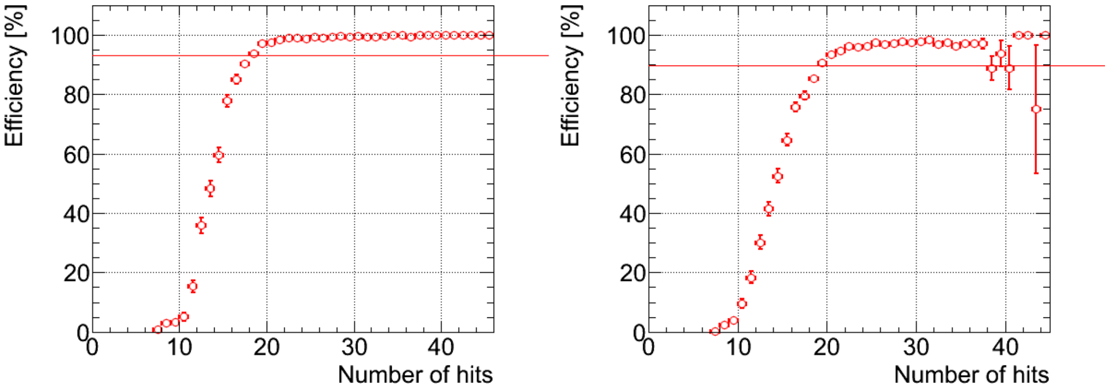

Figure 2.11 – Ring reconstruction efficiency for primary $e^{\pm}$ at 8 AGeV (left) and 25 AGeV (right) as function of the number of hits in the ring. It can be seen that the reconstruction efficiency is close to 100 % for > 18 hits per ring at 8 AGeV and > 20 hits at 25 AGeV.

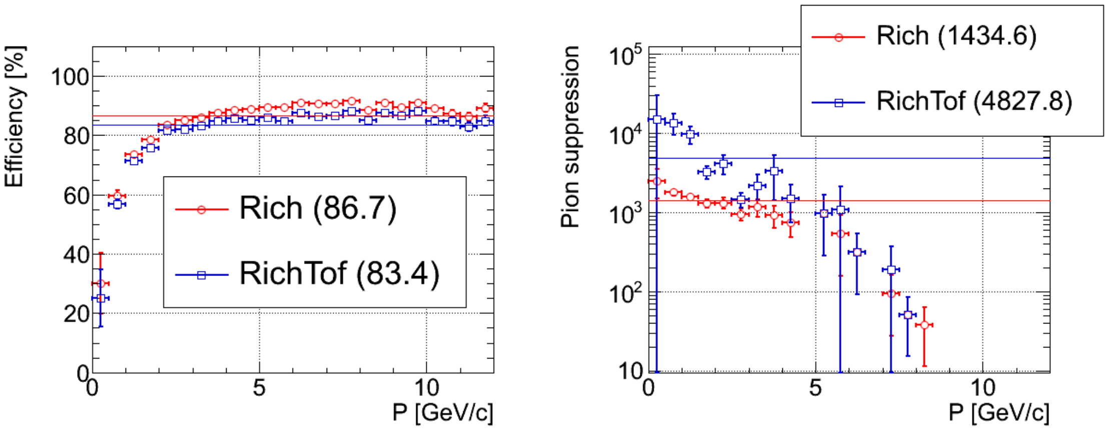

Figure 2.12 – Left: Electron identification efficiency at 8 AGeV as function of momentum for the RICH detector alone and in combination with the TOF detector. Right: Pion suppression factor at 8 AGeV as function of momentum for the RICH and RICH+TOF. Colours represent different reconstruction steps and detectors which are included in the electron identification procedure: RICH (red) and RICH+TOF (blue). The horizontal lines indicate the momentum integrated pion suppression factor which is $\pi_{\text{suppr}} = 1434.6$ for the RICH alone.

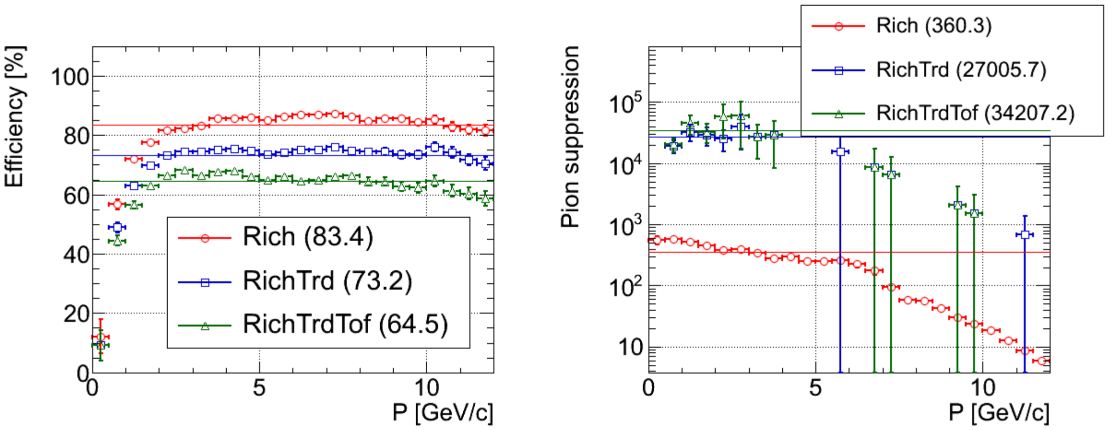

Figure 2.13 – Same as Fig. 2.12 but 25 AGeV beam energy. RICH (red), RICH+TRD (blue), and RICH+TRD+TOF (green). The momentum integrated pion suppression factor for the RICH alone is $\pi_{\text{suppr}} = 360.3$.

A background rejection strategy for the measurement of di-electrons from low mass vector mesons with the CBM-RICH detector by applying various cuts has been developed [80, 81]. The background rejection is essentially based on the use of tracking information from the STS in front of the RICH detector. The cuts are presented in the following.

- γ-conversion cut
  Because of the relatively low invariant mass of conversion pairs, all reconstructed pairs with an invariant pair mass of $m_{ee} < 0.025\,\mathrm{GeV/c^2}$ are assumed to originate from γ-conversions and are removed from the further analysis.

- Track topology cut (Segment track cut)
  The aim of this cut is to suppress background from γ-conversion and π^0 Dalitz decays where either the e^+ or the e^- is seen but the partner is lost. Figure 2.14 schematically shows the types of tracks used in this cut. A *track segment* is a track which leaves the acceptance of the PID subdetectors after being reconstructed in the STS. This is the case for very low momentum tracks. From track segments, only the momentum can be reconstructed but no particle identification is possible. A *global track* is a track which is reconstructed in all detectors but not identified as electron, e.g. an electron not identified due to an imperfect electron efficiency. The third track type is an electron candidate, denoted as *electron track*. Those tracks are selected by requiring a reconstructed primary vertex track with information from all detectors, i.e. STS, RICH, TRD and TOF. In the track segment cut, for each electron track the closest track segment in terms of separation angle $\theta_{e^\pm,\mathrm{segment}}$ between electron and segment track is searched. A two-dimensional cut is finally applied in the plane $\theta_{e^\pm,\mathrm{segment}}$ versus the momentum product of electron track and closest neighbour $\sqrt{p_{e^\pm} \cdot p_{\mathrm{segment}}}$. With this cut, only $1.3\,\%$ of electron tracks from ρ^0 decays are rejected, while electrons from γ-conversions are reduced significantly [6]. In the same way, the segment track cut is used for the suppression of di-electron pairs from π^0 Dalitz decays.

- Track topology cut (Misidentification cut)
  The misidentification cut is similar to the track segment cut. Here, global tracks instead of track segments are combined with electron tracks.

- Transverse momentum cut
  Since e^+ and e^- from the background have a lower transverse momentum p_t than those from the low mass vector mesons, a cut on p_t can be used for background rejection. Typically, a cut at $p_t = 0.2\,\mathrm{GeV/c}$ is applied and all e^+ and e^- below that value are rejected for the further analysis.

Invariant mass spectrum of di-electrons
A full Monte Carlo simulation was performed to evaluate the feasibility of low mass di-electron measurements with the CBM experiment [6, 81]. For these simulations, background was generated using the UrQMD code including di-electrons from γ-conversion as well as π^0 and η Dalitz decays. The signal, i.e. di-electrons from the decay of ρ^0, ω, ϕ mesons, was simulated with the PLUTO event generator and embedded into the UrQMD events. The simulations include the STS, RICH, and TOF detectors for Au+Au collisions at 8 AGeV beam energy (SIS100) and STS, RICH, TRD, and TOF at 25 AGeV (SIS300).

Figure 2.15 shows the simulated invariant mass spectrum of electron pairs for central Au+Au collisions at 8 AGeV and 25 AGeV. The results of low mass vector meson reconstruction after full event reconstruction, electron identification and application of all background rejection cuts are summarised in Tab. 2.2. Parameters of interest are the reconstruction efficiency and the signal-to-background (S/B) ratio for low mass vector mesons.

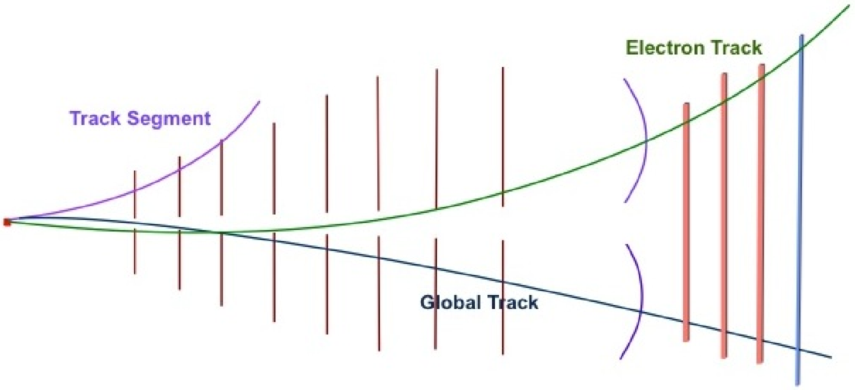

Figure 2.14 – Track types used in the track topology cuts for rejection of background. The vertical lines on the left side symbolise the STS, the two curved lines the RICH, three vertical lines on the right side the TRD, and the rightmost line the TOF detector. Figure taken from [6].

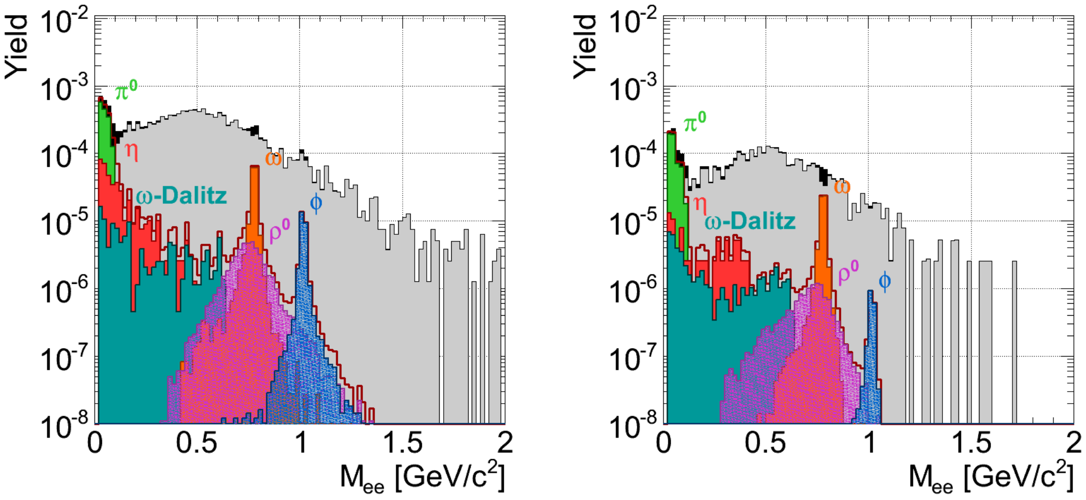

Figure 2.15 – Invariant mass spectra of simulated di-electrons after application of all background rejection cuts. Central Au+Au collisions were simulated at 8 AGeV (left) and 25 AGeV beam energy (right) corresponding to SIS100 and SIS300 scenarios, respectively. Colored histograms represent the hadronic cocktail, the grey histogram the background. The left plot is based on 100 000 events, the right plot based on 200 000 events. Figures taken from [6].

Systematic studies of low mass vector meson reconstruction

The pion suppresion factor of the PID detectors has direct impact on the physics performance since pions misidentified as electrons or positrons contribute to the background as mentioned above. Therefore, the physics performance of the CBM-RICH detector was studied in dependence of the pion suppression factor [6]. For this study, all reconstructed pions in the RICH acceptance were added to the sample of electron candidates. The electron identification was then performed using Monte-Carlo information and assuming pion suppression factors of 100, 500, 1000, 2500, 5000, and 10 000 in each case. In Fig. 2.16, it can be seen that the background drops with increasing pion suppression factor and is close to the ideal case of no misidentified pions for a pion suppression factor > 5000.

The simulated physics performance of the CBM-RICH detector for different values of the pion suppression factor is summarised in Tab. 2.3. For 8 AGeV and 25 AGeV the S/B ratio for ω and ϕ mesons, the physical

	8 AGeV beam energy		25 AGeV beam energy	
Mesons, mass ranges	S/B	efficiency in %	S/B	efficiency in %
ρ^0	–	3.12	–	4.39
ω	0.65	4.10	0.31	5.53
ϕ	0.04	4.89	0.11	7.08
$M_{ee} < 0.2\,\mathrm{GeV/c^2}$	2.04	–	1.44	–
$0.2 < M_{ee} < 0.6\,\mathrm{GeV/c^2}$	0.033	–	0.019	–
$0.6 < M_{ee} < 1.2\,\mathrm{GeV/c^2}$	0.067	–	0.053	–

Table 2.2 – Results of low mass vector meson reconstruction and different invariant mass regions for central Au+Au collisions at 8 AGeV and 25 AGeV beam energy after all cuts. The efficiencies are normalised to a 4π emission of the respective particle. Table adapted from [6].

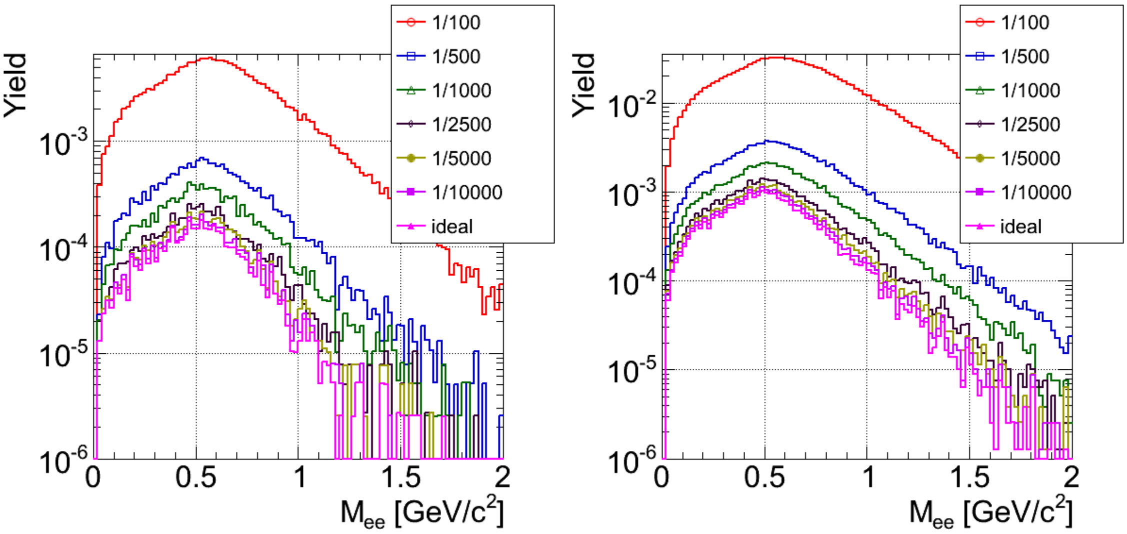

Figure 2.16 – Simulated background assuming different pion suppression factors after application of all cuts. Central Au+Au collisions at 8 AGeV (left) and 25 AGeV (right) beam energy were simulated. Ideal means no misidentified pions. It can be observed that the background drops with increasing pion suppression factor. Figures taken from [6].

background, i.e. electron pairs from γ-conversion and π^0-Dalitz decays, in percent of the total number of pairs in the background, and the fraction of misidentified pions in the electron sample after application of all cuts are shown. With a pion suppression factor of > 5000, the background is dominated by physical sources and low mass vector mesons are reasonably accessible [6].

pion suppression factor	100	500	1000	2500	5000	10000	ideal
			8 AGeV beam energy				
ω: S/B	0.012	0.14	0.27	0.47	0.67	0.83	0.89
ϕ: S/B	0.001	0.015	0.03	0.05	0.07	0.12	0.14
Physical background in %	1.8	18.4	34.7	55.6	69.8	79.5	86.9
Misidentified $\pi^{\pm}$ in %	83.5	53.4	36.4	19.3	10.6	5.7	0.0
			25 AGeV beam energy				
ω: S/B	0.005	0.05	0.10	0.19	0.24	0.26	0.30
ϕ: S/B	0.002	0.02	0.04	0.07	0.10	0.12	0.14
Physical background in %	1.8	18.7	35.9	57.1	69.1	76.9	86.0
Misidentified $\pi^{\pm}$ in %	83.9	52.7	36.0	18.5	10.4	5.2	0.0

Table 2.3 – Signal-to-background ratios, contribution of physical background in percent of the total number of pairs in the background and the contribution of misidentified $\pi^{\pm}$ in percent of the electron sample after application of all background rejection cuts. A pion suppression of > 5000 is needed to have the background dominated by physical sources and to reasonably access low mass vector mesons. Table taken from [6].

Chapter 3

Evaluation of photomultiplier tubes

For the camera of the CBM-RICH detector, multianode photomultiplier tubes (MAPMTs) are considered for a long time as the most promising photon sensor candidate [82]. In this chapter, results from laboratory tests of MAPMTs are presented.

The precise knowledge of the photon sensor characteristics is crucial for understanding the expected detector performance. Therefore, a test stand for the measurement of the spectral response in terms of quantum efficiency (*QE*) and the single photon response in terms of the single photoelectron spectrum, gain, uniformity, and crosstalk has been set up in a dedicated CBM dark room laboratory at BUW. The influence of those quantities on the relative single photon detection efficiency, which can be seen as a figure of merit for a photon sensor, is studied. Results of the measurements are implemented in the CbmRoot framework for a realistic simulation of the CBM-RICH prototype performance (chapter 6).

First, the operating principle and the most important characteristics of photomultiplier tubes (PMTs) for single photon detection are discussed (section 3.1). The features of MAPMTs and the reasons why they are considered as photon sensors for the CBM-RICH camera are exposed in section 3.2 followed by a presentation of the measurement setups used for the characterisation of different MAPMT types in section 3.3. The following sections then present and discuss the results.

3.1 Photomultiplier tubes

PMTs are an excellent tool for the detection of single photons because of their very low noise level compared to other sensor types e.g. silicon based sensors and their fast response time compared to e.g. gas detectors. The operation principle of a PMT is a two-stage process. First, a photon is converted in the photocathode into a photoelectron. Second, this photoelectron is multiplied by a factor of $\approx 10^6$ in a system of typically 8-12 electrodes, so-called dynodes. The photon is converted with a certain probability into a photoelectron which is accelerated by an electrical field and hits the first dynode where it releases δ secondary electrons. δ is referred to as dynode gain. The potential of the following n dynodes increases by $\approx 100\,\mathrm{V}$ each resulting in an overall multiplication factor of δ^n. Due to the statistical nature of secondary electron multiplication, the overall gain fluctuates from event to event.

In nuclear and particle physics, photomultipliers are widely used for the readout of scintillators and in Cherenkov air, water, and ice detectors for astrophysical purposes [83, 84, 85, 86].

In the following, important characteristics of PMTs will be listed.

Quantum efficiency

An important property of PMTs is the spectral response. Due to the photoelectric effect, the photocathode converts incident photons into electrons. The term spectral response refers to the wavelength dependent conversion efficiency. Spectral response can be expressed as radiant sensitivity or quantum efficiency *QE* (also denoted by η).

Radiant sensitivity is the ratio between generated photo current and incident radiant flux at a given wavelength. It has the unit amperes per watt (A/W). *QE* is the ratio between generated photoelectrons and incident photons at a given wavelength. Because quantum efficiency is the more meaningful quantity in the context of single photon measurements, *QE* is used to quantify spectral sensitivity throughout this thesis. It will be given in percent with 100 % corresponding to one emitted photoelectron per incident photon. The maximum *QE* occurs at a slightly shorter wavelength than that of peak radiant sensitivity as photons with shorter wavelength have higher energy.

It can be distinguished between external and internal *QE*. External *QE* refers to the number of generated photoelectrons normalised to the number of photons striking the front glass of the PMT. For the internal *QE*, a normalisation to the number of photons entering the photocathode is made, i.e. reflection on and absorption in the front glass as well as reflection on the photocathode itself are subtracted. The internal *QE* of a photon sensor therefore always has a larger value than its external *QE*. All measurements presented in this thesis will address external *QE*. External *QE* is the quantity of interest for the evaluation of the suitability of a PMT for efficient photon detection. In the following, the term *QE* will be used even though external *QE* is meant.

Most photocathode materials are made of compound semiconductors consisting of alkali metals with low work function. The common *bialkali* (BA) cathode is made of antimony-rubidium-caesium (Sb-Rb-Cs) or antimony-potassium-caesium (Sb-K-Cs). The name bialkali is caused by the two alkali metals used (Rb, Cs or K, Cs). Its spectral sensitivity covers the range from the UV to about 700 nm having a peak *QE* of approximately 25 % at 350 nm to 400 nm. Newly available super bialkali (SBA) and ultra bialkali (UBA) cathodes increase the peak *QE* to 35 % and 43 %, respectively.

A typical *QE* curve, i.e. *QE* as function of wavelength, is shown in Fig. 3.1 for standard, super, and ultra bialkali photocathodes. The short wavelength limit of a PMT is determined by the window material, the long wavelength limit by the photocathode material [87]. Caused by the $1/\lambda^2$ behaviour of the Cherenkov spectrum, the short wavelength limit is of particular interest when using PMTs in Cherenkov detectors.

Collection efficiency

The probability that a photoelectron reaches the first dynode and contributes to the output signal is called collection efficiency α. There is no universally accepted method for measuring the absolute collection efficiency [88].

Dark current

Even when operating a PMT in total darkness, some pulses will be detected. This is mostly due to thermal emission of electrons from the photocathode which are accelerated towards the first dynode and generate secondary electrons in the dynode system just as photoelectrons do. The resulting flow of electrons from the last dynode and measured at the anode is referred to as dark current. For manufacturers, the trade-off between a low work function of the photocathode, leading to a high *QE*, and a low thermal emissivity in order to obtain a low dark current is a technological challenge.

Time resolution

With respect to the time resolution of a PMT, three parameters can be given. The rise time is the time for the

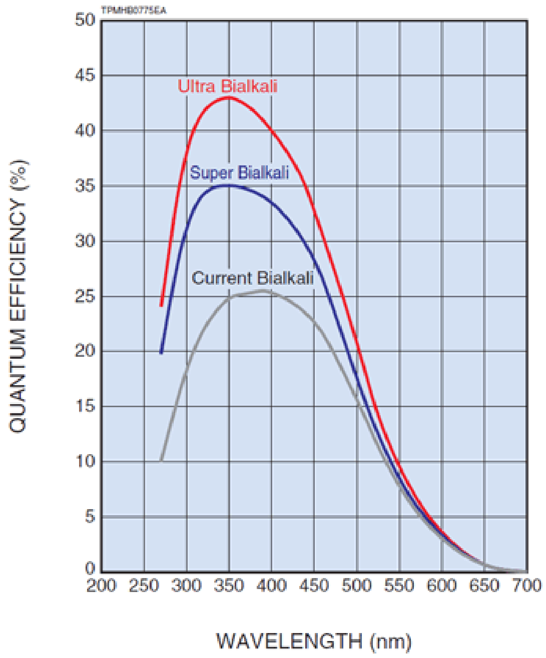

Figure 3.1 – Typical QE curves for ultra, super, and standard bialkali photocathodes. Figure taken from http://www.hamamatsu.com/eu/en/technology/innovation/photocathode/index.html.

output signal to rise from $10\,\%$ to $90\,\%$ of the peak amplitude. The transit time is the interval between the arrival of a photon on the entrance window and the time when the output signal reaches the peak amplitude. The transit time spread, which is denoted here by time resolution, describes the pulse width and is the fluctuation of transit time [89].

Magnetic field resistance

A limiting factor for the operation of PMTs are magnetic fields which bend the trajectories of the relatively slow photoelectrons on their way to the first dynode because the electron covers a relatively large distance with small momentum. For the same reason, the transit time spread is determined at this stage. Compared to the distance between the dynodes, the distance between photocathode and the first dynode is relatively large and the field strength relatively low. In addition, the electron trajectories can be bend more strongly on the way to the first dynode due to the larger volume between photocathode and first dynode. In general, the closer the first dynode to the photocathode the better is the performance of a PMT in a magnetic field. Also, but on a lower level, magnetic fields can bend the trajectories of the secondary electrons within the dynode system.

Single photoelectron spectra

The typical output signal at the anode of a PMT is a pulse whose shape depend on the specific PMT design. The rise time of flat panel MAPMTs (see below) is in the order of 0.8 ns and the time resolution around 0.4 ns. The charge of a single photoelectron pulse equals the elementary charge multiplied by the PMT gain. Taking the typical gain of a H8500D-03 with 12 dynodes of $1.5 \cdot 10^6$, this adds up to a pulse charge of 0.25 pC. The amplitude can be estimated to be 2.5 mV assuming this charge pulse to be rectangular and measured as current flow through a resistor $R = 50\ \Omega$ within $\Delta t = 5$ ns.

A single photoelectron signal can thus be described by a value for time and amplitude and measured with a time and charge sensitive readout. By discretising and sampling the amplitudes of photoelectron signals using an analog-to-digital converter (ADC), one obtains a single photoelectron spectrum, also called pulse

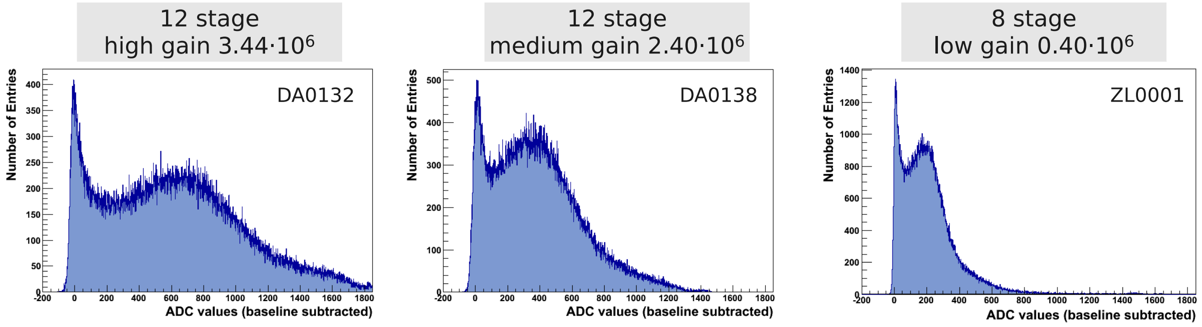

Figure 3.2 – Single photoelectron spectra for three PMTs with different gain. The left plot shows the spectrum for a 12-stage PMT with a gain of $3.44 \cdot 10^6$, the central plot a spectrum for a 12-stage PMT with a gain of $2.40 \cdot 10^6$, and the left plot a spectrum for a 8-stage PMT with a gain of $0.40 \cdot 10^6$. For the 8-stage PMT, the proportionality factor between ADC value and charge is larger by a factor of 2 compared to that for the 12-stage PMTs. It can be seen that the single photoelectron peak is correlated to the PMT gain. See text for a discussion of the general features of a single photelectron spectrum.

height distribution (PHD). Pulse height distributions for single photon signals are shown in Fig. 3.2 exemplarily for three PMTs with different gain. It can be seen that the position of the single photoelectron peak is correlated to the PMT gain.

A single photelectron spectrum is a superposition of two parts, the noise and the signal. The origin of the noise is mainly thermal electron emission. Thermal emission of electrons at the photocathode leads to a single photon signal. Because, however, thermal electrons from the dynodes are less multiplied than electrons from the photocathode, the pulse height distribution of the noise increases towards low amplitudes. There are also pulses with low amplitude from photoelectrons which are inelastically back-scattered by the first dynode [88].

The single photoelectron peak, has a certain width due the statistical nature of secondary electron emission. The width of the single photoelectron peak is also dependent on the number of dynodes and especially on the δ of the first dynode. A large δ results in a good peak resolution.

In the case of MAPMTs, the single photoelectron spectrum has an additional contribution with low amplitudes arising from crosstalk during secondary electron multiplication. In [90] it is shown that the low amplitude contribution from crosstalk can be suppressed by excluding signals from neighbouring anodes. Crosstalk will be quantified in section 3.9.

Peak-to-valley ratio

The separation of single photoelectron signals from the noise is usually done by application of a cut on the amplitude at a value between noise and single photoeletron peak. An important quantity of the PMT single photon detection capability is the peak-to-valley ratio which is defined as the ratio between height of the single photoelectron peak and the valley separating it from the noise. In general, a large peak-to-valley ratio, a narrow single photoelectron peak, and a large gain facilitate the clean measurement of photoelectrons.

3.2 Multianode photomultiplier tubes

MAPMT availability and usage

Designed for a good spatial resolution, MAPMTs are PMTs with a separated dynode and anode structure. MAPMTs have a quadratic shape with commonly 2×2, 8×8, or 16×16 quadratic pixels. MAPMTs are relatively new devices and practically exclusively fabricated by the Japanese company Hamamatsu Photonis

K.K. which brings them to the market as *multianode PMTs* (bare tube without voltage divider) or *multianode PMT assemblies* (with incorporated voltage divider).

MAPMTs were already considered for the use in a RICH detector by HERMES at HERA but this option was abandoned in favour of standard PMTs because of a large dead area associated with MAPMTs at that time [91]. The RICH detector of the HERA-B experiment solved this problem by using a lens system in front of the MAPMTs [92].

Nowadays, MAPMTs with very good geometrical coverage are purchasable and elaborated devices. Therefore, the use in RICH detectors becomes more and more common as replacement for classical but rate-limited multi-wire proportional chambers with CsI-photocathodes. The RICH-1 detector of the COMPASS compass experiment e.g. was upgraded in 2006 and is now operating with 576 Hamamatsu R7600-03-M16 MAPMTs in the central region of the photon detector [93]. The RICH detector of the AMS experiment uses 680 Hamamatsu R7900-M16 MAPMTs [65].

Several experiments envisage MAPMTs as photon sensors for upgrades or as baseline design solution. For instance, plans for upgrades of the LHCb RICH-1 and RICH-2 propose the usage of MAPMTs [94]. The CLAS12 experiment at Jefferson Lab schedules the use of Hamamatsu H8500 [95]. The Compact High Energy Camera from the Small Size Telescopes of the Cherenkov Telescope Array (CTA) will be equipped with Hamamatsu H10966 MAPMTs [96]. The Extreme Universe Space Observatory on the Japanese Experiment Module (JEM-EUSO), which will study Ultra High-Energy Cosmic Rays (UHECR) by observing Extensive Air Showers (EAS) from space, will make use of Hamamatsu R11265-03-M64 MAPMTs [97].

Overview of the tested MAPMT types

The photon sensor for the CBM-RICH camera should satisfy the following requirements which are discussed in more detail in [6].

- Quantum efficiency
  The efficiency of ring finding and the quality of ring fitting increase with the number of hits per Cherenkov ring. Thus, high *QE* and single photon detection efficiency are favourable. In addition to that, the spectral sensitivity of the photon sensors should match the transmission range of the radiator.

- Spatial resolution
  The spatial resolution of the camera, determined by the granularity of the photon sensors and the spacing in between, should be sufficiently small in order not to deteriorate the Cherenkov ring resolution. It was shown that the effect on the ring resolution is comparable to that from chromatic dispersion and multiple scattering when assuming a granularity of approximately 6 mm×6 mm (see section 2.5.2) which is also a good compromise with regard to the number of readout channels.

- Hit rate capability
  For the above mentioned pixel size, a maximum rate of the order of 700 kHz is expected for Au+Au collisions at 35 AGeV and 10 MHz. Assuming the hits stemming from single photons, a sensor size of approximately 5 cm×5 cm, and a gain of the order of 10^6, the average signal current is 5 µA per sensor.

- Dark count rate
  Given the fact that CBM will run triggerless, a very low dark count rate is indispensable. This requirement strongly favours the use of PMTs as photon sensors.

- Time resolution
  The maximum CBM event rate of 10 MHz results in a time separation of subsequent events of 100 ns in average. Since, however, events can be much closer and hits from individual events can arrive on

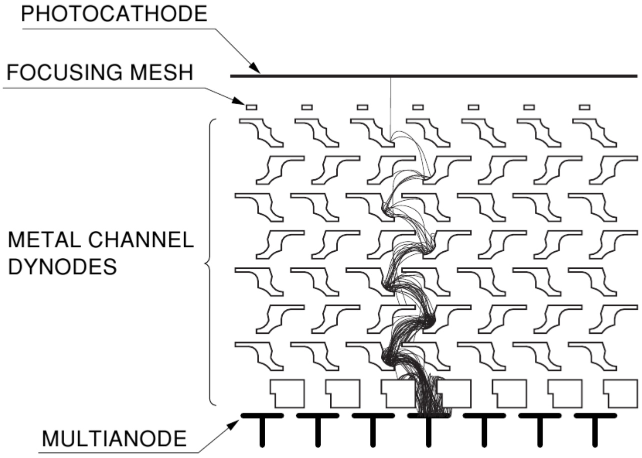

Figure 3.3 – Cross section of a flat panel MAPMT with metal channel dynode structure. Figure taken from [87].

the camera with a certain spread, the time resolution has to be better. Furthermore, a time resolution below 1 ns may help to disentangle hits from different Cherenkov rings.

- Magnetic field resistance
  Because of the magnetic stray field in the camera region, an intrinsic insensitivity of the photon sensors to magnetic fields would simplify or even make unnecessary the implementation of the design options presented in section 2.5.2.

- Life time
  The lifetime of a photon sensor is determined by the integrated anode charge. Assuming a sensor gain of 10^6, the above mentioned pixel size, and one year of operation at maximum hit rates, leads to $Q = 15\,\text{C/cm}^2$. This number is well below the specifications for MAPMTs but it is an issue for MCPs [6].

- Radiation hardness
  Without additional radiation shielding of the camera, a maximum of 100 Gy ionizing dose or 10^{11} n/cm^2 neutron equivalent flux is expected according to FLUKA[1] simulations. For photomultipliers, the glass entrance window is the most radiation sensitive part and fused silica exhibits the best radiation hardness followed by UV-extended borosilicate glass (UV glass) and lime glass. According to [87], a deterioration of the window transmission sets in at dose levels which are 1 to 2 orders of magnitude above those expected for 2 months of running CBM at full intensity.

Balancing all these demands and considering the proposed design options to reduce the magnetic stray field in the region of the camera led to the decision in favour of MAPMTs as baseline solution for the CBM-RICH camera. Therefore, adequate MAPMT types were evaluated in-depth.

The tested types have either 64 or 16 pixels. They possess an unsegmented photocathode and segmented dynodes and anode outputs in a 8×8 or 4×4 matrix. Figure 3.3 shows a cross section of a flat panel MAPMT with metal channel dynode structure.

Table 3.1 lists the tested MAPMT types. They differ in external size, active area, window and photocathode materials, and number of dynodes. Detailed information of the MAPMT characteristics can be found in the

---

[1] FLUKA is a software tool for the calculation of particle transport and interactions with matter and used here for dosimetry calculations, http://www.fluka.org/fluka.php.

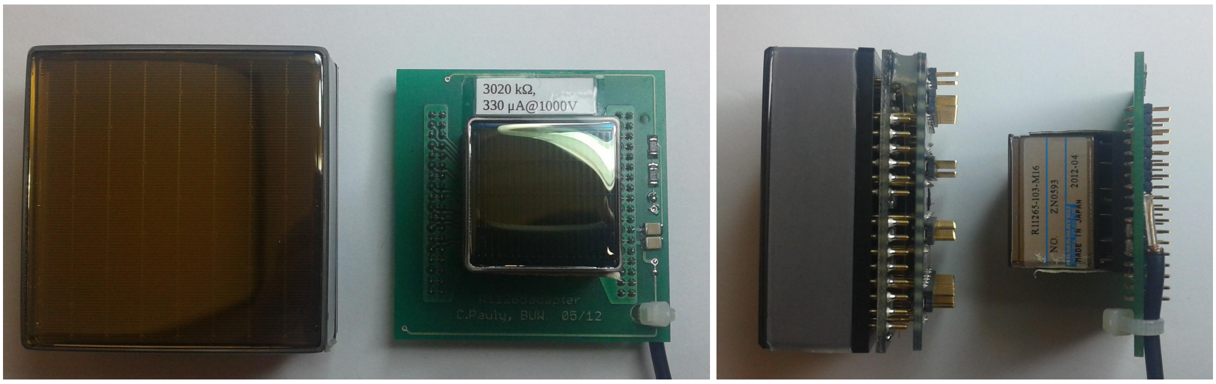

Figure 3.4 – Front (left) and side view (right) of a H8500D-03 with integrated voltage divider and a R11265-103-M16 with home-made voltage divider. The length of the edge is 52 mm for the H8500D-03 and 26.2 mm for the R11265-103-M16.

MAPMT type	external size	active area / external size	window	photo-cathode	no. of dynodes
R11265-103-M16	26.2×26.2 mm^2	77.1 %	UV-window	SBA	12
H8500D-03	52.0×52.0 mm^2	88.8 %	UV-window	BA	12
H10966A-103	52.0×52.0 mm^2	88.8 %	UV-window	SBA	8
R10552-103-M64 bare tube	52.0×52.0 mm^2	88.8 %	UV-window	SBA	8
R10552-03-M64 bare tube	52.0×52.0 mm^2	88.8 %	UV-window	BA	8
H8500C-100-mod8	52.0×52.0 mm^2	88.8 %	borosilicate glass	SBA	8

Table 3.1 – Characteristics of the tested MAPMT types. Because of technical reasons, the combination of a 12 dynode structure with SBA photocathode in a 2" MAPMT is not possible [99]. The Hamamatsu nomenclature is "-03" for UV-window, "-100" for SBA photocathode, and "-103" for UV-window plus SBA photocathode.

data sheets [89, 98]. Figure 3.4 shows photographs of a 52.0×52.0 mm^2 H8500D-03 with integrated voltage divider in comparison to a 26.2×26.2 mm^2 R11265-103-M16 with home-made voltage divider.

For some measurements, a comparison with "bad" MAPMTs was done[2]. Those MAPMTs had been selected by the manufacturer based on single photon measurements. For the "bad" tubes, no clear single photoelectron peak could be measured by the manufacturer for a large number of pixels.

Alternative photon sensor types

Besides MAPMTs, there are also other recent developments like hybrid photon detectors consisting of a vacuum tube with quartz window, multialkali photocathode, and a silicon pixel array as e.g. used in LHCb [100] or silicon PMTs (SiPM[3]) which are up to date still exhibiting relatively large dark noise and optical crosstalk when used for single photon detection (see e.g. [101]). Hybrid photon detectors and SiPMs are currently no option for the CBM-RICH since the requirements concerning rate capability, dark current, and

---

[2] The "bad" MAPMTs are of the type H8500D, i.e. they are equipped with borosilicate windows in contrast to the H8500D-03 MAPMTs with UV-window. Despite of this difference, the direct comparison of those "bad" tubes with H8500D-03 made in this chapter is feasible since all measurements presented are done at wavelengths where the transmittance of UV and borosilicate glass is comparable.

[3] Depending on the manufacturer, silicon photmultipliers (SiPM) are also denoted as avalanche photodiode (APD), or multi-pixel photon counters (MPPC).

radiation hardness cannot be satisfied.

The Barrel DIRC detector of the future PANDA experiment foresees MCP-PMTs as baseline due to their insensitivity to strong magnetic fields [102]. For the CBM-RICH, MCPs are considered as alternative sensor type [6], in particular in case of unexpected inefficacy of the shielding options. The evaluation of MCPs, however, is not within the scope of this thesis.

3.3 Experimental methods

3.3.1 Quantum efficiency measurements with continuous light source

Within this work, significant effort has been made to build a measurement setup in order to measure the *QE* of MAPMTs. Four questions of particular importance were addressed.

1. How accurate are the *QE* values provided by the MAPMT manufacturer?
2. How large are variations of *QE* from tube to tube?
3. What are the *QE* values in the UV range down to 200 nm where the manufacturer does not specify *QE* but where Cherenkov photons are produced more abundantly and a high efficiency is favourable?
4. How homogeneous is the *QE*?

In order to answer these question, *QE* was measured as function of wavelength (*QE curve*) and as function of x and y position on the photocathode (*QE scan*).

The principle of the measurements is based on the illumination of the MAPMT photocathode and the measurement of the generated photo current as function of wavelength. The absolute *QE* is determined from comparison to a calibrated photodiode.

In order to have photons of all wavelength in the interval of interest and because photo currents need to be measured without amplification ($\approx$ pC), the measurements have to be performed in multi photon mode, i.e. many photons impinging on the photocathode, using a DC light source continuous in time and a monochromator continuous in wavelength.

A detailed description of the major components, the measurement procedure, and the precision of the measurements can be found in appendix A.

Figure 3.5 (top) shows a schematic sketch of the setup. A hybrid tungsten and deuterium light source emits a broad light spectrum between 180 nm and 2.6 µm (deuterium 180 nm to 800 nm, tungsten 400 nm to 2.6 µm). Monochromatic light is obtained by using a monochromator with double grating (Spectral Products CM110 Czerny-Turner type). The monochromatic light is focused by a quartz lens onto a filter wheel needed for the suppression of higher orders in the diffraction pattern. It is then coupled to an UV-transparent quartz fibre which is connected to a linear translation stage (xy-stage). By varying the distance between quartz fibre and PMT, the size of the light spot can be adjusted. For measurements of *QE curves*, a light spot of ≈ 1 cm in diameter on the MAPMT centre is used. For *QE scans*, the light spot is reduced to ≈ 1 mm. To minimise stray light striking the PMT, the measurements are done in a dark room laboratory. In addition, the entire light path and the device under test are light shielded.

The PMT to be measured is placed in front of the fibre and illuminated with monochromatic light of low intensity in wavelength steps of 10 nm. The measurement is performed by operating the PMT as a photocell, i.e. shortening the first three dynodes and applying a voltage of ≈ -100 V between the photocathode and the dynode system (cf. Fig. 3.5 bottom). The photo current is measured by a picoamperemeter. In a consecutive

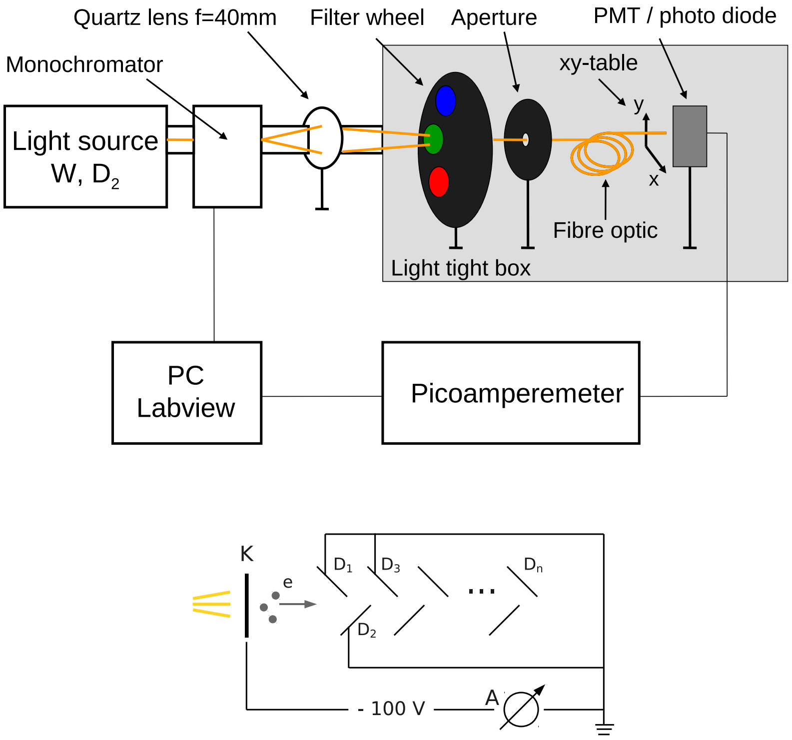

Figure 3.5 – Top: Schematic *QE* setup with fibre optic and xy-stage. Bottom: *QE* circuit with photocathode K, dynode system D_1 ... D_n , voltage supply, and picoamperemeter A.

measurement the PMT is replaced by the calibrated photodiode[4]. This way of determing the *QE* of a PMT requires time stability of the light source which has been demonstrated in tests (cf. appendix A). From the known *QE* of the calibrated photodiode and the measured photo currents, the *QE* of the PMT is calculated via

$$QE(\lambda)_{\mathrm{PMT}} = QE_{\mathrm{diode}}(\lambda) \cdot \frac{\left|I_{\mathrm{PMT}}(\lambda) - I_{\mathrm{PMT,ped}}\right|}{\left|I_{\mathrm{diode}}(\lambda) - I_{\mathrm{diode,ped}}\right|} \tag{3.1}$$

with the PMT current I_{PMT}, the photodiode current I_{diode}, and their dark currents $I_{\mathrm{PMT,ped}}$ and $I_{\mathrm{diode,ped}}$. The dark current can be measured after operating the PMT in total darkness for sufficient time. Figure 3.6 shows the measured current in dependence of time in darkness. It can be seen that the current asymptotically reaches a constant value after ≈ 65 min.

3.3.2 Single photon measurements

When doing a single photon measurement, the PMT has to be operated under high voltage, all dynodes being used for amplification. Thus, a single photon measurement gives information about both the photon-electron conversion in the photocathode and the signal amplification in the dynode system whereas a *QE* measurement reveals information about the former process only.

All single photon measurements were done at the nominal voltage of -1000 V between photocathode and anode for all tested MAPMTs.

---

[4] The calibration curve of the used photodiode (Hamamatsu S1227-1010BQ) is shown in the appendix in Fig. A.1

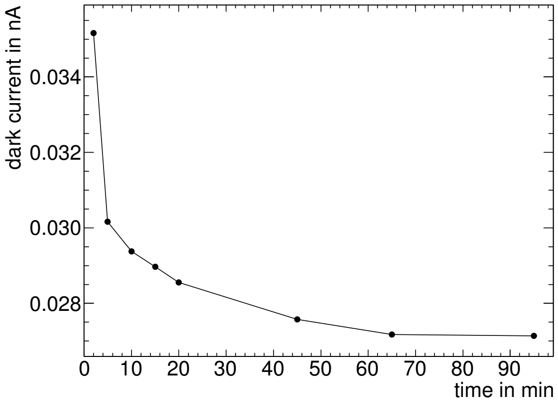

Figure 3.6 – Dark current of a R10552-03-M64 bare tube in dependence of time after installation in the measurement setup. It was stored in darkness. For installation and adjustment in the mounting frame, it was exposed to faint light during 1-2 minutes. Lines between the data points are drawn to guide the eye.

Single photon measurements presented in this thesis are done using LEDs (Roithner UVtop Deep UV-LED, AlGaN) at 245 nm, 275 nm, 350 nm wavelength, and a standard LED from mass production at 470 nm wavelength or using a laser diode at 405 nm (Alphalas Picopower$^{\text{TM}}$-LD Series). The LEDs are powered by a HP 214B pulse generator (alternatively Agilent 33250A arbitrary waveform generator) slightly above threshold voltage with short square pulses of $\approx 25\,\text{ns}$. The laser diode is powered by a dedicated pulse generator. In Fig. 3.7, a schematic view of the single photon measurement setup is shown. The light is coupled to a quartz fibre and guided inside a dark box. A sand-blasted quartz diffuser ensures a homogeneous photon distribution on the PMT surface.

The pulsed LEDs and the laser emit many photons with every pulse which necessitates an attenuation by many orders of magnitude until the single photon level is reached. Attenuation is done geometrically by adjusting the coupling to the fibre and the distance between diffuser and PMT.

The readout chain for single photon measurements in the laboratory is based on the n-xyter chip identical to that used in the CBM-RICH prototype beam tests and described in detail in section 5.2.3.

The GSI Object Oriented On-line Off-line system (Go4) [103], an analysis system based on ROOT [104], was adapted to the use in laboratory and beam test measurements of MAPMTs and the CBM-RICH photon detector. It provides online monitoring and the possibility to store data in the format of ROOT trees for further analysis. For the measurements, amplitude and time information of the PMT signals are recorded. A description of the software is given in section 5.3.3.

Gain determination from single photoelectron peak

The gain of a PMT is defined as the number of electrons at the anode per photoelectron entering the dynode system. The gain as provided by Hamamatsu in the final test sheets in determined as ratio between anode and cathode current measured by illuminating the PMT under test with constant light from a tungsten lamp [89]. Since the gain of a typical PMT is in the order of 10^6, the light intensity has to be very low in order not to induce a too large anode current. This would deteriorate the PMT performance because its aging strongly depends on the collected anode charge which is calculated as the time integrated anode current.

In this work, another method was used to measure the absolute gain. The measurement is done by illuminating the PMT with single photons. The gain can then be determined from the measured anode charge of one registered photoelectron. In other words, for an illumination of the PMT with single photons, the gain is calculated as ratio between the pulse charge at the anode and the elementary charge. Therefore, charge

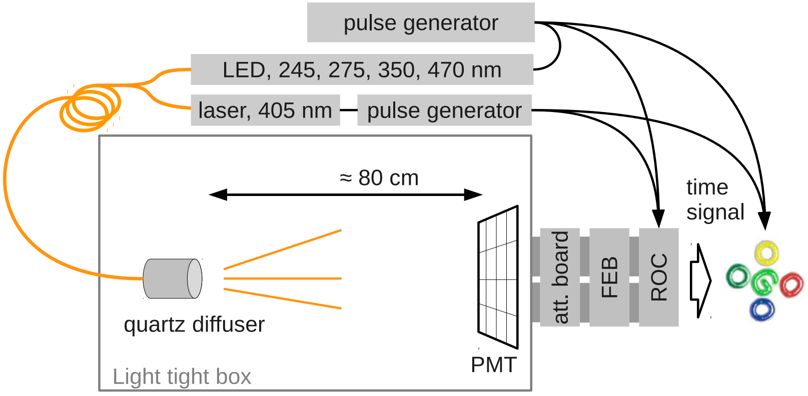

Figure 3.7 – Schematic single photon measurement setup for homogeneous illumination. Free running pulse generators trigger the LED or the laser and send a time signal to the software (Go4) and the readout electronics consisting of charge attenuator board, Front-End-Board (FEB), and Read-Out-Controller (ROC).

sensitive electronics are needed for the readout of the PMT output signal. A advantage of this method is that the total anode charge collected during a measurement is very low. The measurement is therefore not affecting the PMT lifetime.

If the absolute value of the gain is of interest, an accurate charge calibration of the readout electronics has to be done. A thoroughly performed transconductance calibration of the n-xyter chip including an estimation of uncertainties is described in [105]. However, this calibration was done for the n-xyter chip alone without additional charge attenuation as used here. Thus, a new calibration of the readout chain including the necessary capacitive charge attenuator board (see section 5.2.3) was needed. It was performed by using rectangular current pulses of known amplitude and duration which were directly introduced via cable into the sockets foreseen for the PMTs allowing a precise determination of the input charge via $Q = I \cdot t$. The injected current is defined by the voltage amplitude of a pulse from a pulse generator and a 10 kΩ resistor which has to be significantly larger than the input impedance of the n-xyter. The circuit diagram of the pulse source is shown in the appendix in Fig. C.1.

3.3.3 Spatially resolved measurements with pulsed light source

The setup shown in Fig. 3.7 can be modified in order to perform spatially resolved measurements. This is done by removing the diffuser and connecting the light fibre to a pinhole fixed to a xy-stage (Fig. 3.8). With this setup, the size of the light spot on the PMT is ≈ 1 mm in diameter. Spatially resolved measurements presented in this thesis have been done with multi photon pulses, not with single photons. The reason is that at the time of the measurements, the n-xyter based readout was not yet available. Instead, a readout based on Struck SIS3300 8 Channel 100 MHz 12-bit ADCs has been used. Since measurements were done without preamplifier, multi photon pulses were needed in order to generate signal amplitudes large enough to be sampled by the ADCs.

In contrast to the single photon measurements, the measurement software is completely based on ROOT. The measurement programme triggers the pulse generator, sets the position of the xy-stage, and reads out the ADCs. Data is stored in ROOT trees.

Spatially resolved measurements of MAPMTs with full signal amplification are presented in section 4.5 in the context of the determination of crosstalk between neighbouring pixels of MAPMTs covered by a wavelength shifting film.

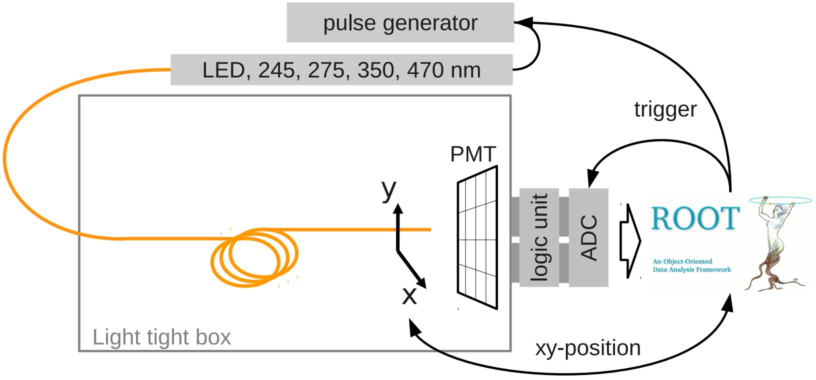

Figure 3.8 – Schematic measurement setup for punctiform illumination with light fibre and xy-stage. The pulse generator and and the ADCs are triggered by the ROOT-based measurement software.

3.4 Quantum efficiency

3.4.1 Wavelength dependent quantum efficiency

Figure 3.9 shows a comparison of *QE* curves for MAPMTs with different combinations of front glass, photocathode, and number of dynodes. Since *QE* is a property of the photocathode and independent from the secondary electron amplification, the latter is irrelevant. Six observations can be made.

1. The maximum *QE* value of SBA photocathodes is 35 % to 40 %, whereas that of BA photocathodes is $\approx 28\,\%$. This corresponds to a relative increase of 25 % to 43 %. The values are in good agreement with the data sheets.

2. For all photon sensors, the *QE* decreases towards large wavelengths and vanishes around 700 nm. As mentioned before, this is due to the photocathode itself [87].

3. The *QE* of photon sensors with UV-window decreases towards small wavelengths. *QE* curves of BA photocathodes on a quartz window indicate that the decrease of *QE* is caused by the window material (Fig. 3.10 right).

4. From the wavelength of peak *QE*, the *QE* difference between SBA and BA decreases towards lower wavelengths which is not shown in the data sheets. The *QE* below 250 nm is approximately equal for SBA and BA. According to [71], this is due to the reflectivity of SBA photocathodes which is higher than that of BA photocathodes. Another reason might be the cutoff caused by the UV glass. Its transmittance is shown as function of wavelength in Fig. 3.10 (left). With smaller absolute *QE*, the difference between BA and SBA is more difficult to judge within the measurement uncertainties.

5. The *QE* curve of the MAPMT with borosilicate glass window drops steeply below 300 nm corresponding to the cutoff of borosilicate glass which can be seen in its transmittance spectrum in Fig. 3.10 (left).

6. The *QE* of the 1" MAPMTs is higher in the UV range compared to 2" MAPMTs by about 4 % absolutely, corresponding to a relative increase of $\approx 50\,\%$ at 200 nm. This observation is due to the thinner front window of the 1" MAPMTs compared to the 2" MAPMTs and matches quantitatively the $\approx 50\,\%$ lower glass thickness (0.8 nm for R11265-103-M16 [98] and 1.5 mm for H8500D-03 [89]).

For the CBM-RICH detector with its UV-transparent CO_2 radiator, the *QE* of the photon sensors is important especially in the UV range. In order to judge the influence of the individual *QE* curves on the overall

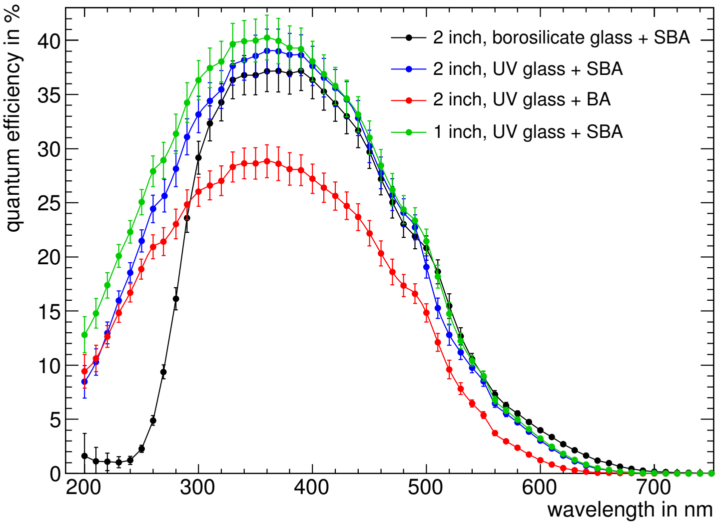

Figure 3.9 – *QE* curves of 2" and 1" MAPMTs with different window and photocathode materials (black: H8500C-100-mod8, 2" borosilicate glass + SBA; blue: H10966A-103, 2" UV glass + SBA; red: H8500D-03, 2" UV glass + BA; green: R11265-103-M16, 1" UV glass + SBA). The red curve shows the arithmetic mean of measurements of four H8500D-03, the green curve the arithmetic mean of measurements of eight R11265-103-M16. The other curves show measurements from single MAPMTs. The measured non-zero *QE* for the MAPMT with borosilicate window around 200 nm is due to stray light passing the monochromator at very short wavelengths. Within errors, however, the measured values are consistent with zero. Lines between the data points are drawn to guide the eye. The contributions to the error bars are discussed in appendix A.3.

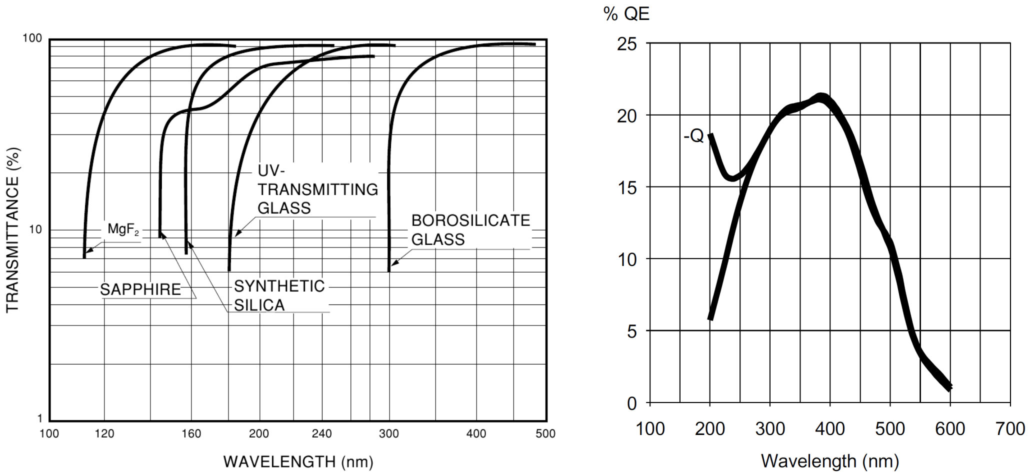

Figure 3.10 – Left: Transmittance of PMT window materials (taken from [87]). Right: *QE* curve for a Planacon XP85012 MCP-PMT with bialkali photocathode, UVFS front window which is equivalent to Schott 8337B, a UV-transmitting borosilicate glass, and quartz window (Q) (taken from [106]).

Cherenkov photon yield, the plot shown in Fig. 3.11 is produced. It shows *QE* curves for the different MAPMT types multiplied by the Cherenkov spectrum, the mirror reflectivity (taken from [71]), and CO_2 transmittance (calculated from [107]). The curves have a maximum around 270 nm for UV glass and 320 nm for borosilicate glass. Their integral gives the relative number of detected Cherenkov photons.

Normalising to the best MAPMT type, the following hierarchy is found: R11265-103-M16 (100 %), H10966A-103 (89.7 %), H8500D-03 (71.6 %), H8500C-100-mod8 (62.6 %). Table 3.2 summarises the results and the

MAPMT type	thickness of front glass	window	photo-cathode	no. of dynodes	relative no. of detected Cherenkov photons
R11265-103-M16	0.8 mm	UV-window	SBA	12	100 %
H10966A-103	1.5 mm	UV-window	SBA	8	89.7 %
H8500D-03	1.5 mm	UV-window	BA	12	71.6 %
H8500C-100-mod8	1.5 mm	borosilicate glass	SBA	8	62.6 %

Table 3.2 – Number of ideally detected Cherenkov photons and MAPMT characteristics.

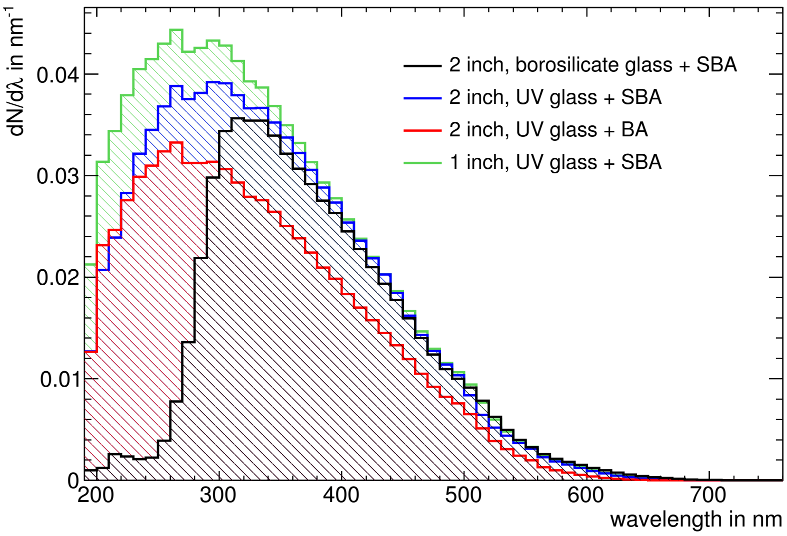

Figure 3.11 – Number of detected photoelectrons per wavelength for different MAPMT types calculated for ultrarelativistic electrons by convolving the number of produced photons in a CO_2 radiator of 1.7 m length with gas absorption, mirror reflectivity, and *QE*. The histograms are normalised to an integral of 1 for the best MAPMT type (1 inch, UV glass + SBA). The integrals of the histograms are a measure of the photon yield.

PMT characteristics. The number of detected Cherenkov photons can be seen as optimum for an ideal PMT readout in the detector. A potential lower single photon detection capability for 8 dynode stages due to a lower peak-to-valley ratio (cf. section 3.10) in the single photoelectron spectrum is not taken into account.

Not all MAPMTs of the same type have exactly the same *QE*. Due to the relatively complicated production process and the final *activation of the photocathode*, i.e. the deposition of the photocathode from the gas phase in the vacuum, tube-to-tube variations occur [99]. In Fig. 3.12 (left) *QE* curves of 7 pieces of H8500D-03 and 8 pieces of R11265-103-M16 are shown. The relative tube-to-tube variation, defined as difference between highest and lowest *QE* normalised to the average *QE* and shown in Fig. 3.12 (right), is 10 % to 15 % for SBA and 10 % to 20 % for BA photocathodes above 320 nm and in this region relatively constant with respect to the wavelength. Except for the very small wavelengths where the error band is too large to make a statement, the situation is different in the UV range. Between 220 nm and 320 nm the relative variation is smaller with only 7 % to 10 % since *QE* is limited by the glass absorption.

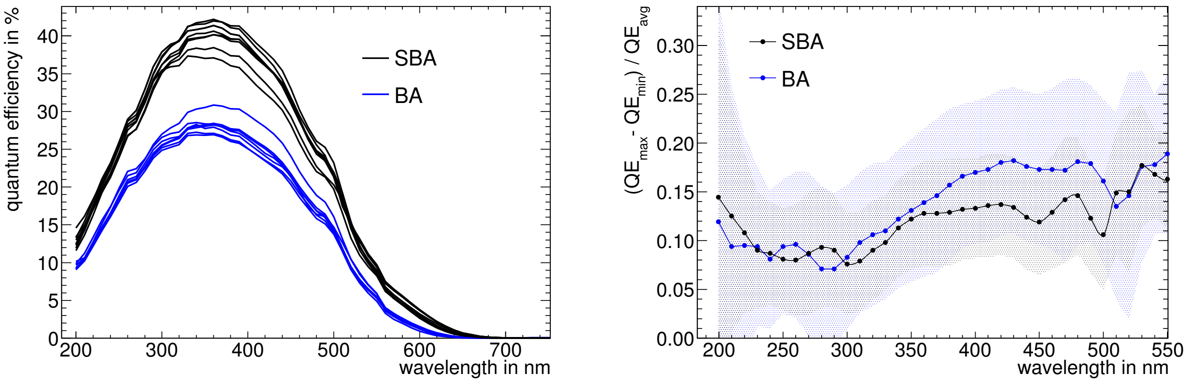

Figure 3.12 – Left: *QE* curves of 7 pc H8500D-03 (BA) and 8 pc R11265-103-M16 (SBA) giving an impression of the tube-to-tube variations. Right: Relative tube-to-tube variation plotted as difference between maximum and minimum *QE* normalised to the average *QE*. Apart from the points at very small wavelengths where the error band is large, it can be seen that the tube-to-tube variation is small in the UV range compared to $\lambda > 320\,\text{nm}$.

3.4.2 Spatially resolved quantum efficiency

The homogeneity of the photocathode sensitivity can be determined by measuring the quantum efficiency as function of x and y position (*QE scan*). *QE* scans of 2" and 1" MAPMTs were performed at different wavelengths. Figure 3.13 shows a high resolution scan at $405\,\text{nm}$ using a spot size of $\approx 1\,\text{mm}$ and a step size of $0.5\,\text{mm}$. It can be seen that the QE is not homogeneously distributed over the whole surface. It varies from $23.7\,\%$ to $27.7\,\%$ which corresponds to a relative difference of $\approx 17\,\%$ between maximum and minimum value.

Three features with respect to this inhomogeneous *QE* distribution can be observed.

1. A general increase of *QE* from top left to bottom right is seen.
   A measurement of a MAPMT in standard orientation[5] for *QE* scans and rotated clockwise by $90°$ shows that the observed global tendency is not a feature from the measurement (Fig. 3.14). Because all scans are done from bottom right to top left, a change in *QE* in this direction could be due to an unstable light intensity. The scans, however, show that the measured pattern also rotates which indicates that it is an intrinsic feature of the MAPMT.

2. An 8×8 grid pattern corresponding to the pixel structure of the MAPMT is seen. Because the observed lines separating the pixels have higher *QE* than the zones within the pixels, the structure cannot originate from gaps between the subdivided dynodes. If the gaps were large enough to be seen, they would appear with lower *QE* in consequence of lower collection efficiency. Furthermore, the first three dynodes of all pixels are connected, so that all dynodes are at the same potential which leads to the same collection efficiency for all dynodes. It is most likely that the grid pattern displays the focusing electrode which is located between photocathode and first dynode.

3. The most prominent feature is a circular area in the centre with relatively low *QE* compared to the rest of the MAPMT (*QE hole*). This is seen in 6 out of 12 tested MAPMTs. Figure 3.15 shows three examples, one H8500D-03 (left), one R10552-03-M64 bare tube (centre), and one R11265-103-M16 (right). According to the manufacturer, two reasons can cause this feature. First, like the tube-to-tube variation of *QE*, the *QE* hole can stem from the activation of the photocathode which is done by introducing the photocathode material into the vacuum through a pinhole in the MAPMT centre as last

---

[5] In standard orientation for *QE* scans, the start mark of the MAPMT is at the top left as seen from the front.

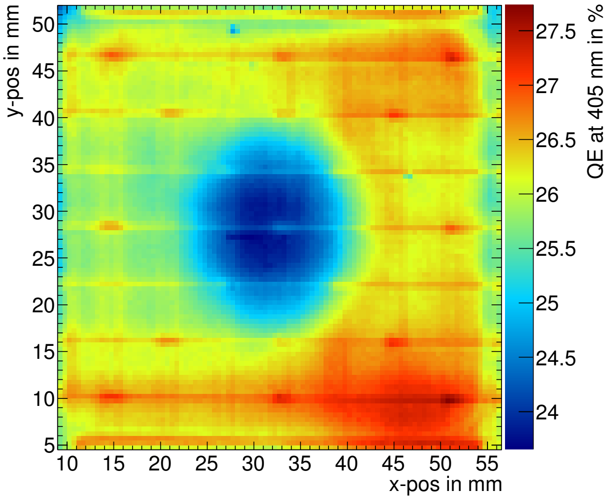

Figure 3.13 – High resolution *QE* scan of a H8500D-03 MAPMT (DA0141) at $405\,\mathrm{nm}$.

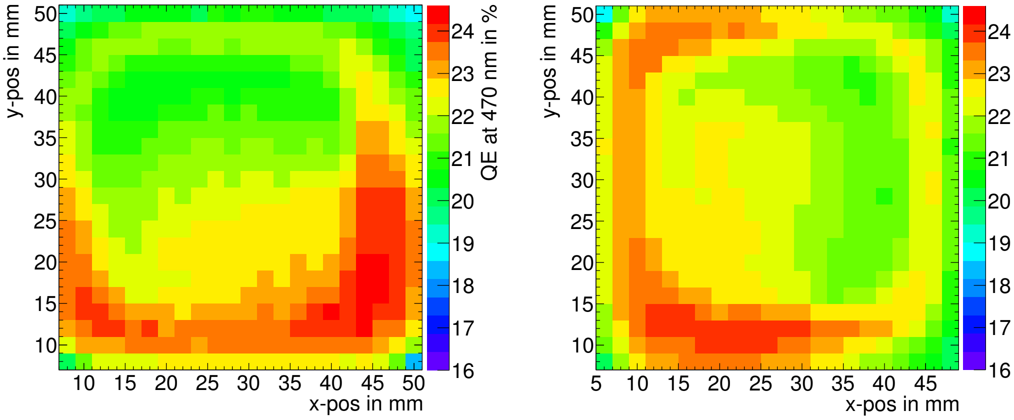

Figure 3.14 – *QE* scans of one H8500C-100-mod8 MAPMT oriented with start mark at the top left as seen from the front (left) and rotated clockwise by $90°$ (right). It can be seen that the pattern in the *QE* distribution rotates with the MAPMT.

step of the production process. Secondly, and with more impact on the *QE* inhomogeneity, a bending of the focusing electrode can result in a change of the amount of photoelectrons arriving on the first dynode [99]. In the latter case, the term *collection efficiency hole* is more precise than *QE* hole. A *QE* hole is also seen in a 1" MAPMT where a more homogeneous deposition of the photocathode from the gas phase onto the MAPMT window and a less pronounced bending of the focusing electrode could be expected due to the smaller size of the MAPMT. A reliable statement on the percentage of 1" MAPMTs with *QE* hole cannot be made since only two pieces were scanned. One of them shows a *QE* hole, the other one does not.

QE scans and the quantification of homogeneity will be discussed in section 4.4 with respect to the coating of MAPMT windows with wavelength shifting films.

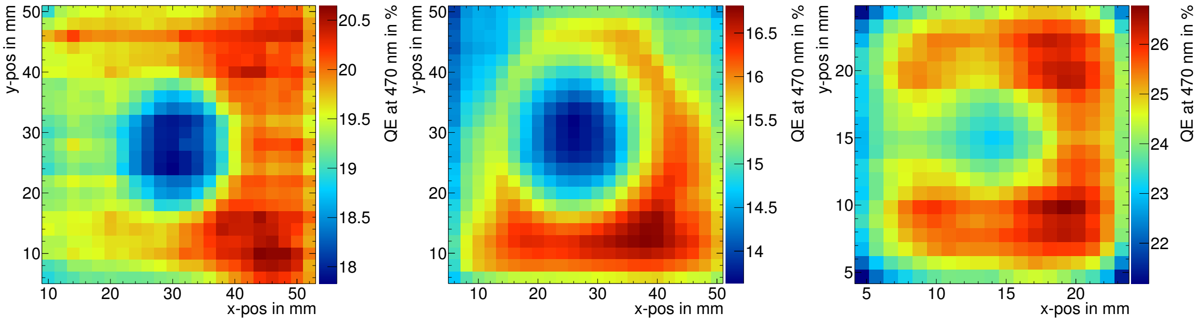

Figure 3.15 – *QE* scans of MAPMTs with low *QE* in the centre. H8500D-03 (left), R10552-03-M64 bare tube (centre), R11265-103-M16 (right).

3.5 Geometrical coverage

The outer dimensions of the MAPMTs of type H8500D-03 and R11265-103-M16 are 52.0×52.0 mm^2 and 26.2×26.2 mm^2, respectively. However, the area covered by the photocathode, the active area, is smaller and can be determined from a high resolution *QE* scan. Figure 3.16 displays the scan from Fig. 3.13 of a H8500D-03 MAPMT extended over the MAPMT edges as three-dimensional plot (left). Also shown is a scan of a R11265-103-M16 MAPMT (right). Fitting a Fermi function to the rising and trailing edges allows the determination of the active area. Here, the active area is defined as area with at least 90 % of the maximum value of the Fermi fit which corresponds to the *QE* of the plateau in the MAPMT centre neglecting the *QE* hole.

Figure 3.17 shows projections on x and y-axis through the MAPMT centre and the Fermi fits to the edges. The distance between the positions of 90 % of the fit maximum is stated. In addition, the distances corresponding to the specified active area in the data sheet are given. For the H8500D-03, this distance is reached at $\approx 50\,\%$ of the Fermi fit maximum, for the R11265-103-M16 at $\approx 30\,\%$. Table 3.3 compares the results with the specifications from the manufacturer.

The measurement presented here quantifies a precisely defined active area (area with $> 90\,\%$ of the plateau *QE*) whereas the manufacturer does not specify the active area clearly.

At 90 % of the maximum value of the Fermi fit the measurement reveals an active area which is relatively $\approx 5\,\%$ smaller than specified for the H8500D-03. For the R11265-103-M16, the measured value is $\approx 12\,\%$ smaller. It can be observed that the edges are more round for the R11265-103-M16 than for the H8500D-03 which could be a reason for the smaller measured active area when demanding at least $QE = 90\,\%$.

Even though the ratio between active area and external size differs for different MAPMT types, it is not needed to be known for the single photon counting experiments presented in section 3.10 since photoelectrons per pixel and per cm^2 total outer PMT area for single MAPMTs will be given.

In the CBM-RICH detector, the MAPMTs will be arranged in a matrix with a certain gap between individual tubes. Thus, the amount of insensitive area due to gaps between MAPMTs plays a role for the number of detected photon per area. Naturally, it depends on the external MAPMT size. It has been demonstrated that a gap width of 1 mm is feasible (cf. section 5.2). For a rectangular array (cf. Fig. 3.18), the ratio between MAPMT surface and instrumented area[6] is then 0.963 for the 2" MAPMT and 0.928 for the 1" MAPMT assuming a gap width of 1 mm.

---

[6] MAPMT surface means the area which is covered by MAPMTs without the gaps in between whereas instrumented area denotes the MAPMT surface plus gaps.

H8500D-03		
external size (S)	52.0×52.0 mm^2	
active area (A) specified	49.0×49.0 mm^2	$A/S = 88.8\,\%$
A measured at 90 % of max. *QE*	47.8×47.9 mm^2	$A/S = 84.7\,\%$
A measured at 70 % of max. *QE*	48.5×48.5 mm^2	$A/S = 87.0\,\%$
A measured at 50 % of max. *QE*	49.0×49.0 mm^2	$A/S = 88.8\,\%$
A measured at 30 % of max. *QE*	49.5×49.4 mm^2	$A/S = 90.4\,\%$
R11265-103-M16		
external size (S)	26.2×26.2 mm^2	
active area (A) specified	23×23 mm^2	$A/S = 77.1\,\%$
A measured at 90 % of max. *QE*	21.5×21.6 mm^2	$A/S = 67.7\,\%$
A measured at 70 % of max. *QE*	22.2×22.2 mm^2	$A/S = 71.8\,\%$
A measured at 50 % of max. *QE*	22.6×22.5 mm^2	$A/S = 74.1\,\%$
A measured at 30 % of max. *QE*	23.0×22.9 mm^2	$A/S = 76.7\,\%$

Table 3.3 – Active area of H8500D-03 and R11265-103-M16 MAPMTs determined from *QE* scans in comparison to the specification. In this thesis, the active area is defined as area with at least 90 % of the maximum value of a Fermi fit to the MAPMT edges. The manufacturer does not specify the active area exactly. It can be seen that for the H8500D-03, the measured active area is in agreement with the specification when defining the active area as area with at least $\approx 50\,\%$ of the maximum *QE* and $\approx 30\,\%$ for the R11265-103-M16.

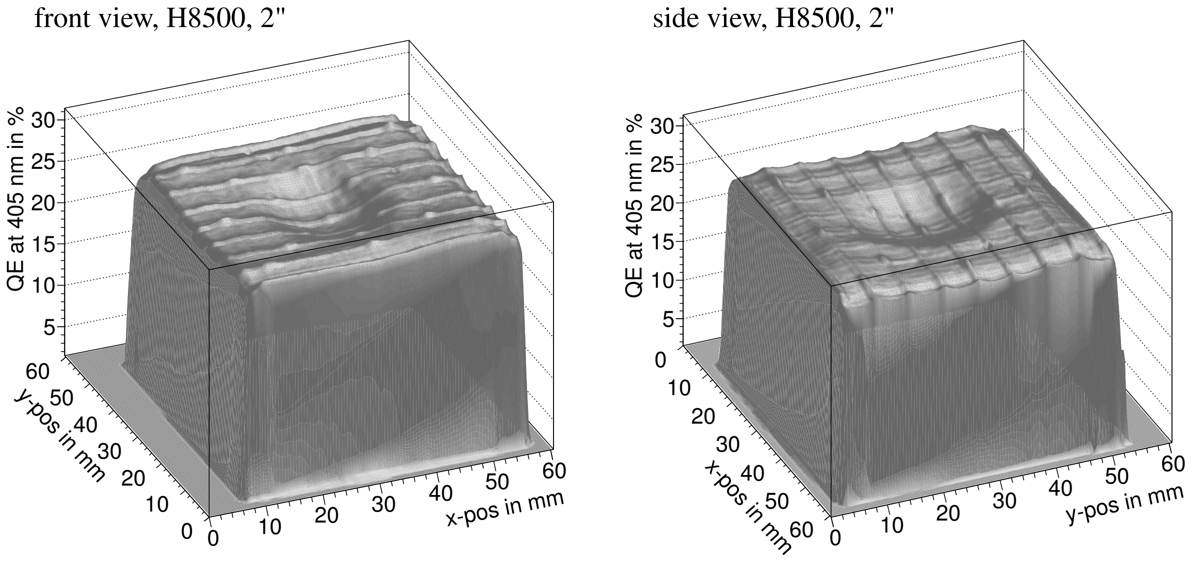

front view, H8500, 2"

side view, H8500, 2"

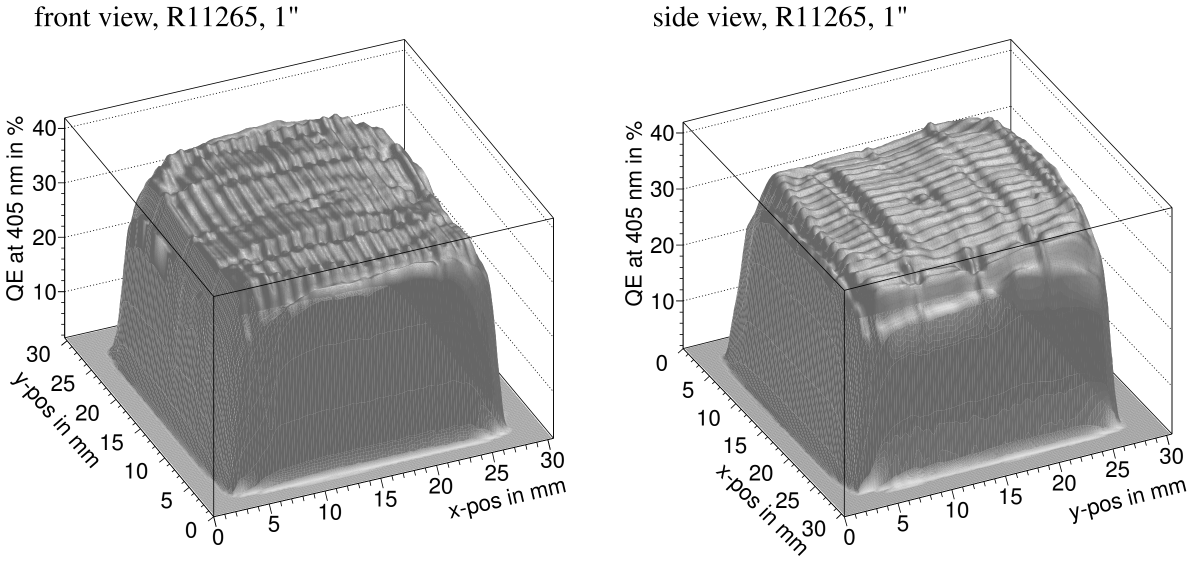

front view, R11265, 1"

side view, R11265, 1"

Figure 3.16 – Three-dimensional representations of *QE* scans at 405 nm from a H8500D-03 (top) and a R11265-103-M16 (bottom) MAPMT from two different sides. Apart from the *QE* hole in the centre, the plateau of the H8500D-03 is rather flat. The plateau of the R11265-103-M16 is also flat in y-direction but more bulgy in x-direction. The structures of the focusing electrode and the dynodes are visible in detail. They differ significantly between H8500D-03 and R11265-103-M16.

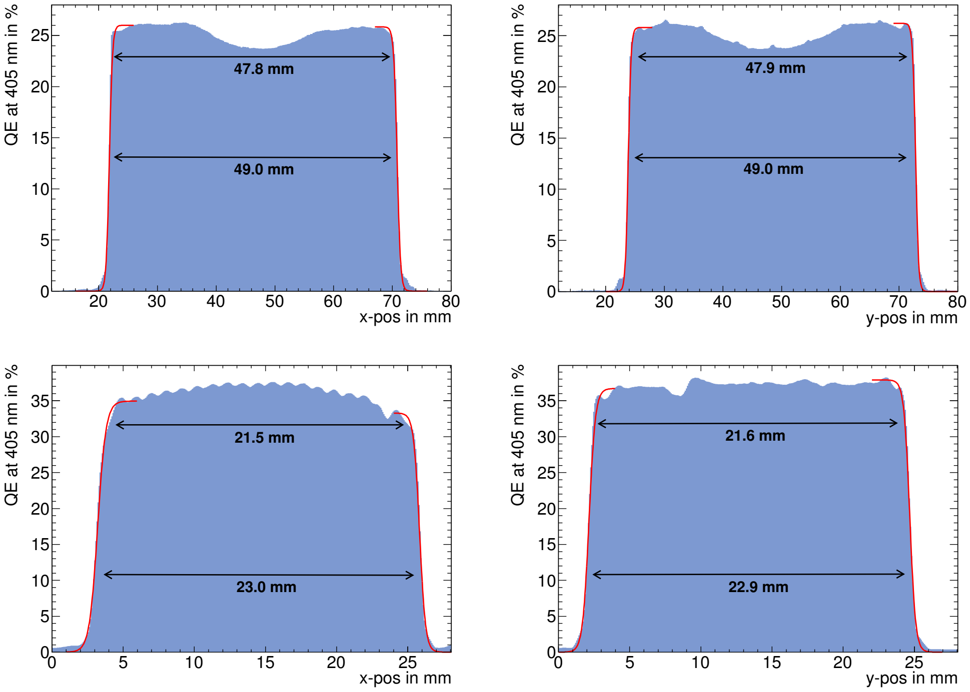

Figure 3.17 – Projection of the *QE* scan of a H8500D-03 (top) and R11265-103-M16 (bottom) on x (left) and y-axis (right). In the measurement, the active area is defined as area with at least 90 % of the maximum value of the Fermi fit. With this definition, the measured value is slightly lower than the specified value from the manufacturer which is not precisely defined. The measurement is in agreement with the specification when demanding at least $QE \approx 50\,\%$ for the H8500D-03 and $QE \approx 30\,\%$ for the R11265-103-M16.

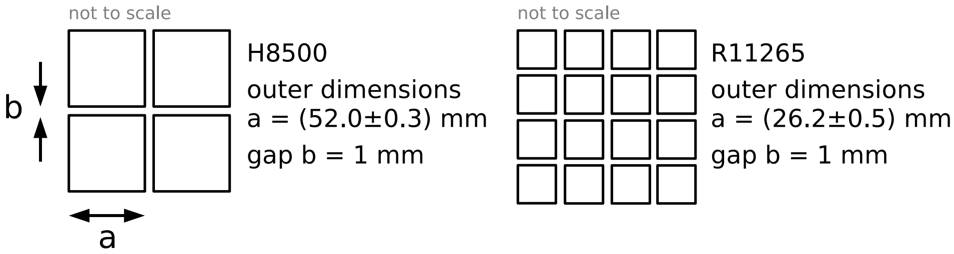

Figure 3.18 – Sketch for calculating the ratio R between MAPMT surface and instrumented area in a rectangular MAPMT array. $R = a^2/(a+b)^2$ with $R = 0.963$ for H8500 and $R = 0.928$ for R11265.

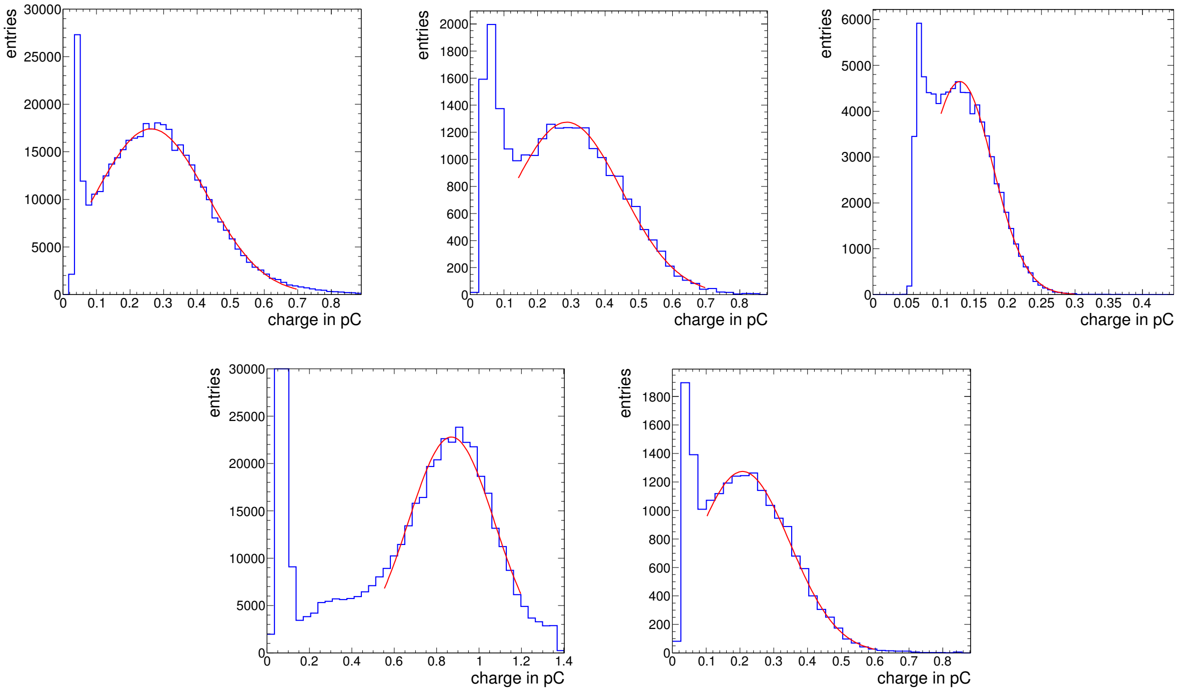

Figure 3.19 – Single photoelectron spectra of a R11265-103-M16, H8500D-03, and H10966A-103 MAPMT (top row from left to right). A hierarchy with respect to the peak-to-valley ratio can be seen. In the bottom row, a spectrum from a R11265-103-M16 with very high gain (left) and a spectrum from a selected “bad” H8500D (right) are shown. For all spectra, channels with the best peak-to-valley ratio are plotted. The red lines display gaussian fits to the single photoelectron peak. Note the different scale on the x-axes.

3.6 Single photoelectron spectra

Figure 3.19 shows single photoelectron spectra from MAPMTs of type H8500D-03, H10966A-103, and R11265-103-M16. Spectra from the channels with largest peak-to-valley ratio have been selected for a comparison of the potential of different MAPMT types. For these best channels, a clear hierarchy with respect to the peak-to-valley ratio can be found. The peak-to-valley ratio is largest for the R11265-103-M16, followed by the H8500D-03. For the H10966A-103, the single photoelectron peak is not very well separated from the noise peak. Due to the 8 dynode stages, the gain is lower in comparison to the 12 stages of the H8500D-03 and R11265-103-M16 resulting in an overlap of single photoelectron and noise peak. The role of the gain gets obvious when looking at the spectrum of a R11265-103-M16 with very high gain (measured to be $5.63 \cdot 10^6$, see section 3.7). For this tube, the peak-to-valley ratio is very large. The spectrum of a selected “bad” H8500D does not differ from the other “average” H8500D-03 indicating that the spectrum of the best channel is no selection criteria. Table 3.4 specifies the peak-to-valley ratios for the tested MAPMT types.

According to the manufacturer, the difference between the H8500D-03 and the R11256103-M16 is the dynode structure which makes the latter the recommended flat panel MAPMT for single photon detection [99].

In order to get an impression of the quality of different channels of the MAPMTs, Fig. 3.20 shows spectra from corner, central, vertical, and horizontal edge pixels. The spectra from different pixels do not significantly differ for the 64-channel 2" MAPMTs. For the 16-channel 1" R11265-103-M16, however, the central pixels shows a larger peak-to-valley ratio than edge and corner pixels. Despite of that the hierarchy in the quality of single photoelectron spectra mentioned above is confirmed when taking pixels from different positions into consideration.

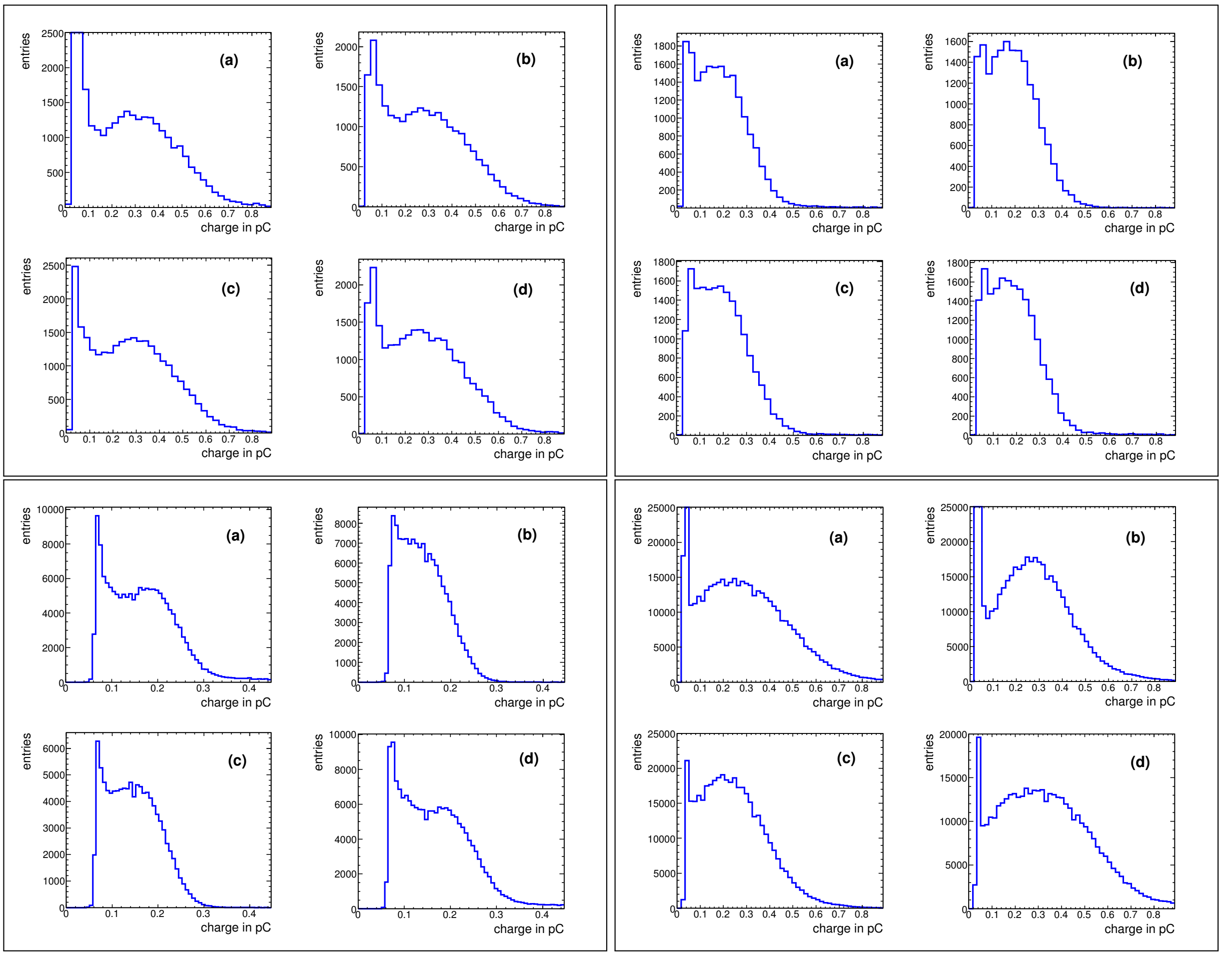

Figure 3.20 – Single photoelectron spectra from an "average" H8500D-03 (top left), "bad" H8500D (top right), H10966A-103 (bottom left), and R11265-103-M16 MAPMT (bottom rigth). Each frame with four spectra corresponds to one MAPMT. Spectra from a corner pixel (a), central pixel (b), and the vertical (c) and horizontal (b) edges are shown.

Fitting the single photoelectron peak

The position of the single photoelectron peak in the spectrum reveals the gain of a PMT. Red lines in Fig. 3.19 show that the peak can be well fitted by a gaussian. The determination of the gain by this method requires a charge calibration of the readout chain. A description of the procedure can be found in section 3.3.2 and results will be given in section 3.7.

The width σ of the single photoelectron peak normalised to the position, given by the mean μ of the fit, is listed in table 3.4 for the different MAPMT types. In contrast to the peak-to-valley ratio, no hierarchy is found.

3.7 Gain

The results of the gain determination presented in Tab. 3.5 are obtained by using the measurement setup outlined in section 3.3.2 and fitting the single photoelectron peak with a gaussian. The listed values for the measured gain indicate the average from all MAPMT pixels.

It can be seen that the gain determined from the position of the single photoelectron peak in the ADC

MAPMT type	serial no.	peak-to-valley ratio	width of spe peak σ/μ
H8500D-03	DA0150	1.25	0.57
H8500D-03	CA5093	1.27	0.47
H10966A-103	ZL0003	1.11	0.38
R11265-103-M16	ZN0733	1.92	0.63
R11265-103-M16	ZN0593	6.85	0.20

Table 3.4 – Peak-to-valley ratio and width of the single photoelectron peak for various MAPMT types. The peak-to-valley ratio is largest for the R11265-103-M16, followed by the H8500D-03 and the H10966A-103. No such hierarchy can be observed for the width σ of the photoelectron peak normalised to the mean μ.

spectrum is in approximate agreement with the specifications from the manufacturer.

However, the measurements systematically fall below the specifications. The relative difference varies from 10 % to 30 %. This variation shows that the discrepancy between measurement and specification is not solely due to a systematic uncertainty in the calibration of the readout chain. It might be partly caused by the exponential background below the single photoelectron peak which was not taken into account in the fits.

In spite of the observed difference, it can be seen that the gain for the MAPMT types with 12 dynode stages, H8500D-03 and R11265-103-M16, is similar and in the order of $1.6 \cdot 10^6 - 2.2 \cdot 10^6$ with two exceptions. One R11265-103-M16 (serial no. ZN0593) has a very high gain of $5.6 \cdot 10^6$. Three H8500D classified by the manufacturer as “bad” have low gain of $1.0 \cdot 10^6 - 1.4 \cdot 10^6$. The specified gain of the 8 stage MAPMT type H10966A-103 is $0.35 \cdot 10^6 - 0.40 \cdot 10^6$. The measured gain is $\approx 0.85 \cdot 10^6$

3.8 Uniformity

Related to PMTs, the term *uniformity* describes the variation of the output signal with respect to the position of the illumination on the photocathode. Since the functional principle of a PMT is based on two steps, the conversion of photons into photoelectrons in the photocathode and the multiplication of secondary electrons in the dynode system, it is desirable for a comlete understanding to determine the uniformity of both parts, the photocathode and the dynode system.

In order to distinguish between those two quantities, the term *gain uniformity* will be used in the following to refer to the variation of the electron multiplication in the dynode system and *homogeneity* for the variation of the photocathode sensitivity with respect to the position. The product of uniformity and homogeneity will be called *total uniformity*. Homogeneity was discussed in section 3.4.2 in the context of *QE* scans. Here, the total uniformity and the gain uniformity will be presented.

In technical literature and MAPMT data sheets, e.g. [87, 89], the uniformity is determined by illuminating the PMT with DC light from a tungsten lamp with blue filter and measuring the anode output current. With this method, only the total uniformity can be obtained. Consequently, only the total uniformity is stated in the final test sheets.

MAPMT type	serial no.	no. of dynodes	single photo-electron peak	measured gain	gain from final test sheet	rel. difference measurement - final test sheet
R11265-103-M16	ZN0593	12	0.90 pC	$5.63 \cdot 10^6$	$6.27 \cdot 10^6$	-10.2 %
R11265-103-M16	ZN0731	12	0.26 pC	$1.63 \cdot 10^6$	$2.03 \cdot 10^6$	-19.7 %
R11265-103-M16	ZN0733	12	0.25 pC	$1.57 \cdot 10^6$	$2.22 \cdot 10^6$	-29.3 %
H8500D-03	DA0140	12	0.31 pC	$1.95 \cdot 10^6$	$2.24 \cdot 10^6$	-12.9 %
H8500D-03	DA0128	12	0.35 pC	$2.19 \cdot 10^6$	$3.17 \cdot 10^6$	-30.9 %
H8500D-03	DA0134	12	0.25 pC	$1.57 \cdot 10^6$	$2.16 \cdot 10^6$	-27.3 %
H8500D-03	DA0150	12	0.27 pC	$1.66 \cdot 10^6$	$2.27 \cdot 10^6$	-26.9 %
H8500D	CA5039	12	0.17 pC	$1.09 \cdot 10^6$	$1.48 \cdot 10^6$	-26.4 %
H8500D	CA5101	12	0.16 pC	$1.00 \cdot 10^6$	$1.20 \cdot 10^6$	-16.7 %
H8500D	CA5535	12	0.22 pC	$1.40 \cdot 10^6$	$1.82 \cdot 10^6$	-23.1 %
H10966A-103	ZL0001	8	0.14 pC	$0.86 \cdot 10^6$	$0.40 \cdot 10^6$	-115 %
H10966A-103	ZL0003	8	0.14 pC	$0.85 \cdot 10^6$	$0.35 \cdot 10^6$	-143 %

Table 3.5 – Average gain of all pixels for different MAPMT types determined from a gaussian fit of the single photoelectron peak in comparison to the Hamamatsu specification for three pieces of R11265-103-M16, four pieces of H8500D-03, three pieces of H8500D which are selected by the manufacturer as “bad” (serial numbers starting by "CA"), and two pieces of H10966A-103. Compared to the average gain of the 12 stage MAPMTs, the measured gain of the 8 stage MAPMTs is lower by a factor of 2. The measured gain is the average of all MAPMT pixels.

3.8.1 Total uniformity

In order to measure the total uniformity on single photon level and compare to the DC measurements from the final test sheet, the setup shown in Fig. 3.8 has been used. A MAPMT of type H800C-100-mod8 was scanned in 160 × 160 steps and the response to pulses with a magnitude of the order of 100 photons was measured in terms of average signal amplitude in each of the 8 × 8 pixels. Figure 3.21 (left) shows the signal amplitude for every pixel normalised to the pixel with the largest amplitude. Since the MAPMT was illuminated by light pulses of many photons, the amplitude is dependent on both the conversion probability in the photocathode and the gain. The measured signal amplitude is therefore proportional to the total uniformity. The comparison with the MAPMT final test sheet (Fig. 3.21 right) shows that the measurements under illumination with many photons reproduce the results from the manufacturer’s DC light measurements qualitatively and also quantitatively fairly well. The ratio of the maximum to the minimum anode output is 1.5 for the measurement and 1.6 on the final test sheet.

3.8.2 Gain uniformity

The exclusive determination of the gain uniformity is feasible when using single photons instead of multi photon pulses or a DC ligth source. In this case, the photoconversion probability in the photocathode is irrelevant because either a signal from a single photon is detected or not. The gain is determined from the position of the single photoelectron peak in the ADC spectrum. In this section, gain uniformity is presented

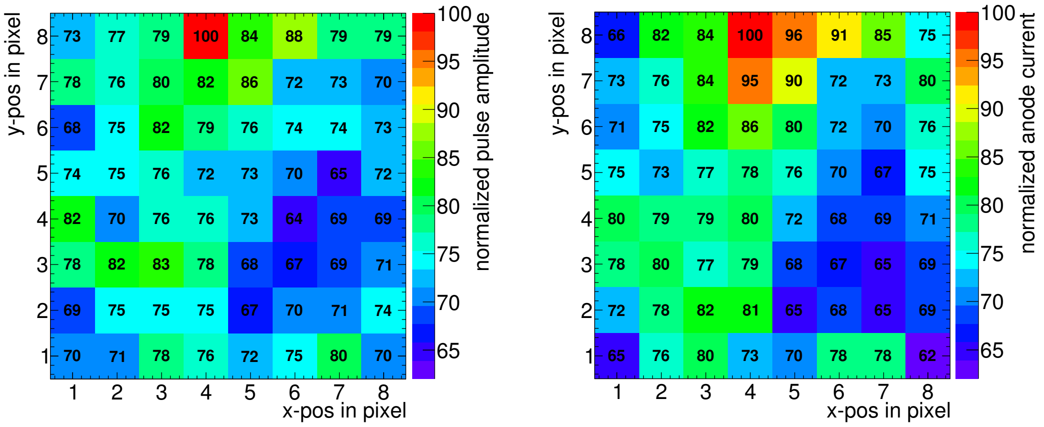

y-pos in pixel	1	2	3	4	5	6	7	8
8	73	77	79	100	84	88	79	79
7	78	76	80	82	86	72	73	70
6	68	75	82	79	76	74	74	73
5	74	75	76	72	73	70	65	72
4	82	70	76	76	73	64	69	69
3	78	82	83	78	68	67	69	71
2	69	75	75	75	67	70	71	74
1	70	71	78	76	72	75	80	70

y-pos in pixel	1	2	3	4	5	6	7	8
8	66	82	84	100	96	91	85	75
7	73	76	84	95	90	72	73	80
6	71	75	82	86	80	72	70	76
5	75	73	77	78	76	70	67	75
4	80	79	79	80	72	68	69	71
3	78	80	77	79	68	67	65	69
2	72	78	82	81	65	68	65	69
1	65	76	80	73	70	78	78	62

Figure 3.21 – Total uniformity of a H8500C-100-mod8 MAPMT. Amplitude per pixel normalised to the hottest pixel from a measurement with light pulses of a magnitude of the order of 100 photons (left) and anode current for a DC current measurement (tungsten lamp with blue filter) from the final test sheet (right). The distributions of both quantities roughly coincide.

MAPMT type	serial no.	gain variation ($\text{gain}_{\text{max}}/\text{gain}_{\text{min}}$)
H8500D	CA5093	1.89
H8500D	CA5101	2.44
H8500D	CA5535	3.13
H8500D-03	DA0128	1.69
H8500D-03	DA0129	1.49
H8500D-03	DA0134	2.08
H8500D-03	DA0136	1.54
H8500D-03	DA0138	1.49
H8500D-03	DA0136	1.43

Table 3.6 – Variation of gain between the pixels with largest and lowest gain within one MAPMT determined from the single photoelectron peak.

which was measured using the setup for a homogeneous single photon illumination depicted in Fig. 3.7.

For nine H8500D-03, the gain was determined in each pixel. The variation of the gain, given as ratio between maximum and minimum gain for every MAPMT is listed in Tab. 3.6. It can be seen that it spreads between 1.43 and 2.08 for the average H8500D-03 and reaches values of 1.89 to 3.13 for the MAPMTs selected by the manufacturer as “bad” (serial numbers starting by "CA"). Compared to the total uniformity, specified by Hamamatsu to be typically 2 and maximal 4 [89], the exclusively measured uniformity of the gain is lower. This result is expected since the total uniformity comprises the contributions from the photocatode and the amplification stage as mentioned before.

The variation of gain within one MAPMT should be considered when grouping the MAPMTs for the final CBM-RICH detector into gain classes.

The measurements of the gain uniformity strengthen the argument that the *QE* holes, discussed in sec-

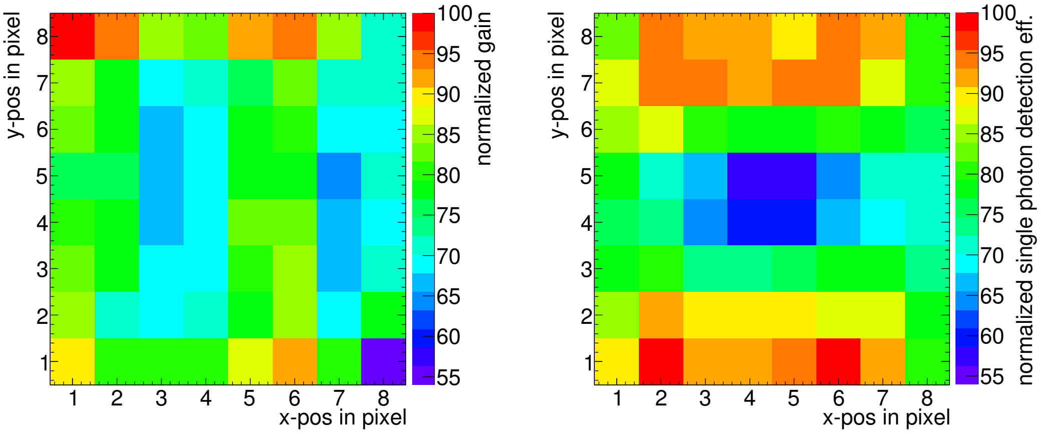

Figure 3.22 – Normalised gain of a H8500D-03 (DA0136) determined from the position of the single photoelectron peak (left) and normalised single photon detection efficiency, determined by photon counting under homogeneous single photon illumination (right). The absence of an area with low gain and the presence of an area with low detection efficiency in the MAPMT centre support the argument that the *QE* hole is not related to the amplification chain of the MAPMT (see section 3.4.2).

tion 3.4.2, have their origin in inhomogeneities of the photocathode and the bending of the focusing electrode and not in the dynode system since gain uniformity distributions from MAPMTs with *QE* hole do not show any circular structures. Figure 3.22 (left) depicts the gain per pixel for one H8500D-03 (serial number DA0136). No decrease of gain in the innermost pixels can be seen but rather a vertical band-like structure. In contrast to that, the normalised single photon detection efficiency (right), measured as described in section 3.10, reveals a clear hole in the MAPMT centre.

3.9 Crosstalk

In general, crosstalk denotes the coupling of a signal to neighbouring channels. As a result, a signal is measured in a channel which originally was not exposed to light. In the case of MAPMTs, there are two sources of crosstalk resulting in the distribution of anode output charge to more than one anode pad.

1. Optical crosstalk denotes crosstalk from the incident light spread in the front window and from photoelectrons travelling on a curved trajectory from photocathode to first dynode. This mainly causes a smearing of the hit position and therefore deteriorates the spatial resolution. This type of crosstalk is mainly affected by the usage of wavelength shifting films because of their isotropic fluorescence.

2. Electrical crosstalk denotes crosstalk from the splitting of the electron avalanche between the dynodes during secondary electron multiplication and on the segmented anodes. Beside a loss of spatial information, this generates additional hits in the neighbouring pixels. If e.g. one pixel is hit by a photon and the fraction of charge collected in a neighbouring pixel passes the threshold, two hits are registered, one true hit and one additional crosstalk hit.

Experimentally, the separate quantification of optical and electrical crosstalk is difficult because both sources of crosstalk affect measurable quantities. In practise, the overall influence of crosstalk on measurable quantities is of interest. In the following, the number of additional crosstalk hits will be studied. The influence of crosstalk on the spatial resolution will be addressed in section 4.5 along with WLS films and in section 5.5 with respect to the sharpness of Cherenkov rings.

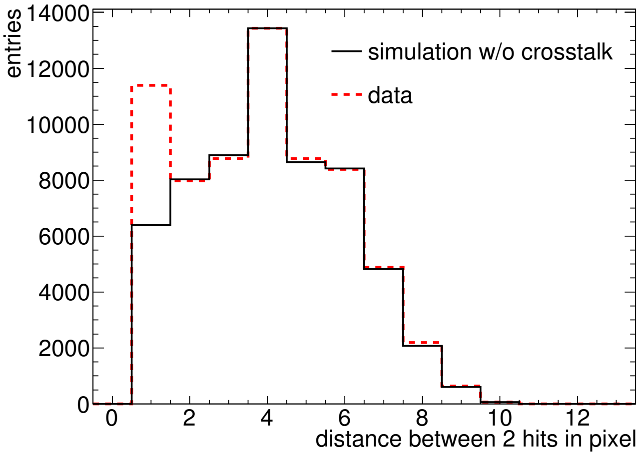

Figure 3.23 – Geometrical distance of hits in 2-hit-events within one MAPMT in simulation (continuous) and data (dashed). Because of crosstalk, simulation and data differ in the second bin ("neighbour bin"). The number of additional crosstalk hits in data is quantified by the excess in the neighbour bin.

Crosstalk measurements for MAPMTs from the H8500 series have already been done by illuminating one pixel locally with a pulsed LED or a tungsten lamp with the help of an aperture mask or an optical fibre [108, 87]. Here, a measurement of additional hits caused by crosstalk on single photon level at a wavelength of 275 nm will be presented. The measurement is based on a homogeneous single photon illumination of the MAPMT without usage of an aperture mask or light fibre which has the advantage that the photons hit the pixels not only in the central part but homogeneously distributed over the whole surface as it will be the case in the RICH detector. Single photons hitting the outer parts of a pixel will create more crosstalk than those hitting the centre.

The analysis is based on a statistical method. In order to estimate the number of additional hits in neighbouring pixels due to crosstalk, the distribution of the geometrical distance of hits in events with exactly 2 hits per MAPMT (2-hit-events) is compared to a simulation without crosstalk (Fig. 3.23). The normalised excess of entries in the bin corresponding to direct and diagonal neighbours in the data compared to the simulation quantifies the crosstalk.

The crosstalk extracted by this method depends on the effective threshold applied to the ADC signal. Figure 3.24 shows the additional hit fraction as function of MAPMT gain for 12 pieces of H8500D-03 and 7 pieces R11265. It can be seen that for a common threshold for all MAPMTs the crosstalk rises with gain. This is expected as for high-gain MAPMTs the relatively small ADC values of the crosstalk hits more likely pass the threshold. A similar plot should be obtained for each MAPMT when varying the gain using different HV settings. If, however, individual thresholds for every MAPMT at 10 % of the single photoelectron peak are applied, the crosstalk is fairly constant. When averaging the values, we see that for H8500D-03 (6.8 ± 1.2) % additional crosstalk hits are found and (3.2 ± 0.7) % for R11265-103-M16 MAPMTs.

For single photon counting, discussed in section 3.10, the crosstalk hit fraction for the individual MAPMTs at the given threshold is considered.

Systematic error

A drawback of the proposed method for crosstalk quantification is the systematic error which depends on the hit multiplicity. If the hit multiplicity is too low, the majority of events has zero or only one hit and the selected 2-hit-events will contain predominantly one real and one crosstalk hit. Thus, the selection of 2-hit-events implies a preselection of additional crosstalk hits resulting in an overestimation of crosstalk. If,

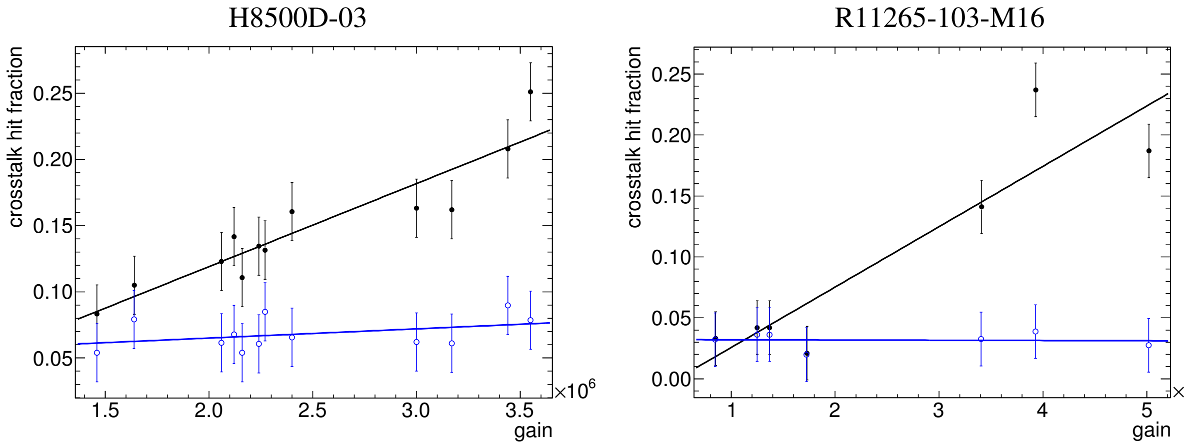

Figure 3.24 – Crosstalk hit fraction as function of gain for common threshold (filled black circles) and for threshold at 10 % of the single photoelectron peak (open blue circles) for H8500D-03 (left) and R11265-103-M16 (right). Lines indicate linear fits to the data. Every data point corresponds to one MAPMT. HV of all MAPMTs was set to the same nominal value of 1000 V.

on the other hand, the hit multiplicity is too low, the crosstalk is underestimated [109].

The hit multiplicity follows a Poisson distribution with a mean value of ≈ 2 hits per event in the analysed data sets. It was shown that this range of hit multiplicity leads to a minimum systematic error [109].

Therefore, the crosstalk values given here can be considered as rough estimate without exact quantification of the systematic error which is currently under investigation. For a comparison of different MAPMTs, in addition, the systematic error is of minor importance when using the same measurement setup and conditions as it is the case in the study presented here.

3.10 Single photon detection efficiency

The ratio between the number of counted pulses under single photon illumination (output pulses passing the ADC threshold) and the number of incident photons is called single photon detection efficiency. The single photon detection efficiency of a PMT is influenced by quantum efficiency, collection efficiency, signal-to-noise-ratio and threshold level. In our measurement, the number of incident photons can not be counted and remains unknown. Hence, only the relative single photon detection efficiency can be determined providing that the single photon source is homogeneous in space and constant in time.

The uncertainty of the single photon counting measurements due to instabilities of the photon source in the measurement setup is below 1 %. The corresponding study can be found in appendix B.

A counted pulse is called *hit*. The term hit is introduced here to make clear that the number of counted pulses contains photoelectron pulses from incident photons and additional pulses from crosstalk (see section 3.9). The number of hits is a measure for the relative single photon detection efficiency. As an example, Fig. 3.25 shows the number of hits per pixel for four pieces of H8500D-03 (left), and one H8500D-03 together with one R11265-103-M16 (right) for a homogeneous single photon illumination at 405 nm. For the quantitative results given below, additional crosstalk hits are subtracted.

Comparison between MAPMTs of the same type

In order to get an impression of the tube-to-tube variation in single photon detection efficiency between different pieces of the same MAPMT type, a comparison of twelve pieces of H8500D-03 has been made.

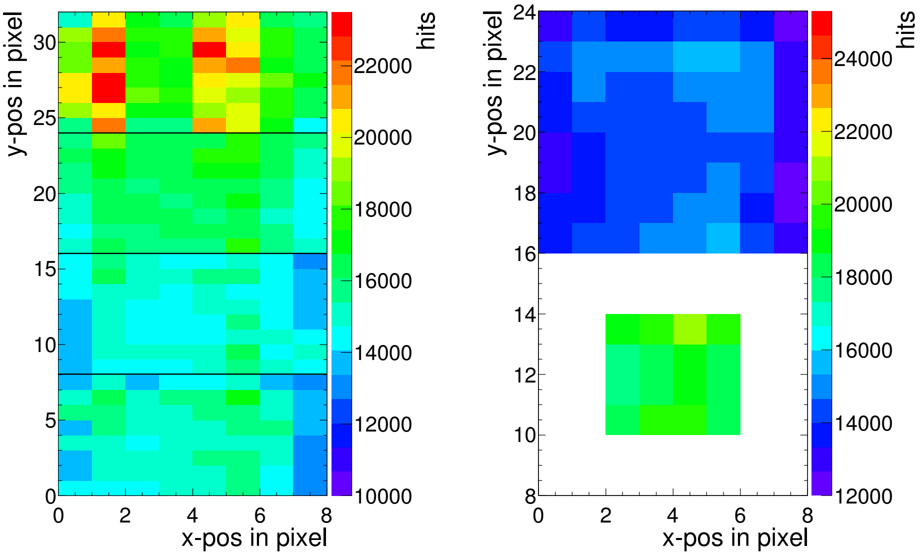

Figure 3.25 – Number of hits per pixel at 405 nm for a homogeneous single photon illumination. Exemplarily shown here are the results for four H8500D-03 (left), and one H8500D-03 together with one R11265-103-M16 (right). Crosstalk hits are not yet subtracted. The left plot reveals the variation among different pieces of H8500D-03. The comparison between H8500D-03 and R11265-103-M16 on the right side shows the higher detection efficiency of the SBA cathode of the R11265-103-M16 compared to the BA cathode of the H8500D-03. Note that the light intensity for both measurements (left and right side) has been different, therefore a direct comparison between the left and the right plot is not possible. Left and right plots are not to scale. The aspect ratio is adjusted to align both plots.

Table 3.7 shows the number of hits per MAPMT for a homogeneous single photon illumination. The spread between the best and the worst MAPMT is 15.7 %, i.e. the best tube detects 15.7 % more photoelectrons than the worst one. All MAPMTs except DA0076 have been produced in a relatively short period between October 2010 and January 2011. It is therefore hypothesised that no optimisation in the production process has been done and the results reflect the tube-to-tube variation. It was observed by other experiments [110], that the quality of the tubes can be improved and the tube-to-tube variation decreased during mass production e.g. for a quantity like afterpulsing which is directly related to the amount of rest gas in the vacuum tube. For the photocathode sensitivity though, it was observed that there is no improvement.

Selected “bad” tubes

The number of hits for the three selected “bad” MAPMTs in comparison with a very good (DA0150) and two average MAPMTs (DA0134, DA0129) is shown in Tab. 3.8. The measurements show that their performance is slightly worse than the reference average. However, it is well within the spread of the unclassified tubes.

Comparison between H8500D-03 and R11265-103-M16

In total, seven pieces of R11265-103-M16 were available for a comparison with H8500D-03. Because not all MAPMT were available at the same time, they had to be measured in two groups. A direct comparison of MAPMTs from different groups is not possible because setting up the measurement another day results in a different light intensity. The first group of three R11265-103-M16 was compared to a MAPMT with average performance (DA0134, cf. Tab. 3.7). Since DA0134 was not available as reference for the measurement of the second group of four R11265-103-M16, a MAPMT with very similar performance as DA0134 was used (DA0140, cf. Tab. 3.7).

MAPMT type	serial no.	hits/MAPMT (crosstalk subtracted)	hits/MAPMT rel. to max
H8500D-03	DA0150	936192	100 %
H8500D-03	DA0128	918526	98.5 %
H8500D-03	DA0147	919711	96.9 %
H8500D-03	DA0154	905826	95.7 %
H8500D-03	DA0132	875387	94.4 %
H8500D-03	DA0134	882638	93.4 %
H8500D-03	DA0140	878420	93.0 %
H8500D-03	DA0129	863763	92.9 %
H8500D-03	DA0141	833094	88.9 %
H8500D-03	DA0138	808731	86.9 %
H8500D-03	DA0076	797726	86.0 %
H8500D-03	DA0136	792326	84.3 %

Table 3.7 – Number of hits per MAPMT for a homogeneous single photon illumination for twelve H8500D-03 MAPMTs at 405 nm. The absolute number and the number relative to the most efficient MAPMT is given. The least efficient MAPMT detects 15.7 % less photons than the most efficient one.

MAPMT type	serial no.	hits/MAPMT (crosstalk subtracted)	hits/MAPMT rel. to reference average
H8500D-03	DA0129	822572	−2.7 %
H8500D-03	DA0150	888892	+5.2 %
H8500D-03	DA0134	824394	−2.5 %
H8500D	CA5093	842670	−0.3 %
H8500D	CA5101	844699	−0.1 %
H8500D	CA5535	841072	−0.5 %

Table 3.8 – Number of hits for a homogeneous single photon illumination for selected H8500D-03 and H8500D at 405 nm. The three MAPMTs with serial numbers starting by DA are used as reference, MAPMTs with serial numbers starting by CA are selected “bad” tubes.

In addition to the number of hits per pixel, Tab. 3.9 lists also the number of hits per instrumented area. Due to the different size of the two MAPMT types, the ratio between active area and gaps between the MAPMTs differs. For this analysis, a realistic gap width of 1 mm between MAPMTs on the carrier PCB board as described in section 5.2 and tested in the real-size RICH prototype is considered. The number of hits per instrumented area is more meaningful in anticipation of the foreseen arrangement of MAPMTs in the CBM-RICH camera. Compared to the H8500D-03, the number of detected photoelectrons per instrumented area for the R11265-103-M16 is 30 % to 47 % larger.

In Fig. 3.9, it was shown that SBA photocathodes have considerable higher *QE* than BA photocathodes. In average, the *QE* value of the seven R11265-103-M16 (SBA) at 400 nm is 43.7 % larger than the average *QE* of the two reference H8500D-03 (BA). This number is very well in agreement with the average increase in hits/pixel for the R11265-103-M16 compared to the two H8500D-03 (cf. Tab. 3.9). One can thus draw the conclusion that the larger single photon detection efficiency of the R11265-103-M16 MAPMTs is solely due to the higher *QE* of the SBA photocathode. There is no benefit from the larger peak-to-valley ratio in the single photoelectron spectrum shown in Fig. 3.19.

MAPMT type	serial no.	hits/pixel (crosstalk subtracted)	hits/pixel rel. to H8500D-03	hits/cm^2 (crosstalk subtracted)	hits/cm^2 rel. to H8500D-03
H8500D-03	DA0140	201057	-	458077	-
R11265-103-M16	ZN0593	304623	+51.5 %	663685	+44.9 %
R11265-103-M16	ZN0731	284522	+41.5 %	619891	+35.3 %
R11265-103-M16	ZN0733	284435	+41.5 %	619703	+35.3 %
H8500D-03	DA0134	12566	-	28629	-
R11265-103-M16	ZN0557	17237	+37.2 %	37554	+31.2 %
R11265-103-M16	ZN0591	17098	+36.1 %	37252	+30.1 %
R11265-103-M16	ZN0734	18317	+45.8 %	39908	+39.4 %
R11265-103-M16	ZN0768	19318	+53.7 %	42088	+47.0 %

Table 3.9 – Number of hits per pixel and per cm^2 instrumented area for R11265-103-M16 in comparison with H8500D-03 at 405 nm. The different ratio between active area and gaps due to different tube size is considered assuming 1 mm gap between neighbouring tubes.

Single photon detection efficiency vs. blue sensitivity

It is desirable to get an idea of the single photon detection efficiency of MAPMTs from the final test sheet provided by the manufacturer. The single photon detection efficiency itself is not given. Among the given parameters[7], the blue cathode sensitivity index has been found to be strongly correlated with the measured relative single photon detection efficiency (see Fig. 3.26 right). An exception from this correlation is observed for two MAPMTs with a strongly pronounced *QE* hole (cf. section 3.4.2). The blue sensitivity index is a measure for the current of photoelectrons from the photocathode when illuminating the MAPMT with a tungsten lamp and a blue filter. The blue sensitivity index is correlated with the measured *QE* at 400 nm (Fig. 3.26 left).

The result shows that a high blue sensitivity index is an indication for a high single photon detection efficiency.

---

[7] Cathode luminous sensitivity in µA/lm, anode luminous sensitivity in A/lm, anode dark current in nA, cathode blue sensitivity index, and gain are provided with every MAPMT

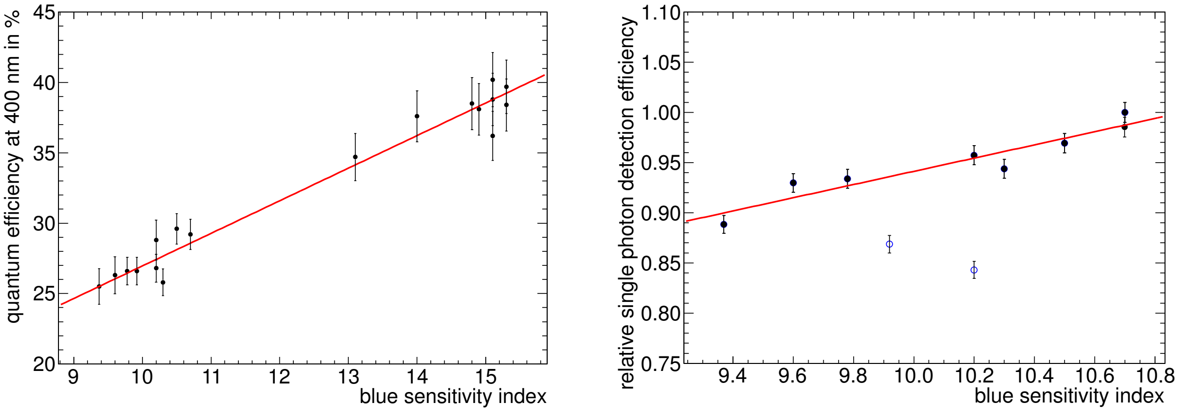

Figure 3.26 – Left: Measured *QE* versus blue sensitivity index from the final test sheets for nine MAPMTs with BA and nine MAPMTs with SBA photocahtode. A strong correlation can be observed. The red line indicates a linear fit to the data. Right: Relative single photon detection efficiency versus blue sensitivity index for H8500D-03 MAPMTs. A strong correlation can be seen except for two MAPMTs which show a strongly pronounced *QE* hole (open circles). The red line indicates a linear fit to the data points excluding the two MAPMTs with strong *QE* hole.

3.11 Summary

In this chapter, different types of Hamamatsu MAPMTs were characterised regarding their suitability for the use in the CBM-RICH camera using dedicated measurement setups.

Wavelength dependent absolute quantum efficiency measurements show a higher peak efficiency of SBA compared to BA photocathodes. The relative increase is 40 % to 60 % at around 360 nm and decreases towards smaller wavelengths. At 200 nm no difference between SBA and BA photocathodes is observed. It is shown that borosilicate entrance windows are no option for the use in an UV-transparent gaseous RICH detector due to a cutoff at 300 nm [8]. It could be shown that the *QE* around 200 nm is directly proportional to the thickness of the MAPMT front glass demonstrating that the front glass is the limiting factor in this wavelength region. When convolving the wavelength dependent *QE* with the Cherenkov spectrum, a clear hierarchy of MAPMT types is obtained. Normalised to the best option, R11265-103-M16, the number of detected photons decreases for H10966A-103 (89.7 %), H8500D-03 (71.6 %), and H8500C-100-mod8 (62.6 %).

A *QE* scan of a MAPMT surface reveals a spatial variation in photocathode sensitivity of 17 %. For six out of twelve H8500D-03 and for one out of two measured R11265-103-M16, a remarkable decrease of *QE* in a circular shape in the MAPMT centre could be observed (*QE hole*). Since *QE* measurements are done without using the PMT amplification chain, it is shown that the *QE* holes are not caused by the secondary electron multiplication in the dynode system but originate from the photocathode and the fosusing electrode. This is confirmed by the absence of *QE* holes in spatially resolved gain measurements.

It was shown that single photon detection is possible with all tested MAPMT types. For the H8500, this result is interesting with respect to the statement from the manufacturer who does not recommend this MAPMT type for single photon detection. However, the result is in agreement with findings from other collaborations [95, 111].

The shape of single photoelectron spectra from different pixel positions does not differ systematically. Apart from single channels with bad spectra, no difference between centre, corner, or edge pixels can be seen. A

---

[8] Another reason why UV glass is preferred is its radiation hardness which is superior to that of borosilicate glass [87].

comparison of the best channels of the corresponding MAPMTs reveals a clear hierarchy, the R11265-103-M16 showing the largest peak-to-valley ratio, followed by the H8500D-03, and H10966A-103. No such hierarchy is found with respect to the width of the single photoelectron peak.

The average gain of MAPMTs was determined from the position of the single photoelectron peaks using a calibration measurement of the readout chain. The gain of MAPMTs with 8 dynode stages is measured to be lower by a factor of 2 compared to 12 stage MAPMTs. The variation of gain between the pixels spreads between 1.43 and 2.08 for a set of H8500D-03.

It has been shown that in single photon counting mode, the ratio of hits coming from crosstalk is 6.8 % for the H8500D-03 and 3.2 % for the R11265-103-M16 when applying an ADC threshold at 10 % of the single photoelectron peak. There is very little variation for different MAPMTs of the same type. The number of crosstalk hits increases linearly with gain for a given threshold.

The variation in single photon detection efficiency within a set of twelve H8500D-03 MAPMTs is 15.7 %. At 405 nm R11265-103-M16 MAPMTs detect 30 % to 47 % more photons than H8500D-03 MAPMTs. This number corresponds to the increase in *QE* what leads to the conclusion that the larger single photon detection efficiency of the R11265-103-M16 is solely due to the higher *QE* and the shape of the single photelectron spectra plays an inferior role. This is supported by the observation of a strong correlation between the relative single photon detection efficiency and the blue sensitivity index for both MAPMT types.

Finally, three H8500D, selected by Hamamatsu as “bad” because of poor single photoelectron spectra and relatively low gain, were reviewed. Their relative single photon detection efficiency was found to be well within the spread of the other H8500D-03 which, again, underpins the argument that, given the sound single photoelectron response of H8500D-03 and R11265-103-M16, the photocathode sensitivity can be seen as fundamental indicator of the single photon detection efficiency.

New Hamamatsu development H12700

Hamamatsu Photonics K.K. announced the release of a newly developed 2" MAPMT for January 2014 [112]. It will have the same outer shape as the H8500 and the dynode structure of the R11265. According to the manufacturer, it will therefore combine the good geometrical coverage of the H8500 with the good single photoelectron peak and the low crosstalk of the R11265. Test samples are currently under investigation in the laboratory in Wuppertal.

Chapter 4

Wavelength shifting films

The use of wavelength shifting (WLS) films applied on the front window of photon sensor devices aims at increasing the integral quantum efficiency. Due to the high UV transparency of the CO_2 radiator of the CBM-RICH detector, a high photon detection efficiency of the CBM-RICH photon detector at small wavelengths is favourable. WLS films absorb UV photons and re-emit photons at larger wavelengths where the quantum efficiency of common photocathodes is higher. As mentioned in section 3.2, the CBM-RICH photon detector will be equipped with MAPMTs with bialkali or super bialkali photocathodes and UV-windows. So far, no results on the performance of WLS films on MAPMTs with UV-window have been reported. In the last years, an extensive R&D program in collaboration with the Hochschule Esslingen has been carried out in order to study the performance of WLS films on MAPMTs with UV-window and to develop and optimise a suitable application process. The latter as well as the characterisation of the films in terms of absorption and fluorescence measurements was done in Esslingen, whereas all characterisation of WLS films on PMTs was done in Wuppertal. This chapter aims at summarising the results of the R&D program with a focus on the evaluation of the performance of WLS films on MAPMTs with respect to the detection efficiency. After a brief introduction (section 4.1) and a presentation of application techniques (section 4.2), quantum efficiency measurements are presented in section 4.3. In a first cycle, the influence of the film thickness on the quantum efficiency was studied and a set of four MAPMTs was prepared for an in-beam test. In a second cycle, the effect of WLS films on MAPMTs with BA and SBA photocathode with optimised thickness was investigated. MAPMTs were prepared for a second in-beam test. The film homogeneity is discussed in section 4.4 and the influence of WLS films on the crosstalk in section 4.5.

4.1 Introduction to WLS films

Figure 4.1 shows a *QE* curve of a typical H8500D-03 MAPMT together with a simulation of the number of Cherenkov photons produced per wavelength interval in a thin quartz radiator of 4 mm thickness. It can be seen that the *QE* is low in the UV range whereas the Cherenkov spectrum rises according to $1/\lambda^2$.

The usage of organic molecules as WLS films on phototubes with standard glass windows in a gaseous Cherenkov detector was proposed in a pioneering investigation already in 1973 [113]. Several groups studied WLS films on top of photon detectors with standard glass as an alternative to expensive devices with LiF, MgF_2, and GaF_2 windows [114, 115, 116], which, furthermore, were not available as large-area sensors. These papers discuss evaporated WLS films. Dip-coated films were first mentioned in [117]. WLS films sprayed from a methyl alcohol solution are presented in [118, p. 212].

According to [114], incident UV photons are absorbed by the molecules of the WLS film and form excited molecular states which can de-excite by the emission of photons at larger wavelengths. For p-Terphenyl,

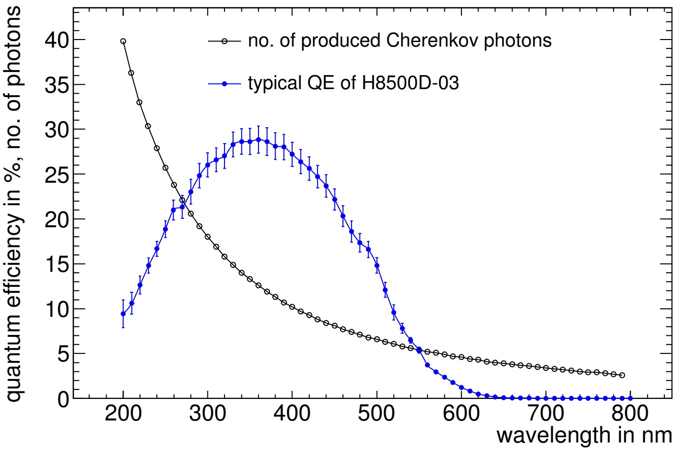

Figure 4.1 – Number of produced Cherenkov photons in a 4 mm thick UV-transparent quartz radiator and quantum efficiency of a typical H8500D-03 MAPMT. It can be seen that in contrast to the $1/\lambda^2$ Cherenkov emission spectrum, the quantum efficiency of the MAPMT is rather low in the UV range.

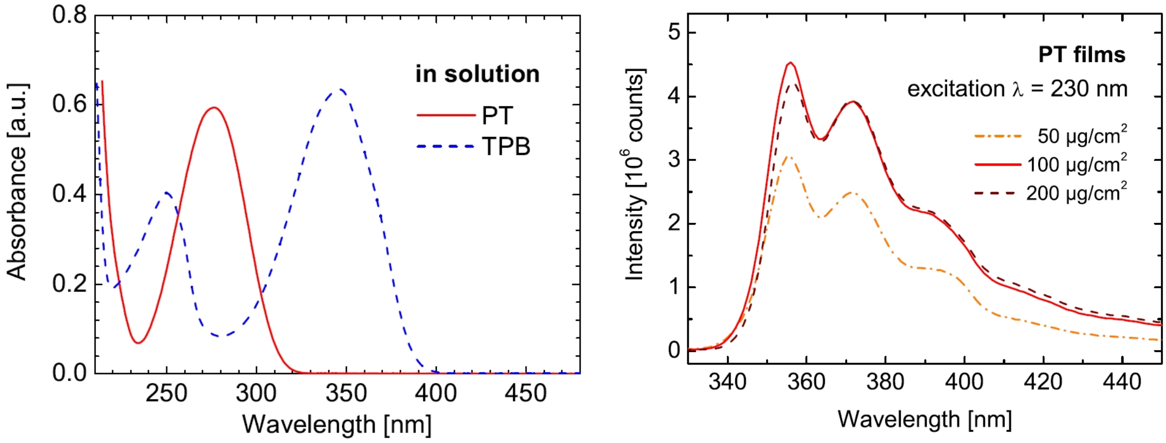

Figure 4.2 – Absorption spectra pf PT and PTB in cyclohexane (left) and fluorescence spectra of evaporated PT films of different thickness at an excitation wavelength of 230 nm (right). Figures taken from [6].

a decay time of these excited states of the order of 1 ns to 2 ns is reported [113]. The angular distribution of fluorescence was studied using a probe of sodium salicylate. It was shown that fluorescence photons are emitted isotropically in a certain thickness range [119].

In this thesis, films with p-Terphenyl (PT) will be studied, since initial experiments with PMTs coated with PT and Tetraphenyl-butadiene (TPB) revealed that PT is a suitable molecule for the use as wavelength shifter deposited on the front window of PMTs [120]. Absorption and fluorescence spectra are shown in Fig. 4.2. PT absorbs light at wavelengths below 300 nm and emits fluorescence photons mainly between 350 nm and 390 nm. The absorption of PTB in contrast, peaks between 300 nm and 400 nm. When comparing with the sensitive wavelength region of bialkali and super bialkali photocathodes shown in Fig. 3.9, it becomes clear that PTB is not suited to increase the integral *QE*. p-Terphenyl consists of a benzene ring and two phenyl groups as depicted in Fig. 4.3. Its molecular formular is $C_{18}H_{14}$.

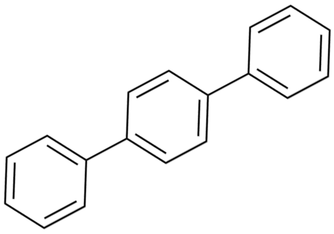

Figure 4.3 – Chemical structure of p-Terphenyl. Figure taken from [121].

4.2 Application techniques

The goal of processes for the deposition of WLS coatings on PMT windows is to produce films with the desired absorption and emission spectra in the wavelength range of interest. This requires in particular a precise control of the film thickness. In addition, the films should be homogeneous and mechanically resistant. In the case of CBM, the process itself should be fast and simple in order to be able to coat ≈ 1000 MAPMTs in a reasonable time and at a moderate costs.

Three different application techniques have been studied. Initially, PMTs were coated by means of evaporation, a variant of physical vapour deposition, from a resistively heated molybdenum boat in a vacuum evaporator at a base pressure of about $3 \cdot 10^{-6}$ mbar. When heating the boat, the solid material evaporates, travels through the vacuum and condensates from the gas phase on the substrate resulting in a thin solid film. The film thickness increases linearly with material load which is determined by evaporation rate and deposition time [122]. The importance of the film thickness will be discussed in section 4.3.

Later, the studies were focused on wet-chemical application methods, namely spin-coating and dip-coating. In wet-chemical application, in contrast to the evaporation method where pure PT is evaporated, the wavelength shifting molecule is deposited from a solution containing a binder and a solvent. In the spin-coating process, the solution is applied on the rotating substrate. During rotation, the solution spreads due to the centrifugal force and the volatile solvent evaporates. Some trials of spin-coating were made but this method was discontinued because the size of the MAPMTs is not suitable for standard spin-coating machines. The dip-coating process consists of immersion of the substrate into the solution and pulling it out with a constant speed. Provided that the evaporation rate of the solvent is sufficiently high, a higher pulling velocity results in a larger film thickness [6]. This rather counterintuitive finding can be explained as follows. When pulling, the film is lifted with the substrate stretching the meniscus. The larger the pulling speed, the more material is lifted with the substrate and the longer the time for the solvent to evaporate and the thicker the solid film. The dependence of the film thickness on the pulling velocity is shown in Fig. 4.6.

The binder is needed for a sufficient resistivity of the solid film. The binder has to be transparent in the wavelength region of interest in order not to absorb photons. For the WLS films studied here, paraloid as binder and dichloromethane as solvent were used. In a dip-coating process, many parameters have to be optimised. Pullling speed, concentration of binder and active molecule need to be optimised but also ambient conditions like temperature, pressure, and humidity will affect the vapour pressure and therefore the result. Best results were obtained using a solution containing 15 g/l PT and 24 g/l paraloid in dichloromethane. The concentration of PT had to be close to saturation at room temperature in order to obtain the required layer thickness.

The setup at Hochschule Esslingen consists of a glass vessel and a stepper motor. Connected to the stepper motor is a specially developed metal cage for the MAPMT. In order to protect the MAPMT from the solution, it is impermeable. The solution gets in contact with the MAPMT only at the front window. The setup is shown on a photograph in Fig. 4.5. Pulling speed was between 10 cm/min and 40 cm/min [6].

All three application processes are schematically shown in Fig. 4.4.

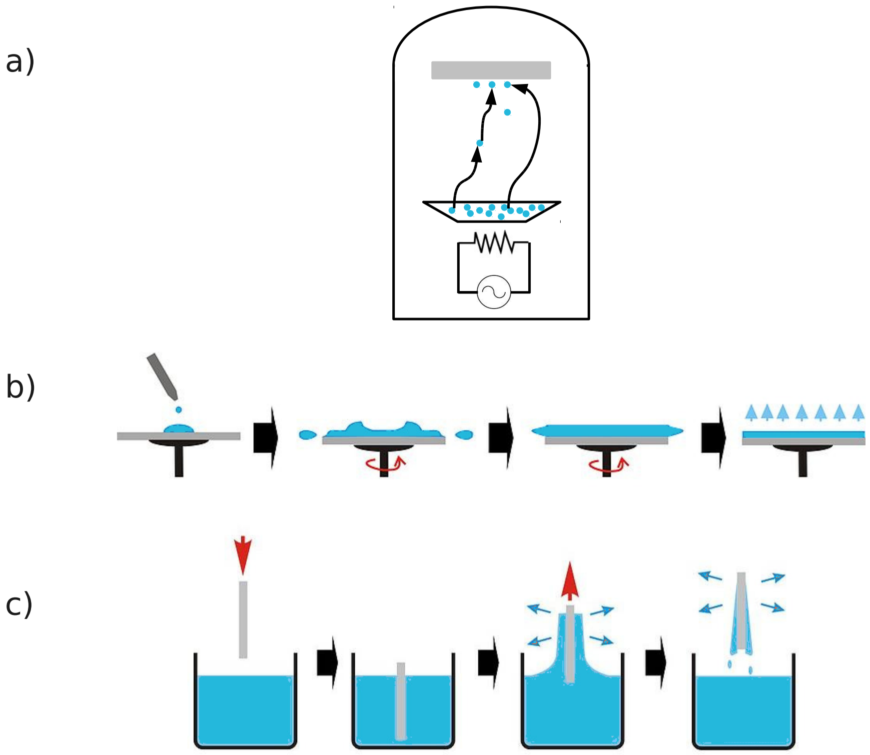

Figure 4.4 – Application methodes for WLS films. Evaporation from a resistively heated molybdenum boat in a vacuum chamber (a), spin-coating (b), and dip-coating (c). The wavelength shifting molecules in (a) and the solution in (b) and (c) are shown in turquoise. The substrate to be coated is shown in grey. Figures (b) and (c) taken from [123].

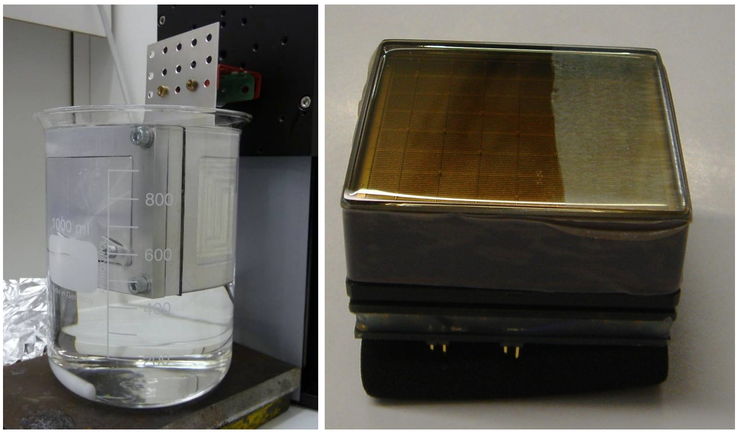

Figure 4.5 – Dip-coating setup (left) and dip-coated MAPMT of type H8500D-03 (right). The film was partially removed on the left side. Figures taken from [6].

Compared to evaporated WLS films, dip-coated films are easier to apply and mechanically more resistant [124]. In contrast to spin-coated layers, they are more homogeneous.

In consequence of the results presented below and considering the above-mentioned advantages, dip-coating is the preferred application method for WLS films on MAPMTs in the CBM-RICH detector.

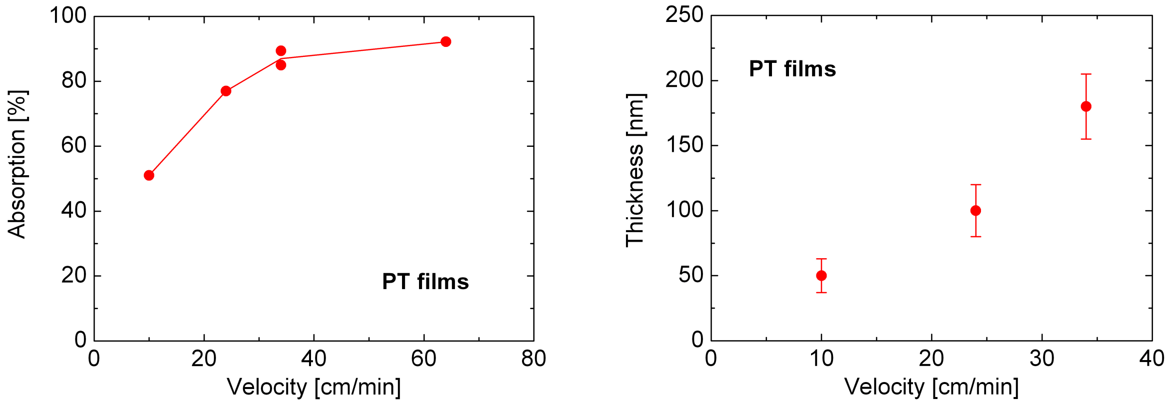

Figure 4.6 – Absorption at 220 nm (left) and thickness (right) of dip-coated WLS films on quartz substrates as function of pulling speed. The film thickness was measured by means of SEM. Figures taken from [6].

4.3 Quantum efficiency

4.3.1 Evaporated WLS films on PMTs with borosilicate window

As mentioned in section 4.1, a positive effect of a PT film on a PMT in terms of *QE* could be shown for PMTs with borosilicate windows. It was found that the gain due to the WLS film, given as the wavelength dependent *QE* convoluted with the Cherenkov spectrum, in the following called *QE gain*, does not depend on the film thickness above a certain lower limit. This limit is determined by the complete absorption of UV photons by the WLS film. Thicker films do not further increase but also do not decrease the *QE* gain. According to [120], no variation of *QE* gain is observed between $0.5\,\mu m$ and $1.8\,\mu m$ for a Photonis XP3102 PMT with with evaporated PT film compared to the bare borosilicate window.

4.3.2 Evaporated WLS film on MAPMT with UV-window

One H8500-03 MAPMT was coated at CERN by means of evaporation with a WLS film of PT. The film thickness was determined to be $\approx 1\,\mu m$. The MAPMT was covered on the left side during the evaporation process in order to be able to compare uncoated and coated parts of the same MAPMT without necessity of removing the film completely. A photograph of the front of this MAPMT is shown in Fig. 4.7.

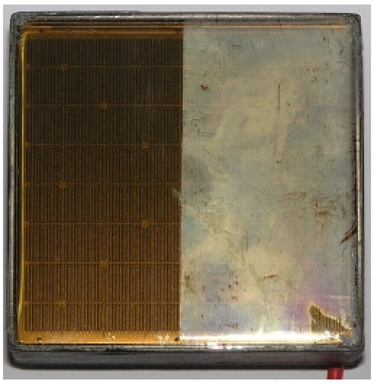

Figure 4.7 – Photograph of a H8500-03 MAPMT which was coated on the right half with a WLS film by means of evaporation. The films appears more opaque on the photograph than seen by eye.

Figure 4.8 shows the *QE* curves of the coated and uncoated side. Three regions can be identified. At wavelength below 270 nm the *QE* is higher with WLS film (a), between 270 nm and 340 nm it is lower (b),

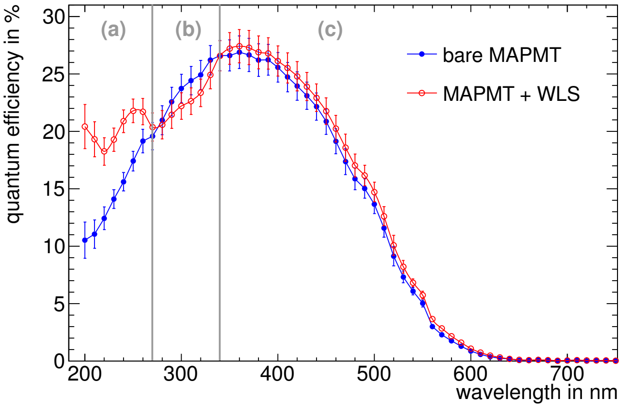

Figure 4.8 – *QE* curves of coated and uncoated side of a H8500-03 MAPMT with an evaporated WLS film on one side. The vertical lines separate three wavelength regions with an increased *QE* below 270 nm (a), lower *QE* between 270 nm and 340 nm (b), and increased *QE* above 340 nm (c) of the WLS coated MAPMT when compared to the uncoated one.

and above 340 nm it is higher again (c). The increase in region (a) is due to the shifting of UV photons to wavelengths where the *QE* of the photocathode is larger. In region (b) the decrease is caused by the overlap between the absorption range of PT with the wavelength range where the bare MAPMT is also sensitive. The overlap region exists only for PMTs with UV-window. For borosilicate windows, the *QE* is vanishing in the absorption range of PT resulting in a higher *QE* for coated borosilicate MAPMTs at all wavelengths. Since absorption of photons from the wavelength region (b) decreases the *QE* for PMTs with UV-window, an optimum range and upper limit for the film thickness should exist.

In order to better understand the diverse effects of WLS films on the *QE* in different wavelength regions (fluorescence in (a) and reduced transmission in (b)), a simulation of *QE* of a coated MAPMT based on the measured *QE* curve of an uncoated MAPMT and the measured absorption of PT films of different thicknesses has been performed [125]. The product of fluorescence efficiency and total collection efficiency[1] of the film entered as free parameter. It was shown that the reduced *QE* in the wavelength region (b) can indeed be understood from the bare PMT sensitivity and the absorption characteristics of the WLS film.

In summary, in contrast to PMTs with standard glass windows [120], an optimum layer thickness exists for MAPMTs with UV-extended window. A trade-off has to be made between absorption of UV photons which contribute to an increase of integral sensitivity when shifted and absorption of photons at wavelengths where also the bare PMT is sensitive. Because of the reasons mentioned in section 4.2, the optimisation of the layer thickness was pursued with dip-coated WLS films. In the following section, the corresponding *QE* measurements will be discussed.

4.3.3 Dip-coated WLS films on MAPMTs with UV-window and BA photocathode

Dip-coated WLS films on MAPMTs were produced at Hochschule Esslingen. The solid films are discernible due to their frosted surface which is more or less visible depending on the viewing angle. Figure 4.9 shows photographs of one MAPMT with WLS film and one without taken from different viewing angles. While the film is clearly visible from ≈ 90° viewing angle, it is almost invisible from ≈ 45°.

---

[1] Fluorescence efficiency is the probability that an absorbed UV photon causes the re-emission of a photon with longer wavelength. The term total collection efficiency in the context of WLS films denotes the probability that a UV photon is absorbed by the WLS film. It is affected by scattering in the film, reflection at the interface between film and PMT window, and other variables [6].

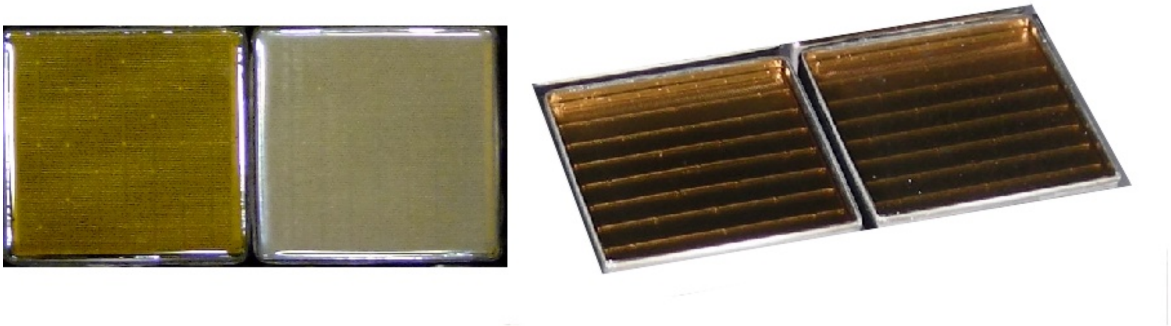

Figure 4.9 – Photographs of H8500D-03 MAPMTs with and without dip-coated WLS film from two different viewing angles. On both photographs, the left MAPMT is uncoated, the right one coated. From a viewing angle of $\approx 90°$ the WLS film is clearly visible (left) whereas from $\approx 45°$ it is almost invisible (right).

Three H8500D-03 with UV-window and bialkali photocathode were coated with a PT film. By choosing different pulling speeds, namely 10 cm/min, 24 cm/min, and 34 cm/min, film thicknesses of 50 nm, 100 nm, and 180 nm, respectively, were obtained.

The wavelength dependent *QE* was measured with a light spot of $\approx$ 1 cm on the MAPMT centre (see section 3.3.1).

QE curves of the three MAPMTs with and without coating are shown in Fig. 4.10 (left). A direct comparison of the *QE* gain due to WLS films in dependence of the film thickness is difficult because of the tube-to-tube variation of *QE* among different MAPMTs of the same type (cf. section 3.4.1). Therefore, the difference between *QE* with and without WLS film is normalised to the maximum *QE* of the bare MAPMT according to $(QE_{\text{WLS}} - QE_{\text{bare}})/QE_{\text{bare,max}}$. The normalised difference will be called *relative QE gain*. A positive relative *QE* gain indicates a higher *QE* with WLS film compared to the bare MAPMT, a negative value means a loss. The corresponding curves are shown in Fig. 4.10 (right) for the PMTs with the three dip-coated films as well as for the MAPMT which was coated with PT by means of evaporation. For wavelengths below 270 nm, the increase caused by the dip-coated films is higher than for the evaporated film. Within the series of dip-coated films, the increase in *QE* rises with increasing films thickness. However, from the absorption and fluorescence measurements, no further increase towards thicker films is expected (cf. saturation of absorption for pulling speeds $>$ 34 cm/min (thickness $>$ 200 nm) shown in Fig. 4.6). Whereas the evaporated film shows a decrease in *QE* between 270 nm and 340 nm, no such decrease is observed for the much thinner dip-coated films. For wavelengths between 400 nm and 600 nm, the evaporated films show a slight increase in *QE*, in contrast to the dip-coated films, which can be attributed to an increased efficiency due to light scattering in the evaporated WLS film as will be discussed in section 4.3.5.

For the beam tests at the CERN PS in autumn 2011 and 2012 (cf. section 5.2.2), MAPMTs were dip-coated with PT films in order to investigate the influence of WLS coated MAPMTs on the detection of Cherenkov photons under real conditions. In 2011, before the thickness dependence was studied, four H8500D-03 were coated using a pulling speed of $\approx$ 15 cm/min resulting in a film thickness between 50 nm and 100 nm. The *QE* curves are shown in Fig. 4.11 together with the relative *QE* gain. The latter varies for the four films between (36 ± 9) % and (47 ± 9) % at 200 nm. The error on the relative *QE* gain is obtained by propagating the error of the absolute *QE* values with and without WLS film which varies from 1.5 % to 2.5 % absolutely (see appendix A.3). A slight decrease of *QE* between 300 nm and 600 nm is observed.

For the 2012 beam test, after the study of thickness dependence, four H8500D-03 were coated with films of $\approx$ 200 nm thickness. The *QE* curves and the relative *QE* gain are depicted in Fig. 4.12. The improved film thickness results in a relative *QE* gain between (50 ± 9) % and (64 ± 10) % at 200 nm which is significantly

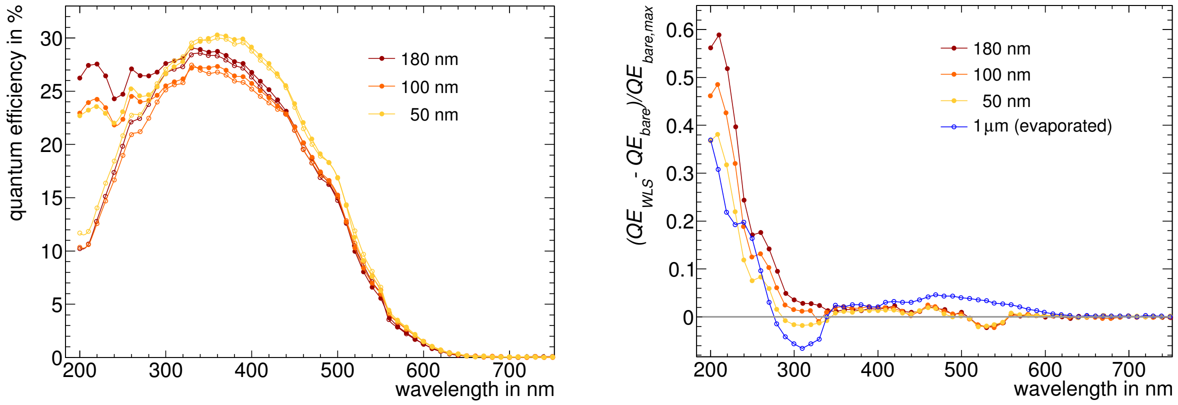

Figure 4.10 – Left: *QE* curves of MAPMTs with dip-coated WLS films of 50 nm, 100 nm, and 180 nm thickness (full symbols) and reference measurements without films (open symbols). Right: Difference between WLS coated and uncoated MAPMT normalised to the maximum *QE* of the uncoated MAPMT. The normalisation allows for a better comparison of the films since different MAPMTs have a different *QE*. An increase of relative *QE* gain with increasing film thickness can be observed. For comparison, the curve from the evaporated WLS film is also plotted. The reduced *QE* between 270 nm and 340 nm with evaporated WLS film translates into negative values. Error bars are omitted in both plots for better visibility.

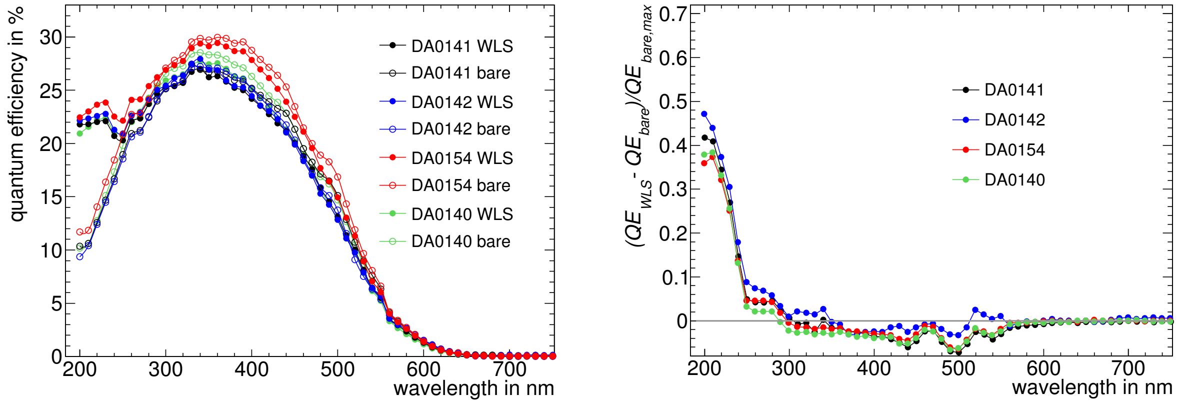

Figure 4.11 – Left: *QE* curves of H8500D-03 MAPMTs with dip-coated WLS films for the CERN beam test 2011. The film thickness is between 50 nm and 100 nm. Right: Difference between WLS coated and uncoated MAPMT normalised to the maximum *QE* of the uncoated MAPMT. The increase of *QE* at small wavelengths is smaller than that for the WLS films in Fig. 4.10. At wavelengths between 300 nm and 600 nm, a slight decrease in *QE* is observed due to absorption of the WLS films. Error bars are omitted for better visibility.

larger than for the 2011 films. Again, the relative *QE* gain is very similar for the four films.

The four films on the MAPMTs with serial numbers DA0141, DA0142, DA0147, and DA0154 in Fig. 4.12 reveal a surprisingly high QE in the wavelength range where UV photons are shifted to larger wavelengths. Around 220 nm, the *QE* reaches values comparable to the peak *QE* of the MAPMTs. Since the WLS films emit fluorescence photons isotropically, in principle a larger *QE* than the peak *QE* is not possible. Even achieving the value of peak *QE* is only possible in the case of 100 % collection efficiency and fluorescence efficiency of the film. The curves for these three films might be explained by the trapping of fluorescence photons in the WLS film due to total reflection at the WLS - air interface [126], i.e. photons which are emitted from the wavelength shifting molecules into directions pointing away from the photocathode might be reflected and have a second chance to strike the photocathode.

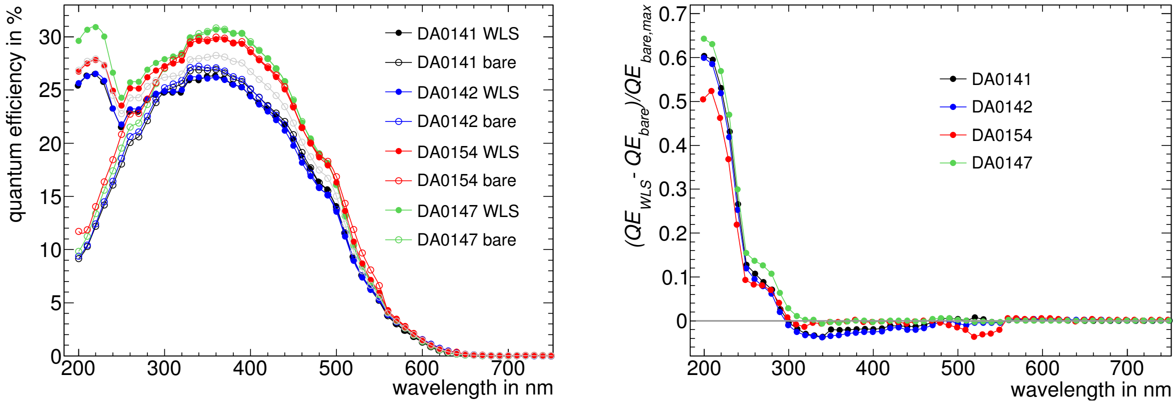

Figure 4.12 – Left: *QE* curves of H8500D-03 MAPMTs with dip-coated WLS films for the CERN beam test 2012. The film thickness is ≈ 200 nm. Right: Difference between WLS coated and uncoated MAPMT normalised to the maximum *QE* of the uncoated MAPMT. The relative *QE* gain at small wavelengths is larger than for the 2011 films in Fig. 4.11 due to the optimised film thickness. Error bars are omitted for better visibility.

4.3.4 Dip-coated WLS films on MAPMTs with UV-window and SBA photocathode

MAPMTs with UV-window and super bialkali photocathode were dip-coated with PT films at Hochschule Esslingen for the use in the 2012 beam test. Two types of MAPMTs were used, one 2" H10966A-103 and four 1" R11265-103-M16 (cf. Tab. 3.1). Pulling speed and resulting film thickness of ≈ 200 nm were the same as for the H8500D-03 used in the 2012 beam test. Figure 4.13 displays the results of the *QE* measurements. The relative *QE* gain is between (51 ± 7) % and (54 ± 7) % at 200 nm for the R11265-103-M16 and (68 ± 7) % for the H10966A-103.

The high relative *QE* gain of the H10966A-103 (SBA photocathode, 2") in comparison to the H8500D-03 MAPMTs (BA photocathode, 2") can be explained by the higher peak *QE* of the SBA compared to the BA photocathode. UV photons are shifted to wavelengths where the detection probability is larger in case of SBA while in the UV range it is comparable for both photocathode materials (cf. section 3.4.1).

For the R11265-103-M16 (SBA photocathode, 1"), two opposed effects have to be taken into account. The higher *QE* of the SBA compared to the BA photocathodes is favourable for a larger relative *QE* gain. The thinner front window of the 1" R11265-103-M16 in comparison to the 2" H8500D-03 and H10966A-103 MAPMTs, however, disfavours a high relative *QE* gain in the UV region because the better UV transmittance already allows a higher QE of the bare MAPMTs in this wavelength region.

In contrast to the previously discussed films on different MAPMT types, a diverse behaviour is visible for R11265-103-M16 MAPMTs between 300 nm and 600 nm. The relative *QE* gain of the MAPMT with serial number ZN0593, for instance, is positive whereas it is negative for ZN0731. Since the relative *QE* gain in this wavelength region is believed to be determined by light scattering in the WLS film (cf. section 4.3.5), this indicates that film-to-film variations in terms of roughness occur on the small 1" MAPMTs.

4.3.5 Improvement of quantum efficiency due to light scattering on the WLS film surface

An increase in *QE* above wavelengths of 340 nm is observed in Fig. 4.8 for the evaporated WLS film on a H8500D-03 and in Fig. 4.13 for a dip-coated WLS film on a R11265-103-M16. According to the absorption and fluorescence spectra of PT shown in Fig. 4.2, no wavelength shifting is expected at these wavelengths. A decrease of *QE* in the visible wavelength region can easily be attributed to a loss of transmittance of the WLS film. Possible reasons for an increase of *QE* are discussed e.g. in [127, 128]. The authors report on

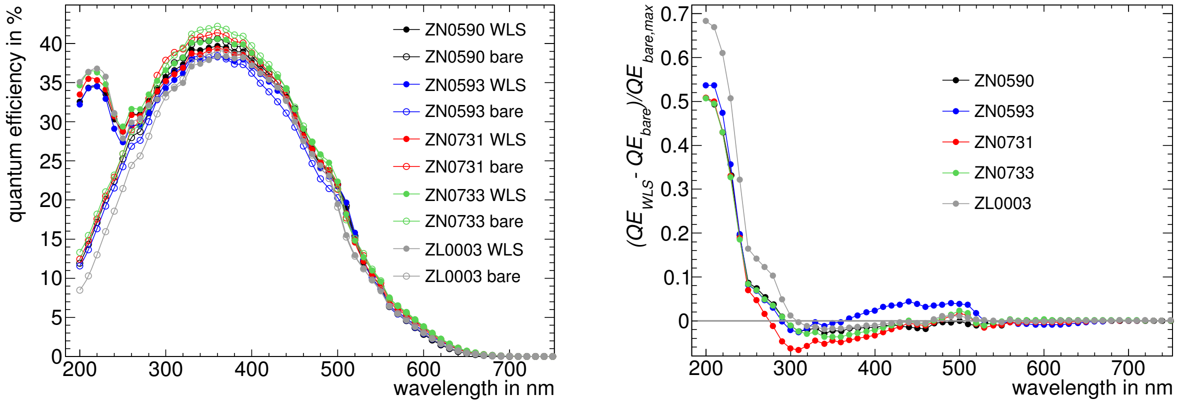

Figure 4.13 – Left: *QE* curves of R11265-103-M16 and H10966A-103 MAPMTs with dip-coated WLS films for the CERN beam test 2012. Right: Difference between WLS coated and uncoated MAPMT normalised to the maximum *QE* of the uncoated MAPMT. The relative *QE* gain of the H10966A-103 in the UV range is larger than that of the R11265-103-M16. Error bars are omitted for better visibility.

increased *QE* due to light scattering on WLS films with a rough surface which has two effects.

1. Photons impinging orthogonally on the PMT are either refracted into the WLS film and the PMT or they are reflected by the front window or the photocathode. On a flat surface, reflected photons move away from the PMT and will be lost without being converted into a photoelectron. If, on the other hand, the surface is rough, a large fraction of the reflected photons will have a possibility to strike the surface a second time with a larger angle thus with a higher probability of being absorbed (cf. Fig. 4.14). In short, the overall reflectance is reduced.

2. Photons which are refracted by the inclined surface will enter the photocathode under a larger angle than in the case of no refraction. In consequence, their way through the photocathode is larger and the probability of being converted into a photoelectron increases. The emission of the generated photoelectron from the photocathode, in contrast, is not affected since it is determined only by the electric field vector and the mean depth of the origin of generation [129]. The direction of the photons at the interface between WLS film and PMT window will not change as much as in the case of an air - window interface because the refractive indices of WLS film and glass are more similar than those of air and glass. The same holds for CO_2 instead of air ($n_{\text{p-Terphenyl}} \approx 1.5$ [130], $n_{\text{UV-glass}} = 1.476$ [131] [2], $n_{\text{air}} = 1.00028$ [132], $n_{CO_2} = 1.00045$ [68] at 600 nm).

The concept of increasing the *QE* by using rough surfaces is independent of the process of wavelength shifting. It is well known in wafer processing for the production of solar cells. The formation of regular microscopic pyramids on the wafer surface, known as *texturization*, reduces the reflectance and increases the absorption probability due to light trapping of the totally reflected light inside the wafer [133]. In the case of WLS films, the surface is more irregular though and resembles more a lambertian than a textured surface.

The accuracy of the *QE* measurements of MAPMTs with WLS films presented above is high enough to detect the improvement of quantum efficiency due to light scattering. It is most strongly pronounced for the evaporated WLS film and observed also for one dip-coated film. By dipping the PMT several times and by finding an adequate concentration of PT in the solution, one can obtain optimally frosted films in order to maximise the increase in *QE* in the visible wavelength region due to scattering. Details in particular

---

[2] at 587.6 nm, Schott 8337B (borosilicate glass for sealing to Kovar metal and tungsten, UV-transmitting).

with regard to the MAGIC telescope can be found in [130]. The enhancement of the *QE* in the visible wavelength region is effective in Cherenkov detectors with radiators non-transparent for UV photons, e.g. Imaging Atmospheric Cherenkov Telescopes (IACTs). For the CBM-RICH detector with its UV-transparent CO_2 radiator, however, the overall *QE* gain is more determined by the WLS effect in the UV range. That is why the effort of the R&D program aimed at a high *QE* at short wavelengths.

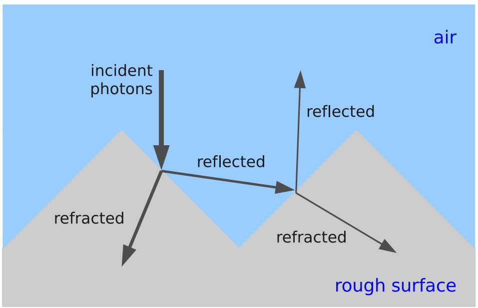

Figure 4.14 – Reflection and refraction on a rough surface. Incident photons reflected on the surface have a possibility to strike the surface a second time with a larger angle and with a higher probability of being absorbed.

4.4 Homogeneity

Figure 4.15 shows *QE* scans for the H8500-03 MAPMT which was evaporated with a PT film on the right side. Scans at 230 nm, 245 nm, and 470 nm reveal an increased *QE* on the coated side in agreement with the *QE* curve in Fig. 4.8 at all three wavelengths. *QE* scans at 240 nm and 470 nm of one H8500D-03 MAPMT (DA0141) with thickness optimised dip-coated WLS film on the whole front window are displayed in Fig. 4.16. In addition, the *QE* scans of the bare MAPMT are shown. Both the evaporated and the dip-coated WLS films do not show any particularities like structures or regions with low *QE*. Also here, the strongly enhanced *QE* in the UV and the unchanged *QE* in the visible wavelength region can be observed (cf. *QE* curve in Fig. 4.12 for DA0141, measured in the MAPMT centre).

An example where the application of a WLS film leads to an inhomogeneous distribution of *QE* over the PMT surface is shown in Fig. 4.17. The *QE* scan of a round singleanode PMT with a diameter of 1" (Hamamatsu XP3102) at 245 nm clearly drops towards the PMT edges which can be explained by the isotropic fluorescence and/or a variable film thickness. At 470 nm, where the WLS film is transparent, the *QE* is homogeneous over the whole PMT surface.

In order to quantify the WLS film homogeneity, the difference between maximum and minimum *QE* on the

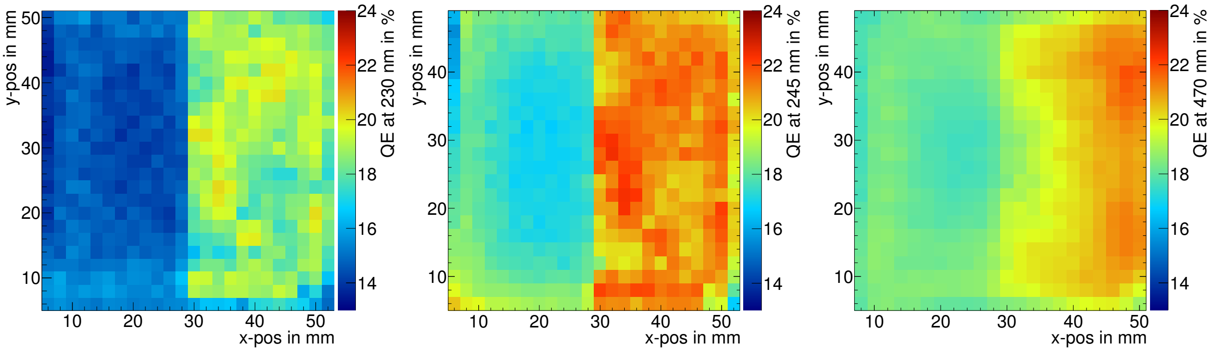

Figure 4.15 – *QE* scans of a H8500-03 MAPMT with evaporated WLS coating one the right side at 230 nm (left), 245 nm (centre), and 470 nm (rigth). For all wavelengths an increase in *QE* is observed which is quantitatively in agreement with the *QE* curve in Fig. 4.8.

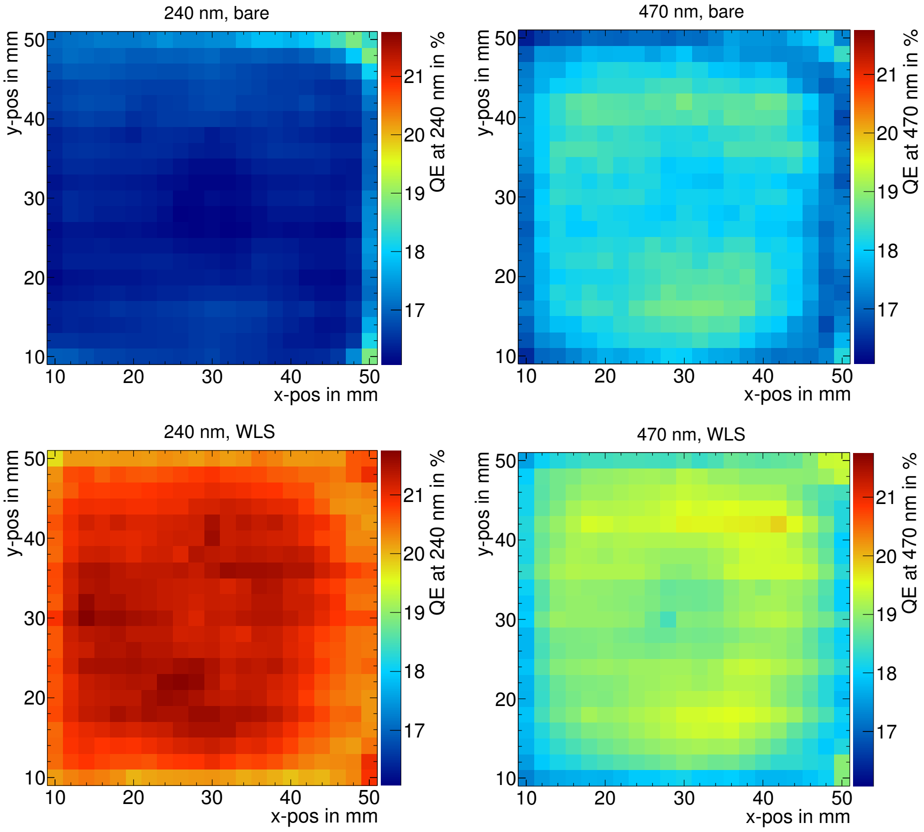

Figure 4.16 – *QE* scans of a H8500D-03 (DA0141) without (top line) and with (bottom line) thickness optimised dip-coated WLS film at 240 nm (left) and 470 nm (right). The homogeneity of the films is quantified by the parameter h (see text).

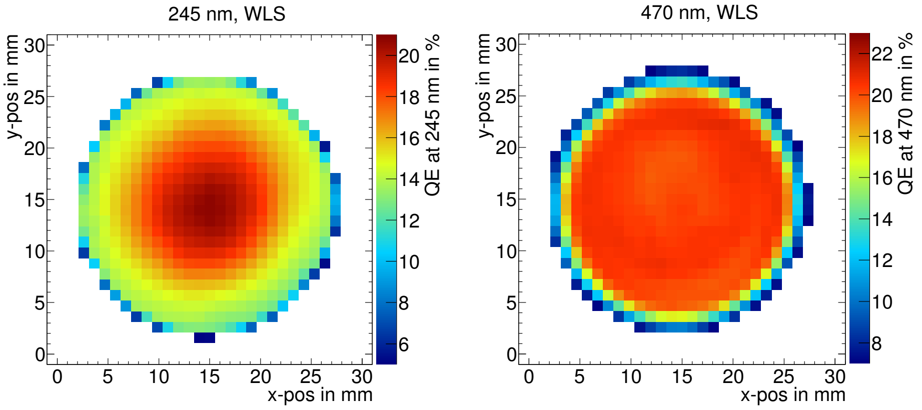

Figure 4.17 – *QE* scans of a 1" XP3102 singleanode PMT with evaporated WLS film. The *QE* decreases towards the edges at 245 nm (left) whereas it is relatively homogeneously distributed at 470 nm (right).

PMT surface at a given wavelength normalised to the maximum value is calculated for the different films:

$$h = \frac{QE_{\text{max}} - QE_{\text{min}}}{QE_{\text{max}}}. \tag{4.1}$$

With this definition, h is a measure for the variation of *QE* over the PMT surface. Since also the *QE* of the bare PMTs varies over the surface (see Fig. 3.13), h_{WLS} of the coated PMTs is compared to h_{bare} of the

PMT type	application technique	h_{WLS}	h_{bare}	Δh_{norm}
H8500-03 (ZF0004)	evaporation	0.111	0.119	$-7\,\%$
XP3102 (PM2)	evaporation	0.251	0.156	$61\,\%$
XP3102 (PM4)	evaporation	0.279	0.154	$81\,\%$
H8500D-03 (DA0141)	dip-coating (optimised)	0.143	0.105	$36\,\%$
H8500D-03 (DA0154)	dip-coating (optimised)	0.123	0.096	$28\,\%$

Table 4.1 – Homogeneity of different WLS films at $240\,\mathrm{nm}$ to $245\,\mathrm{nm}$. One MAPMT evaporated on one side, two evaporated singleanode PMTs, and two dip-coated MAPMTs are listed.

respective bare PMT. The normalised difference Δh_{norm} between h_{WLS} and h_{bare},

$$\Delta h_{\mathrm{norm}} = \frac{h_{\mathrm{WLS}} - h_{\mathrm{bare}}}{h_{\mathrm{bare}}}, \tag{4.2}$$

gives then an estimate of the homogeneity of different WLS films (see Table 4.1).

It can be seen that the evaporated films on the round 1" PMTs (XP3102) show a decrease of *QE* homogeneity by $61\,\%$ to $81\,\%$ when measured in terms of Δh_{norm}, i.e. in comparison to the bare PMTs. The optimised dip-coated films on the 2" MAPMTs (H8500D-03) exhibit a decrease of homogeneity in terms of Δh_{norm} of $28\,\%$ to $36\,\%$. The most homogeneous layer is the evaporated one on the 2" MAPMT (H8500-03) with an increase of homogeneity of $7\,\%$. A slight increase could be explained by the isotropic fluorescence of the WLS film, thus smoothing the inhomogeneities of the photocathode.

4.5 Crosstalk

The usage of WLS films is expected to reduce the spatial resolution of a MAPMT because of the isotropic emission of fluorescence photons. According to the definition of crosstalk in section 3.9 and the two discussed sources of crosstalk, WLS films contribute to the optical crosstalk by emitting photons under inclined angles through the MAPMT front window. In this thesis, the term *charge sharing* will be used for the ratio between charge collected at the anode pad of an illuminated pixel of a MAPMT and the charge collected in the eight next neighbouring pixels (four direct neighbours and four diagonal neighbours). This section will give a comparison of the charge sharing on the uncoated and coated side of the H8500-03 MAPMT with evaporated WLS film on its UV-window.

The MAPMT has been scanned with high resolution using the setup described in section 3.3.3 with a spot size of $1\,\mathrm{mm}$ and a step size of $0.35\,\mathrm{mm}$. In contrast to the *QE* measurements, the amplified signal from the dynode system was measured.

Qualitative view on crosstalk
Figure 4.18 shows the charge collected at the anode normalised to the maximum measured in scans along the x and y-axes at $245\,\mathrm{nm}$. The plots superimpose the signals from all eight pixels in a row or column as function of illuminated position.

Scan (a) was done such that it covers four pixels without and four pixels with WLS film. Apart from the larger signals of the coated pixels, it can be seen that the signal from one pixel extends significantly into the neighbouring pixels.

Scans (b) and (c) cover eight uncoated and eight coated pixels, respectively. It can be observed that in the case of WLS coating the edges are less steep and the extension of the signals into the neighbouring pixels is more pronounced. Both observations indicate the presence of more crosstalk with WLS films than without.

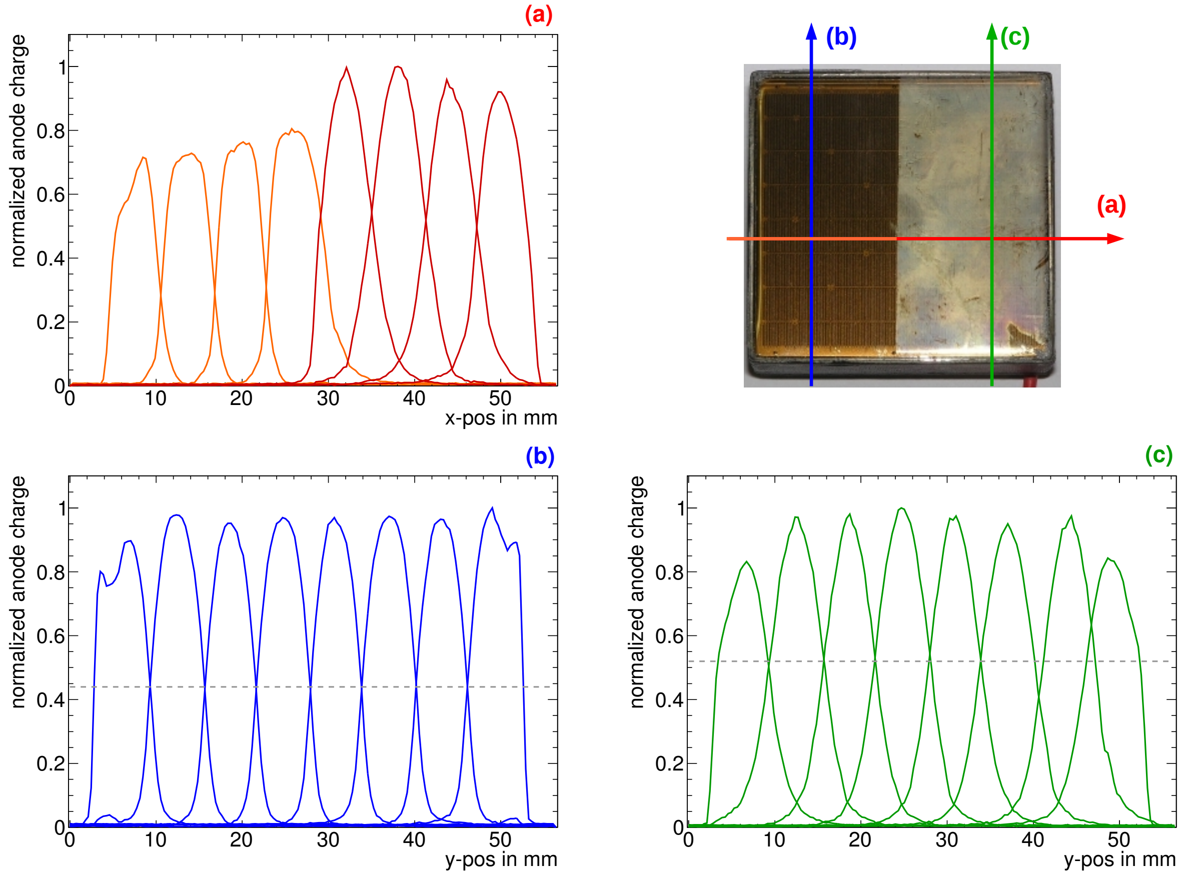

Figure 4.18 – Superposition of normalised ande charge from channels along three axes through the coated and uncoated pixels of a H8500-03 MAPMT at 245 nm. The right half of the MAPMT is coated by means of evaporation with a WLS film of about 1 µm thickness. Scan (a) shows larger signals of coated compared to uncoated pixels. Signals from one pixel significantly extent into neighbouring pixels. The comparison between (b) and (c) reveals that crosstalk is more pronounced with than without WLS film which manifests in the less steep edges of pixels with WLS film and a consequently larger overlap between signals from different pixels. This finding is visualised by the different position of the dashed lines which approximately connect the crossing points of signals from neighbouring pixels.

Quantification of crosstalk

In Figure 4.19, the normalised charge is shown as a function of x and y-position. Each bin of the left histogram is filled with the charge collected in the MAPMT channel with maximum signal when the light spot is at the corresponding bin coordinates. The right histogram is filled with the sum of charge collected in all MAPMT channels. The reason for the pixel structure in the left plot is the distribution of charge to several pixels when the light source points between the pixels.

Figure 4.20 (left) shows a detail of the left plot with nine pixels. For the quantification of crosstalk, the charge at the anodes of all nine channels is measured when the innermost part of the central pixel is illuminated by the light spot (Fig. 4.20 right). In the following, the illumination of the innermost $3{\times}3$ mm^2 will be used as basis for the specification of the crosstalk value. The square in the central pixel indicates the

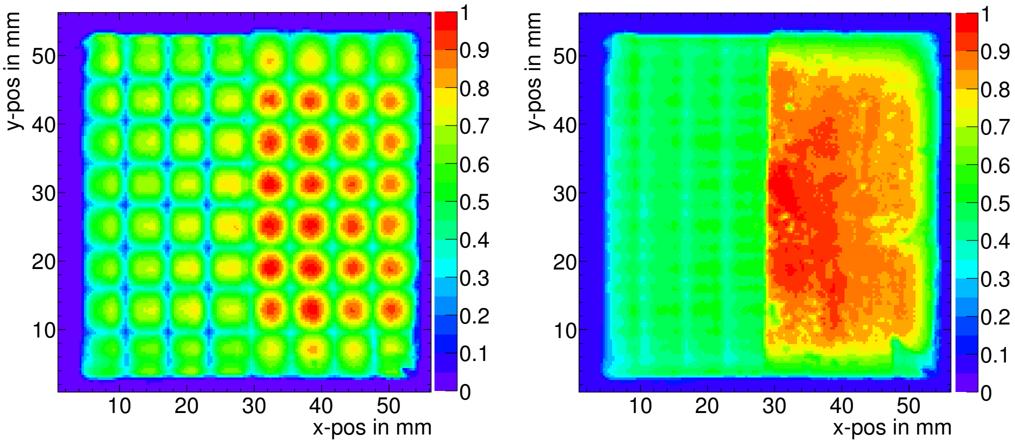

Figure 4.19 – Normalised anode charge distribution at 275 nm measured on a H8500-03 MAPMT. The right half of the MAPMT is coated by means of evaporation with a WLS film of about 1 µm thickness. Left: histogram filled with charge collected in the MAPMT channel with maximum signal. Right: histogram filled with charge collected in all MAPMT channels.

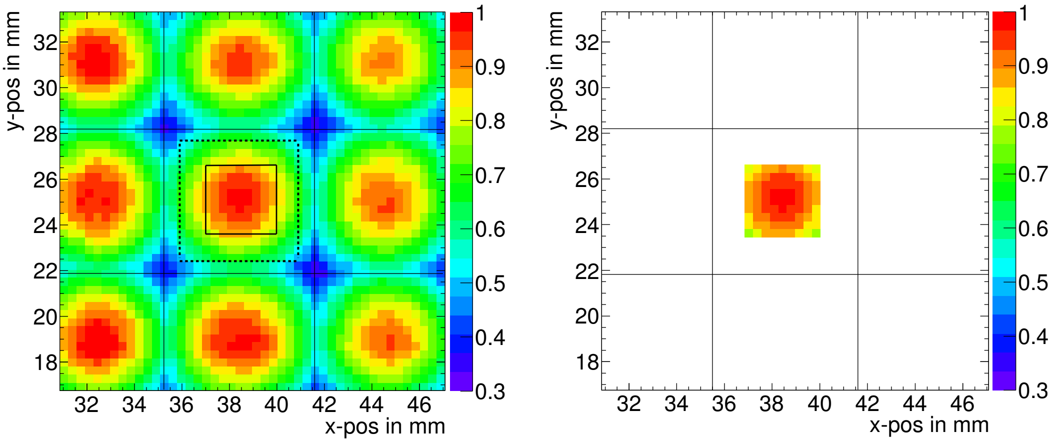

Figure 4.20 – Left: Detail of the left plot of Fig. 4.19. The square indicates the most central 3×3 mm^2 of one pixel, the dashed square the innermost 5×5 mm^2. Right: Same plot showing only the innermost 3×3 mm^2 of one pixel illuminated. The crosstalk into the neighbouring pixels is determined when this area is illuminated.

innermost 3×3 mm^2. The dashed square indicates the innermost 5×5 mm^2. The size of the entire pixel is 6.125×6.125 mm^2.

Tables 4.2 and 4.3 show the crosstalk for a coated and an uncoated pixel at 275 nm and 470 nm, respectively. The crosstalk without coating (left tables) is independent from the wavelength. It adds up to 11.6 % at 275 nm and 11.0 % at 470 nm. These values are in agreement with similar measurements of uncoated MAPMTs done by using a pinhole mask, illuminating the centre of one pixel, and measuring the anode output charge in the neighbouring channels. For a single photon illumination at 350 nm and a pinhole mask of 3×3 mm^2, [108] reports a value of 7.7 %. For a comparison with the value measured by Hamamatsu with a pinhole mask and using a tungsten lamp (DC light) with blue filter, an illumination of the innermost 5×5 mm^2 has to be considered since also Hamamatsu uses an illuminated area of 5×5 mm^2. An advantage of the measurement presented above is that only one measurement has to be performed and the illuminated area can be chosen in the analysis. For 5×5 mm^2, the charge in the neighbouring channels adds up to 33.4 % which is consistent with the value of 34.6 % reported by Hamamtsu [134]. Taking into account that, due to the light spread, the absolute value depends strongly on the distance between optical fibre and MAPMT, the measurements presented here match very well the results from literature. Even though the absolute value of crosstalk depends on the specific experimental setup, the good agreement with literature for comparable measurement conditions shows that the method is well suited for a comparison of charge sharing with and without WLS film.

The results presented in the following are determined from an illuminated area of 3×3 mm^2. The crosstalk with WLS coating at 275 nm is 62 % which corresponds to an increase by a factor of 5 in comparison to the uncoated part of the MAPMT. The reason for the higher crosstalk with WLS coating is the isotropic fluorescence of the WLS film. At 470 nm the crosstalk with WLS coating is 23.8 %. Even though the WLS film is not active at this wavelength, there is an increase in crosstalk by a factor of 2 due to light scattering at the milky surface of the film.

It is important to mention that the measurement was done with light pulses of a magnitude around 100 photons. The determined crosstalk represents the charge sharing between neighbouring pixels. There is no threshold applied on the signal amplitude. In contrast to these measurement with multi photon pulses, when determining single photon crosstalk, part of the charge in the neighbouring pixels will be below threshold. As a result, the values stated above are larger than the single photon crosstalk. It will be shown in section 5.6.3 that the use of WLS films does not significantly decrease the sharpness of Cherenkov rings.

0.3	2.6	0.3
1.7	100	2.8
0.5	2.9	0.5

3.4	12.7	2.8
13.0	100	11.7
3.1	12.5	2.8

Table 4.2 – Crosstalk of the uncoated pixel P35 (left) and the coated pixel P38 (right) of a H8500-03 MAPMT in percent at 275 nm.

0.2	2.4	0.3
1.7	100	2.4
0.5	2.6	0.9

1.2	5.0	1.0
4.6	100	4.7
1.2	4.9	1.2

Table 4.3 – Crosstalk of the uncoated pixel P35 (left) and the coated pixel P38 (right) H8500-03 MAPMT in percent at 470 nm.

4.6 Summary

In previous studies, it had been shown that p-Terphenyl is a well suited molecule for the use as wavelength shifter deposited on the front window of PMTs because of its absorption spectrum and its fluorescence spectrum that matches the quantum efficiency curves of bialkali and super bialkali photocathodes. WLS films from p-Terphenyl have been applied on MAPMTs by means of evaporation or physical vapour deposition techniques. The studies show that dip-coating is the favoured method because of technological reasons (fast process in comparison to evaporation, size of MAPMTs not suitable for standard spin-coating machines) and superior performance (mechanically more resistant films in comparison to evaporation, more homogeneous films in comparison to spin-coating).

QE curves show that in contrast to PMTs with borosilicate window, an optimum film thickness exists for the application of WLS films on PMTs with UV-window. Due to the overlap of the absorption spectrum of p-Terphenyl with the wavelength region where uncoated PMTs with UV-window are sensitive, a reduction of *QE* is observed in the case of too thick WLS films. Based on systematic studies, an optimised dip-coating process has been developed at Hochschule Esslingen resulting in homogeneous WLS films of $\approx$ 200 nm thickness.

When applying these WLS films on different types of MAPMTs, a hierarchy of *QE* gain of the coated with respect to the uncoated MAPMT at a wavelength of 200 nm can be seen. The *QE* gain depends on the photocathode material and the thickness of the front window. It is larger for SBA than for BA photocathodes because UV photons are shifted to a wavelength region of higher *QE* whereas the *QE* of bare MAPMTs is comparable for SBA and BA at small wavelengths. The *QE* gain of MAPMTs with a surface area of 1"× 1" is smaller than that of 2"× 2" MAPMTs because the relatively thin front glass of the small MAPMTs allows for a higher *QE* at small wavelengths without WLS films. The relative increase of *QE* is as follows:

1. $+ (68 \pm 7)$ % at 200 nm for one tested H10966A-103 (2"× 2" SBA photocathode, UV-window),
2. $+ (50 \pm 9)$ % to (64 ± 10) % at 200 nm for a set of four H8500D-03 (2"× 2" BA photocathode, UV-window),
3. $+ (51 \pm 7)$ % to (54 ± 7) % at 200 nm for a set of four R11265-103-M16 (1"× 1" SBA photocathode, UV-window).

The increase of detected Cherenkov photons due to WLS films will be discussed in section 5.5.6 and 5.6.2 along with results from in-beam tests.

The homogeneity of WLS films is quantified as relative difference between maximum and minimum *QE* on the coated MAPMT surface normalised to the relative difference of the bare MAPMT. The evaporated WLS film on a H8500-03 MAPMT is the most homogeneous one, followed by the optimised dip-coated films on H8500D-03. Evaporated films on round 1" PMTs show a strong decrease of *QE* towards the edges.

Crosstalk in terms of charge sharing was studied on the basis of a high resolution scan of the H8500-03 MAPMT with evaporated p-Terphenyl film on one side. The charge collected in the pixels adjacent to the illuminated pixel for the uncoated side is very well in agreement with the values reported in literature. For the side with WLS film, it is enhanced by a factor of 5 at 275 nm. This value, however, was obtained without application of a threshold in amplitude. For the detection of single photons for instance, a threshold can easily be applied for the suppression of crosstalk.

When detecting Cherenkov rings, the higher *QE* due to WLS films on the MAPMT windows translates into a larger number of detected photoelectrons per ring. The *QE* curves for the various MAPMT types and WLS films presented here are used as input for Monte Carlo simulations of the number of detected photoelectrons per Cherenkov ring in section 6.2.5.

In summary, the increased *QE* due to WLS films and the good control of the application procedure regarding reproducibility and homogeneity make the usage of WLS films beneficial for the CBM-RICH photon detector. Tests of the radiation hardness of WLS films are needed for the final decision. In any case, due to the good removability with isopropyl alcohol, the usage of WLS films is not a big risk.

Chapter 5

RICH prototype beam tests

Several prototypes were constructed during the CBM-RICH research and development phase [6]. The most recent prototype, which has been built in order to test the full system and the interplay of all components, is described in this chapter as well as results from two beam test campaigns in autumn 2011 and 2012. Its excellent performance can be seen as proof of principle for the proposed RICH layout. The components and the setup of the RICH prototype (in the following simply called *prototype*) are described in section 5.1 with a focus on the camera system in section 5.2. A description of the experimental setup at CERN is presented in section 5.3. The main part of this chapter is dedicated to the beam test data analysis (section 5.4) and the results, which, given the different measurements in 2011 and 2012, are discussed separately in section 5.5 and 5.6.

5.1 The RICH prototype setup

To verify the concept of the CBM-RICH detector a real-size prototype was constructed. It is real-size in the most important dimension, i.e. the radiator length which largely defines the number of generated Cherenkov photons. The three main components of the prototype are a gaseous CO_2 radiator volume, high reflectivity UV mirror tiles and a photon camera composed of MAPMTs. Radiator, mirror tiles, and the MAPMTs are those foreseen for the final CBM-RICH detector. Dealing with real-size modules allowed first studies of system integration issues. The intention to build this prototype detector was driven by the following considerations:

1. Verification of the concept of the CBM-RICH detector,
2. Testing the ring finding and fitting algorithms,
3. Validation of the CBM-RICH simulations with the CbmRoot framework through comparison with real test data,
4. Fixing tolerances for mirror misalignment and gas impurities,
5. Getting experience in building and running the RICH detector, including gas-system, mirror alignment, data readout, and ring reconstruction.

The prototype was tested at the PS/T9 beam line at CERN in autumn 2011 and autumn 2012 with different camera layouts.

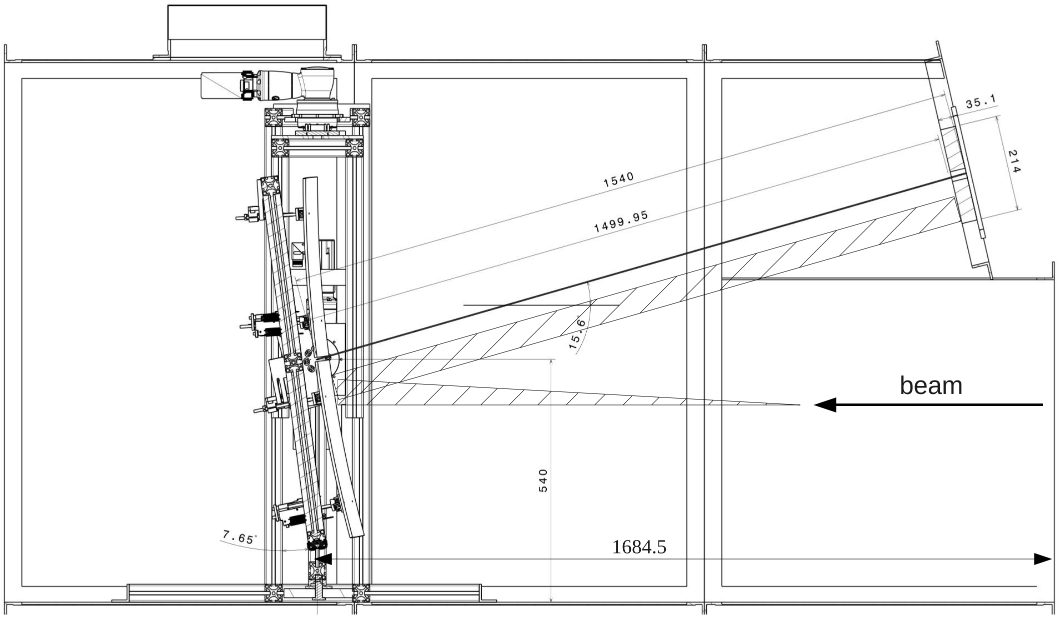

Figure 5.1 – Technical drawing of the CBM-RICH prototype box with mirrors on a rotatable frame. The camera is mounted on the upper right side. The hatched area visualises the Cherenkov cone and its reflection onto the camera. The gas-system (not shown here) is assembled in a separate rack.

Geometry

Figure 5.1 shows a technical drawing of the detector box, a $2.4\,\mathrm{m} \times 1.2\,\mathrm{m} \times 1.4\,\mathrm{m}$ gas-tight body made from stainless steel. Front and back side are made of 10 mm, respectively 20 mm thick plastic boards. They enclose a beam entrance and exit window which are made of 2 mm thick plastic in order to minimise particle scattering. A photograph of the prototype box is shown in the upper left panel of Fig. 5.2.

Mirror system

The mirror system consists of four square shaped spherical mirror tiles. They have a size of $40\,\mathrm{cm} \times 40\,\mathrm{cm}$ each and a radius of curvature of $R = 3\,\mathrm{m}$. Mirror tiles from three different manufacturers were characterised in order to find the best mirror in terms of reflectivity and surface quality[1]. For the selection of suitable mirror tiles, two quantities were studied: Integral reflectivity and D_0. Integral reflectivity is the wavelength dependent reflectivity convoluted with the Cherenkov spectrum. D_0 is defined as the diameter of a circle which contains 95 % of the reflected light in the projected image of a point-like source placed in the focal point of the spherical mirror. Details of measurement procedures and results of the mirror characterisation can be found in [6, 71]. Exhibiting the best performance, the mirror tiles from JLO-Olomouc, Czech Republic, were chosen. They consist of a 6 mm thick SIMAX glass substrate coated with Al+MgF_2 on the front. Aluminium provides a good reflectivity in both the visible and the UV wavelength region down to below 200 nm. The MgF_2 layer serves as protective layer in order to prevent the formation of aluminium oxide which is strongly UV absorbing. As usual for optical mirrors, the reflective coating is deposited on the front of the substrate in order to prevent absorption of UV photons in the glass. The disadvantage of front-coated mirrors is the absence of mechanical robustness.

Measurements show that the JLO-Olomouc mirror tiles have a reflectivity of $\approx 80\,\%$ at 200 nm. Integral reflectivity for Cherenkov photons from 200 nm to 800 nm is $(88 \pm 1)\,\%$, i.e. $(88 \pm 1)\,\%$ of Cherenkov photons impinging on the mirror surface are reflected [6].

For the prototype, four mirror tiles are mounted to an aluminium frame using three actuators per mirror tile.

---

[1] Test mirrors from Flabeg (Germany), Compas (Czech Republic), and JLO-Olomouc (Czech Republic) were investigated.

Each actuator can be moved in forward and backward direction within a range of 3 cm. This allows to align the mirrors such that they have a common focal point. To reflect the Cherenkov light onto the camera, the mirrors are rotated around the x-axis by an angle of $7.65°$ as shown in Fig. 5.1 [2]. The aluminium frame with the mirrors is the innermost part of three gimbal-mounted frames. This system is remote-controlled and allows moving the focal point to different positions on the camera (*ring positions*). This is very useful for systematic studies during beam tests because the Cherenkov rings can be easily moved to different parts of the detector which is equipped with different MAPMT types. Photographs of the mirror system from the back and the front are shown in Fig. 5.2 (bottom).

Camera

The camera is located at the upper front segment of the prototype box at a distance of 1.54 m from the mirror surface although the nominal focal point of the spherical mirrors is at $R/2 = 1.50$ m. Due to modifications during the construction procedure, this dimension differs slightly from the anticipated value. However, the reduction of the radiator length of ≈ 2.7 cm due to the rotation angle of the mirrors nearly compensates this difference. The residual difference between focal length and distance between mirror and camera adds up to only 0.9 % of the focal length and is not expected to have significant influence on the ring sharpness. The upper-right panel of Fig. 5.2 shows a photograph of the readout electronics. A detailed description of the camera will be given in section 5.2.

Gas system

The gas system of the prototype is designed to be used, with minor changes, also for the larger radiator volume of the final CBM-RICH detector. The design is based on the gas systems for the Time Projection Chamber of the STAR experiment [135] and the Muon Tracking Detector of the PHENIX experiment [136] at RHIC. The main purpose is to provide pure CO_2 gas at a stable overpressure of 2 mbar leading to a pion Cherenkov threshold of 4.65 GeV/c. Nominally, the system operates as a closed-circuit system with the majority of the gas recirculating through the prototype and the addition of fresh gas when needed. It is operated as open system when purging.

The purity of the gas is monitored with oxygen and humidity analysers. Up to 30 % of the circulating gas can be passed through a purifier and a dryer in order to remove oxygen and moisture. The purifier contains active copper and reduces the oxygen content at an operating temperature of 220 °C. The dryer contains molecular sieves. During operation in the beam tests, values of 100 ppm oxygen and 200 ppm water content could be reached.

The system is computer-controlled, i.e. several parameters are read out at a given rate. If a parameter passes a certain limit, corrective action is initiated. All relevant parameters are stored for documentation and data analysis. Details on the gas system can be found in [6].

5.2 The RICH prototype camera system

5.2.1 Mechanical layout

The prototype camera is designed as one single module, which can be mounted from outside to the prototype box. A printed circuit board (PCB), the so-called *MAPMT carrier board*, serves as interface between the radiator volume inside the detector box and the ambiance. Figure 5.3 shows a sketch of the carrier board and its position on the upper front side of the prototype box. The MAPMTs tested so far (cf. Tab. 3.1) have pin

---

[2] This rotation leads to a reduction of the radiator length of ≈ 2.7 cm at the level of the centre of the lower two mirrors. This, in turn, reduces slightly the number of Cherenkov photons and the Cherenkov ring radius.

Figure 5.2 – Top: CBM-RICH prototype from the front. The quadratic beam entrance window and the camera housing are marked with arrows (left). Readout electronics (right). Bottom: Mirror tiles mounted on the rotatable frame from back (left) and front (right).

row connectors for signal and ground connection. The matching surface-mounted (SMD) socket connectors are soldered on the inner side of the carrier board so that the MAPMTs can be plugged directly on the board. Vias guide each channel to the outer side of the board. The outer side of the carrier board has connectors to which all other electronic components are plugged.

Since the board is the interface between radiator and the outside, it has to be gas and light tight. It is therefore coated by black lacquer (see Fig. 5.4) and vias are specially sealed (*plugged vias*).

The HV supply is provided by pin connectors which are soldered to the carrier board in case of MAPMTs with HV pins (H8500D-03, R11265-103-M16) or by SHV[3] connectors mounted to the aluminium frame of the carrier board in case of MAPMTs with HV cable (H8500C-03). In both cases, all supply cables and connectors are connected to the carrier board. Like this, the carrier board with MAPMTs can be mounted and dismounted without the need of plugging cables and connectors. The carrier board together with its aluminium frame also serves as common signal ground for all signal and HV connections.

Having only the photon sensors and their integrated active voltage dividers inside of the radiator volume and other parts outside has several advantages. First, no interface layer in front of the photon sensors is needed. Such a layer would cause a loss of photons even when using a highly UV-transparent material like fused silica. Having the other electronic components outside has the advantage that, secondly, maintenance is easier and can be done without unmounting the camera module which would lead to contamination of the radiator gas. Third, dissipated heat from the readout electronics will be given off to the ambiance and does

---

[3] Huber+Suhner SHV (Safe High Voltage)

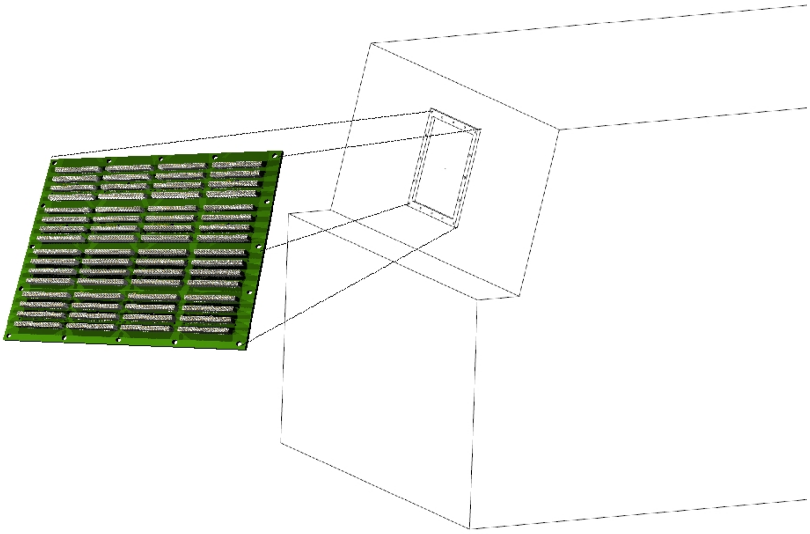

Figure 5.3 – Isometric view of the prototype box with a sketch of the MAPMT carrier board in the 4×4 layout for the 2011 beam test. Here, the internal side of the carrier board is shown. Every MAPMT is plugged to four connectors with 32 pins each (16× signal and 16× ground).

not lead to a temperature gradient inside the radiator. The heat dissipation of four H8500C/D MAPMTs is $4 \times 0.17\,\mathrm{W} = 0.68\,\mathrm{W}$ [89] which is small compared to that of the readout electronics in case of the n-xyter readout ($\approx 18\,\mathrm{W}$ per unit of four MAPMTs).

With the modular concept used for the camera system of the prototype, also larger areas can be equipped with MAPMTs and readout electronics. This scalability is important for the construction of the full CBM-RICH detector.

5.2.2 Configuration for the 2011 and 2012 beam tests

Camera layout for the 2011 beam test

For the beam tests in autumn 2011 and autumn 2012, two different MAPMT carrier boards were used. Figure 5.4 shows photographs of the two boards. The 2011 layout is designed for being equipped with 4×4 H8500 MAPMTs of different type with a total of 1024 channels (see Fig. 5.4 bottom left). The area on the carrier board instrumented with MAPMTs covers $21.4\,\mathrm{cm} \times 21.4\,\mathrm{cm}$. The spacing between two MAPMTs is 2 mm. Given the size of the MAPMTs, $52\,\mathrm{mm} \times 52\,\mathrm{mm}$, one Cherenkov ring fits on four MAPMTs.

To test the effect of wavelength shifting films (WLS), four MAPMTs were covered with p-Terphenyl. The corresponding *QE* curves are shown in Fig. 4.11.

Camera layout for the 2012 beam test

The bottom right panel of Fig. 5.4 shows the carrier board of the camera tested in 2012. Apart from the modified carrier board, it follows the same concept as the 2011 detector. It is equipped with additional R11265-103-M16 MAPMTs and XP85012 Micro Channel Plate photon sensors (MCP)[4].

The 2012 board is slightly larger with an array of 4×3 pieces of H8500 MAPMTs, 8 pieces of R11265-103-M16 MAPMTs, and an array of 2×2 pieces of XP85012 MCPs.The total number of channels is 1152, the spacing between two MAPMTs 2 mm and between two MCPs 1 mm.

---

[4] As mentioned in section 3.2, the evaluation of MCPs is not within the scope of this thesis.

year	photon sensor type	quantity	WLS coating	notation in Fig. 5.4
2011	H8500D-03	6	no	(1)
	H8500C-03	3	no	(2)
	H8500-03	1	1/2	(3)
	H8500D-03	4	yes	(4)
	H10966A-103	2	no	(5)
2012	H8500D-03	3	no	(1)
	H8500C-03	1	no	(2)
	H8500D-03	4	yes	(4)
	H8500D	2	no	(6)
	H10966A-103	2	yes	(7)
	XP85012	3	no	(8)
	R11265-103-M16	4	no	(9)
	R11265-103-M16	4	yes	(10)

Table 5.1 – Photon sensors used during the 2011 and 2012 beam tests.

6 pieces of H8500 and 4 pieces of R11265-103-M16 are covered with optimised dip-coated WLS films. For the corresponding *QE* curves, see Fig. 4.12 and Fig. 4.13.

Since only eight MAPMTs of type R11265-103-M16 were available for the beam test, they were arranged in a circular structure to comprehend the maximal Cherenkov ring expected from electrons traversing the radiator. In such a configuration, small variations of the ring centre position are compensated in first order due to the partial but rotationally symmetric coverage of the ring.

Table 5.1 lists the types of photon sensors mounted on the carrier boards for the beam tests. Specifications can be found in Tab. 3.1.

5.2.3 Front-end electronics

The readout chain comprises three parts, attenuator board, front-end board, and readout controller, whose functionalities will be briefly described in the following paragraphs. Figure 5.5 shows the sequence of these components in the readout chain. MAPMTs and front-end electronics (FEE) are connected in a way that the analogue part of the signal is transmitted on PCB tracks and connectors without cables in between. The footprint of all components matches that of the MAPMTs. All electronics can thus be placed behind the MAPMTs without hampering a dense MAPMT packing.

Attenuator board

The dynamic input signal range of the n-xyter chip (see next paragraph) is $1.2 \cdot 10^5$ electrons. Given the typical gain of a H8500D-03 with 12 dynodes being $1.5 \cdot 10^6$, a single photoelectron signal will be of the order of $1.5 \cdot 10^6$ electrons. In order to measure also the tail of the signal and taking into account that gain variations about a factor of 2 can occur (cf. section 3.7), the usage of the n-xyter chip necessitates an attenuation of the PMT signals by a factor of $\approx 1/50$ for H8500D-03. For the 8 dynode stage H10966A-103 MAPMTs, the attenuation has to be lower. The signal attenuation is done by using a capacitive attenuation

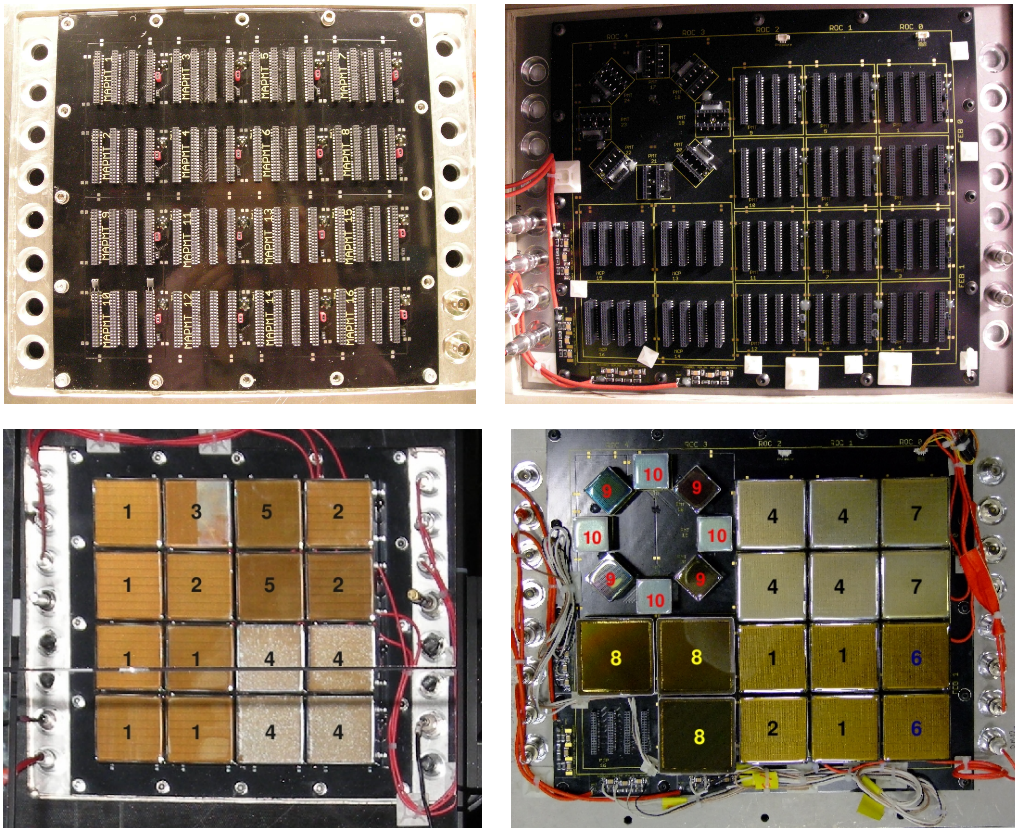

Figure 5.4 – Top row: Photographs of the MAPMT carrier boards for the beam tests 2011 (left) and 2012 (right). Each H8500 MAPMT and MCP is plugged to four connectors with 32 pins each (16× signal and 16× ground), each R11265 MAPMT to two connectors with 8 signal pins each. Bottom row: Photographs of the photon sensors plugged to the 2011 (left) and 2012 carrier board (right). The numbers refer to different types of photon sensors: 1. H8500D-03; 2. H8500C-03; 3. H8500-03 half-coated with WLS; 4. H8500D-03 with WLS; 5. H10966A-103, 8-stage, SBA; 6. H8500D selected as "bad"; 7. H10966A-103, 8-stage, SBA with WLS; 8. XP85012; 9. R11265-103-M16; 10. R11265-103-M16 with WLS. The WLS film can be recognised by its frosted surface (cf. Fig 4.9).

board. Its electric circuit is shown in Fig. 5.6.

The attenuation factor is given by the ratio of the capacitances C_2 and C_1. Each board has 128 channels and can be used for two 64 channel MAPMTs. Its dimensions are adjusted to fit the size of two H8500 MAPMTs. Several boards were fabricated and equipped with identical resistors R_1 and R_2 and capacitors C_1. The capacitors C_2 differ for each MAPMT type. They were soldered on the boards after the determination of the appropriate attenuation factors for each type of MAPMT in the laboratory. The used capacitances and resistors for the beam tests 2011 and 2012 are listed in Tab. 5.2.

Front-end board

The front-end board (FEB) is designed as a general purpose board, i.e. it is not tuned for a particular detector type. It contains one n-xyter chip, one single channel 12 bit analogue-to-digital converter (ADC) and provides 128 channels. The board design was done by Rafal Lalik and Volker Kleipa at the GSI Detector Lab. For the laboratory and beam tests presented in this thesis, the design versions *Revision C* and *Revision D* were used.

The *neutron-x-y-time-energy readout* (n-xyter) chip was developed by the Faculty of Physics and Applied Computer Science of the AGH University of Science and Technology, Krakow, and is able to measure both

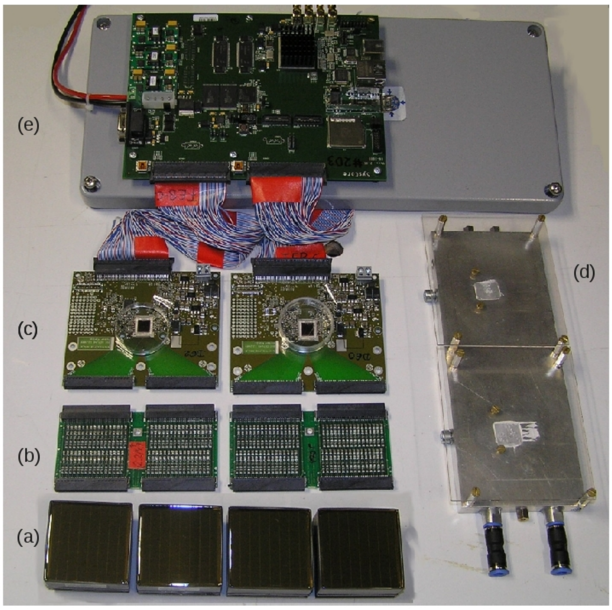

Figure 5.5 – Photograph of all components of the readout chain consisting of four MAPMTs (a), two attenuator boards (b), two n-xyter FEB modules (c), water colling plate (d), and SysCore ROC (e). The analogue signals from the MAPMT to the ADC on the front-end board are transmitted on PCB tracks and connectors without cables in between. Data from the FEB to the ROC is transmitted by twisted pair flat cables. Photograph taken from [137].

year	photon sensor type	R_1	R_2	C_1	C_2	attenuation factor
2011	H8500D-03	$100\,\Omega$	$10\,\mathrm{k}\Omega$	10 pF	470 pF	$1/47$
	H8500C-03	$100\,\Omega$	$10\,\mathrm{k}\Omega$	10 pF	470 pF	$1/47$
	H8500-03	$100\,\Omega$	$10\,\mathrm{k}\Omega$	10 pF	470 pF	$1/47$
	H10966A-103	$100\,\Omega$	$10\,\mathrm{k}\Omega$	10 pF	220 pF	$1/22$
2012	H8500D-03	$100\,\Omega$	$10\,\mathrm{k}\Omega$	10 pF	470 pF	$1/47$
	H8500C-03	$100\,\Omega$	$10\,\mathrm{k}\Omega$	10 pF	470 pF	$1/47$
	H10966A-103	$100\,\Omega$	$10\,\mathrm{k}\Omega$	10 pF	100 pF	$1/10$
	XP85012	$100\,\Omega$	$10\,\mathrm{k}\Omega$	10 pF	220 pF	$1/22$
	R11265-103-M16	$100\,\Omega$	$10\,\mathrm{k}\Omega$	10 pF	680 pF	$1/68$

Table 5.2 – Capacitances, resistors and resulting theoretical attenuation factors of the attenuator boards used during the 2011 and 2012 beam tests.

time and amplitude of the signal. It is an application-specific integrated circuit (ASIC) realised in $0.35\,\mu\mathrm{m}$ CMOS technology and designed within the joint research activity DETNI[5] for the common readout of three different neutron detectors [138]. Since it is not possible to efficiently trigger on neutrons, the architecture of the n-xyter chip is designed to be self triggered and data-driven (see section 2.4.2). It has 128 channels with low noise preamplifiers and shapers. Each channel has two analogue shapers with different time constants. The fast shaper (shaping time 19 ns for 30 pF input capacitance) is optimised for a good time resolution. The discriminated signal is used to produce a signal time stamp. The slow shaper (shaping time 140 ns for 30 pF

---

[5] DETNI - Detectors for Neutron Instrumentation, http://jra1.neutron-eu.net/jra1

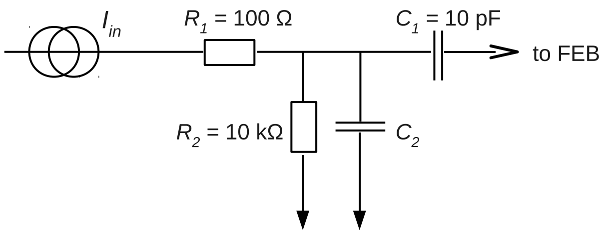

Figure 5.6 – Electric circuit of the attenuator board. The attenuation factor is given by the ratio between capacitances C_2 and C_1. Depending on the gain of the MAPMT type, different capacitors C_2 are used, e.g. $C_2 = 470\,\text{pF}$ for a H8500 MAPMT resulting in an attenuation factor of ≈ 50.

input capacitance) is optimised for pulse energy, i.e. pulse height resolution and therefore used as energy channel with peak detection. Analogue-to-digital conversion is done consecutively for each channel on the single channel fast ADC. The fast shaper, in addition, controls the reset of the peak detection facilitating the system being self triggered without external reset. For every channel, pulse height and time stamp are stored in a fifo (first-in, first-out). The data is read out continuously from the fifos through a token ring procedure that reads channels with data and skips channels without. The digital precision of the time stamp mechanism is 1 ns, timing resolution in the order of 2 ns to 4 ns. The maximum hit rate per channel is 160 kHz [138].

As will be shown later, the n-xyter FEBs have been proven to work very well in the beam tests. They are, however, not optimised for the use in the final CBM-RICH detector and will be replaced by more suitable front-end electronics [6].

Readout controller

Since the n-xyter provides the pulse height in analogue form, it is converted on the FEB by the ADC into digital data. Because of conversion time, the pulse height information is delayed with respect to the time stamp. The recombination as well as the data transfer and the control of the n-xyter and ADC functionality is the task of the readout controller ROC [139]. The used SysCore ROC is an FPGA-based board and was developed at the Kirchhoff Institute for Physics in Heidelberg [140]. The developed software allows to configure and control the ROC from any Linux PC. The communication is performed via a 100 Mbit Ethernet link. Alternatively, an optical link can be used. Parameters of the n-xyter and the ADC can be accessed and changed using serial busses. For this purpose, Linux is running on the ROC and slow control can be done by text files which include the appropriate commands. The *ROClib* software package provides a user interface to the ROC for configuration of n-xyter and ADC (e.g. setting of thresholds) whereas data readout is done by the data acquisition system *DABC* and monitoring by *Go4*. The role of DABC in the data acquisition system of the beam test setup will be discussed in section 5.3.2, the Go4 monitoring in section 5.3.3.

Shielding against light and electromagnetic noise

In order to minimise the pick-up of electromagnetic noise, the readout electronics on the outer side of the MAPMT carrier board are covered by an aluminium box (see top left panel of Fig. 5.2). This box also serves as additional light shielding since the black lacquer on the carrier board is not completely intransparent.

It turned out that especially the attenuator boards are sensitive to picking up noise. They are therefore individually and tightly covered by an additional copper shielding as can be seen in Fig. 5.7.

5.3 Experimental setup at CERN

In this section, the setup of the CBM-RICH prototype for a common beam test campaign with other CBM subdetector prototype systems at the CERN PS will be described. In the first subsection, the buildup of the subdetectors in the cave will be presented. The second subsection presents the common but heterogeneous

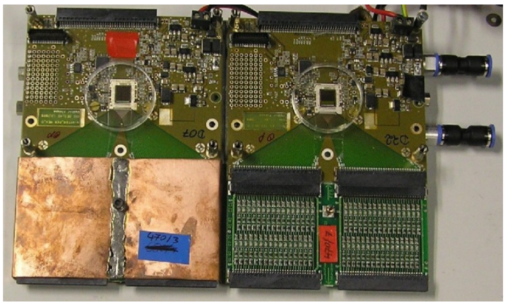

Figure 5.7 – Photograph of the copper shielding of an attenuator board. For the beam tests, all attenuator boards were individually shielded in order to minimise the pick-up of electromagnetic noise.

data acquisition system and the online monitoring system. The focus will be kept on the beam test 2011 since most of the analysis presented in this thesis will be based on 2011 data. Only for the evaluation of WLS films on different types of MAPMTs, data from the 2012 beam test campaign will be presented (see section 5.6.2). Finally, the conducted measurement programmes will be exposed.

5.3.1 Subdetectors

The common CBM beam test campaigns in 2011 and 2012 were conducted at the CERN PS/T9 beam line. Protons with a momentum of 24 GeV/c from the PS are directed onto a production target. Secondary electrons, muons, and pions are then guided to the various beam lines in the experimental hall. At T9, the magnets can be adjusted such that positively or negatively charged beam particles with momenta from 1 GeV/c to 10 GeV/c can be selected. The theoretical momentum resolution is 0.24 % depending on the settings of collimators. By varying the current in the most downstream quadrupole magnet, the beam focus can be moved forward and backward. The horizontal and vertical RMS size of the beam is 10 mm to 30 mm and 5 mm to 12 mm, respectively, and the intensities are up to 10^6 particles per spill of about 300 ms duration [141], also depending on the chosen momentum resolution and collimator settings.

Figure 5.8 depicts the arrangement of all subdetectors built up in the beam line. A total of 7 m was instrumented with CBM prototype detectors. Two threshold Cherenkov counters for triggering and particle identification are permanently installed in the beam line in the front part of the cave. They are filled with CO_2 and the pressure can be adjusted in order to separate electrons, muons, and pions which produce light only when traversing the radiator with velocities above threshold. The identification of particles is done by combining the signals from both counters.

Downstream of the Cherenkov counters, a finger scintillation detector (Sc1) for triggering and a fibre hodoscope (Hodo) [142] for triggering and tracking are installed. The RICH prototype is mounted on a table with rails in order to easily move the whole detector laterally out of the beam. This was done to allow the subsequent subdetectors measurements with a minimum material budget in front. The RICH is followed by four different TRD prototype systems, two layers from Bucharest, four layers from Münster, four layers from Frankfurt, and two layers from Dubna[6]. Two RPC layers as prototype for the TOF detector are mounted behind the TRD detectors. A second scintillation detector (Sc2) for triggering and a Pb-glass calorimeter (Pb-glass) for triggering and particle identification are installed at the end of the setup.

5.3.2 Data acquisition

The data acquisition (DAQ) is performed using the Data Acquisition Backbone Core (DABC) framework [143]. An overview of the DAQ system, which was set up for the CBM beam test 2011 at the CERN PS, is given in [144].

---

[6] In the CBM collaboration, different groups are working in parallel on R&D for the TRD detector. The decision on the final design or whether different designs will be combined, has not been made yet.

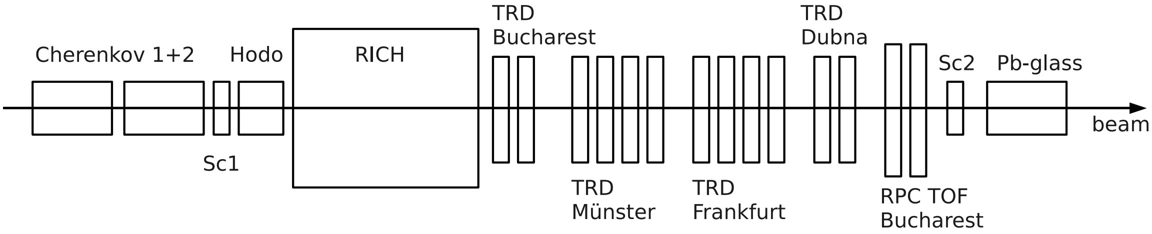

Figure 5.8 – Experimental setup for the beam test campaign at the CERN PS in 2011.

A heterogeneous beam test setup with different subdetectors using different types of FEE requires a flexible software organisation in order to treat various data inputs in one common DAQ system. With the C++ based DABC framework, different data sources can be combined with event-builder processes which run on normal Linux PCs. DABC can also take data from the EPICS[7] slow control system and include it in the data stream.

Figure 5.9 schematically shows the DAQ system set up for the 2011 beam test. Eight different subdetectors had to be read out via three different FEE systems, among which six were conventionally beam-triggered and two free running (ROCs of the RICH prototype and the fibre hodoscope). In order to allow DABC event building, special trigger synchronisation messages were inserted into the ROC data stream from a VULOM[8] via Low Voltage Differential Signaling (LVDS) cables. Although the readout for the RICH prototype is free-running, these synchronisation messages can be used in the later offline data analysis, e.g. for a time cut around the arrival time of a beam particle for the suppression of uncorrelated noise (cf. 5.4.1).

The different FEE systems are connected to two DABC event builder nodes (PC1, PC2) via Ethernet in the case of the ROCs for the RICH. The slow control data is read out by a third DABC node (PC3). DABC packs all data into a MBS event container structure[9]. PC1 then combines the data from the DABC processes, writes the data files and serve the online monitoring clients. The data is written into so-called list-mode (“lmd”) files, a standard GSI data protocol.

5.3.3 Online monitoring

For the proper operation of the prototype, detector settings and collected data have to be monitored, ideally in real time. For the beam test, an online monitoring system was set up which can be seen as interface between the data acquisition system and the operator.

The data flow from the photon sensors to the final data file is shown schematically in Fig. 5.10. The hardware part consists of the MAPMTs and the components of the readout chain described in section 5.2.3. The software part is based on DABC and the C++ and ROOT based *GSI Object Oriented On-line Off-line system* (Go4) [103, 145].

The use of Go4 is twofold, it can directly connect to DABC via the so-called MBS stream server in order to monitor the detectors online, or it can process data stored in list-mode files. In addition, it provides the possibility to store data like ADC values, hit coordinates and timing information in ROOT trees. In this way, Go4 serves as tool to, firstly, process the raw data from the ADCs and, secondly, perform an analysis on a higher level.

---

[7] The Experimental Physics and Industrial Control System (EPICS) is an open source software for slow control, http://www.aps.anl.gov/epics/. It is used by the CBM Collaboration as common detector control system.

[8] The GSI VME-bus Universal Logic Module (VULOM) is a FPGA-based electronic logic module developed by J. Hoffmann at GSI.

[9] The Multi Branch System (MBS) is a general purpose data acquisition system developed at GSI, http://www-win.gsi.de/daq/.

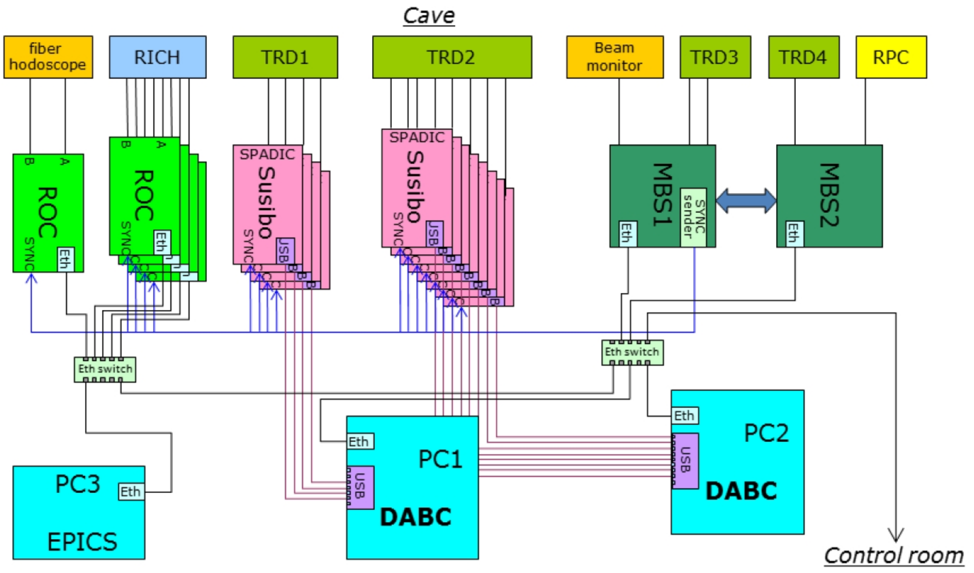

Figure 5.9 – DAQ system set up for the 2011 beam test. A total of eight subdetectors was read out via three different FEE systems, MBS, Susibo/SPADIC, and ROC. The latter is used for the RICH. See text for details. Figure taken from [144].

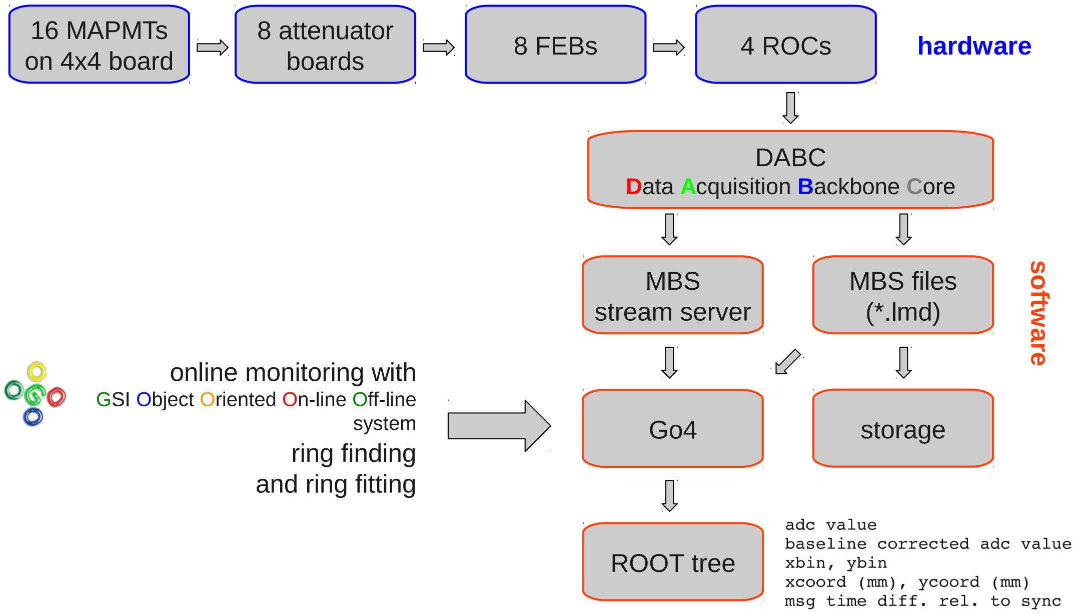

Figure 5.10 – Data flow in the CBM-RICH prototype during beam tests.

The data analysis in Go4 is split into three analysis steps [144]. Each step produces intermediate data which is used by the subsequent analysis step. The first step unpacks the raw data from the DAQ. All subdetectors with the same FEE system share the same analysis code for the first step. The second step, on the other hand, is detector specific. In the case of the RICH, it maps the DAQ channels to the detector display and performs a more advanced analysis related to ring recognition and fitting. The third step provides the correlation of data from different subdetectors. Particle identification using the two threshold Cherenkov detectors and the Pb-glass calorimeter, for instance, is done in the third step.

Because of the plug-in architecture, user specific analysis can easily be implemented into the Go4 code. The structure allows the parallel development of analysis code by the different subdetector groups for different beam tests. The detector specific code of the second and third analysis step is organised in a modular way in separate source code directories with a top class name prefix indicating the campaign, e.g. “cern-oct11”, and detector specific subdirectories[10], e.g. “cern-oct11/go4/RICH”.

Technically, each analysis step is defined by an event processor class. The following paragraphs will focus on the RICH specific development done for the 2011 beam test. Some important features, mainly implemented into the RICH processor class “cern-oct11/go4/RICH/TRICHProc”, will be presented.

ADC spectra and baseline correction

Figure 5.11 shows single photoelectron spectra of all 128 input channels of one n-xyter chip. At the outset, low ADC values signify large signals and vice versa. It can be seen that the baseline differs for different channels resulting in unsteady ADC spectra from different channels (Figure 5.11 top left). This channel-to-channel offset variation is an internal feature of the n-xyter ASIC, and is in particular strongly dependent on temperature. Therefore a baseline correction has to be performed by recording the ADC signals of all channels without applying an input signal in the so-called “test trigger mode” of the FEB. In this mode, an internal trigger signal initiates the readout and subsequent ADC conversion of all 128 input channels. The values are stored in a “pedestal file” which is used to invert and align the spectra (Figure 5.11 top right). A projection of the channels of one MAPMT on the y-axis is shown in Fig. 5.11 for uncorrected (bottom left) and baseline corrected spectra (bottom right).

Camera event display

Due to the complicated layout of PCB tracks on the MAPMT carrier board and the mixup of channels at the connectors of the twisted pair cables between FEBs and ROCs, adjacent MAPMT channels do not correspond to adjacent FEB channels. This is advantageous in terms of crosstalk because in most of the cases electronic crosstalk in the readout electronics will not be seen as crosstalk between neighbouring MAPMT pixels. However, MAPMT channels have to be mapped to FEB channels which is done in the second analysis step of Go4 with the help of the class “MAPMT_Cell”. The look-up table “mapmt-geometry.txt” relates ROC, FEB, MAPMT, and MAPMT pixel numbers as well as spatial coordinates of every channel of the camera. An excerpt from that file is shown in Fig. 5.12.

The correct mapping has been cross checked by introducing pulses from a pulse generator via a contact needle directly into the connectors on the MAPMT carrier board. With that, a 2D histogram with 32×32 pixels for the 4×4 MAPMTs with 64 channels each can be used as camera event display. The bins of the histogram are filled with hits of the corresponding coordinate. Histograms for integrated ring display as well as for single event displays were implemented. Since Go4 can directly connect to DABC, the position of Cherenkov rings on the camera can be monitored in real time which is especially favourable while changing ring positions by rotating the mirror.

Run statistics monitor

For systematic studies of the prototype performance, data sets with sufficient statistics had to be collected. For some analyses, an accuracy on the percent level was required. Since the intensity of the beam varies with running conditions of the beam line, the online monitoring of run statistics was essential in order not to record too small data sets on the one hand and not to waste precious beam time on the other hand. For this reason, histograms showing the number of hits per MAPMT and the number of hits on the whole camera were prepared[11].

---

[10] For the 2011 beam test, four subdirectories were established: “RICH”, “BUCHAREST”, “DUBNA”, and “MSFFM”.

[11] Later, when the external particle identification using the threshold Cherenkov counters was adjusted, the monitoring of run statistics could be precised with respect to the particle species. With ring finding and fitting, the number of specific particles (electrons, pions, and muons) instead of hits could be precisely monitored.

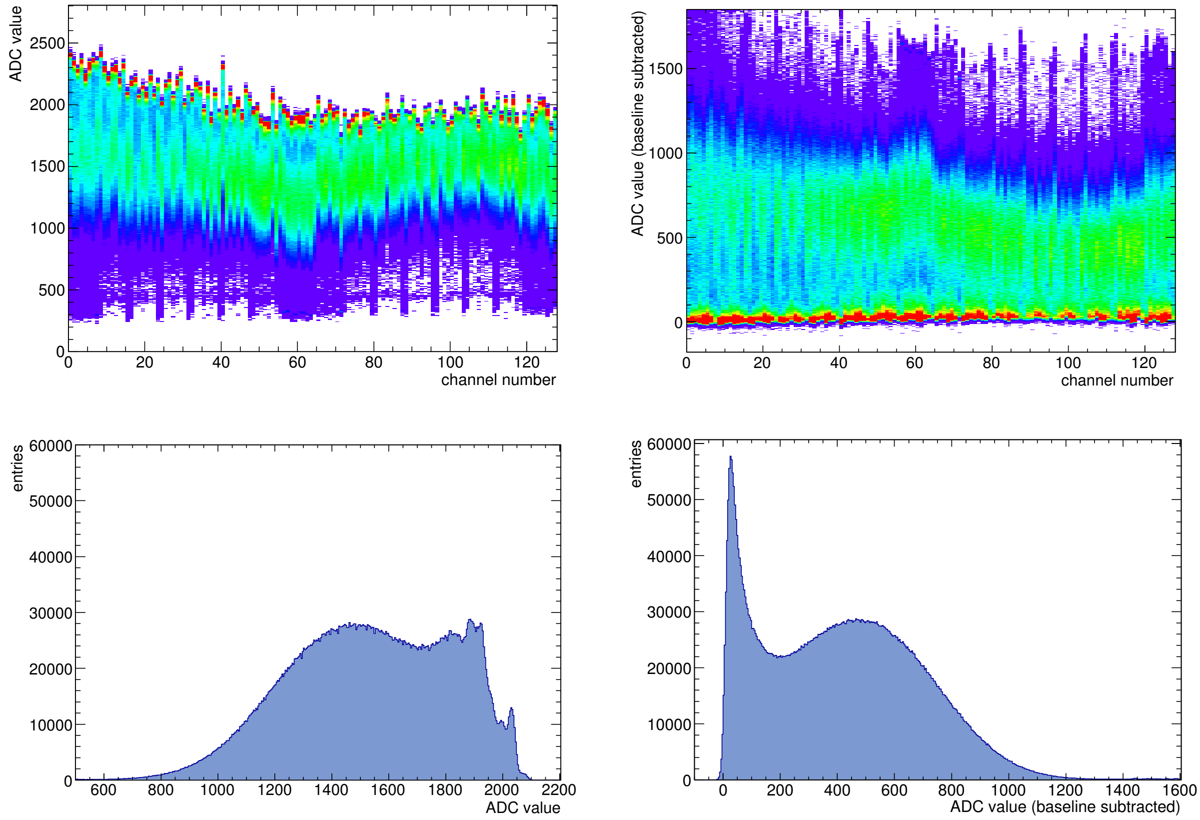

Figure 5.11 – Top left: ADC spectra from all 128 ADC channels of one n-xyter chip under single photon illumination. Top right: Aligned ADC spectra after baseline correction. Lower line: Projections of all 64 channels of one MAPMT (channels 65 to 128) on the y-axis for uncorrected (left) and corrected spectra (right). It can be seen that these sum spectra are much better aligned after the baseline correction.

```
#roc feb  febch  mapmt  pixel  xcoord  ycoord  xbin  ybin
#------------------------------------------------------
0    0    0        1      1     0       207.5   0      31
0    0    1        1      5     26      207.5   4      31
0    0    2        1      3     13      207.5   2      31
0    0    3        1      7     39      207.5   6      31
0    0    4        1      2     6.5     207.5   1      31
0    0    5        1      6     32.5    207.5   5      31
0    0    6        1      4     19.5    207.5   3      31
0    0    7        1      8     45.5    207.5   7      31
0    0    8        1      9     0       201     0      30
.    .    .        .      .     .       .       .       .
3    2   127      16   1024     207.5   0      31       0
```

Figure 5.12 – Excerpt from the MAPMT mapping file “mapmt-geometry.txt”.

Monitoring of ring fit results

The proper performance of the prototype can be controlled in the easiest way by monitoring the Cherenkov ring radius and the number of hits per ring. This is possible to do online due to the plug-in architecture of the Go4 analysis code and the call of the ring finding and ring fitting routines in the RICH processor “TRICHPRoc.cxx” for every event[12]. The fit results, e.g. ring radius, ring centre, and ring width, are displayed in histograms for different types of particles and for events and rings.

Figure 5.13 shows a screenshot of the online monitoring display with the most important histograms used to monitor the prototype performance during a beam test.

---

[12] In the context of the Go4 analysis, an *event* is defined as entity of time correlated hits whereas a *ring* contains only those hits which where found by the ring finder and used for ring fitting. The algorithms are described in section 2.5.3.

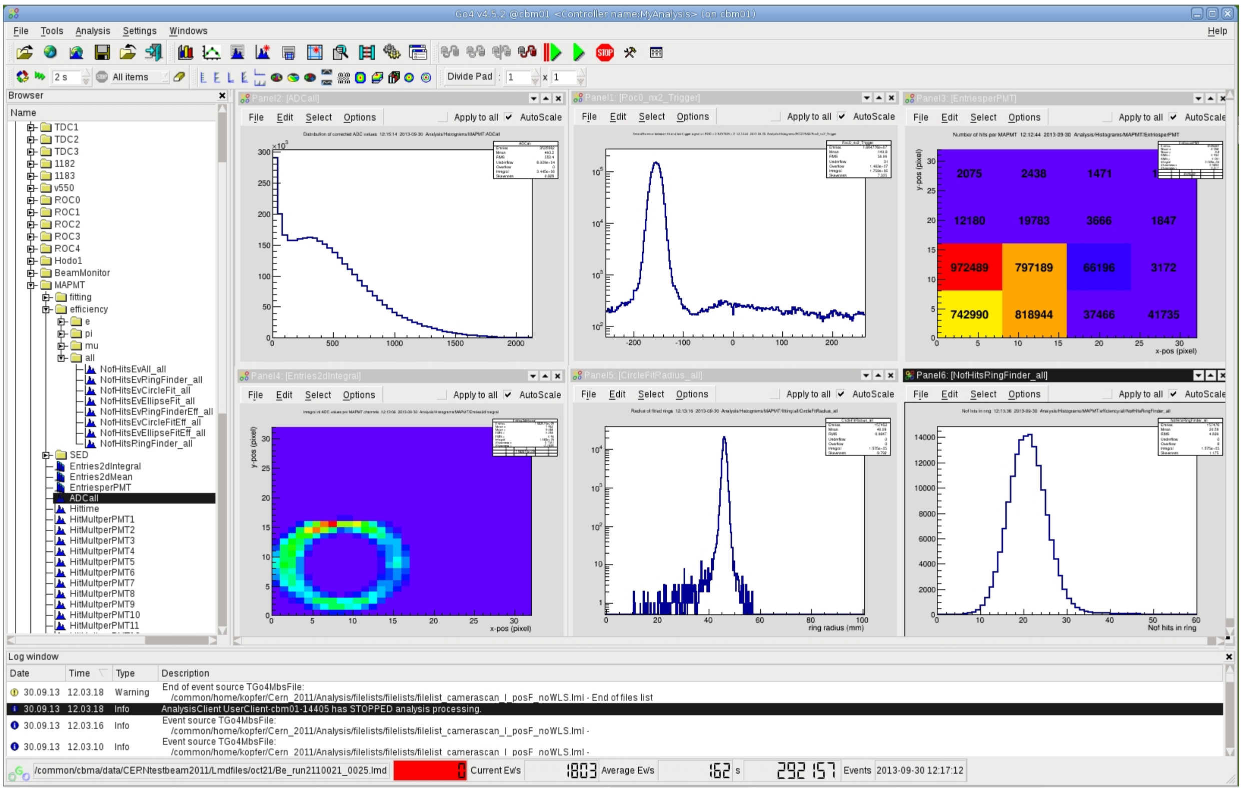

```
Log window
Date      Time      Type     Description
30.09.13  12.03.18  Warning  End of event source TGo4MbsFile:
                               /common/home/kopfer/Cern_2011/Analysis/filelists/filelists/filelist_camerascan_I_posF_noWLS.lml - End of files list
30.09.13  12.03.18  Info     AnalysisClient UserClient-cbm01-14405 has STOPPED analysis processing.
30.09.13  12.03.16  Info     Event source TGo4MbsFile:
                               /common/home/kopfer/Cern_2011/Analysis/filelists/filelists/filelist_camerascan_I_posF_noWLS.lml -
30.09.13  12.03.10  Info     Event source TGo4MbsFile:
                               /common/home/kopfer/Cern_2011/Analysis/filelists/filelists/filelist_camerascan_I_posF_noWLS.lml -
/common/cbma/data/CERNtestbeam2011/Lmdfiles/oct21/Be_run2110021_0025.lmd  0  Current Ev/s  1803  Average Ev/s  162  s  292 157  Events  2013-09-30 12:17:12
```

Figure 5.13 – Screenshot of the online monitoring display of Go4. On the left side, all available histograms can be selected for display. The six histograms show the sum ADC spectrum of all 1024 channels, time difference between hits and synchronisation messages and number of hits per MAPMT (top row from left to right) and integrated rings, ring radius and hit multiplicity distribution (bottom row from left to right).

5.3.4 Measurement programme and detector setting

During the two weeks of beam time in Oktober and November 2011, parameters from both the beam and the prototype were varied. For the data analysis and results presented in this thesis, a camera scan and a momentum scan are of particular importance. During the camera scan, the Cherenkov rings were focused onto different parts of the camera in order to compare different MAPMT types and the effect of WLS films. Figure 5.14 shows different ring positions and the nomenclature for the 2011 and 2012 camera layouts.

Two strategies have been pursued in order to evaluate the hit multiplicity per Cherenkov ring with and without WLS films.

Camera scan 2011 – quasi-simultaneous measurement

In the first test during the campaign 2011, ring positions D and F (equipped with H8500D-03 MAPMTs) were used as reference positions. Having two reference positions allows for consistency checks.

In order to compare H8500D-03 with H10966A-103 MAPMTs, the Cherenkov rings were focused onto position C which is equipped with two H8500C-03 and two H10966A-103. Direct comparisons with the reference positions can be made.

In order to investigate the effect of WLS films, the rings were focused on position H with four WLS coated H8500D-03 MAPMTs. Subsequently, reference measurements on positions D and F were performed. The change of ring position by rotating the mirror can be done within several minutes. This method of measuring is therefore referred to as quasi-simultaneous measurement. Since the WLS coated MAPMTs differ from the reference MAPMTs and tube-to-tube fluctuations are of the order of the WLS effect to be investigated, a thorough correction for variations in the single photon detection efficiency for every pixel of each MAPMT has to be done by illuminating all MAPMTs quasi-homogeneously with single photons from a pulsed LED (see section 5.4.4).

The used WLS films have a thickness between 50 nm and 100 nm and were applied before the systematic studies of the film thickness. The corresponding *QE* curves are shown in Fig. 4.11.

Camera scan 2012 − consecutive measurement

The second study on WLS films during the 2012 campaign was done by first measuring Cherenkov rings on MAPMTs with WLS films on position C (H8500D-03), then cleaning these MAPMTs, and measuring a second time on the same MAPMTs without WLS coverage. When measuring in this way, the efficiency correction can be omitted at the expense of a correction for variations of the refractive index of the radiator due to temperature and pressure changes during the time consuming cleaning process. It is time consuming because the camera module has to be dismounted. This causes an air flow into the detector. Afterwards, the volume has to be purged with CO_2 until acceptably low O_2 and H_2O levels have been reached. This type of measurement is called consecutive measurement.

In order to make cross checks and evaluate WLS films on different types of MAPMTs, also measurements on ring positions K, B, E, and I were performed.

Regularly, measurements on position A were done to monitor the detector stability. Position A was chosen because the MAPMTs were not subject to the cleaning.

In practice, the WLS films were removed in two steps. At the beginning, all MAPMTs highlighted in blue in Fig. 5.14 were coated. During the first removal, WLS films were removed from all MAPMTs except two MAPMTs. A second removal was done in order to clean also these MAPMTs. For the analysis, data from before and after the first cleaning are considered (see section 5.6.2).

The *QE* curves of the WLS films used for the 2012 beam test are shown in Fig. 4.12 and 4.13.

Momentum scan

By changing the currents in the eleven magnets of the beam line, particles of different momentum ranges can be selected. In order to test the electron pion separation capabilitiy of the prototype in dependence of particle momentum, a momentum scan between 2 GeV/c and 10 GeV/c in steps of 1 GeV/c was performed.

LED runs

In most cases a beam particle results in less than 30 hits on the camera. This makes it difficult to systematically study the camera performance in terms of single photon spectra where hits from all channels are desired. Therefore, measurements with LEDs of 245 nm and 350 nm wavelength were carried out in addition to the beam measurements. The LED illuminated all channels homogeneously with single photons, which enabled systematic measurements of single-photon spectra for the whole camera.

The results of the LED measurements are also used for the extraction of correction factors for all MAPMT pixels (see section 5.4.4).

Detector settings

If not specified otherwise, the ADC threshold was set to a register value of 28 which is only slightly above the noise edge and corresponds to less than 10 % of the single photoelectron peak. For the data considered in the analysis, all MAPMTs were operated at a nominal voltage of −1000 V in 2011. In the 2012 beam test, the voltage settings were tuned for each MAPMT individually. Using the rail mounting, the prototype was

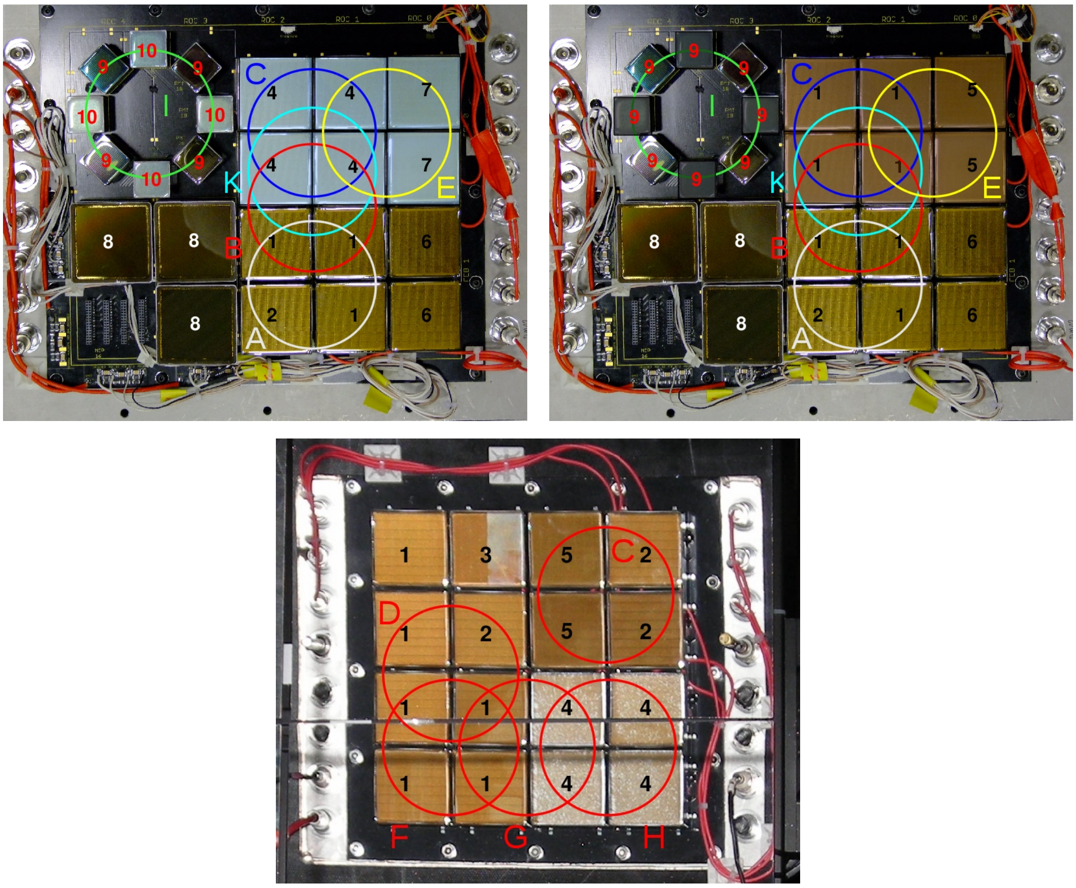

Figure 5.14 – Illustration and nomenclature of ring positions during the beam test campaigns 2012 (top) and 2011 (bottom). The movable mirror was used to reproducibly focus the Cherenkov rings onto different MAPMTs. In 2011, data with WLS film was taken at position H; data without WLS film at the reference positions D and F. In 2012, the data with WLS was taken at position B, C, E, I, K (top left); data without WLS film at the same positions after a (partial) removal of the WLS films (top right). In the top row, MAPMTs initially coated by WLS films are highlighted in blue. See text for details. The WLS films on the lower picture can be recognised by their frosted appearance. See Fig. 5.4 for the MAPMT types.

positioned such that the beam went through the centre of the lower right of the four mirror tiles when seen from the front. Given the relatively large size of one mirror tile, the whole Cherenkov cone is then reflected by a single mirror tile without any photons escaping through the gap between mirror tiles.

5.4 Data analysis

5.4.1 Applied cuts and resulting noise

The hardware ADC threshold value was adjusted only slightly above the noise edge. Due to efficient shielding and cable-free transmission of the analogue signals, a very low noise rate of up to 10 kHz for the whole photon detector can be achieved[13]. This rate originates mainly from dark noise due to thermal emission of the MAPMT photocathodes. This corresponds to a noise rate of maximal 10 Hz per channel. This, together with a timing cut, enables a clean detection of Cherenkov photons with almost no noise hits as can be seen in the upper left panel of Fig 5.19. The time cut selects events within a time window of 100 ns. The time

---

[13] During beam pauses, the noise rate is read off from the ROCs for individual FEBs.

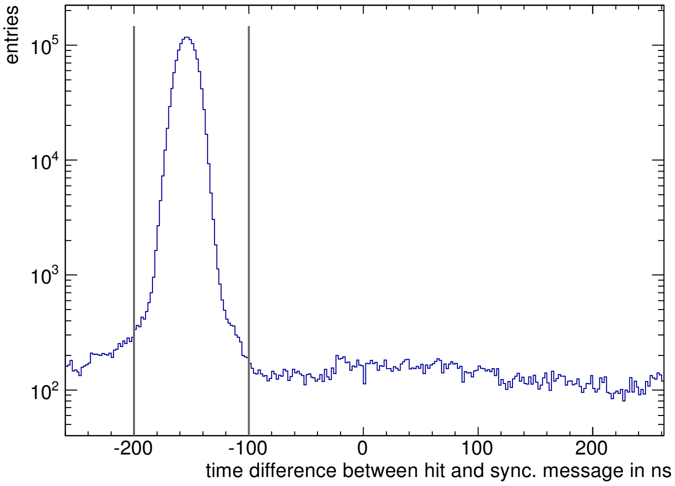

Figure 5.15 – Distribution of time difference between hit and synchronisation message. In order to reduce noise, only hits between 200 ns and 100 ns before the (delayed) synchronisation message are selected. The grey lines indicate the time cut window.

distribution is shown in Fig 5.15. With that it turns out that a cut on the signal amplitude is unnecessary for further suppression of noise. The low noise rate and the application of the timing cut result in 10^{-3} noise hits per event.

5.4.2 Ring reconstruction

The ring finding and fitting algorithms called in Go4 are the same as used for the simulations (see 6.1.4). This is very favourable when comparing beam test results with simulations.

5.4.3 External particle identification

External, i.e. independent, particle identification (PID) during the beam tests was done by two threshold Cherenkov counters Cherenkov1 and Cherenkov2 (see section 5.3.1). External PID is needed for two purposes.

1. As electrons are ultrarelativistic in the momentum range of PS/T9, the electron hit multiplicity is constant. This is not the case for muons and pions because of their relatively large mass. Therefore, fit results from electron rings are good quantities for systematic studies. In order not to bias the analysis with muon and pion data, clean electron samples are required[14].
2. One major goal of the prototype tests was the determination of the electron pion separation capability. In order to get quantitative results, clean electron and pion samples have to be identified independently from the information provided by the prototype.

Figure 5.16 shows the signals from Cherenkov2 plotted versus those from Cherenkov1 at a particle momentum of 8 GeV/c. The pressure in each of the two Cherenkov counters was adjusted such that electrons leave

---

[14] The easiest and most efficient way to record clean electron samples is to measure at momenta below the muon and pion threshold. This, however, was not possible during the momentum scan and at times due to compromises to be made with other subdetector groups.

signals in both Cherenkov counters, muons only in Cherenkov1, and pions do not make signals in any of the two counters. Accordingly, electrons, muons, and pions can be separated in the data by applying the indicated cuts.

Given the nature of the Cherenkov effect, signals from the different particle species are more difficult to separate for increasing momenta. At high momenta, β of different particles gets more similar. Thus, the radiator pressure has to be regulated more accurately in order to adjust the refractive index n for obtaining the exact Cherenkov thresholds. As a consequence, a clean PID at large particle momentum necessitates tight cuts to the disadvantage of efficiency.

For the determination of the pion suppression from the momentum scan, very clean electron and pion samples are generated by applying tight cuts. As can be seen in Fig. 5.16, pions and muons are close. Thus, the pion cut was restricted to only one bin. Nevertheless, the very clean pion sample still contains muons which manifest as shoulder towards large radii in the prototype distribution of pion radii (see Fig. 5.17 left).

In order to determine the percentage of muons in the pion sample, the so-called pion contamination, the information from the prototype was used. The ring radius distributions for pions and muons in the prototype were fitted individually with gaussian functions. The fit parameters of both fits were then used as start parameters for a fit of the sum of two gaussians to the pion distribution. In Fig. 5.17 (left), it can be seen that the resulting fit approximates the complete radius distribution of the pion sample very well. On the right side, the integrals of the muon and the pion fit functions as illustrated as dotted area. The muon contamination is quantified as the ratio between both integrals. It is found that the pion sample contains $1.4\,\%$ muons.

Taking this muon contamination into account in the calculation of the pion suppression factor is very difficult due to the non-gaussian shape of the tails. As can be seen in the later analysis, it is the non-gaussian contribution of the tails which makes up the number of pions misidentified as electrons (see Fig. 5.28). Therefore, the muon contamination is not taken into account.

5.4.4 Pixel-by-pixel correction for 2011 data

Measurements with LEDs illuminating the whole camera with single photons are used for the determination of the relative detection efficiency of each of the 1024 pixels. The analysis of the LED measurements results in a correction factor for each pixel which is taken into account for the study of WLS films (see section 5.5.6).

The event display of the LED run at 350 nm is shown in Fig. 5.18 (top left). Data is taken at this wavelength because due to their transparency at 350 nm, no effects from the WLS films are expected (cf. absorption spectrum of PT in Fig. 4.2 and *QE* curves in Fig. 4.11). The determination of correction factors is therefore independent from WLS effects.

It can be seen that the LED illumination is smooth but shows a gradient in intensity towards the upper right. In order to compensate the gradient, a global fit on the whole camera was performed. Linear, quadratic and gaussian 2D functions have been used to fit the data. Every fit function has four free parameters which is significantly lower than the number of sampling points. This is a precondition to fit the global gradient of illumination intensity without being sensitive to individual MAPMT efficiency variations. Given the low number of degrees of freedom of the fits, no gradient in the MAPMT efficiency is discernible. It turned out that the gaussian fit exhibits the lowest χ^2 value and is therefore taken to normalise the data. Figure 5.18 (top right) shows the gaussian fit function. The ratio between the entries in the event display and the fit is the correction factor which represents the inverse of the relative single photon detection efficiency and which is shown for every pixel in Fig. 5.18 (bottom left). The correction factors are normalised to an average of 1 in order to be able to compare absolute numbers of hit multiplicity.

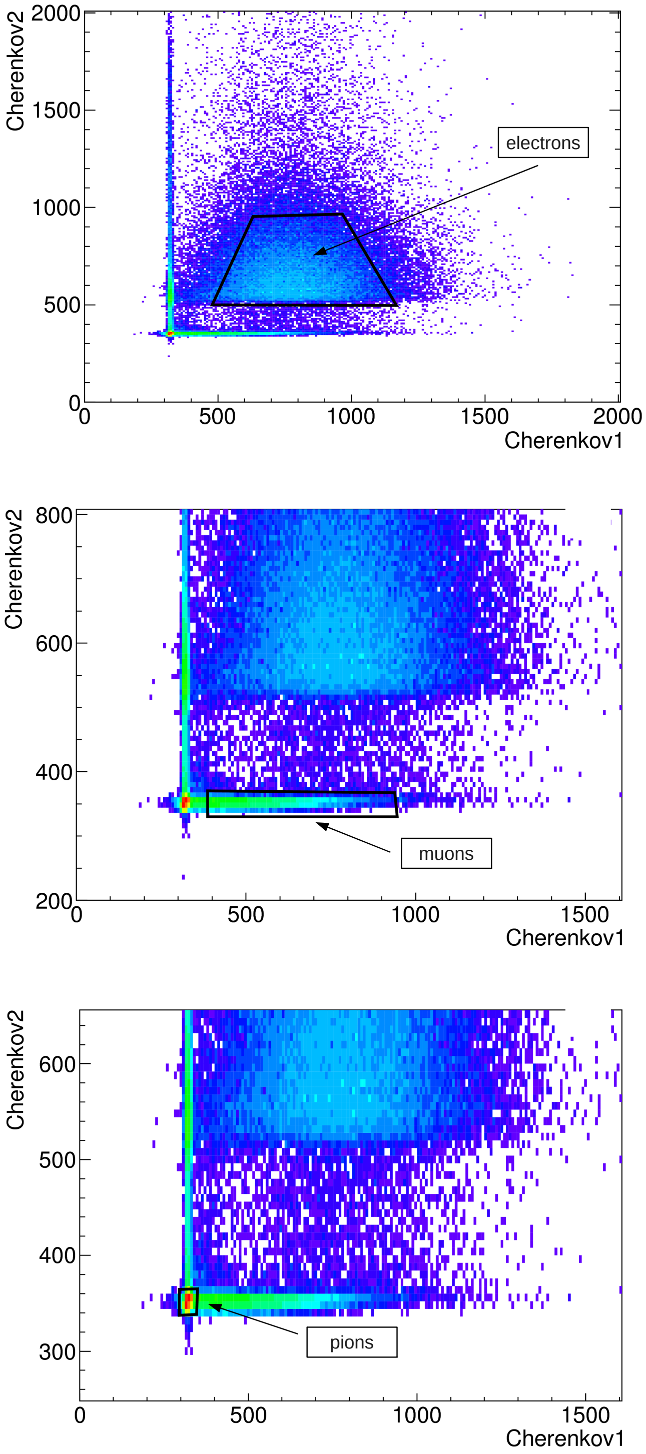

Figure 5.16 – External particle identification using two threshold Cherenkov counters. The plots show signals from Cherenkov2 versus those from Cherenkov1. The pressure of the radiator is adjusted such that electrons leave signals in both counters, muons only in Cherenkov1, and pions do not leave signals. By applying appropriate cuts (shown as black lines), electrons (top), muons (centre), and pions (bottom) can be cleanly separated. Shown here are the signals at 8 GeV/c. With increasing particle momentum, the adjustment of the Cherenkov threshold for the different particle species gets more difficult.

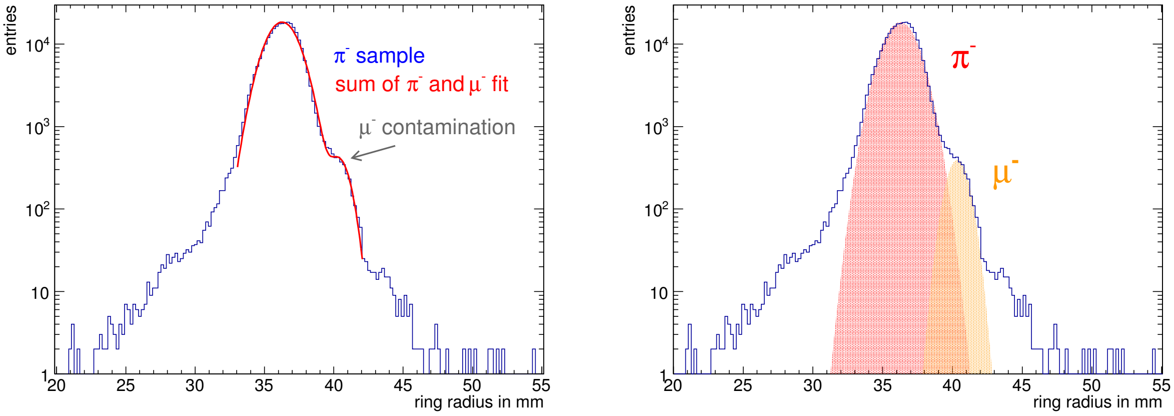

Figure 5.17 – Left: Radius distribution of the pion sample at 8 GeV/c. The muon contamination can be observed as shoulder towards large radii. The red curve is a fit of the sum of two gaussians to the data. The start parameters of the fit are taken from fits of single gaussians to the main peak in the muon distribution and to the main peak in the pion distribution. It can be seen that the pion distribution including the muon contamination is well approximated by the two-gaussian fit. Right: Radius distribution of the pion sample with the single-gaussian fits to the muon and pion distribution. The muon contamination is given by the ration of the two integrals shown here as dotted areas.

In the analysis, correction factors for every pixel will be used. The result shows that the single photon detection efficiency varies by a factor of 1.5 among the pixels of individual MAPMTs.

Also shown in Fig. 5.18 is the correction factor per MAPMT (bottom right) for a comparison to the variation of single photon detection efficiency per MAPMT measured in the laboratory. The difference between best and worst MAPMT in the beam test data is 18 % which is comparable to the result from laboratory data of 16 % (see section 3.10).

It is worth to mention that by definition additional crosstalk hits are considered in the correction factors, i.e. the correction factors shown in Fig. 5.18 are proportional to the single photon detection efficiency and are not biased from crosstalk.

In order to correct hit multiplicities for the tube-to-tube and pixel-to-pixel variation of single photon detection efficiency, the following procedure has been implemented in the RICH processor and is called for every ring:

1. for each single event: identification of pixels belonging to a ring,
2. calculating the arithmetic mean of the correction factors of pixels contributing to the ring,
3. dividing the uncorrected hit multiplicity by the average correction factor,
4. adding the corrected hit multiplicity value to a histogram.

5.4.5 Pressure and temperature correction

As described in section 5.3.4, the effect of WLS films in the 2012 data is evaluated by comparison with a reference measurement done after removing the MAPMTs. The rather long time between the measurements requires a correction for pressure p and temperature T because the refractive index of the radiator varies with these quantities.

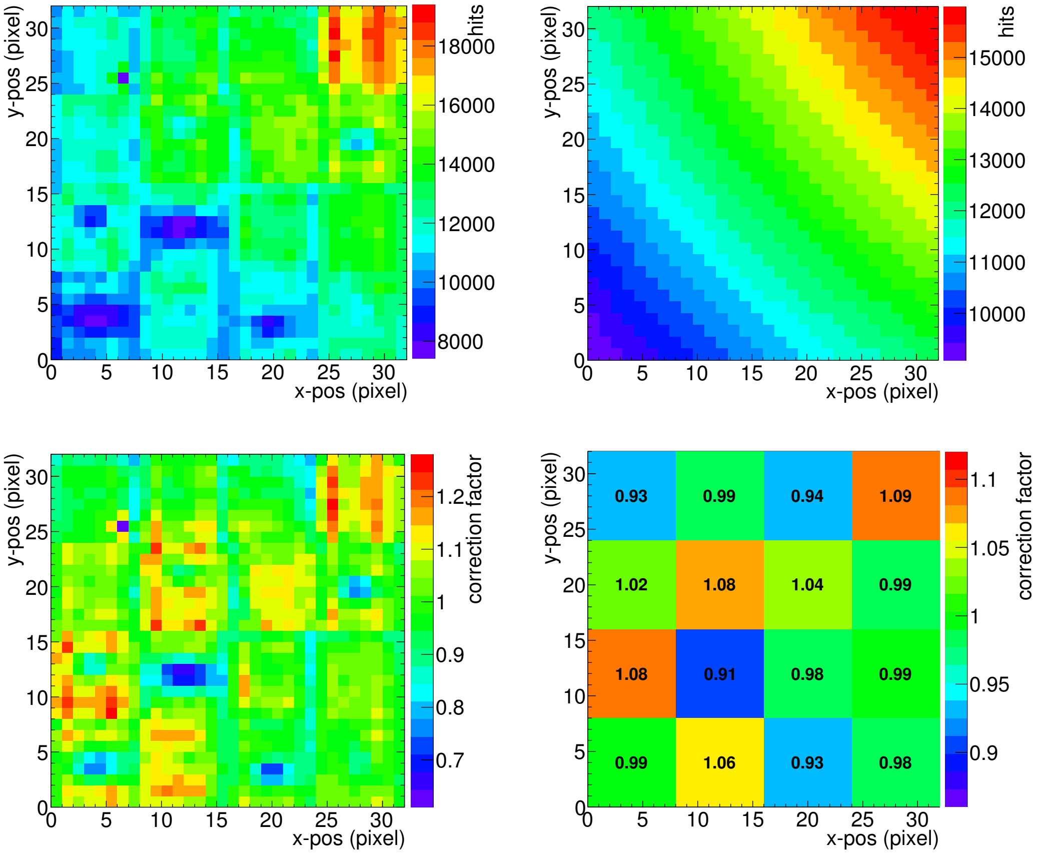

Figure 5.18 – Determination of correction factors for the 2011 camera from LED measurements. Top left: Event display of a LED measurement at 350 nm. Top right: Global fit for correction of the intensity gradient of the LED illumination. Bottom: correction factors for every pixel calculated as ratio between hits in the event display and value of the fit function normalised to an average of 1 (left) and per MAPMT (right).

In addition, the analysis of the momentum scan 2011 requires a p and T correction because the data sets with different momentum were taken over a period of several days and nights.

According to equation (5.1), the refractive index n increases with increasing pressure and decreasing temperature. This behaviour can be understood intuitively when considering the analogy between optical density and mass density. The dependence of n on p and T reads

$$n(p,T) = 1 + (n_0 - 1) \cdot \frac{T_0}{p_0}\frac{p}{T}, \tag{5.1}$$

with $n_0 = 1.00045$ being the refractive index of CO_2 at $\lambda = 600\,\mathrm{nm}$ and standard conditions ($p_0 = 1000\,\mathrm{mbar}$, $T_0 = 273.15\,\mathrm{K}$).

Both the number of generated Cherenkov photons N and the ring radius r on the camera plane depend on the refractive index of the radiator as can be read from equations (5.2) and (5.3) respectively:

$$N(n) = 2\pi\alpha L Z^2 \sin^2\left(\arccos\frac{1}{\beta n}\right) \cdot \int_{\lambda_1}^{\lambda_2} \frac{1}{\lambda^2}\mathrm{d}\lambda, \tag{5.2}$$

$$r(n) = L \cdot \tan\theta_C = L \cdot \tan\left(\arccos\frac{1}{\beta n}\right), \tag{5.3}$$

with L the radiator length, β the incident particle velocity in units of the velocity of light, λ_1 and λ_2 the lower and upper limits of the wavelength interval, to which the photon sensor is sensitive, α the fine structure constant, and Z the charge of the incident particle.

When inserting (5.1) in (5.2) and (5.3), complicated curves for $N(n)$ and $r(n)$ are found. However, since $n - 1 \ll 1$ for CO_2, the number of produced Cherenkov photons and the ring radius is quasi linear in n.

When correcting the data, a common value for p and T has to be chosen. Because results will be compared to simulations done for standard conditions, the data is corrected to $p = 1000\,\text{mbar}$ and $T = 273.15\,\text{K}$.

5.4.6 Electron pion separation

The separation of electrons and pions is the major task of the CBM-RICH detector and was tested in dependence of the particle momentum with the prototype during the beam test 2011. The pion suppression factor is defined in section 2.4.1 as number of pions which are reconstructed in the STS and have a track projection lying in the RICH acceptance divided by the number of such pions which are misidentified as electrons.

The definition for the prototype has to be slightly modified due to absence of the STS. In the context of prototype measurements, the pion suppression factor π_{suppr} is the number of pions which are identified in Cherenkov1 and Cherenkov2 and generate a ring in the prototype divided by the number of such pions identified as electrons according to a condition on the ring radius in the prototype. A pion suppression factor of $\pi_{\text{suppr}} = 5000$ for instance signifies that 1 out of 5000 pions is misidentified as electron.

The pion efficiency $\pi_{\text{eff}} = 1/\pi_{\text{suppr}}$ can be understood as number of pions creeping under the electron peak in the radius distribution and being misidentified as electrons divided by the number of all pions (see Fig. 5.28). To determine the pion efficiency, the electron efficiency e_{eff} is set to 95 %, i.e. the electron cut in the radius distribution is done such that it includes 95 % of all electrons. Choosing a larger electron efficiency means a wider electron cut which results in a lower separation capability between electrons and pions because more pions are lying under the electron peak.

The determination of π_{eff} and π_{suppr} is based on the selection of clean pion and electron samples using the two threshold Cherenkov counters. The procedure is the following.

1. Generation of clean electron and pion samples by cutting on signals from Cherenkov2 and Cherenkov1.
2. Pressure and temperature correction of electron and pion radius distributions according to equation (5.1).
3. Definition of electron cuts at $\pm k\sigma$ around μ with μ and σ being the mean and width of a gaussian fit to the electron radius distribution. The factor k is adjusted such that 95 % of all electrons are within the interval $\mu \pm k\sigma$. Depending on the momentum, k can vary slightly for different data samples.
4. Calculation of π_{eff} as ratio between the number of pions within the interval $\mu \pm k\sigma$ and the number of all pions.

5.5 Results from the 2011 beam test

During the beam tests at the T9 beam line at the CERN PS, clean Cherenkov rings could be detected as can be seen in the upper left panel of Fig. 5.19. Also shown are integrated rings of electrons, muons, and pions at 6 GeV/c whose different radii become apparent.

It can be observed that the rings in the integrated event display are somewhat blurred. The reason is the beam divergence. While a parallel translation of the beam results in an unchanged ring position, it changes as function of the incident angle of the beam particles. However, the fuzziness of the integrated ring display is irrelevant in the data analysis since always single events are fitted.

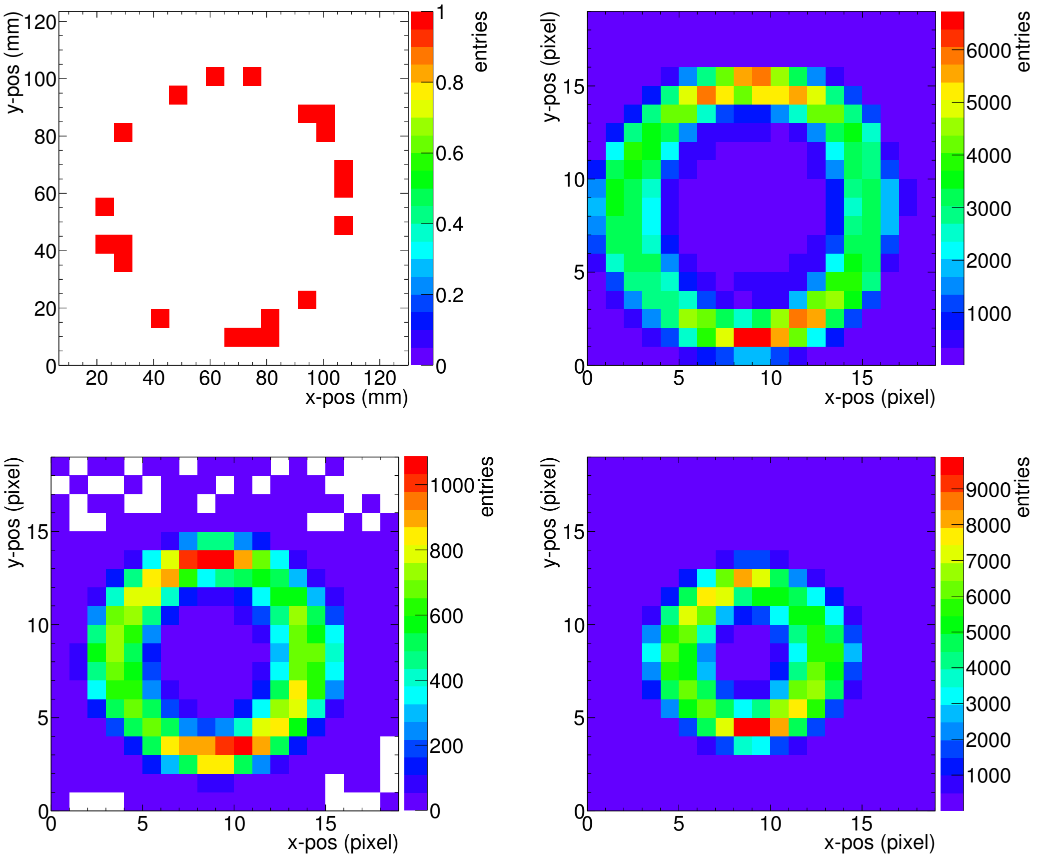

Figure 5.19 – Electron ring from a typical single event (top left), event-integrated ring images from e^-, μ^-, π^- at 6 GeV/c (top right, bottom left, bottom right).

5.5.1 Ring radius and ring centre

Depending on the position of the Cherenkov ring on the camera, the electron ring radius extracted from the beam test data is 4.56 cm to 4.67 cm. Figure 5.20 shows the distributions of ring radii for electrons and pions at a particle momentum of 8 GeV/c. The ring resolution, given as ratio between the sigma and the mean of a gaussian fit, is $1.3\,\%$ for electron rings and $3.0\,\%$ for pion rings.

The measured ring resolution for electron rings with ≈ 22 photoelectrons is in very good agreement with the theoretical expectation discussed in section 2.5.2: Considering that no magnetic field was present in the radiator volume during the beam tests, equation (2.11) yields an expected ring resolution of $1.1\,\%$.

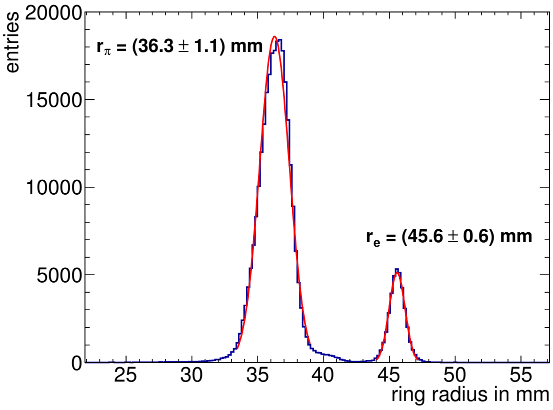

Figure 5.20 – Distribution of fitted electron and pion radii at 8 GeV/c. The numbers state mean and sigma of gaussian fits to the data. The fits are indicated by the red curves.

The centre of the fitted rings is used to check the reproducibility of setting the ring position by rotating the focusing mirror. Figure 5.21 shows the distribution of x and y-coordinates of the fitted ring centres for two runs with the same ring position (position A). Between both runs, the mirror was rotated many times to different ring positions. The variation of the ring centre in both x and y-direction is not larger than 0.1 mm which shows that the setting of ring positions is reproducible.

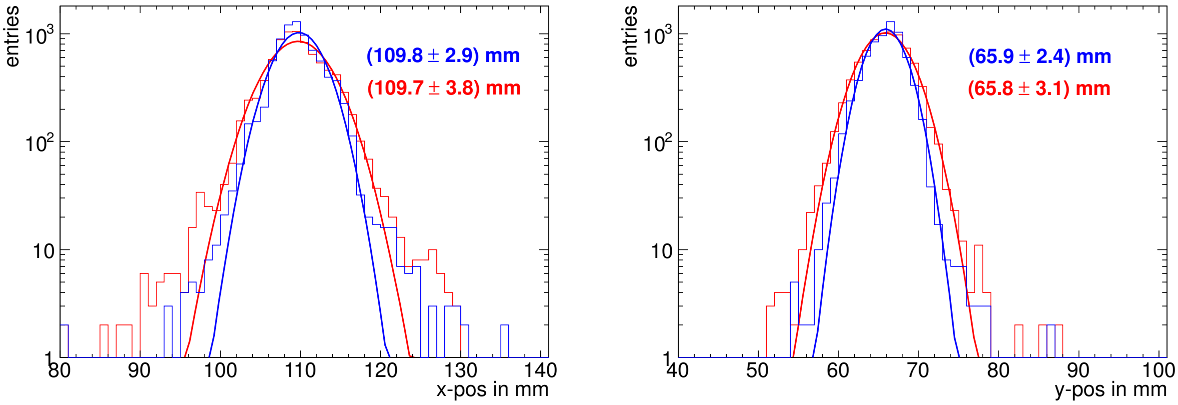

Figure 5.21 – Reproducibility of ring positions. Shown are the distributions of fitted ring centres for two runs at the same ring position (run197 in red and run326 in blue). Between both runs, five days have passed and the focusing mirror was moved many times. The left plot shows the x-coordinate, the right plot the y-coordinate. Gaussian fits to the distribution indicate that the ring centre does not change by more than 0.1 mm. Given values denote mean and sigma of the gaussian fits to the data. It can be concluded that the setting of ring positions by rotating the mirror is reproducible.

5.5.2 Hit multiplicity

In a RICH detector, the dependence of the ring finding efficiency and the ring fitting quality on the number of detected photoelectrons per ring makes the latter an important quantity. In the following, this quantity will be called hit multiplicity. For electrons it is constant for all momenta at the PS/T9 beam line when using a CO_2 radiator at normal pressure. Therefore only electrons, which are identified with the two threshold Cherenkov counters, are considered in the study on hit multiplicity.

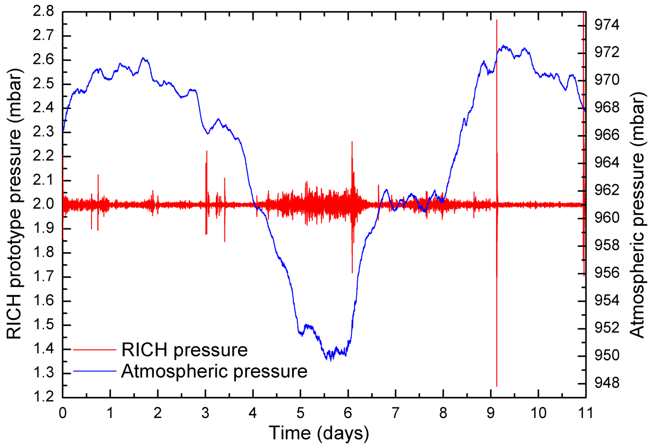

Figure 5.22 – Atmospheric pressure and pressure in the RICH prototype (top) during the 2011 beam test as measured with the gas system. Figure taken from [146].

In this thesis, hit multiplicity refers to the number of hits after ring finding and fitting. This is true for data presented in this chapter and for simulations presented in chapter 6. The number of hits after ring finding typically differs from the number of hits per event which includes hits excluded by the ring finder like e.g. additional noise hits which are in principal uncorrelated in time or electronic crosstalk but also real hits due to stray light. The given hit multiplicities include additional crosstalk hits in both data and simulation.

As a result of the statistical nature of single photon detection, the hit multiplicity distribution follows a poisson statistics if no boundary conditions prevail. In the case of a perfect poissonian distribution, the width of the hit multiplicity distribution should be given by $\sqrt{\lambda}$ with λ being the mean. As can be seen in Fig. 5.25, this condition is nearly satisfied.

Given the large mean value < 20, the hit multiplicity distribution can be well approximated by a gaussian whose mean value will be stated throughout this thesis as hit multiplicity. The error on the fit parameters is $< 0.5\,\%$ for the mean and $< 2.4\,\%$ for sigma.

The absolute hit multiplicity as measured with H8500D-03 MAPMTs at PS/T9 (temperature ca. $20\,°\mathrm{C}$, pressure ca. $960\,\mathrm{mbar}$) is ≈ 22 photoelectrons per ring (see Fig. 5.25). This number is in agreement with earlier performance studies [120] and is a direct verification of the CBM-RICH concept.

A hit multiplicity of 22 photoelectrons leads to a figure of merit of $N_0 = 145\,\mathrm{cm}^{-1}$.

More detailed studies on hit multiplicities will be discussed in the following sections.

5.5.3 Dependence of ring radius and hit multiplicity on the refractive index

During the beam test 2011, temperature and pressure varied with weather conditions. In Fig. 5.22 the atmospheric pressure and the pressure in the RICH prototype is shown as function of time. It can be seen that the differential pressure in the detector was stabilised at a level of $(2.00 \pm 0.15)\,\mathrm{mbar}$ although the barometric pressure changed in the range of 37 mbar.

Figure 5.23 shows the ring radius r and the hit multiplicity N_{det} as function of n, which is calculated according to equation (5.1). The red curves show the expected curves $r(n)$ and $N_{\mathrm{det}}(n)$ given in equations (5.3) and (5.2) normalised[15] to the data points at $n = 1.000398$. The variation of r and N_{det} with n shows good agreement between data and expectations and hence it can be concluded that the system is understood and under control.

---

[15] Due to the normalisation, gas absorption, mirror reflectivity, and quantum efficiency of the photon sensors can be neglected.

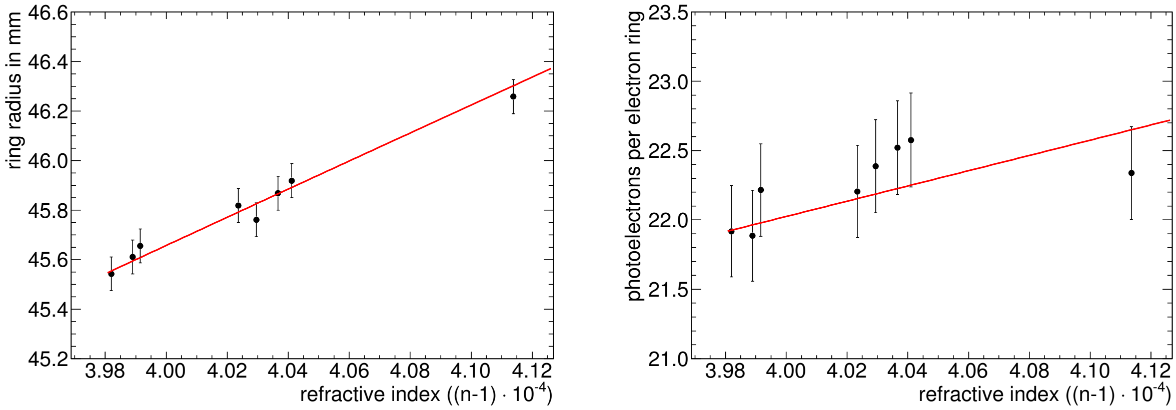

Figure 5.23 – Radius (top) and hit multiplicity (bottom) of electron rings as function of refractive index of the radiator gas. Error bars of the data points are those derived in section 5.5.4. The red lines indicate the slope expected from theory (equation (5.3) and (5.2)) taking into account the geometry of the prototype. The red lines are scaled to the data point at $n = 1.000398$. Note that the lines are not fits to the data.

5.5.4 Stability of ring radius and hit multiplicity

For the evaluation of results in terms of ring radius and hit multiplicity, the stability of these quantities has to be determined. This is done by comparing results from runs with the same detector settings (ring position, ADC threshold, HV) and with temperature and pressure correction. For the 2011 data, both the stability of ring radius and hit multiplicity is studied.

Figure 5.24 shows the difference between the measured value and the calculated value of ring radius and hit multiplicity in percent of the calculated value. The maximum of this difference will be called variation. The latter is calculated according to equation (5.2) and (5.3). For the refractive index, pressure and temperature from the corresponding run are taken into account.

It is found that the ring radius varies by $0.15\,\%$, the hit multiplicity by $1.5\,\%$ at most. The relatively large variation of hit multiplicity compared to that of the ring radius shows that the ring fitting results do not depend on the absolute hit multiplicity on that level. This supports the fact that the ring finding efficiency, defined as the number of events in which at least one ring was found divided by the number of events with at least one hit, is close to $100\,\%$ for events with more than 18 hits [6].

The results show that the variation of the mean values between different runs is larger than the errors of the fit parameters stated in section 5.5.2. Therefore, the variation of the mean values derived here will be used in the following as errors when comparing results in terms of ring radius and hit multiplicity.

5.5.5 Comparison between H8500D-03 and H10996A-103

For the comparison of different MAPMT types, the correction factors deduced from LED measurements are set to 1, since exactly the individual MAPMT differences are of interest here. It is this tube-to-tube variation which is balanced by the correction factors for comparison of WLS effects using different MAPMTs in chapter 5.5.6.

It is foud that the hit multiplicity on ring position C with two H8500D-03 and two H10996A-103 MAPMTs (see section 5.3.4 and Fig. 5.14) is $(7.7 \pm 1.4)\,\%$ lower than that of the reference position F.

This illustrates that, for the used signal attenuation, the higher quantum efficiency of the SBA photocathode does not compensate the lower gain of the 8 dynode stages. This observation is in line with earlier laboratory

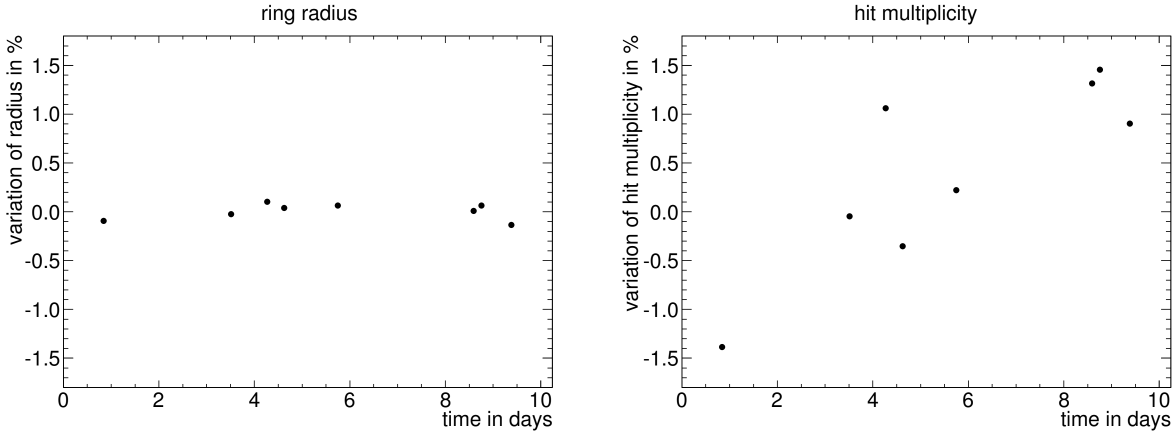

Figure 5.24 – Stability of ring radius and hit multiplicity during the 2011 beam test. Each data point corresponds to one run. Shown are the difference between the measured value and the calculated value of ring radius (left) and hit multiplicity (right) in percent of the calculated value. The calculation takes into account pressure and temperature of the runs. In the case of the hit multiplicity, a systematic increase with time might be observable. The origin of that effect is unclear. A correlation with the gas purity was ruled out [147].

measurements which also showed a significantly worse performance of the 8-stage MAPMTs in particular considering the single photoelectron spectrum. The result might be influenced by the attenuation factor chosen for the attenuator boards which damp the MAPMT signals by a factor of about 22 (see section 5.2.3). To gain more knowledge on the 8-stage MAPMTs, the attenuation factor for this MAPMT type was reduced in the 2012 beam test. The analysis, however, is not in the scope of this thesis.

5.5.6 Hit multiplicity with and without WLS films

Consistency check with reference ring positions

Figure 5.25 (left) shows the hit multiplicity for runs with ring position D and F. Both are equipped with the same type of MAPMTs and should thus exhibit the same hit multiplicity. It differs by 2 photoelectrons per electron ring. On the right panel of Fig. 5.25, the hit multiplicity is shown taking into account the pixel-by-pixel correction factor from the LED measurements for correction of tube-to-tube variations. It can be seen that after the correction, hit multiplicities from position D and F agree as it is expected. This shows that the application of the correction factors produces a consistent result. It is worth to mention that the correction does not simply shift the histograms along the x-axis. The appropriate correction factor is rather applied to each ring before filling the histogram (see section 5.4.4).

Quasi-simultaneous measurement

Figure 5.26 shows the distribution of hit multiplicity of position H (WLS) and the reference F (no WLS). Correction factors deduced from LED measurements are taken into account. In addition, position G was measured, which covers two coated and two uncoated MAPMTs.

The efficiency corrected hit multiplicity at position F, G, H, i.e. bare, half coated, and coated MAPMTs is (22.2 ± 0.3), (23.7 ± 0.4), (24.9 ± 0.4) photoelectrons per electron ring, respectively. This corresponds to a relative increase of $(6.8 \pm 1.6)\,\%$ for the half coated and $(12.2 \pm 1.7)\,\%$ for the coated position when compared to the uncoated one. The results are summarised in Tab. 5.3.

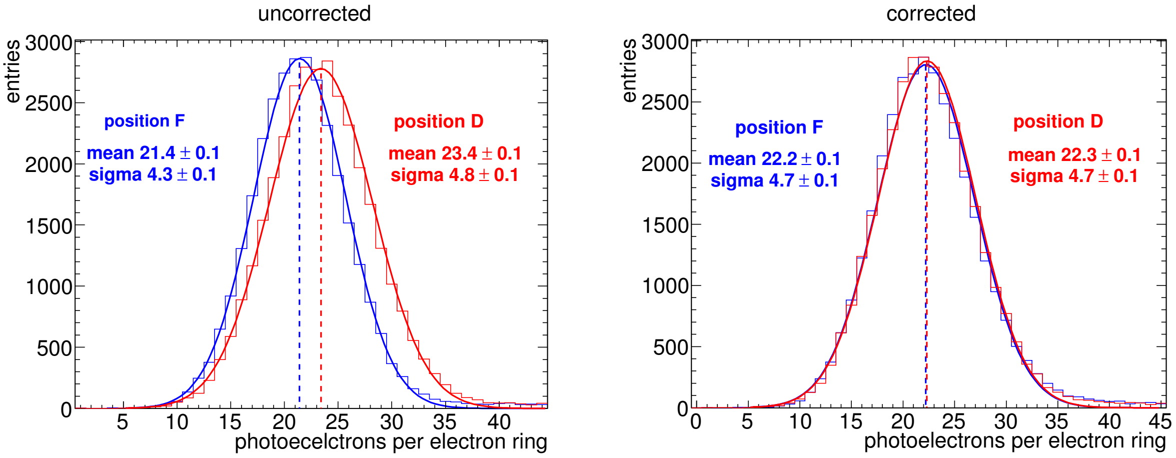

Figure 5.25 – Uncorrected (left) and corrected hit multiplicity (right) of reference ring positions D and F measured during the beam test 2011. The correction is based on the extraction of correction factors from LED measurements and reflects the tube-to-tube variation of the single photon detection efficiency. Uncorrected hit multiplicities differ by 2 photoelectrons per electron ring whereas the corrected values are equal within errors. This shows that the result is consistent only after applying the correction.

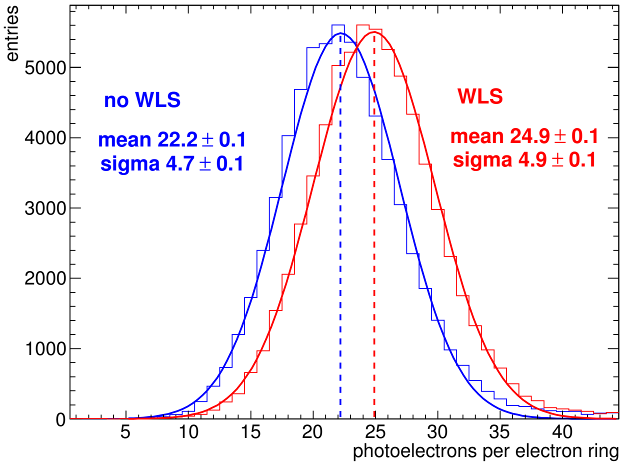

Figure 5.26 – Hit multiplicity distribution with and without WLS films measured during the beam test 2011.

5.5.7 Electron pion separation

Figure 5.27 shows the ring radius versus incident particle momentum. The data sets at different momenta were taken over a period of five days. Pressure and temperature varied which causes varying ring radii clearly visible for electrons on the left plot of Fig. 5.27. A p and T correction according to equation (5.1) is performed and is the basis for the further analysis. On the right plot, it can be observed that the correction aligns the electron radii at all momenta.

Figure 5.28 depicts a projection of Fig. 5.27 along the radius axis at 10 GeV/c. By using the two threshold Cherenkov counters for PID, electrons and pions can be separated and are marked in blue and red respectively.

Electron identification is done by applying a cut $\mu_e \pm k\sigma_e$ around the mean of a gaussian fit to the electron peak as described in section 5.4.6. In Fig. 5.28, the value for k is chosen such that $e_{\text{eff}} = 95\,\%$. Pions within

ring position	photocathode material	no. of dynodes	WLS	hit multiplicity	rel. to ring position F
F	BA	12	no	22.2 ± 0.3	–
D	BA	12	no	22.3 ± 0.3	$(+0.5 \pm 1.5)\,\%$
G	BA	12	1/2	23.7 ± 0.4	$(+6.8 \pm 1.6)\,\%$
H	BA	12	yes	24.9 ± 0.4	$(+12.2 \pm 1.7)\,\%$
C	SBA/BA	8/12	no	20.4 ± 0.3	$(-7.7 \pm 1.4)\,\%$

Table 5.3 – Hit multiplicities for different ring positions on the 2011 camera. Pixel-by-pixel and tube-to-tube variations of the single photon detection efficiency are corrected as described in section 5.4.4. Compared to H8500D-03 MAPMTs (position F and D), the hit multiplicity is lower when using H10966A-103 MAPMTs (position C). The usage of WLS films increases the hit multiplicity by $(12.2 \pm 1.7)\,\%$.

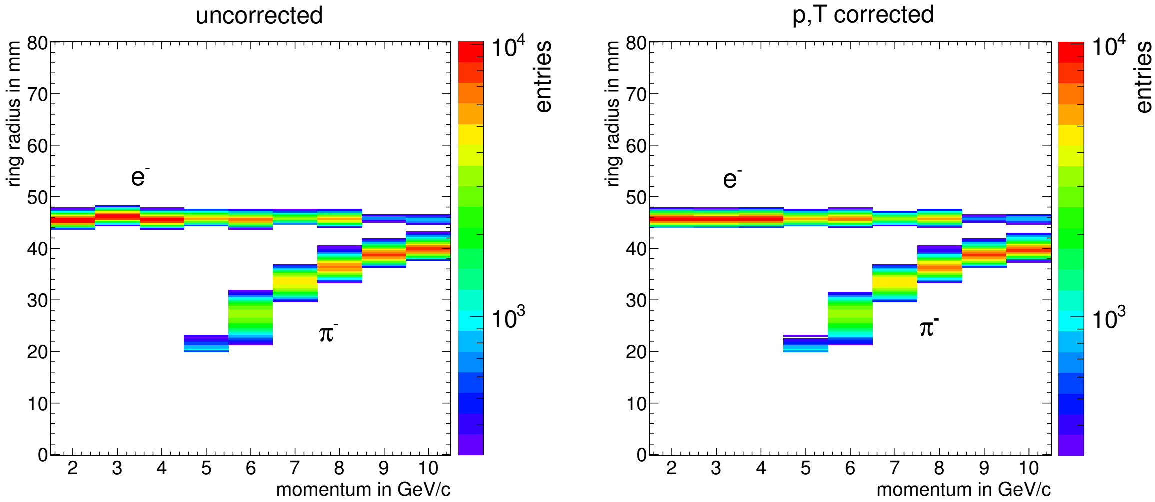

Figure 5.27 – Radius versus momentum for a mixed beam of electrons and pions without correction (left) and with correction for p and T (right). Data from the momentum scan in steps of 1 GeV/c is shown. Electron rings show constant radii of $\approx$ 46 mm over the whole momentum range after p and T correction. From 2 GeV/c to 4 GeV/c, only entries from electrons can be seen because pions are below the Cherenkov threshold. The pion radii are small at 5 GeV/c with $\approx$ 20 mm and increase towards larger momenta. Electron and pion radii come closer with increasing momentum and the separation between electrons and pions gets more and more difficult. Radii below $r = 20$ mm are omitted.

the cut are misidentified pions. The ratio between the number of all pions and the number of misidentified pions is the pion suppression factor π_{suppr}.

The pion suppression factor is shown in Fig. 5.29 as function of momentum. It is monotonically decreasing with increasing momentum which can be understood since the pion radius comes closer to the electron radius. The numerical values are given in Tab. 5.4. For momenta $<$ 7 GeV/c the pion suppression factor cannot be calculated due to too low statistics. At 7 GeV/c, only four misidentified pions are found in the data set of $\approx$ 34000 pions. At lower momenta, no misidentified pions are found.

The electron efficiency depends on the width of the cut in the electron radius distribution given by the parameter k. The same holds true for the number of misidentified pions. Hence, the pion suppression factor depends on the electron efficiency. In Fig. 5.30, the pion suppression factor is plotted for electron efficiencies between 93 % and 99 %. A general trend can be observed: the larger e_{eff}, the lower π_{suppr}. In

momentum p	π_{suppr} at $e_{\text{eff}} = 93\,\%$	π_{suppr} at $e_{\text{eff}} = 95\,\%$	π_{suppr} at $e_{\text{eff}} = 99\,\%$
7 GeV/c	11307	8481	2827
8 GeV/c	4509	3714	435
9 GeV/c	4026	2684	169
10 GeV/c	1144	740	4.9

Table 5.4 – Pion suppression factors of the CBM-RICH prototype between 7 GeV/c and 10 Gev/c at 93 % to 99 % electron efficiency. The electron pion separation capability decreases with increasing momentum and increasing electron efficiency.

detail, for $e_{\text{eff}} = 93\,\%$ the pion suppression factor is $\pi_{\text{suppr}} = 11307$ at 7 GeV/c and $\pi_{\text{suppr}} = 1144$ at 10 GeV/c whereas for $e_{\text{eff}} = 99\,\%$ it is $\pi_{\text{suppr}} = 2827$ at 7 GeV/c and $\pi_{\text{suppr}} = 4.9$ at 10 GeV/c (see Tab. 5.4).

On the one hand, the pion suppression factors extracted from the beam test data are pessimistic because up to $1.4\,\%$ muons are contained in the pion sample (see section 5.4.3). Since muon radii are between those of electrons and pions, muons in the pion sample are likely to be within the electron cut and therefore identified as misidentified pions.

On the other hand, the pion suppression extracted from beam test data quantifies the electron pion separation capability for a very low hit occupancy of the camera. The pion suppression factors for high occupancies are lower (see section 6.5).

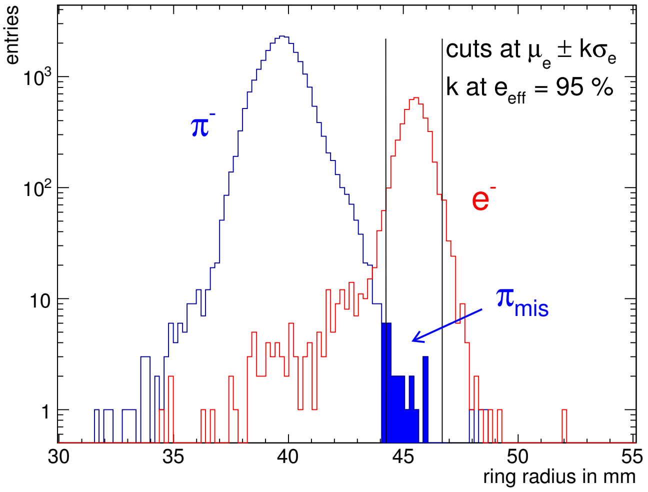

Figure 5.28 – Radius distribution of electrons and pions at 10 GeV/c. PID is done with the two threshold Cherenkov detectors. In the prototype, particles with a radius within the cuts at $\mu_e \pm k\sigma_e$ are identified as electrons. Here, k is adjusted such that electrons within the cuts add up to 95 % of all electrons. Pions within this range are misidentified as electrons. The pion suppression factor is given by the ratio of the number of all pions to the number of misidentified pions.

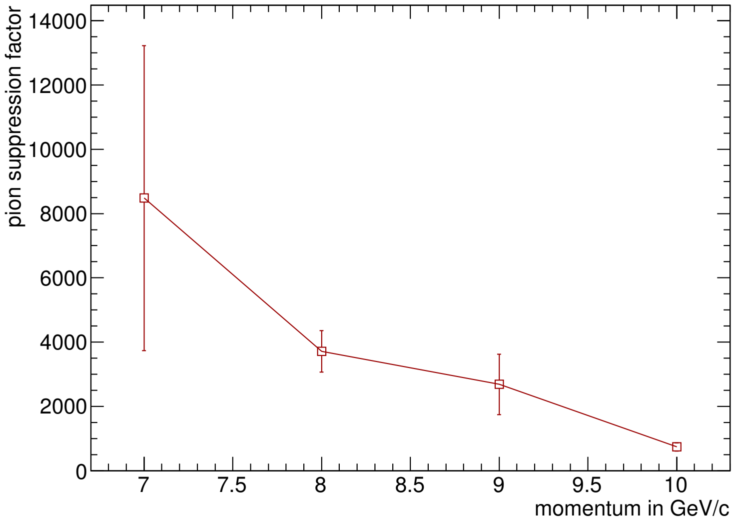

Figure 5.29 – Pion suppression factor at $e_{\text{eff}} = 95\,\%$ in dependence of momentum measured with the RICH prototype. A monotonous decrease with momentum is observed because pion radii increase and almost converge with the electron radius at $10\,\text{GeV/c}$. Hence, the separation capability of the detector decreases. Error bars are statistical only. The error bar at $7\,\text{GeV/c}$ is relatively large because only four misidentified pions are found in the data set. The relatively small error bar at $8\,\text{GeV/c}$ is due to the big data set from a run of $\approx 4\,$hours. Lines between the data points are drawn to guide the eye.

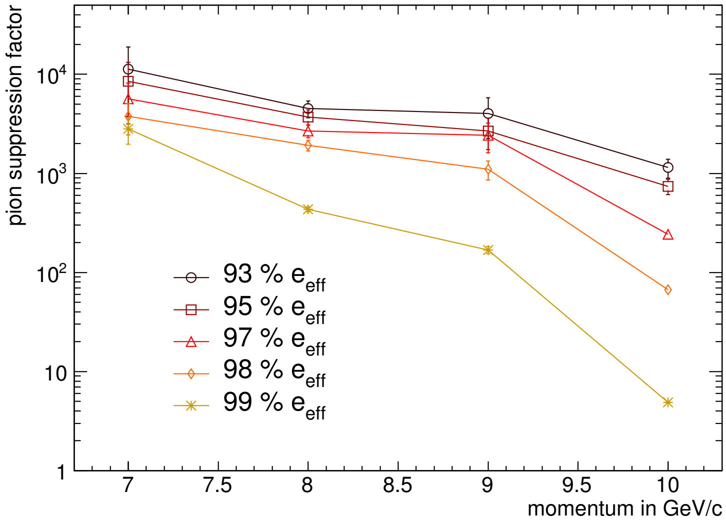

Figure 5.30 – Momentum dependent pion suppression factor of the RICH prototype for electron efficiencies between $93\,\%$ and $99\,\%$ in logarithmic scale. The curve at $95\,\%$ electron efficiency (squares) corresponds to the curve shown in Fig. 5.29 Error bars are statistical only. Lines between the data points are drawn to guide the eye.

5.6 Results from the 2012 beam test

5.6.1 Stability of hit multiplicity

The stability of hit multiplicity for reference position A was monitored between the runs with and without WLS films using different ring positions. In Fig. 5.31 the measured hit multiplicity between run 21 and run 92 is shown. In addition, the hit multiplicity corrected for pressure and temperature as described in section 5.4.5 is plotted. The correction slightly smoothes the values. In contrast to the p, T correction discussed in the previous sections, here the data is normalised to standard conditions. Because of that, the average hit multiplicity increases from 22.5 to 25.2 photoelectrons per electron ring (+12 %). The relative increase corresponds to the factor

$$\frac{p_0}{T_0} / \frac{p}{T} = 1.12 \tag{5.4}$$

with standard pressure $p_0 = 1000\,\text{mbar}$, standard temperature $T_0 = 273.15\,\text{K}$, and average conditions in the cave, $p = 960\,\text{mbar}$, $T = 293\,\text{K}$.

The relative standard deviation of the p and T corrected hit multiplicity of the reference position A is $0.91\,\%$. This value is taken as error on the hit multiplicity for the 2012 data.

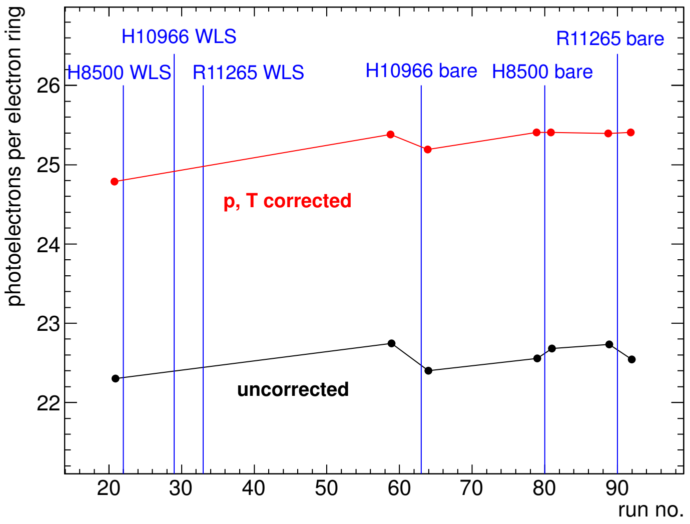

Figure 5.31 – Stability of hit multiplicity in the 2012 data used for the WLS analysis. Shown in black is the uncorrected hit multiplicity of seven runs with reference position A. The red dots show the hit multiplicity of these runs after pressure and temperature correction according to equation (5.1). The vertical lines indicate the runs of data taking with and without WLS films on different types of MAPMTs.

5.6.2 Hit multiplicity with and without WLS films

The effect of WLS films on different types of MAPMTs is determined from consecutive measurements with and without WLS films on the ring positions illustrated in Fig. 5.14.

In contrast to the 2011 data presented in section 5.5.6, no comparison of the hit multiplicity from rings completely covering coated and completely covering uncoated data is feasible. The reason is the fact that only $4/8$ of MAPMTs on position I were initially coated and one MAPMT respectively two MAPMTs remained coated for the reference measurement on position C and K respectively position E after WLS removal[16] (see Fig. 5.14).

Therefore, the relative difference between the p, T corrected hit multiplicities with and without WLS film has to be weighted with the fraction of coated to uncoated MAPMTs of the respective measurement.

The result in terms of p and T corrected hit multiplicity is summarised in Tab. 5.5. The relative error is calculated by propagating the absolute errors of the measured hit multiplicities. The relative increase is the following:

1. $(21.2 \pm 1.4)\,\%$ for H10966A-103,
2. $(18.2 \pm 1.5)\,\%$ for H8500D-03,
3. $(18.0 \pm 1.4)\,\%$ for R11265-103-M16.

This hierarchy is expected from the *QE* curves of WLS films on the respective MAPMT types as discussed in section 4.6.

To cross-check the data, more ring positions with and without WLS films on H8500D-03 MAPMTs, namely B and K, are analysed. The relative increase is $(18.1 \pm 1.6)\,\%$ for position K and $(16.7 \pm 1.4)\,\%$ for position B which is well in agreement with the result from position C within errors.

The relative increase of hit multiplicity due to WLS films on H8500D-03 MAPMTs determined from the 2011 beam test data ($(12.2 \pm 1.7)\,\%$, see section 5.5.6) is lower than 2012 ($(18.2 \pm 1.5)\,\%$) as a result of the inferior performance of the WLS films seen already in the *QE* curves in Fig. 4.11.

5.6.3 Ring sharpness

When using WLS films on the MAPMTs, two effects can lead to a decrease of the ring sharpness.

1. Isotropic fluorescence:
   Due to the isotropic fluorescence of WLS films, the majority of wavelength shifted photons pass the MAPMT front window under a more inclined angle than without WLS film. Because the window has a certain thickness, the photon will thus enter the photocathode at a different position compared to the point of incidence on the window surface and the ring sharpness is therefore expected to decrease.
2. Chromatic dispersion:
   Since chromatic dispersion is more pronounced in the UV range (see section 2.5.1), the enhanced UV sensitivity with WLS coating may lead to a decrease in ring sharpness.

The ring sharpness is quantified by the parameter *dR* which is the RMS of the distribution of the distance between each hit and the ring fit (see section 2.6). Figure 5.32 shows such distributions for rings measured on position F and H during the beam test 2011 (left) and on position C 2012 (right). In both cases, *dR* increases by $0.3\,\text{mm}$ at $r = 45.6\,\text{mm}$ for WLS coated MAPMTs corresponding to a decrease of ring sharpness. This, however, is small compared to the absolute value of $dR = 2.4\,\text{mm}$. The increase is not significant compared to the granularity of the MAPMTs (pixel size of $6.125\times6.125\ \text{mm}^2$).

The decrease of the ring sharpness due to the use of WLS films on the MAPMT windows is therefore no criterion for exclusion.

---

[16] Data after the second WLS removal is not included in the analysis because it turned out that the hit multiplicity on the reference position changed by ≈ 0.7 photoelectrons per electron ring which is roughly twice as much as the variation seen in Fig. 5.31. Using this data would increase the error on the determined hit multiplicity.

MAPMT type	run no.	absolute hit multiplicity	fraction of coated MAPMTs	$1/f$	relative increase WLS / no WLS
R11265-103-M16	33 (pos. I)	26.7 ± 0.2	4/8	2	$(18.0 \pm 1.4)\,\%$
	90 (pos. I)	24.5 ± 0.2	0/8		–
H8500D-03 (2011)	20 (pos. H)	27.6 ± 0.4	4/4	1	$(12.2 \pm 1.7)\,\%$
	21 (pos. F)	24.6 ± 0.3	0/4		–
H8500D-03	22 (pos. C)	28.3 ± 0.3	4/4	$4/3$	$(18.2 \pm 1.5)\,\%$
	80 (pos. C)	24.9 ± 0.2	1/4		–
H8500D-03	32 (pos. K)	4.83 ± 0.04	1/1	1	$(18.1 \pm 1.6)\,\%$
	93 (pos. K)	4.09 ± 0.04	0/1		–
H8500D-03	17 (pos. B)	27.2 ± 0.2	2/4	2	$(16.7 \pm 1.4)\,\%$
	78 (pos. B)	25.1 ± 0.2	0/4		–
H10966A-103	29 (pos. E)	7.77 ± 0.07	1/1	1	$(21.2 \pm 1.4)\,\%$
	63 (pos. E)	6.41 ± 0.06	0/1		–

Table 5.5 – Increase of hit multiplicity on different types of MAPMTs due to the usage of WLS films during the 2012 beam test. f is the fraction of coated to uncoated MAPMTs of the respective measurement. The relative increase in the last column is calculated by multiplying the relative difference of hit multiplicity by $1/f$. The error of the relative increase is calculated by propagating the errors of the absolute hit multiplicities. For comparison with the 2011 data, the value from Tab. 5.3 is listed here with p, T correction.

The influence of charge sharing between pixels on the ring sharpness seems to be rather low with respect to the results presented in section 4.5 for multi photon pulses. This can be understood when considering two facts. First, for the detection of single photons the amplitude threshold cuts part of the crosstalk. Second, *dR* roughly corresponds to already half of the pixel size and the fraction of photons which are both shifted to larger wavelengths and emitted under large angles does not significantly increases *dR*.

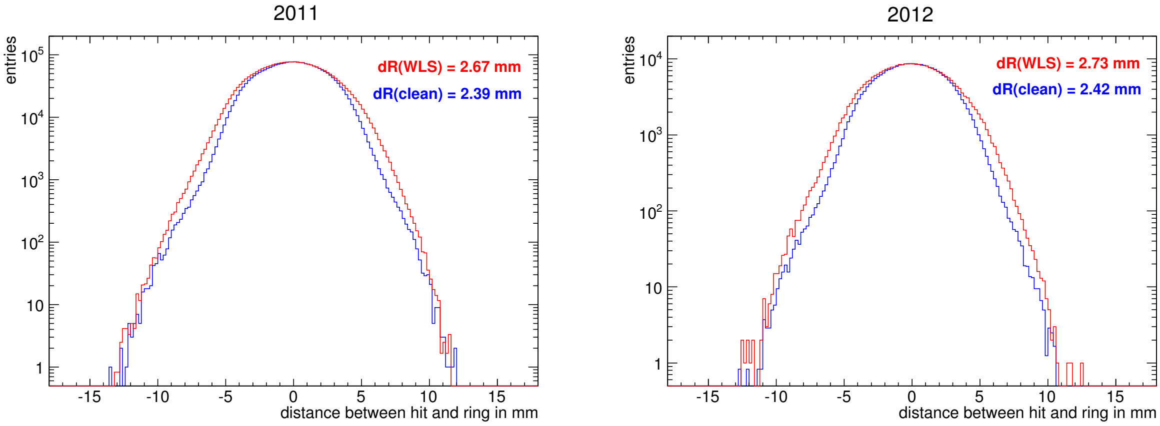

Figure 5.32 – Ring sharpness with and without WLS films in beam test data 2011 (left) and 2012 (right). The parameter *dR* is the RMS of the distribution of the distance between hits and the fitted ring. It is measurably larger when using WLS films. However, the increase is negligible when compared to the MAPMT pixel size of $6.125 \times 6.125\ \text{mm}^2$.

5.7 Summary

A real-size prototype detector was constructed in a joint venture by all groups of the CBM-RICH collaboration. The contribution of the Wuppertal group was the development of the photon camera. During two successful beam test campaigns at the CERN PS, clean Cherenkov rings with a very low noise level could be detected and were the basis for systematic studies of the prototype performance.

The online monitoring software Go4 was adapted to map the data from the front-end boards to the camera display and to generate hit arrays as input for the ring finding and fitting algorithms.

Two types of correction schemes were developed for the data analysis. Firstly, a pixel-to-pixel and tube-to-tube variation of the single photon detection efficiency of MAPMTs of the same type was needed. For this purpose, a correction factor for each pixel of the camera was determined from a global and homogeneous single photon illumination with LEDs.

Secondly, the influence of pressure and temperature on the refractive index of the radiator was studied. It could be shown that the dependence of ring radius and hit multiplicity on the refractive index and hence on pressure and temperature is exactly as expected from theory. This is the precondition for the normalisation of data from different runs to common conditions in order to allow comparison.

From the data analysis of the 2011 beam test, it can be deduced that the 8 dynode stage MAPMTs with SBA photocathode (H10966A-103) see less photons than MAPMTs with 12 dynode stages and BA photocathode (H8500D-03). This means that the increased quantum efficiency of the SBA photocathodes does not compensate the lower detection efficiency of 8 stage MAPMTs when using the attenuator boards from the 2011 setup.

The data analysis of the 2011 and 2012 beam tests reveals a conclusive picture of the effects of WLS films deposited on the MAPMT front window. On all types of MAPMTs, the gain in detected photoelectrons with thickness optimised dip-coated films is significant. Roughly 20 % more photoelectrons are detected with WLS films compared to uncoated MAPMTs. The gain is larger for SBA than for BA photcathodes and larger for thicker than for thinner front windows. In detail, this means that the gain is larger for H10966A-103 MAPMTs with $(21.2 \pm 1.4)\,\%$ than for H8500D-03 with $(18.2 \pm 1.5)\,\%$ and R11265-103-M16 with $(18.0 \pm 1.4)\,\%$.

The usage of WLS films decreases the ring sharpness measurably. The parameter dR is $0.3\,$mm larger with than without WLS films which is, however, small compared to the absolute value of $dR = 2.4\,$mm at $r = 45.6\,$mm. The decrease of ring sharpness due to the isotropic fluorescence or chromatic dispersion when using WLS films is thus not an issue.

The electron pion separation capability, quantified by the pion suppression factor, decreases monotonously from 8480 at $7\,$GeV/c to 740 at $10\,$GeV/c given an electron efficiency of $95\,\%$.

The pion suppression factor can be increased at the expense of electron efficiency. At $10\,$GeV/c and $e_{\text{eff}} = 93\,\%$ for instance, $\pi_{\text{suppr}} > 1100$. On the other hand, $\pi_{\text{suppr}} < 10$ at $e_{\text{eff}} = 99\,\%$.

The measured pion suppression factor is well above the required value of at least 100 (see section 2.4.1). However, it is expectable that the pion suppression factor of the prototype in response to a beam of single particles is better than that of the CBM-RICH detector in response to a heavy-ion collision. A direct comparison is thus inappropriate. For further conclusions, see section 6.5.

Chapter 6

Implications for Monte Carlo simulations of the RICH performance

Besides the proof of concept, a major goal of the prototype development presented in chapter 5 is the utilisation of obtained results for realistic detector performance and feasibility studies of physics measurements. This also holds for the MAPMT evaluation (chapter 3) and the studies of WLS films (chapter 4). In this chapter, lessons from laboratory measurements and beam tests are translated into applicable information for simulations.

Since all important characteristics of the prototype, i.e. radiator length, radius of curvature of the mirror, type and arrangement of photon sensors, as well as the reconstruction algorithms, are the same for the prototype and the full CBM-RICH detector, it is possible to validate the full CBM-RICH detector simulations through comparison of ring quality parameters with data from prototype beam tests.

Section 6.1 introduces the Monte Carlo simulations of the CBM-RICH detector and the prototype. Important input parameters are discussed in section 6.2. Realistic values for those parameters are extracted from laboratory measurements and beam tests which are subsequently implemented in the simulation tool. The simulations are verified in section 6.3. After summarising in section 6.4, ring quality parameters from protoype and full RICH simulations are compared in section 6.5 in order to draw conclusions.

6.1 Simulation of the RICH performance with GEANT

6.1.1 Monte Carlo methods

Monte Carlo (MC) methods are stochastic techniques based on random numbers and probabilities used to investigate a problem. These methodes were introduced by S. Ulam and N. Metropolis and named after the Monte Carlo Casino where random numbers also play a role [148].

MC simulations are an indispensable tool both in the R&D and analysis phase of a physics experiment. During detector development, simulations help to predict and later verify the detector performance. This is done by carrying out studies on the detector acceptance, the response to particle collisions, and the feasibility of physics measurements. During detector operation and data analysis, simulations are required for a proper interpretation of the results. In a full MC simulation, all processes are described: Collisions of beam particles with the target, the stepwise passage of all particles through the detector, and the detector response. Accordingly, a MC simulation consists of three steps: event generation, transport, and detection. Commonly, the term *simulation* refers to the transport step and *reconstruction* to the detection step.

6.1.2 Event generation

For the event generation, a distinction between two cases has to be made depending on whether simulations of the prototype or the full RICH detector will be made.

- Prototype simulations:
  During the beam tests at the PS/T9 beam line, a mixed beam of electrons, muons, and pions entered the prototype. The beam intensity was low enough to be able to treat each incident particle individually. Event generation in this case restricts to the generation of single particles. Since muons are not of interest, only electrons and pions are generated. Their momentum and spatial distribution is adjusted according to the beam properties at the beam line. The corresponding parameters and values are listed in Tab. D.1 in the appendix.

- Simulations of the full RICH detector:
  For the simulation of the detector response to heavy ion collisions, event generation is done by using the Ultra Relativistic Quantum Molecular Dynamics (UrQMD) event generator [27, 28]. UrQMD is a heavy ion transport model in the energy range from SIS to RHIC[1] designed for the study of heavy ion related effects like multifragmentation, collective flow, particle production and correlations.

6.1.3 Simulation

In order to simulate the processes that a particle undergoes inside the detector, the detector geometry is implemented in the transport engine GEANT3 (GEometry ANd Tracking) [149] . A transport engine like GEANT simulates the passage of a particle through matter and is widely used in the area of high energy, nuclear, and accelerator physics. The transport engine tracks a particle stepwise through the different volumes of the detector and calculates at each step its interaction probability by using so-called physics lists which contain all known interaction cross sections of particles with matter. After an interaction, tracks of primary and secondary particles are extrapolated until the next interaction occurs. The simulation of primary and secondary particles stops if they have left the simulated volume, or if their energy is below an adjustable limit.

The exact geometry of the prototype is implemented in a geometry file. It consists of several volumes which are defined by their shape, dimension, and material. The mother volume is the cave and all other volumes are defined inside the cave as daughter volumes with the common coordinate system of the mother volume.

The materials and their properties (chemical composition, mass, density, radiation length, absorption length) are defined in a media file. Together with its tracking parameters needed for the transport (sensitivity, magnetic field flag, electrical field flag etc.), a material is referred to as medium. A field flag indicates the possible existence of a magnetic or electrical field, and its use is to save computing time if no field is present. Even though a field itself is defined in a separate field map, it is useful to set the corresponding flag to zero in such a case, since without field, particles can be extrapolated e.g. through the vacuum with large step size which significantly saves computing time.

As it is the case for event generation, a distinction between RICH prototype and full RICH simulations has to be made for the transport simulation. The geometry file of the prototype consists of the

- RICH barrel composed of an aluminum box filled with CO_2, and a beam entrance window,

- mirror tiles made of SiO_2,

---

[1] SIS is the Schwerionensynchrotron at GSI in Darmstadt, RHIC the Relativistic Heavy Ion Collider at BNL in Brookhaven.

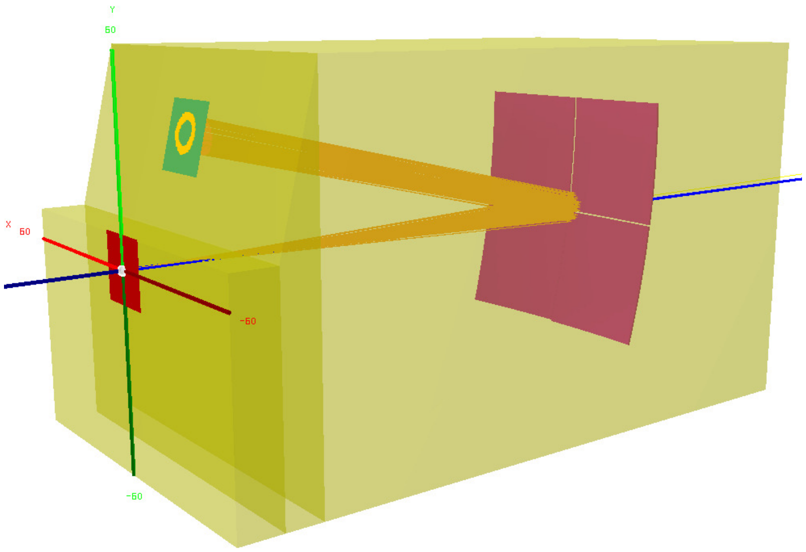

Figure 6.1 – Prototype visualisation with CbmRoot. Different materials are indicated by different colors: radiator (light yellow), beam entrance window (red), mirrors (purple), and camera (green). Also shown are Cherenkov photons from an electron (dark yellow).

- camera made of CsI. Only the "active" photocathode is simulated[2].

The material properties will be discussed in section 6.2. Figure 6.1 shows the prototype geometry as visualised with CbmRoot. The gas volume is shown in light yellow, the beam entrance window in red, the mirrors in purple, and the camera in green.

For the full RICH detector, supporting elements and dimensions are different. The main components, radiator, mirror tiles, and camera, however, are composed of the same materials.

6.1.4 Reconstruction

Each Cherenkov photon, which is reflected by the mirror and reaches the camera, creates an object called Monte Carlo Point (MC point). In average, one electron passing the prototype results in 255 MC points [6]. In the step of reconstruction, a task called Hit Producer creates hits from the MC points by applying a granularity mask with a realistic pixel size (6.125×6.125 mm^2 for the H8500 MAPMT) and a gap between MAPMTs of 2 mm. In addition, a certain number of noise hits is produced and distributed homogeneously over the camera.

Both signal and noise hits are taken as input for the ring finding algorithm which is based on the standard implementation of the Hough transform finder in CbmRoot (see section 2.5.3). There is one difference in the reconstruction scheme between the prototype and the full RICH detector concerning track guidance[3]: Since no tracking information is available in the prototype simulation due to the absence of tracking detectors, effects due to imperfect track reconstruction in the STS cannot be taken into account.

The ring finding and fitting algorithms used for the analysis of data taken with the prototype are exactly the same as used for the prototype MC simulation. Thus, a direct comparison between beam test data and simulation is possible.

---

[2] It should be noted that at a later stage, also the front glass of the MAPMTs should be simulated in order to account for scintillation for instance.

[3] For the full CBM-RICH detector simulation, the prediction of the track position on the camera plane is used for ring-track matching in the third step of the ring reconstruction (see section 2.5.3).

Important input parameters to the Hit Producer are the quantum efficiency of the photon sensors, the noise rate, the smearing of hit position due to mirror inhomogeneities and crosstalk, and the number of additional cross talk hits. The implementation of realistic values for those parameters is discussed in section 6.2.

6.2 Implementation of realistic input parameters according to laboratory measurements and beam test results

6.2.1 Radiator

The medium used for the radiator gas in this thesis is called *RICHgas_CO2_dis_Ogawa_Mehu* according to the references for the absorption properties [107] and the refractive index [68] of CO_2.

The definition of the radiator in the media file is shown in Fig. 6.2. The wavelength dependent optical properties of a dielectric medium are given in columns in the case of a GEANT media file. The first column specifies the photon energy. The second column gives the corresponding absorption length in cm, the third the detection efficiency and the fourth the refractive index.

The absorption length, defined as distance x where the intensity has dropped to $1/e$, is calculated from the absorption cross σ section given in [107] using the Beer-Lambert-Law

$$I(x) = \frac{1}{e} I_0 = I_0 e^{-\sigma x n} \tag{6.1}$$

with the concentration n of absorbing molecules.

The refractive index (column 4) is taken from [68] for standard conditions (pressure $p = 1000\,\mathrm{mbar}$, temperature $T = 0\,^\circ\mathrm{C}$).

Figure 6.3 depicts the dependence of absorption length and refractive index on the wavelength. In addition, the values defined in *RICHgas_CO2_dis* are plotted, which has been the standard medium for the CBM-RICH radiator.

It can be seen that the new medium is defined at more wavelength points. The definition of optical properties at more points gives more precise results since GEANT does a linear interpolation by default although the absorption length and the refractive index are not linear in n.

In the case of the absorption length, the values from [107] differ from the old standard. In the new definition, the absorption length is slightly shorter leading to more absorbed Cherenkov photons and thus a lower number of photons arriving at the camera.

In the case of the refractive index, old and new definition do not differ significantly. The chromatic dispersion of CO_2 can be clearly seen in Fig. 6.3 (right). Chromatic dispersion is a contribution to the broadening of Cherenkov angle resolution discussed in section 2.5.

The total relative error for the determination of the refractive index n is stated in [68] to be only $8\,‰$ and is therefore neglected in the further discussion.

6.2.2 Mirror

The medium used for the mirror tiles is called *RICHglassJLO*. In contrast to the radiator which is defined as dielectric, the mirror tiles are defined as metal. In the case of a medium boundary from dielectric to metal, GEANT simulates two effects for optical photons[4]: complete absorption and reflection. The definition of

---

[4] In GEANT, “a photon is considered to be optical when its wavelength is much greater than the typical atomic spacing” [149]. This holds true for all Cherenkov photons.

```
RICHgas_CO2_dis_Ogawa_Mehu    -2  12. 16. 6. 8.   1.977e-3  1 2
                               0  1  20.   .001
                              79
                              1.77  5000 1.0  1.000446525
                              2     5000 1.0  1.000448273
                              2.1   5000 1.0  1.000449086
                              ...
                              7.131 4.65 1.0  1.000561596
                              7.149 3.95 1.0  1.000562318
                              7.212 3.13 1.0  1.000564858
```

Figure 6.2 – Properties of the radiator gas as implemented in the media file. The name of the medium is *RICHgas_CO2_dis_Ogawa_Mehu*. The first line of numbers states, from left to right, the number of components (2), the atomic weight of the components (12 for C, 16 for O), the atomic numbers of the components (6 for C, 8 for O), the mass density in g/cm^3, the weight of each component in the mixture (1× C, 2× O). The second line states a sensitivity flag, a field flag, the maximum field value in kgauss, and the boundary crossing precision (see [149] for details). The parameter in the third line gives the number of lines used to define the optical properties of the medium (79 in this case). The following lines contain the photon energy in eV ($1.77\,\text{eV} \mathrel{\widehat{=}} 699.9\,\text{nm}$, $7.212\,\text{eV} \mathrel{\widehat{=}} 171.8\,\text{nm}$) and the corresponding absorption length in cm, the detection efficiency of the radiator, and the refractive index. The whole list can be found in appendix D.

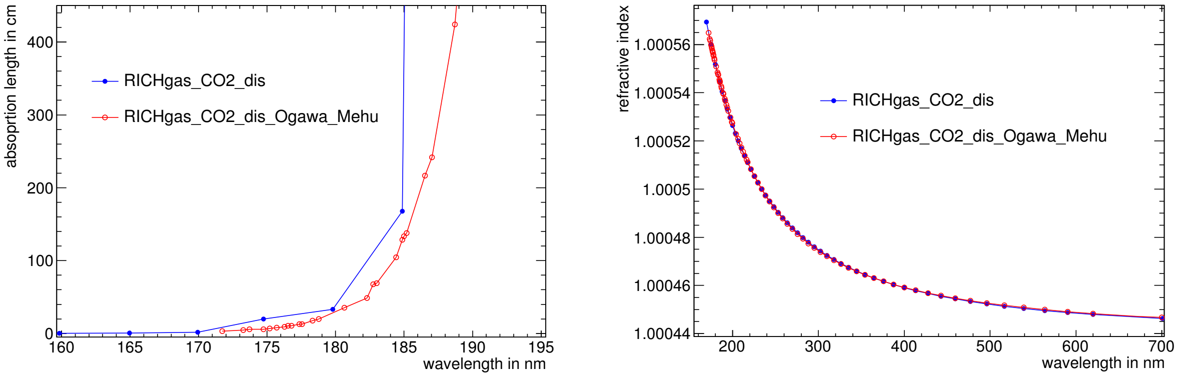

Figure 6.3 – Absorption length (left) and refractive index (right) as function of wavelength. Open red symbols show the values from the newly defined medium *RICHgas_CO2_dis_Ogawa_Mehu*, filled blue symbols those from the old standard definition *RICHgas_CO2_dis*. In *RICHgas_CO2_dis_Ogawa_Mehu*, the absorption length is calculated from the absorption cross section given in [107]. The refractive index is taken from [68]. Both references state the values at standard conditions ($p = 1000\,\text{mbar}$, $T = 0\,°\text{C}$). Lines between the data points indicate the linear interpolation done by GEANT.

a metal therefore contains the absorption probability instead of the absorption length as in the case of a dielectric medium.

Figure 6.4 shows an excerpt of the definition of the mirror properties in the media file. The absorption probability P_{abs} is calculated from the average reflectivity R of the four mirror tiles, measured at BUW and given in [71], according to $P_{\text{abs}} = 1 - R$.

Since the measurements of the reflectivity are done only down to 200 nm, an extrapolation to 180 nm has to be made. At 180 nm the absorption length of the radiator gas is only $\approx 30\,\text{cm}$ (see Fig. 6.3 left). That means that an extrapolation below this wavelength is not needed because $> 99.5\,\%$ of Cherenkov photons of 180 nm wavelength are absorbed on their way to the camera.

The manufacturer JLO provided data from a measurement of another piece of the same type of mirror tile down to 180 nm. The extrapolation is done by taking the values from the JLO measurement at 190 nm

```
RICHglassJLO      -2  28.09  16.  14.  8.  2.2  1.  2.
                   1  0  20.  .0001
                   63
                   1.5485 0.1572    1.0  0
                   1.5681 0.1532    1.0  0
                   1.5882 0.1522    1.0  0
                   ...
                   6.1942 0.2253    1.0  0
                   6.5202 0.2503    1.0  0
                   6.8824 0.2603    1.0  0
```

Figure 6.4 – Properties of the mirror tiles as implemented in the media file. The name of the medium is *RICHglassJLO*. The material is composed of SiO_2. The second column of the optical properties contains the absorption probability in contrast to the RICHgas which is defined by the absorption length. The refractive index of the RICHglass is set to 0. The whole list can be found in appendix D.

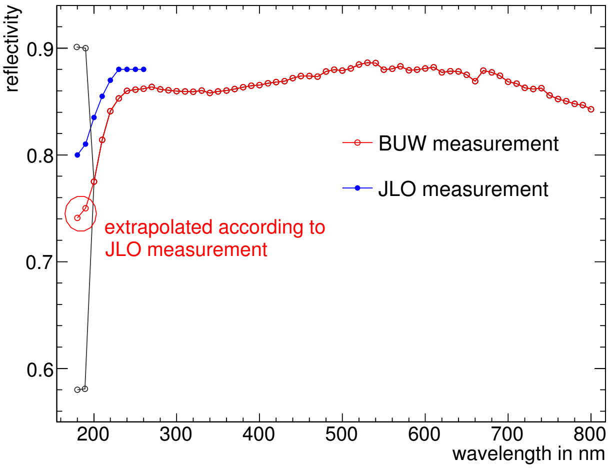

Figure 6.5 – Wavelength dependent mirror reflectivity as measured at BUW and by the manufacturer JLO. The BUW measurement shows the average reflectivity of the four mirror tiles mounted in the prototype (open red symbols). The JLO data shows the results from a measurement of another mirror tile of the same type (filled blue symbols). Since the BUW measurement only goes down to 200 nm, the two data points at 180 nm and 190 nm are extrapolated. They are calculated by subtracting from the JLO data points the difference between JLO and BUW data at 200 nm. The grey symbols show an assumed reflectivity of 90 % and 58 % in order to study the influence on the hit multiplicity. A full MC simulation of the prototype reveals that the hit multiplicity varies only by ± 0.1 photoelectrons per electron ring when assuming a reflectivity of (74 ± 16) % with 74 % being the value implemented in *RICHglassJLO* at 200 nm.

and 180 nm and subtracting the difference between JLO and BUW measurement at 200 nm. In this way, the absolute reflectivity from the BUW measurement is extrapolated assuming the shape of the curve as measured by JLO. Figure 6.5 shows the JLO and BUW measurement including the extrapolation from 200 nm to 180 nm.

The error made by the extrapolation of the mirror reflectivity can be estimated by assuming a very high or a very low reflectivity for the wavelength interval 180 nm to 200 nm. A full MC simulation of the prototype shows that the hit multiplicity varies by only ± 0.1 photoelectrons per electron ring when implementing a reflectivity of 90 % and 58 % respectively instead of 74 % which is the value obtained from the extrapolation (see Fig. 6.5). The simulated hit multiplicities are listed in Tab. 6.1.

mirror reflectivity between 180 nm and 190 nm	hit multiplicity
90.0 %	26.6
74.0 % to 75.0 %	26.5
58.0 %	26.4

Table 6.1 – Simulated hit multiplicity of the prototype for electron rings detected by H8500D-03 MAPMTs in dependence of the mirror reflectivity between 180 nm and 190 nm. The value from *RICHglassJLO* is 74.0 % at 180 nm and 75.0 % at 190 nm. Even when the reflectivity varies by $\pm 16\,\%$, the influence on the hit multiplicity is low (± 0.1 photoelectrons per electron ring).

6.2.3 Noise

The analysis of beam test data shows that for the ≈ 1000 channels of the prototype in average 10^{-3} noise hits occur per event within a time window of 100 ns. The noise level was read from the dark rate (see section 5.4.1). This means that in 1 out of 1000 events, one pixel fires because of uncorrelated noise. This very low number allows to neglect noise in the prototype simulations, i.e. the number of randomly firing pixels per event is set to *nofNoiseHitsInRich* $= 0$. With the same argument, noise was neglected in the prototype simulations done for the Technical Design Report for the CBM-RICH detector [6].

In the case of simulations of the full CBM-RICH detector with $\approx 55\,000$ channels, the number of noise hits per event is still < 1.

Systematic studies of the ring reconstruction algorithms with respect to the noise level have shown that the CBM-RICH detector can tolerate 1 % of noisy channels easily [6]. For 55 000 channels, this percentage corresponds to 550 firing channels. The number extrapolated from beam test results is well below.

It is worth to mention, however, that the conditions during the beam tests were almost ideal, i.e. a relatively low number of channels, few additional electronics in the vicinity, low "noise" from the accelerator, etc. These conditions may be less favourable in the CBM cave. In addition, in high multiplicity events, additional photons will be produced in the radiator volume due to scintillation, resulting in ≈ 250 homogeneously distributed hits on the camera (see section 2.5.2) which have to be considered when simulating the full CBM-RICH detector. Furthermore, the high rates in a heavy ion collision may result in more noise in the photon sensors. Therefore, rate tests with MAPMTs are envisaged.

6.2.4 Additional crosstalk hits

Implementation of crosstalk in the reconstruction

The adding of crosstalk hits was implemented by Dmytro Kresan originally in the Prototype Hit Producer and then adopted to the Hit Producer for the full detector. For every Cherenkov photon hitting a MAPMT pixel, hits in the four direct neighbouring pixels are added with a probability given by the parameter *fCrossTalkHitProb*. Hits are added in the four diagonal neighbouring pixels with the probability *fCrossTalkHitProb*/4. The fact that the probability for crosstalk in a diagonal pixel is $1/4$ of the crosstalk in a direct neighbour is verified by the laboratory measurements summarised in Tab. 4.2 and 4.3.

Quantification of the additional crosstalk hit fraction

In section 3.9, the number of additional hits in neighbouring pixels due to crosstalk was quantified for H8500D-03 and R11265-103-M16 MAPMTs. It was found that the additional hit fraction strongly depends

pmtType	MAPMT type	WLS	ring position in beam test	no. of measured MAPMTs
6	H8500D-03	no	position F (2011)	4
10	H8500D-03	yes	position H (2011)	4
13	R11265-103-M16	no	position I (2012)	4
14	R11265-103-M16	yes	position I (2012)	4
15	H8500D-03	no	position C (2012)	4
16	H8500D-03	yes	position C (2012)	4
17	H10966A-103	no	position E (2012)	1
18	H10966A-103	yes	position E (2012)	1

Table 6.2 – Possible values for the parameter *pmtType* which is used to select different types of MAPMTs with and without WLS coating for the creation of hits from MC points. The implemented *QE* values are the average of the given number of MAPMTs at the corresponding ring position from the 2011 and 2012 beam tests. *pmtType* 6 and 15 correspond to different MAPMTs of the same MAPMT type. As will be shown later, the difference in hit multiplicity is in the order of 1.1 % and caused by tube-to-tube fluctuations. Numerical *QE* values for each MAPMT type can be found in appendix D.

on the ADC threshold. If the threshold is fixed to 10 % of the single photoelectron peak, the crosstalk hit fraction is fairly constant, having values of (6.8 ± 1.2) % for H8500D-03 and (3.2 ± 0.7) % for R11265-103-M16.

In order to simulate the prototype performance during the beam tests, the crosstalk probability should be adjusted according to the threshold at that time. Even though the crosstalk differs from tube to tube, for practical reasons it is quantified globally with a common value for each MAPMT type. Average values from laboratory measurements, which are comparable to those from the beam tests, are chosen. For H8500D-03 MAPMTs, the crosstalk probability is set to *fCrossTalkHitProb* $= 0.02$ which corresponds to an additional hit fraction of 10 % in all neighbouring pixels. For R11265-103-M16 MAPMTs, *fCrossTalkHitProb* $= 0.01$, corresponding to an additional hit fraction of 5 % (cf. Fig. 3.24).

6.2.5 Photon detection efficiency

Implementation of quantum efficiency in the reconstruction

When creating hits from MC points (see section 6.1.4), the Hit Producer takes into account the quantum efficiency of the MAPMTs. The quantum efficiency is tabulated as function of wavelength for several types of MAPMTs with and without WLS films as measured in the laboratory and presented in section 3.4 and 4.3. The selection of the MAPMT type used for the reconstruction as well as the selection of coated or uncoated MAPMTs is done via the parameter *pmtType*. According to the selection, the corresponding *QE* table is accessed.

Based on the measurements, eight *QE* tables have been added to the six existing tables for different photon sensor types[5]. Table 6.2 lists the MAPMT type and the corresponding ring positions for the eight new values of the parameter *pmtType*.

---

[5] The existing *QE* tables are for a Protvino-type PMT, data sheet values for Hamamatsu H8500, CsI photocathode (NIM A 433 (1999) 201, HADES), data sheet values for Hamamatsu H8500-03, and an estimation for H8500C/D-03 with WLS film.

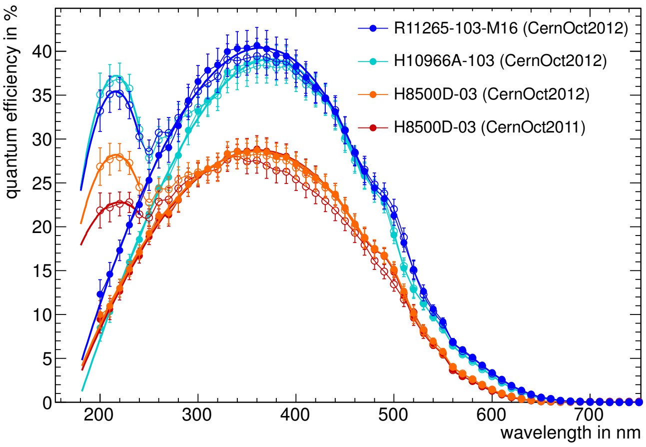

Figure 6.6 – *QE* curves of R11265-103-M16, H10966A-103, and H8500D-03 MAPMTs without (filled symbols) and with WLS films (open symbols). Since measurements are done only down to 200 nm, *QE* values below are calculated by fitting and extrapolating the curves. Thick lines indicate fits to the data between 470 nm and 200 nm for uncoated and between 240 nm and 200 nm for coated MAPMTs. Because of the lowest χ^2 among different fit functions, a polynomial of the order 3 is used for the uncoated and a polynomial of the order 2 for the coated MAPMTs. The *QE* values at 190 nm and 180 nm are obtained by evaluating the fit functions at these wavelengths.

Extrapolation of quantum efficiency below 200 nm

As it is the case for the mirror reflectivity, the quantum efficiency is measured only down to 200 nm and therefore has to be extrapolated to 180 nm, where the gas absorption dominates. The extrapolation is done by fitting the measured *QE* curves and evaluating the value of the fit at 190 nm and 180 nm.

Figure 6.6 shows the *QE* curves of R11265-103-M16, H10966A-103, and H8500D-03 MAPMTs without (filled symbols) and with WLS films (open symbols). The curves show averaged *QE* curves from four MAPMTs of different ring positions from the 2011 and 2012 beam tests in the case of R11265-103-M16 and H8500D-03. This allows a direct comparison between the results from simulation and beam tests. In the case of H10966A-103, only the *QE* curve from one MAPMT is plotted.

Polynomial functions of different order have been used to fit the data between 470 nm and 200 nm in the case of bare MAPMTs and because of the more winding curves between 240 nm and 200 nm in the case of coated MAPMTs. Among the different fit functions, polynoms of the order 3 and 2 have the lowest χ^2 for bare and coated MAPMTs, respectively. Thus, the *QE* values at 190 nm and 180 nm are obtained by evaluating a fitted polynom of the order 3 to the bare *QE* curves and a polynomial of the order 2 to the *QE* curves with WLS films.

The error made by the extrapolation of the quantum efficiency is estimated by simulating the influence of different fit functions on the hit multiplicity.

Figure 6.7 shows three different functions used to fit the *QE* curve of uncoated H8500D-03 MAPMTs. The results in terms of hit multiplicity for electron rings detected with H8500D-03 MAPMTs are shown in Tab. 6.3. The hit multiplicity varies between 25.5 photoelectrons and 27.1 photoelectrons per electron ring for the two extreme cases that the *QE* is set to 0 % below 200 nm and to 9.5 % (measured value at 200 nm), respectively, showing the importance of a careful extrapolation in this wavelength range. Within a series of polynomials, the extrapolated *QE* is higher the higher the order of the polynomial. The used polynomial of the order 3 reveals a hit multiplicity of 26.3 photoelectrons which is just in the middle of the two extreme cases. The variation is ±0.8 photoelectrons.

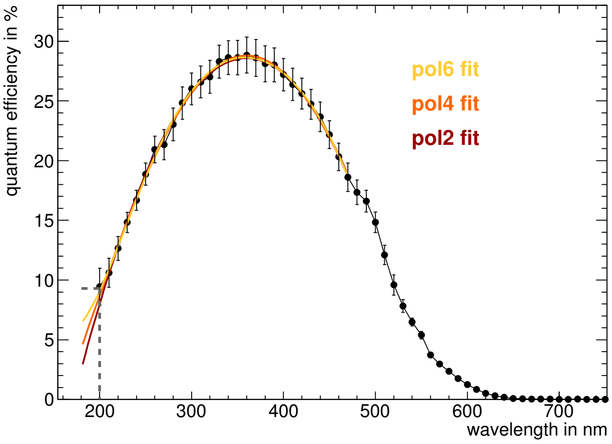

Figure 6.7 – *QE* curves of H8500D-03 MAPMTs fitted with different polynomials between 470 nm and 200 nm. Dotted lines show two additional cases where the *QE* below 200 nm is set to 0 % and 9.5 %, respectively, for uncertainty evaluation. The *QE* values at 190 nm and 180 nm are calculated by extrapolating the fits. By using these values in a full MC simulation of the prototype, the influence of different extrapolations on the hit multiplicity can be estimated (see Tab. 6.3).

fit function	*QE* at 180 nm	hit multiplicity
no fit	9.5 %	27.1
pol6	6.4 %	26.7
pol4	4.3 %	26.5
pol3	3.2 %	26.3
pol2	2.5 %	26.2
no fit	0.0 %	25.5

Table 6.3 – Extrapolation of *QE* values to 180 nm based on polynomial fits. Also listed are two cases where the *QE* is set to 0 % and 9.5 %. The third column states the hit multiplicity for electron rings obtained in a full MC simulation of the prototype using the extrapolated *QE* values below and the measured *QE* values above 200 nm. It can be seen that the hit multiplicity varies around the value of the chosen fit function (26.3 photolectrons for a polynom of the order 3) by ±0.8 photoelectrons.

Collection efficiency

The photon detection efficiency is determined by quantum efficiency and collection efficiency. Since only quantum efficiency is measured, the collection efficiency enters in the reconstruction as a global factor given by the parameter *collectionEff*. For the time being *collectionEff* is set to 100 %. By comparing simulation with beam test results, *collectionEff* will be quantified in section 6.3.1 for different MAPMT types.

6.2.6 Ring sharpness

Adjustment of *dR*

As seen in section 5.6.3, not all hits are located directly on the fitted ring which leads to a non-zero *dR* parameter. For the 2012 beam test data, the ring sharpness is quantified to be $dR = 2.42$ mm for ring position C without WLS films and $dR = 2.73$ mm with WLS films (see Fig. 5.32).

A minimum *dR* is given by the granularity of the MAPMTs. Furthermore, scattering of photons on the mirror and in the MAPMT front glass can lead to an increased *dR*. Since these contributions have not been measured, their impact on *dR* is simulated by adjusting a smearing parameter such that *dR* in simulation and data agree.

In the Rich Hit Producer, to every hit position $x_{\text{hit}}, y_{\text{hit}}$ a gaussian smearing is applied with a given sigma in order to accommodate a non-zero *dR*. The parameter *sigma_0* is used to quantify the smearing and applied to all photons impinging on the camera

$$\left.\begin{aligned} x_{\text{hit}} &\to x_{\text{hit}} + \text{gauss}(0, \textit{sigma\_0}) \\ y_{\text{hit}} &\to y_{\text{hit}} + \textit{gauss}(0, \textit{sigma\_0}) \end{aligned}\right\} \quad \forall\, \lambda.$$

In the case of WLS coated MAPMTs, an additional parameter *sigma_wls* is implemented to additionally smear the hit position due to the isotropic fluorescence of the WLS films. The WLS smearing is only applied for photons $< 300\,\text{nm}$ because only photons below that wavelength are absorbed by the films and isotropically re-emitted (see Fig. 4.2)

$$\left.\begin{aligned} x_{\text{hit,wls}} &\to x_{\text{hit}} + \text{gauss}(0, \textit{sigma\_0}) + \textit{gauss}(0, \textit{sigma\_wls}) \\ y_{\text{hit,wls}} &\to y_{\text{hit}} + \textit{gauss}(0, \textit{sigma\_0}) + \textit{gauss}(0, \textit{sigma\_wls}) \end{aligned}\right\} \quad \text{for } \lambda < 300\,\text{nm}$$

$$\left.\begin{aligned} x_{\text{hit,wls}} &\to x_{\text{hit}} + \text{gauss}(0, \textit{sigma\_0}) \\ y_{\text{hit,wls}} &\to y_{\text{hit}} + \textit{gauss}(0, \textit{sigma\_0}) \end{aligned}\right\} \quad \text{for } \lambda \geq 300\,\text{nm}$$

Table 6.4 (second column) shows the simulated *dR* without smearing for different MAPMT types, i.e. both smearing parameters are set to zero. The values for *dR* differ for the different MAPMTs mounted on different ring positions. On ring position C, Cherenkov rings are projected onto four MAPMTs of the same type mounted in a matrix with a gap of 2 mm in between. The situation is different for ring position I (see Fig. 5.14), where eight small MAPMTs are arranged in a circular shape covering only $\approx 75\,\%$ of the Cerenkov rings. Four from eight MAPMTs are turned by 45° following the shape of a ring. In this layout, the tangents of the rings cross the MAPMTs horizontally whereas for the rectangular layout, the tangents cross half of the MAPMTs diagonally. In the former case, the distance between pixel centre and fitted ring is relatively small. Thus, *dR* is smaller at position I than at the other positions. At position E (rectangular layout, two H10966A-103, two H8500D-03), *dR* is slightly larger than that of position C. A possible explanation could be the SBA photocathode whose photoelectron emission might have another directional characteristic due to its lower work function.

In order to match the ring sharpness in the simulation with that extracted from beam test data, *sigma_0* and *sigma_wls* are varied until agreement between *dR* from simulation and data is obtained. Table 6.4 shows the values for the smearing parameters determined for the different MAPMT types and the resulting parameter *dR*.

The ring sharpness has direct influence on three important parameters, the number of multiple hits, the number of lost hits during the step of ring finding, and the hit multiplicity. The impact of the ring sharpness on these parameters is investigated by performing a full MC simulation of the prototype using ultrarelativistic electrons and $\textit{pmtType} = 6$. The simulation is done for values from $\textit{sigma\_0} = 0\,\text{mm}$ to $\textit{sigma\_0} = 5\,\text{mm}$ corresponding to $\textit{dR} = 2.28\,\text{mm}$ to $\textit{dR} = 3.84\,\text{mm}$.

Influence of ring sharpness on pixel occupancy

Due to the finite MAPMT pixel size, the occurrence of two or more MC points on one pixel is possible. Given the rather low quantum efficiency $< 40\,\%$, only one hit is generated in most of such cases. With a certain probability, however, more than one hit is created on one pixel.

MAPMT type	*dR* (MC) no smearing	*sigma_0*	*sigma_wls*	*dR* (MC)	*dR* (data)
R11265-103-M16 (pos. I) clean	2.25 mm	0.40 mm	–	2.28 mm	2.28 mm
R11265-103-M16 (pos. I) WLS	2.39 mm	0.40 mm	0.61 mm (×2)	2.44 mm	2.44 mm
H8500D-03 (pos. C) clean	2.29 mm	0.90 mm	–	2.42 mm	2.42 mm
H8500D-03 (pos. C) WLS	2.43 mm	0.90 mm	1.64 mm	2.73 mm	2.73 mm
H10966A-103 (pos. E) clean	2.31 mm	1.80 mm	–	2.52 mm	2.52 mm
H10966A-103 (pos. E) WLS	2.53 mm	1.80 mm	1.98 mm	2.69 mm	2.69 mm

Table 6.4 – *dR* in 2012 beam test data (data) and simulation (MC). In the simulation, *dR* is adjusted to match the value extracted from beam test results via the parameter *sigma_0* which smears every hit position according to a gaussian. The parameter *sigma_wls* is used to smear the hit position for photons of wavelengths $< 300\,\mathrm{nm}$ in the case of WLS coated MAPMTs. For comparison, the simulated *dR* without smearing is shown in the second column. The factor of 2 for the R11265-103-M16 indicates that only half of the MAPMTs was coated with WLS films in the test beam. The user is reminded that the unit of *sigma_0* and *sigma_wls* in the Hit Producer is cm.

For fixed pixel size, ring radius, and hit multiplicity, the number of double, triple, quadruple etc., generally speaking *multiple* hits, only depends on the ring sharpness. With increasing *dR*, the rings get wider and cover more pixels. For quantification, a simulation based on 100 000 rings with $r = 45.6\,\mathrm{mm}$ and 23 hits per ring was performed for different values of *dR*. Figure 6.8 shows the result of a simulation for the 2011 photon detector with 32×32 pixels. On the top line, the integrated event displays of the 100 000 rings are shown for three different values of *dR*.

The lower panel of Fig. 6.8 shows the number of hits per pixel for the three different values of *dR* on a logarithmic scale. In most of the cases, only one hit per pixel occurs as expected. In some cases, also multiple hits occur and their fraction decreases more strongly for large *dR* than for small *dR*.

Because MAPMTs cannot count multiple hits which simultaneously strike one pixel separately, one hit from each double hit, two hits from each triple hit etc. are lost[6]. Taking this into account, 8.6 % of hits are lost in the realistic case of $dR = 2.42\,\mathrm{mm}$. For wider rings, the fraction of lost hits decreases and adds up to 6.3 % for $dR = 2.98\,\mathrm{mm}$ and 4.0 % for $dR = 3.84\,\mathrm{mm}$.

The number of lost hits could be reduced by using MAPMTs with a smaller pixel size. The R11265 MAPMT, for instance, is available with 8×8 instead of 4×4 pixels. The usage of these MAPMTs, however, would increase the number of needed electronic channels according to the pixel number by a factor of four which is hardly affordable in view of the rather small performance gain.

Influence of ring sharpness on ring finding

As described in section 2.5.3, all hits belonging to a ring are selected by the ring finder. If a hit is too distant, it is not included in the hit array used for the ring fit. In consequence, for sharp rings, nearly all hits from one event will be included in the ring fit whereas for wide rings, more hits will be excluded. The number of lost hits, given as the difference between hits per event and hits per found ring, is therefore expected to rise with increasing *dR*.

---

[6] Weighting the hits according to the corresponding ADC amplitude might help to count also multiple hits. This, however, has not been studied yet

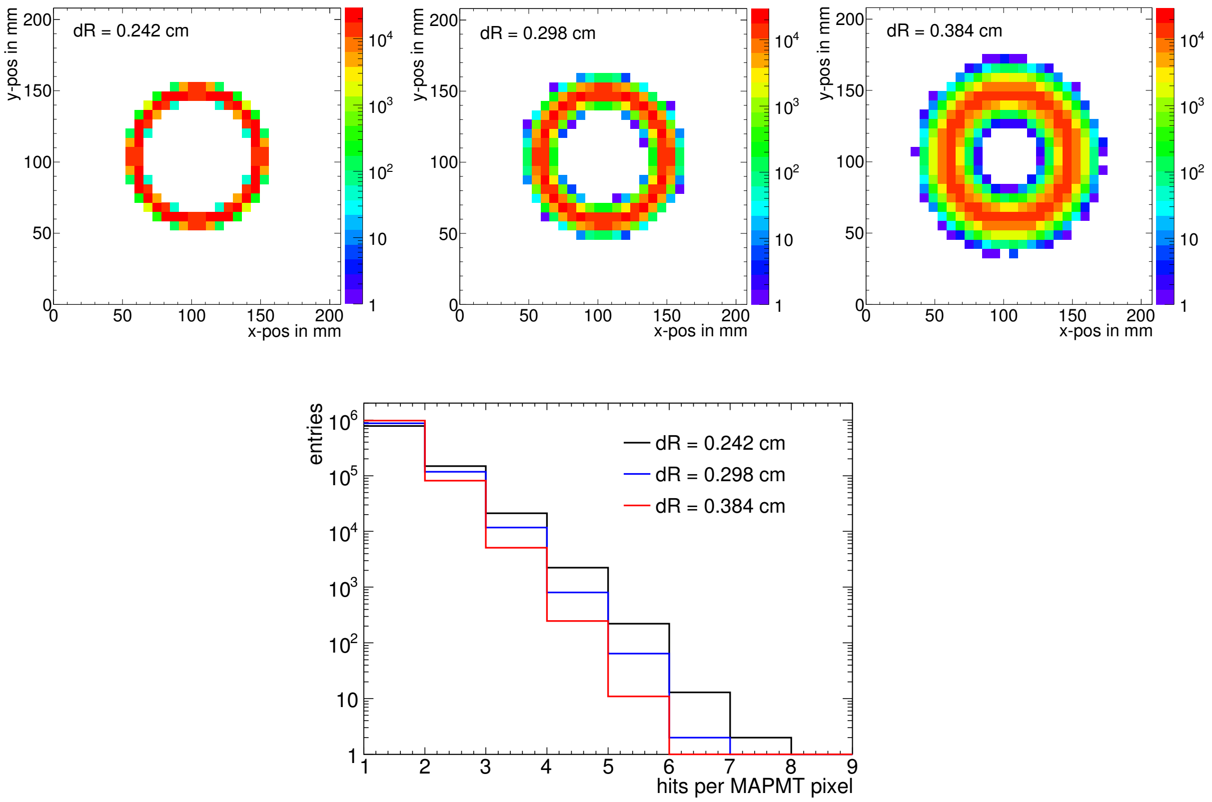

Figure 6.8 – Top: Simulation of $100\,000$ rings of radius $r = 45.6$ mm and 23 hits each for three different values of *dR*. The smaller *dR*, the sharper the ring. $dR = 2.42$ cm corresponds to the measured value during the beam tests. Bottom: Distribution of the number of hits per MAPMT pixel for the three values of *dR*. Beside the most common case of one hit per pixel, it can be seen that also double, triple, quadruple etc. hits occur. For $dR = 2.42$ cm, even one septuple hit occurs within $100\,000$ rings. For wider rings, i.e. increasing *dR*, multiple hits become less frequent. From the plot it can be deduced that for the realistic case of $dR = 2.42$ cm, 8.6 % of all hits are lost because the MAPMT cannot count multiple hits separately (see text).

Influence of ring sharpness on the hit multiplicity

Figure 6.9 shows the fraction of multiple hits as well as the number of lost hits during ring finding as function of *dR*. As previously discussed, the former decreases and the latter increases with *dR*.

Also shown in Fig. 6.9 is the distribution of the hit multiplicity as function of *dR* which exhibits a maximum around $dR = 0.3$. The existence of a maximum hit multiplicity is a result of the two distributions of multiple hits and lost hits showing opposite trends. For small *dR*, the hit multiplicity is relatively low due to the high pixel occupancy. It increases according to the decreasing pixel occupancy towards larger *dR* until its maximum is reached around $dR = 0.3$. At $dR > 0.3$ cm, the strongly increasing number of rejected hits by the ring finder predominates and the the hit multiplicity drops.

In summary, the strong dependence of the hit multiplicity on the ring sharpness shows that the realistic adjustment of the smearing parameters is essential for the quantitative interpretation of MC simulations.

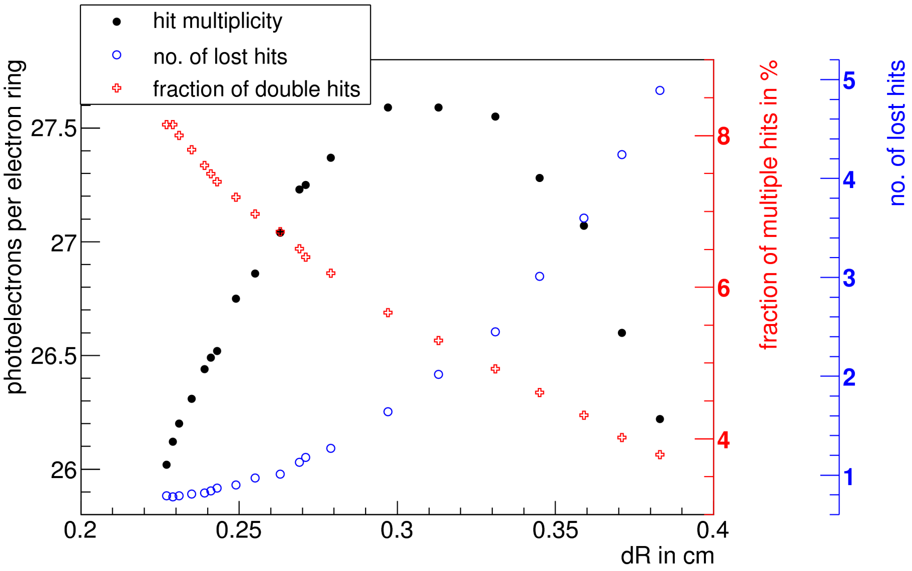

Figure 6.9 – Hit multiplicity, fraction of multiple hits, and number of lost hits during ring finding per event as function of dR. The hit multiplicity distribution has a parabolic shape with a maximum around $dR = 0.3\,\text{cm}$. The increase of hit multiplicity up to $dR = 0.3\,\text{cm}$ can be understood by considering the fraction of multiple hits, i.e. the fraction between the occurrence of more than one hit on one MAPMT pixel and the occurrence of only one hit per pixel. The occupancy of MAPMT pixels is relatively large for sharp rings. Hence, the hit multiplicity is relatively low. Towards larger dR, i.e. broader rings, the probability of multiple hits decreases which leads to a larger hit multiplicity. The decrease of the hit multiplicity towards large dR can be explained by the increasing number of lost hits, i.e. the difference between the number of hits before and after ring finding. At $dR > 0.3\,\text{cm}$, the average distance between hit and ring is so large that the probability of hits being rejected by the ring finder predominates. This, in turn, results in a decreasing hit multiplicity.

6.3 Verification of Monte Carlo simulations through comparison with beam test results

In this section, the parameters discussed in section 6.2 will be used for prototype simulations. It will be shown how accurate beam test results can be reproduced in terms of ring radius, hit multiplicity, performance gain with WLS films, and pion suppression.

6.3.1 Ring radius and hit multiplicity

For the simulation of the hit multiplicity, the following input files and input parameters have been used.

- Simulation
  - 20 000 electrons
  - 3 GeV/c
  - spatial distribution according to PS/T9 beam characteristics (see Tab. D.1)
- Reconstruction
  - mirror: *RICHglassJLO*
  - radiator: *RICHgas_CO2_dis_Ogawa_Mehu*
  - *nofNoiseHitsInRich* $= 0$
  - *fCrossTalkHitProb* $= 0.02$ for H8500D-03 and H10966A-103, *fCrossTalkHitProb* $= 0.01$ for R11265-103-M16 MAPMTs
  - *sigma_0* according to Tab. 6.4
  - *collectionEff* $= 1.0$
  - *pmtType* $= 6, 13, 15, 17$ (see Tab. 6.2)

Ring radius and radius resolution
Since electrons are simulated with constant momentum of 3 GeV/c, also their ring radius is constant. Moreover, the ring radius is maximal due to the saturated Cherenkov angle for electrons, which, at this momentum, are ultrarelativistic. The radius distribution is fitted by a gaussian leading to a mean of $r = 46.7$ mm and a width of $\sigma_r = 0.6$ mm. The relative radius resolution is thus $\sigma_r/r = 1.3\,\%$ which is in excellent agreement with the the measurement (see section 5.5.1). Also the absolute value of the ring radius is in good agreement with the measurement when correcting the measured value (see Fig. 5.20) to standard conditions, that is to say $r_{\text{meas}} = 47.4$ mm.

Hit multiplicity
The resulting hit multiplicities are shown in Tab. 6.5 together with the beam test results. Because of the circular layout of MAPMTs at ring position I, the measured hit multiplicity at this position is corrected for a rectangular MAPMT layout with a gap width of 2 mm as it is the case for the other ring positions[7]. In this way, all numbers are comparable.

---

[7] The geometrical coverage of the MAPMTs on ring positions with rectangular layout is $x_{\text{rect}} = 97.2\,\%$, that of ring position I $x_I = 75.2\,\%$ [150]. Hence, the hit multiplicity of ring position I has to be multiplied with $x_{\text{rect}}/x_I = 129.3\,\%$ in order to compare with the other positions. To compare the hit multiplicity of the 1" R11265 with the 2" H8500, the geometrical coverage of the corresponding MAPMTs mounted in an array as discussed in section 3.5 must be considered.

MAPMT type	run no.	measured hit multiplicity	MC	rel. difference
R11265-103-M16	90 (pos. I) (2012)	31.7 ± 0.2	31.8 ± 0.8	0.3 %
H8500D-03	20 (pos. F) (2011)	24.6 ± 0.3	26.5 ± 0.8	7.7 %
H8500D-03	80 (pos. C) (2012)	24.9 ± 0.3	26.8 ± 0.8	7.6 %
H8500D-03	78 (pos. B) (2012)	25.1 ± 0.2	26.8 ± 0.8	6.8 %
H10966A-103	63 (pos. E) (2012)	25.6 ± 0.3	29.9 ± 0.8	16.8 %

Table 6.5 – Hit multiplicity in beam test data and simulation, corrected for a geometry with 2 mm gap between MAPMTs. The errors in the simulation are determined from the uncertainty of the extrapolation of mirror reflectivity and quantum efficiency. For the discussion of the difference between data and simulation see text.

For the R11265-103-M16 MAPMTs, a very good agreement between data and simulation is observed. For H8500D-03 MAPMTs, the simulated value is 7 % to 8 % larger than the beam test result. In the case of H10966A-103 MAPMTs, the simulation overestimates the measurement by 17 %.

The observation of a larger hit multiplicity in simulation is expected since the parameter *collectionEff* is set to 100 % in the reconstruction whereas the collection efficiency of the MAPMTs is certainly lower. Provided that no other losses are present, the collection efficiency of the different MAPMT types can be extracted from the last column of Tab. 6.5. Accordingly, the collection efficiency of the R11265-103-M16 is close to 100 % and that of the H8500D-03 is $\approx$ 93 %. This is significantly larger than the statement from the manufacturer, who does not provide measured but only simulated values: $\approx$ 70 % for H8500 and $\approx$ 90 % for R11265 [112, 151].

For the H10966A-103, it was already mentioned in section 5.5.5 that losses in the readout might have occurred. Thus, no statement is made here for this MAPMT type. In addition to this indirect way of determining collection efficiency, prospects of a direct measuring method are currently studied in Wuppertal.

For further detector simulations, the difference between simulated and measured hit multiplicity stated in Tab. 6.5 should be used as global but MAPMT type specific factor (set by the parameter *collectionEff*) for a realistic simulation of the overall detection efficiency. The validity of this approach is supported by the fact that the same difference for the same type of MAPMT (ring position F in 2011, C and B in 2012) is obtained.

6.3.2 Performance gain with WLS films

The simulation of the detector performance with WLS films on top of the MAPMT front windows is done by using input files and parameters as listed in section 6.3.1. In addition, the WLS smearing parameter *sigma_wls* is set for the different MAPMT types according to Tab. 6.4. WLS coated MAPMTs are considered by setting the parameter for the MAPMT type to $pmtType = 10, 14, 16, 18$ (see Tab. 6.2).

The hit multiplicities for each MAPMT type with and without WLS film and the relative increase are summarised in Tab. 6.6. Errors given in Tab. 6.5 are propagated in order to estimate the error on the simulated hit multiplicity gain. Agreement between simulation and data within errors for all MAPMT types can be observed. The hierarchy observed in the data and discussed in section 5.6.2 is reproduced in simulations.

With that, it is shown that the overall detection efficiency of the camera is simulated correctly for both uncoated and WLS coated MAPMTs.

MAPMT type	run no.	hit multiplicity gain data	hit multiplicity gain MC
R11265-103-M16 (2012)	33 (pos. I) WLS	$(18.0 \pm 1.4)\,\%$	$(14.8 \pm 3.9)\,\%$
	90 (pos. I) clean	–	–
H8500D-03 (2012)	22 (pos. C) WLS	$(18.2 \pm 1.5)\,\%$	$(18.3 \pm 4.7)\,\%$
	80 (pos. C) clean	–	–
H8500D-03 (2011)	20 (pos. H) WLS	$(12.2 \pm 1.7)\,\%$	$(10.9 \pm 4.6)\,\%$
	21 (pos. F) clean	–	–
H10966A-103 (2012)	29 (pos. E) WLS	$(21.2 \pm 1.4)\,\%$	$(23.1 \pm 4.3)\,\%$
	63 (pos. E) clean	–	–

Table 6.6 – Increase of hit multiplicity due to the usage of WLS films during the 2011 and 2012 beam test. Within errors, data and simulation are in agreement which shows that the gain in hit multiplicity is correctly simulated.

6.3.3 Electron pion separation

In order simulate the ring radii from electrons and pions in dependence of momentum, a sample of 400 000 electrons and pions with a uniform momentum distribution between 2 GeV/c and 10 GeV/c is generated. They are tracked through the prototype and Cherenkov rings are reconstructed assuming the characteristics of H8500D-03 MAPMTs.

Plotting the fitted ring radii versus particle momentum gives an impression of the convergence of pion and electron radii towards large momenta (see Fig. 6.10). Comparing the simulation with beam test data (see Fig. 5.27) shows qualitative agreement.

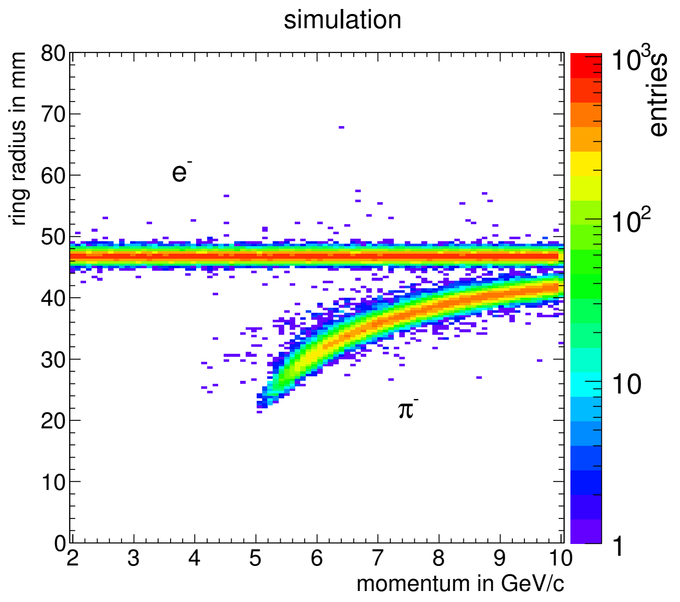

Figure 6.10 – Ring radius versus momentum for a simulated sample of electrons and pions of uniform momentum distribution between 2 GeV/c and 10 GeV/c. A good qualitative agreement between simulation and data (see Fig. 5.27) can be observed.

For a quantitative comparison, the pion suppression factor of the prototype is calculated from a simulation with the following input files and input parameters.

- Simulation
  - 250 000 electrons, 500 000 pions for each momentum
  - 2 GeV/c to 10 GeV/c in steps of 1 GeV/c
  - spatial distribution according to PS/T9 beam characteristics (see Tab. D.1)
- Reconstruction
  - mirror: *RICHglassJLO*
  - radiator: *RICHgas_CO2_dis_Ogawa_Mehu*
  - *nofNoiseHitsInRich* $= 0$
  - *fCrossTalkHitProb* $= 0.02$
  - *sigma_0* $= 0.09\,\mathrm{cm}$
  - *collectionEff* $= 1.0$
  - *pmtType* $= 6$ (see Tab. 6.2)

In this study, many more electrons and pions compared to the studies on hit multiplicity are simulated in order to have a reasonably low statistical error. Since the number of pions within the electron cut determines the pion suppression factor, the number of simulated pions (500 000 for each momentum) is larger than the number of electrons (250 000 for each momentum). This is also the reason why, in the following, the pion suppression factors are shown only down to 7 GeV/c. At lower momenta, the number of simulated pions within the electron cut gets too low, so that special MC methods would be needed to get reliable results. Given the nearly gaussian radius distribution, simply increasing the statistics is not effective.

Figure 6.11 compares the simulated radius distribution for electrons and pions with that from beam test data in the two momentum slices of 8 GeV/c and 10 GeV/c. A general agreement between simulation and data can be observed at both momenta. On closer inspection, it can be seen that at 8 GeV/c the tails of the distribution are wider in the data towards low radii. In addition, the pion distribution exhibits a clear shoulder towards large radii which was identified in section 5.4.3 as muon contamination. Even though muons are not contained in the simulated sample, the distributions are separated far enough to have exact agreement in the pion suppression factor in data and simulation ($\pi_{\mathrm{suppr,data,8\,GeV/c}} = 3714 \pm 646$, $\pi_{\mathrm{suppr,sim,8\,GeV/c}} = 3759 \pm 331$). At 10 GeV/c, only the electron distribution exhibits a tail towards low radii. The shoulder due to muons is pronounced less strongly in the data. However, since electron and pion distributions are much closer at 10 GeV/c, the muon contribution within the electron cut in the data is most probably the reason for the much lower pion suppression factor in data when compared to simulation ($\pi_{\mathrm{suppr,data,10\,GeV/c}} = 740 \pm 129$, $\pi_{\mathrm{suppr,sim,10\,GeV/c}} = 2598 \pm 189$).

The procedure for the determination of the pion suppression factor from simulated events is exactly the same as that used for the beam test data described in section 5.5.7. In this way, results from simulation and data can be directly compared.

Figure 6.12 (top) shows the simulated pion suppression factor as function of momentum for electron efficiencies between $e_{\mathrm{eff}} = 93\,\%$ and $e_{\mathrm{eff}} = 99\,\%$ in a linear scale. Figure 6.12 (bottom) shows a comparison of the pion suppression factor from simulation and from beam test data. It combines Fig. 6.12 (top) and Fig. 5.30. Since the pion suppression factor in data varies over 3 orders of magnitude, a logarithmic scale is chosen.

The following observations can be made.

1. The simulated pion suppression factor drops monotonically from $7\,\mathrm{GeV/c}$ to $10\,\mathrm{GeV/c}$ for all electron efficiencies.
2. The simulated pion suppression factor decreases with increasing electron efficiency as discussed in section 5.5.7.
3. The simulated pion suppression factor
   - drops less strongly with increasing momentum compared to the measurement,
   - is quantitatively in agreement with the measurement from $7\,\mathrm{GeV/c}$ to $9\,\mathrm{GeV/c}$ and for electron efficiencies $\leq 97\,\%$.

In summary, it can be said that the implementation of realistic input parameters into the simulation tool leads to simulated pion suppression factors which very well agree with the beam test results. The prototype performs as expected in terms of electron pion separation capability up to $9\,\mathrm{GeV/c}$ and not too demanding electron efficiency ($e_{\mathrm{eff}} \leq 97\,\%$).

At $10\,\mathrm{GeV/c}$, the prototype does not reach the simulated pion suppression factor. One possible reason is the muon contamination in the pion data sample (see Fig. 6.12 and section 5.4.3).

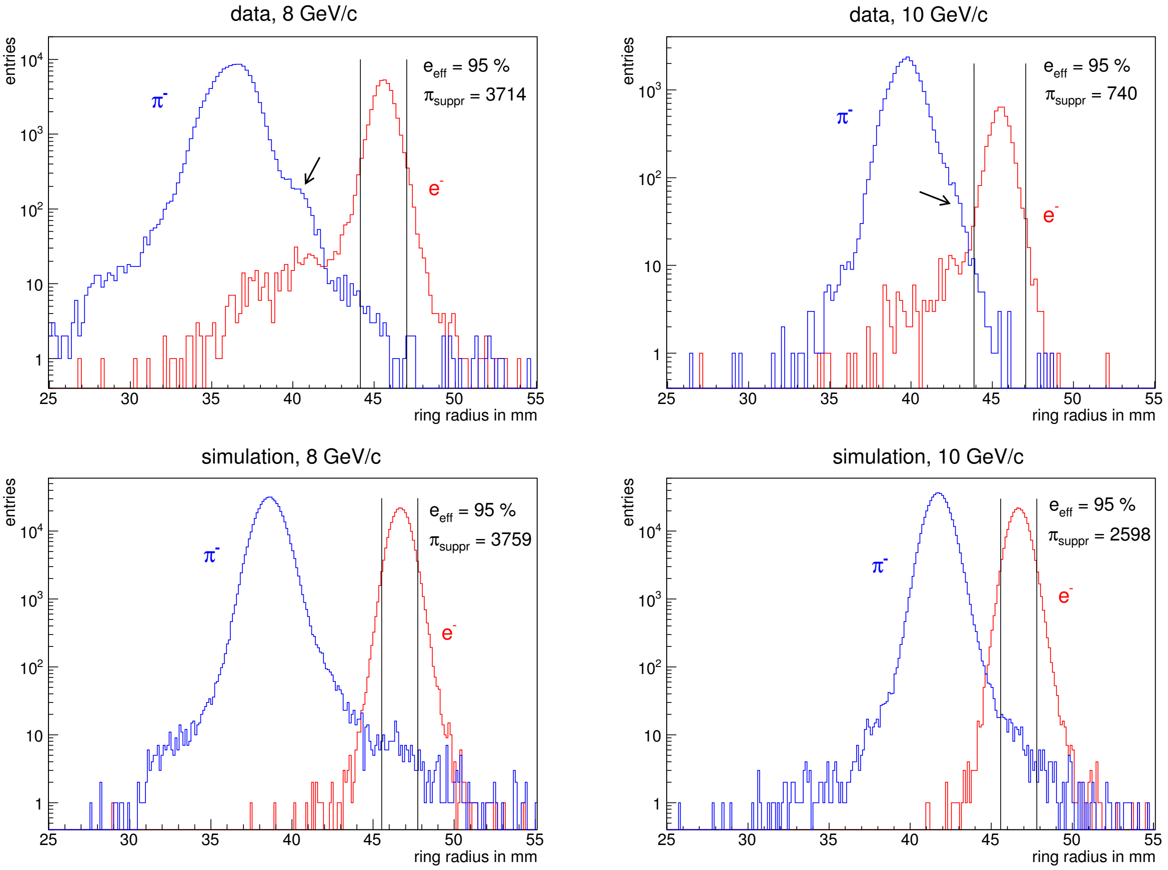

Figure 6.11 – Comparison of electron and pion radius distributions in simulation (bottom) and data from the 2011 beam test (top) at 8 GeV/c (left) and 10 GeV/c (right). In addition to a general agreement between simulation and data in both momentum slices, the following observations can be made: At 8 GeV/c, longer tails towards low radii for electrons and pions are present in the data for both pions and electrons. Furthermore, a shoulder towards large radii can be observed in the data set from the test beam (arrow, top left panel). The shoulder is due to a contamination of the pion sample with muons (see section 5.4.3). The vertical lines indicate the electron cut for $95\,\%$ electron efficiency, i.e. $95\,\%$ of all electrons are located within the indicated interval. Since electron and pion radii are well separated at 8 GeV/c, muons do not creep below the electron cut significantly, resulting in a very good agreement of the pion suppression factor between data and electrons. At 10 GeV/c, the muon contamination is less strong (arrow, top right panel). However, muon radii are so close to electron radii that muons are most probably the reason for the much lower pion suppression factor in data compared to simulation at 10 GeV/c. The shift on the radius axis between data and simulation is due to differences in pressure and temperature which are $p = 1000$ mbar, $T = 0$ °C in simulation and $p = 960$ mbar, $T = 20$ °C in beam test data.

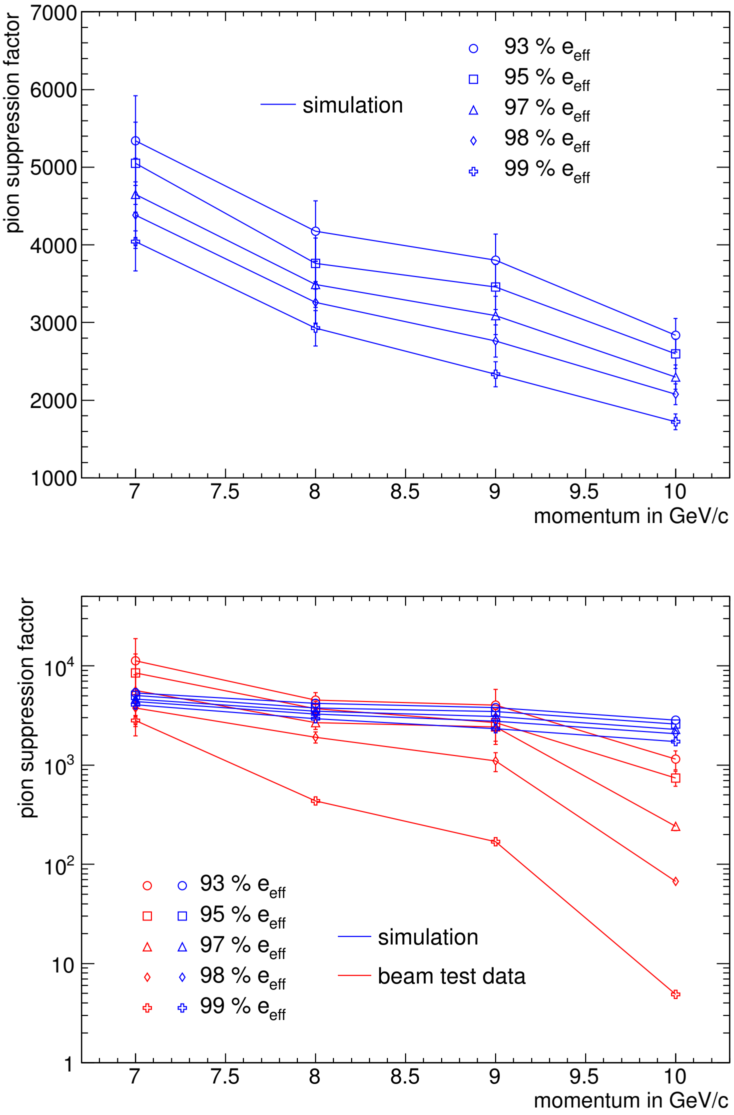

Figure 6.12 – Top: Simulated pion suppression factor as function of momentum for different electron efficiencies in linear scale. Bottom: Comparison of simulated and measured pion suppression factor in logarithmic scale. Pion suppression factors below 7 GeV/c cannot be given due to limited statistics. Simulation and data are in agreement up to 9 GeV/c and $e_{\text{eff}} \leq 97\,\%$. See text for further discussion. Lines between the data points are drawn to guide the eye.

6.4 Summary

Detector simulations for both the prototype and the full RICH detector are performed with the CbmRoot framework. It includes the transport engine GEANT3 for simulating the interactions of particles in the detector. Naturally, dimensions in the geometry files of the prototype and the full RICH detector differ. The media for the important parts however, radiator, mirror, and photon sensors, are the same. Also the reconstruction algorithms are the same for prototype data analysis, prototype simulation and full RICH detector simulation. Therefore, it was possible to verify the detector simulations through comparison with data from prototype beam tests.

The wavelength dependent refractive index and absorption length of the radiator have been updated using well-defined values from literature. The previously measured mirror reflectivity has been extrapolated in order to cover the full sensitive wavelength range of the detector.

More realistic input parameters have been implemented also in the reconstruction step. For this purpose, results from laboratory and beam test measurements have been used. The following parameters were adapted.

- A realistic number of additional noise hits, derived from the measured noise rate during the beam tests, was implemented.
- Additional hits in neighbouring pixels due to crosstalk were added to the real hits with a probability extracted from LED measurements.
- Measured quantum efficiency curves of three different MAPMT types (H8500D-03, H10966A-103, R11265-103-M16) with and without WLS coating were implemented and used for the generation of hits from MC points. The measurements were extrapolated from 200 nm to 180 nm in order to cover the full sensitive wavelength range of the detector.
- The ring sharpness was adjusted via a smearing parameter. In the case of WLS coated MAPMTs, a second smearing parameter was adjusted to simulate the additional smearing due to the isotropic fluorescence in the UV region. The importance of a realistic adjustment of the ring sharpness has been demonstrated by simulating its influence on the hit multiplicity.

With that, a global factor for the collection efficiency has been deduced from comparison of hit multiplicities in data and simulation. With that method, the collection efficiency has been determined to be close to 100 % for the R11265-103-M16 and approximately 93 % for the H8500D-03 MAPMT which is in both cases significantly larger than the simulated but not measured value stated by the manufacturer.

The simulated gain in hit multiplicity with WLS coated MAPMTs compared to uncoated MAPMTs is in agreement with beam test data for all tested MAPMT types, i.e. the performance of the WLS films is understood.

An ultimate quantity for testing the validity of the simulations is the pion suppression factor. It was found that the simulated pion suppression factors agree very well with data up to 9 GeV/c at electron efficiencies up to 97 %.

In summary, the CBM-RICH simulation tool has been updated and successfully verified.

6.5 Conclusion and outlook

The simulation tool for CBM-RICH detector simulations was updated and verified with results from laboratory and beam test measurements. Due to the realistic size of the prototype and the usage of the same ring reconstruction algorithms for beam test data analysis, prototype simulations, and simulations of the full detector, updates and improvements presented in this chapter can be directly used also for physics performance studies of the full CBM-RICH detector.

Pion suppression and comparison of ring quality parameters in prototype and heavy ion simulations
Detector parameters on the ring level such as hit multiplicity and performance gain with WLS films will not differ when simulating the response of the CBM-RICH detector to a heavy ion collision from those presented in sections 6.3.1 and 6.3.2.

The situation is expected to be different for the electron pion separation. The pion suppression factor of the CBM-RICH detector in a heavy ion collision is lower that that for a beam of single particles discussed in section 6.3.3 due to the very high ring and hit densities on the photon camera in the case of a heavy ion collision with particle multiplicites of the order of 1000. Indeed, the simulations presented in section 2.6 for Au+Au collisions show that the electron pion separation capability does not stay on the same level: Integrated over momentum from 0 GeV/c to 12 GeV/c, Fig. 2.12 and 2.13 indicate $\pi_{\text{suppr}} = 1435$ and $\pi_{\text{suppr}} = 360$ at $e_{\text{eff}} \approx 85\,\%$ for Au+Au collisions at 8 AGeV and 25 AGeV, respectively. In contrast, beam test data based on single particle track events show $\pi_{\text{suppr}} = 5247$ for single electrons and pions at a higher electron efficiency of $e_{\text{eff}} = 93\,\%$ and integrated from 7 GeV/c to 10 GeV/c. Extrapolating to the whole momentum range, the pion suppression factor in beam test data is roughly one order of magnitude larger than that achieved for heavy ion collisions.

However, the comparison of ring quality parameters for the updated prototype simulations with those from simulations of the CBM-RICH response to heavy ion collisions allows to draw conclusions on the pion suppression factor.

In section 2.6, the ring quality parameters hit multiplicity N_{det}, ring radius r, ring radius resolution σ_r/r, ring sharpness *dR* were presented for standard simulations of central Au+Au collisions at 25 AGeV beam energy. In these heavy ion simulations, the findings from this chapter are not included. In the prototype simulations, in contrast, updated numbers are used. Table 6.7 compares the ring quality parameters from the prototype with those from the full RICH simulation. It is found that all parameters are comparable. Hence, it can be concluded that results for the ring reconstruction efficiency, the electron identification efficiency, and the pion suppression factors shown in Fig. 2.11 to 2.13 are validated.

	prototype data	prototype simulation	full RICH simulation$^{(\dagger)}$
hit multiplicity N_{det} $^{(*)}$	24.6	26.5	26.1
ring radius r	47.4 mm	46.7 mm	43 mm to 52 mm $^{(\ddagger)}$
radius resolution σ_r/r	1.3 %	1.3 %	1 % to 2 % $^{(\ddagger)}$
ring sharpness *dR*	2.42 mm	2.42 mm	3 mm to 4 mm $^{(\ddagger)}$

Table 6.7 – Ring quality parameters from prototype data and prototype simulation in comparison to the full CBM-RICH simulation. The agreement between data and simulation for the prototype was discussed in the previous sections. Here, it shall be emphasised that the experimentally verified ring quality parameters from the prototype are in agreement with the results from full CBM-RICH simulations mentioned in section 2.6. As a result, also the simulated pion suppression can be considered well-grounded.
$^{(*)}$*pmtType* $= 6$, $^{(\dagger)}$findings from chapter 6 not considered, $^{(\ddagger)}$depending on ring position on the 2.4 m^2 camera plane

Outlook

The aim of this chapter is to validate the detector simulations done so far and to provide a complete set of realistic input parameters for further simulations based on reliable measurements. Corresponding documentation is provided on a wiki page[8]. The relevant code is committed to the CbmRoot repository and available for other users[9]. The simulation of the pion suppression factor under CBM beam conditions and the feasibility of physics measurements including the realistic input parameters presented in this chapter would be the next step.

In particular, the influence of using different MAPMT types on the ring reconstruction and electron identification efficiencies and thus the overall CBM-RICH performance should be studied. In this regard, it might be worth to envisage the optimisation of the ring finding and fitting algorithms for a certain hit multiplicity.

---

[8] http://cbm-wiki.gsi.de/cgi-bin/view/Rich/CbmRichSimulationParameters

[9] new geometry files including mirror and gas properties are committed to the CbmRoot repository: *rich_prototype_v14b.geo* (prototoype) and *rich_08b.geo* (full RICH). Quantum efficiencies of different MAPMT types are hard-coded in *CbmRichProtHitProducer.cxx* (prototype) and *CbmRichHitProducer.cxx* (full RICH) and can be selected in the macro *run_reco.C*.

Chapter 7

Summary

With the objective of contributing to the development of the Ring Imaging Cherenkov detector of the CBM experiment, the following results were obtained over the course of this thesis. Many of them have been incorporated into the CBM-RICH Technical Design Report.

In order to characterise MAPMT candidates for the CBM-RICH camera, a test stand for quantum efficiency and single photon measurements was set up in a dedicated dark room laboratory. It was found that the gain and the spatial homogeneity of all tested MAPMT types are, within certain limits, in agreement with the specifications from the manufacturer. The specified peak values for the quantum efficiency of super bialkali and bialkali photocathodes were also confirmed by measurements. In addition, the spectral dependence of the quantum efficiency was measured down to 200 nm where no information from the manufacturer is provided but which is of particular importance for the Cherenkov photon statistics. The quantum efficiency for super bialkali and bialkali photocathodes was shown to be comparable in the deep UV range. Furthermore, a reduced quantum efficiency in the centre of the photocathode was observed for some MAPMTs.
Single photon measurements revealed that all MAPMT types studied show a clear single photoelectron spectrum in almost all channels and can be used for single photon detection in the CBM-RICH camera. This is in contrast to the recommendation from the manufacturer who does not advertise the H8500C/D for single photon detection. In terms of relative single photon detection efficiency, a hierarchy between the tested MAPMT types could be observed which can be solely explained by differences in quantum efficiency. This means that the single photon detection efficiency, a crucial parameter for the CBM-RICH detector, is basically determined by the quantum efficiency. It could be shown that the latter correlates with the blue sensitivity index provided on every final test sheet. Thus, a rough estimate of the single photon detection efficiency of every MAPMT can be obtained at first glance from the final test sheet.
The additional hit fraction due to crosstalk between neighbouring pixels was found to be a function of the effective threshold and hence of the MAPMT gain and consequently the applied voltage. It is larger for the H8500C/D than for the R11265 and fairly constant for individual MAPMTs of the same type if a common threshold relative to the single photoelectron peak is applied.

To enhance the UV-sensitivity of MAPMTs, a wet-chemical dip-coating process for the application of wavelength shifting films on the front windows of 1" and 2" MAPMTs was developed in collaboration with Hochschule Esslingen and Justus-Liebig-Universität Gießen. The process is fast and produces homogeneous and reproducible films. In a systematic study, the film thickness was optimised for the UV-windows of the two most promising MAPMT types. Measurements of coated MAPMTs show a strongly increased quantum efficiency in the UV and no decrease in the visible wavelength range with respect to uncoated MAPMTs.

The feasibility of the CBM-RICH concept was proven within two beam test campaigns at the CERN PS/T9 beam line with a real-size CBM-RICH prototype detector. This thesis endeavoured to compile all relevant information for a complete description of the prototype with a focus on the camera, the readout, the online monitoring, and the data analysis. The photon camera, constructed by the Wuppertal group, performed very well with a level of uncorrelated noise below $10\,\mathrm{Hz}$ per channel. Given the triggerless readout concept of the CBM experiment, this low noise level is of major importance.

By analysing the data, RICH specific parameters like the number of photoelectrons per Cherenkov ring, the ring radius, the radius resolution, the ring sharpness, and the influence of radiator temperature and pressure on the detector performance were quantified and shown to be in very good agreement with expectations from theory. With a hit multiplicity of 22 photoelectrons per Cherenkov ring, the detector's figure of merit was measured to be $N_0 = 145\,\mathrm{cm}^{-1}$.

The use of WLS coated MAPMTs leads to an increase in hit multiplicity of 18 % to 21 % depending on the MAPMT type. A decrease in ring resolution due to the isotropic fluorescence and the enhanced sensitivity to chromatic dispersion when using WLS films was measured. However, it is small compared to the absolute ring resolution and no criterion for excluding the use of WLS films.

The electron pion separation capability of the prototype was measured as function of momentum with a mixed electron and pion beam of low intensity. In this case, the pion suppression factor is well above the required value up to momenta of 9 GeV/c at electron efficiencies up to 97 %.

The CBM-RICH simulation tool was updated with experimental data from the MAPMT characterisation. Important parameters like quantum efficiency and the additional hit fraction due to crosstalk were implemented for a more realistic description of the detector response.

The simulations were then verified through comparison with beam test data. The pion suppression factor, measured in the beam tests and being a conclusive parameter combining practically all detector specific parameters, was reproduced in simulation thus proving the sound understanding of the detector.

In a third step, simulations were improved by implementing additional parameters and specifying their values which could be obtained only from real data, amongst them the ring sharpness determined by a variety of effects such as the scattering of photons on the mirror surface, in the MAPMT window, and in the wavelength shifting layer when applied. It turned out that an exact implementation of the ring sharpness is essential for a realistic detector simulation.

The agreement between simulated ring quality parameters for the prototype and the full RICH detector validates the physics simulations done so far and shows that the required pion suppression factor for physics measurements with the CBM-RICH detector will be reached with the foreseen detector design.

Conclusion and outlook

With respect to the CBM-RICH camera, the feasibility of the design concept has been proven. Integrated in a real-size prototype, the camera works very well showing beautiful rings, exactly as expected. Three issues, however, shall be addressed before completion of the R&D phase: the decision about the sensor type, the shielding of the magnetic stray field from the CBM dipole magnet in the region of the camera, and the choice of appropriate front-end electronics.

Appendix A

Quantum efficiency measurement setup

A.1 Optical components

Photodiode

The quantum efficiency is calculated from the measured photo currents of PMT and a calibrated photodiode

$$QE(\lambda)_{\mathrm{PMT}} = QE_{\mathrm{diode}}(\lambda) \cdot \frac{\left|I_{\mathrm{PMT}}(\lambda) - I_{\mathrm{PMT,ped}}\right|}{\left|I_{\mathrm{diode}}(\lambda) - I_{\mathrm{diode,ped}}\right|}. \tag{A.1}$$

In this setup, a Hamamatsu S1227-1010BQ photodiode is used. Its calibration curve is shown in Fig. A.1.

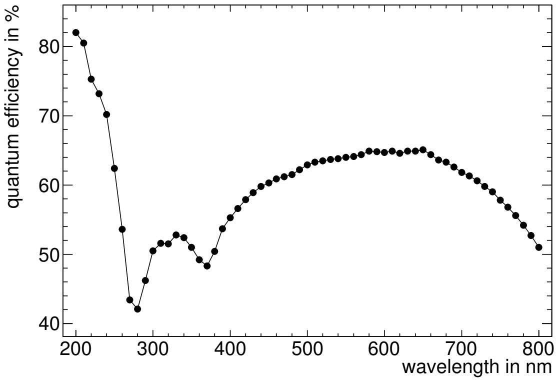

Figure A.1 – Calibration curve of the Hamamatsu S1227-1010BQ photodiode used for *QE* measurements.

Light source and monochromator

The spectrum of the Spectral Products deuterium and tungsten-halogen hybrid light source spreads continuously from 180 nm to 2.6 µm. The monochromator is a Spectral Products CM110 Czerny-Turner type monochromator with double grating. The manufacturer states an accuracy of 0.2 nm and a band pass of 1 nm. The first grating has a blaze of 200 nm and selects wavelengths from 180 nm to 450 nm, the second grating has a blaze of 500 nm and selects wavelengths between 330 nm and 1000 nm. The monochromator has a grating mask on the first grating in order to block stray light which originates from the unused first order spectrum.

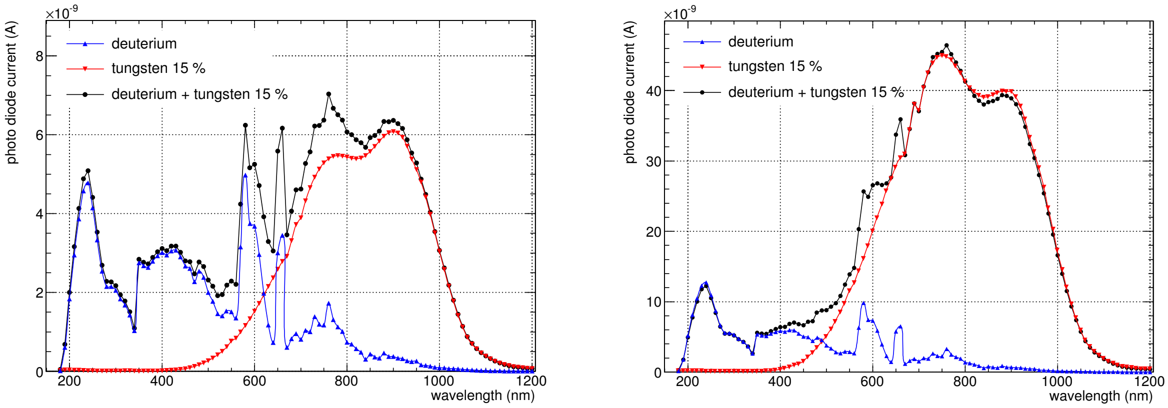

Figure A.2 – Spectra of the deuterium and tungsten-halogen hybrid light source as measured with the calibrated photodiode and the setup in Fig. 3.5. The tungsten-halogen lamp can be continuously regulated, here to 15 % of the maximum power. The drop in the long wavelength range is due to the spectral response of the photodiode. Left: Original light bulb (ASBN-D1-W150-L). It was new at the time of the measurements. Right: Replaced light bulb (ASBN-W-075B). The measurement was done near the end of the light bulb lifetime.

The current of the photodiode as a function of wavelength after inserting the grating mask is shown in Fig. A.2. Even though the light intensity, in particular for the deuterium lamp, varies strongly with wavelength, the *QE* curves turn out to be smooth because intensity peaks cancel out (cf. Fig. A.8).

Changing from one grating to the other is an important part of the measurement process. When the monochromator rotates another grating into the beam, the full light intensity is focussed on the exit slit. To prevent the PMT from being illuminated with high intensity, the beam path is blocked during the changing of gratings by rotating the filter wheel to a blocking position.

Filter wheel and order sorting filters

As the gratings of the monochromator work periodically, higher orders have to be suppressed. This is done by longpass filters which attenuate short and transmit longer wavelengths. There are three of them with transition wavelengths of 320 nm, 520 nm and 660 nm respectively. They are inserted into the optical path before the wavelength is set to 340 nm, 560 nm and 700 nm. The measured transmittance of the order sorting filters is shown in Fig. A.3 (left).

The filters are mounted on a wheel that is moved by a stepper motor equipped with a worm gear able to do 1000 steps/s. The distance between two filters corresponds to 11950 steps. The motor is powered by a 12 V DC voltage supply. Another use of the filter wheel is to block the light during a changing of gratings (see above).

Fibre optic

A quartz fibre (UV 1000/1060AT, NA 0.22, Acrylat Tefzel Jacket, length 5 m, PVC protective tube, both ends polished, CeramOptec) is used to guide the light between the filter wheel and the diode or the PMT. An advantage of its use is the possibility of space-resolved measurements using the xy-stage and the reduction of detecting stray light inside the light tight box. It is important to minimise that kind of stray light because PMT and diode generally have a different size of effective area. The disadvantage of using the optical fibre is its attenuating behaviour in the deep UV (Fig. A.3 right). However, at 180 nm the photo current is still higher than the dark current of max. 10^{-12} A by two orders of magnitude and by 3 orders of magnitude at 240 nm.

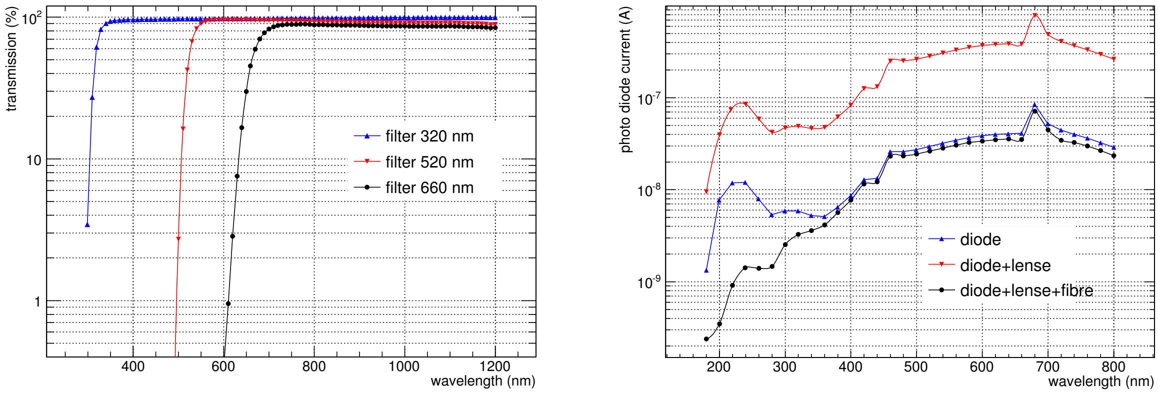

Figure A.3 – Left: Transmission of the order sorting filters as measured with a Varian Cary 500 spectrophotometer. Right: Photodiode current as function of wavelength with and without optical fibre. The attenuating behaviour of the fibre below 350 nm can be seen.

A.2 Software

A Labview programme to control the monochromator and to measure the PMT and photodiode current as a function of wavelength has been written (*QE_main_Test.vi*). Parameters that have to be set are the wavelength range, the stepsize, and the wavelength at which the changing of grating 1 to grating 2 occurs. It is recommended to change the gratings at 340 nm as with grating 1 more stray light passes the monochromator than with grating 2. At 340 nm grating 2 starts to let pass the light. A flowchart of *QE_main_Test.vi* is shown in (Fig. A.4)

A.3 Accuracy of *QE* measurements

Wavelength accuracy

The accuracy of the monochromatic light was measured with two narrowband interference filters (405 nm ± 1% and 546 nm ± 1%) placed into the beam path. The wavelength dependent photodiode current was measured with and without filters. The ratio between the current with and without filters is called "transmission". The monochromator's output wavelength differs by 1 nm from the wavelength of maximum filter transmission at 405 nm and by 2 nm at 545 nm as can be seen in Fig. A.5 (the wavelength of maximimum transmission of the 546 nm filter is 545 nm according to the annexed measurement). Since the filters and the annexed measurements come from the year 1975 and without error estimation, the wavelength accuracy of the monochromator can not be plotted with errors. However, from the measurements the conclusion is drawn that the accuracy is sufficient for the intended application.

Reproducibility

Due to the successive measurements of PMT and photodiode, the reproducibility of *QE* measurements with the constructed setup is determined by the time stability of the light source and the consistency of the optical path. In order to have a constant light intensity the lamps should be switched on 90 minutes before starting a measurement (30 minutes if only the deuterium lamp is used). Fig. A.6 (left) shows that the measurements are reproducible after warming up the lamps. Between measurement 1 and measurement 2 the setup was completely disassembled. The concordance between both measurements shows that the measurement setup

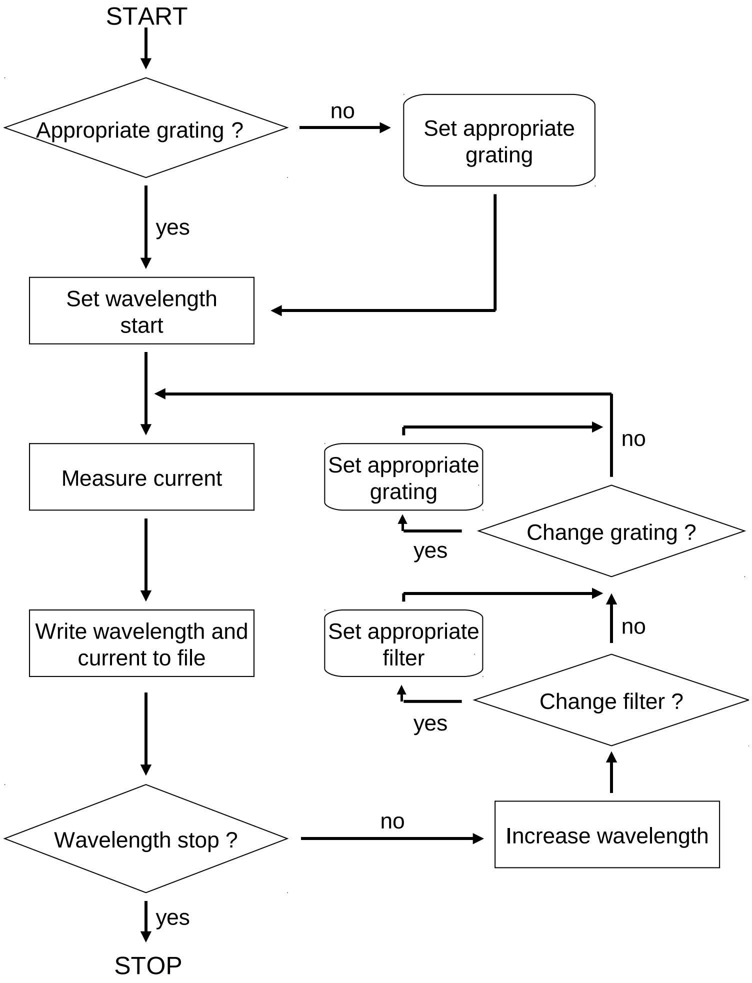

Figure A.4 – Flowchart of the programme *QE_main_Test.vi* to measure the PMT and photodiode current as a function of wavelength.

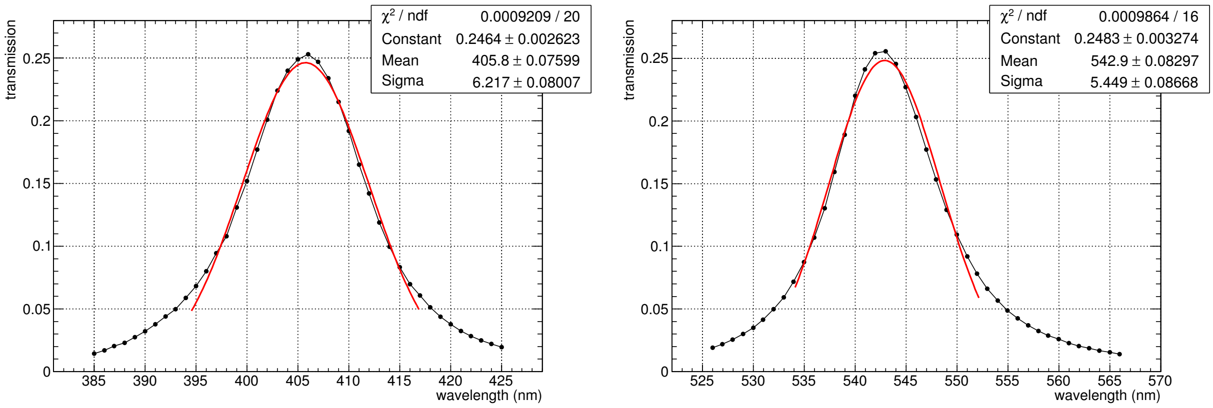

Figure A.5 – Ratio between the photodiode current with and without narrowband filters as a function of wavelength. Left: 405 nm filter: Right: 546 nm filter.

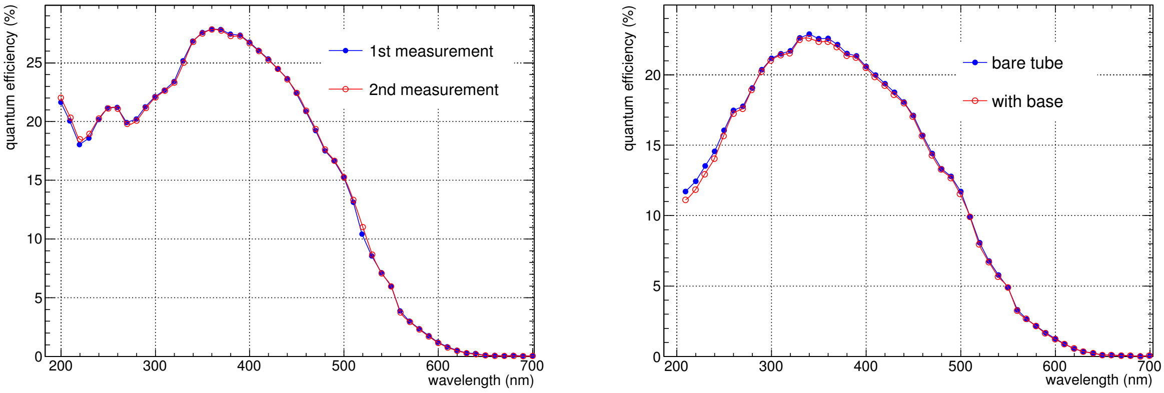

Figure A.6 – Left: *QE* curves of a H8500-03 MAPMT with wavelength shifting coating. The setup has been completely dis and reassembled between the two measurements. It is shown that the measurements are reproducible. Right: *QE* curve of a R10552-03-M64 MAPMT as a bare tube and with a home made base with unsoldered resistor between cathode and dynode system.

is well under control.

Modification of PMTs for *QE* measurements

As mentioned in section 3.3.1 the dynodes of the PMT have to be shorted for *QE* measurements. The dynode pins of bare tubes, i.e. PMTs without base, are directly accessible. If using a PMT with base, in particular a compact MAPMT assembly as the H8500, a 1 MΩ resistor between cathode and dynode system has to be unsoldered. The results are the same if one measures a bare tube or a PMT with base and unsoldered resistor as can be seen in Fig. A.6 (right).

Error bars

Using the Gauss law of error propagation

$$\sigma_f^2 = \sum_{i=1}^{k} \left(\frac{\partial f}{\partial x_i} \sigma_{x_i} \right)^2 \tag{A.2}$$

it is possible to calculate the error σ_f of a function f with k arguments x_i and their errors σ_{x_i} as long as the σ_{x_i} are independent, not too large, and f is not strongly non-linear.
Inserting $f = QE(\lambda)_{\text{PMT}}$ (equation A.1) in (A.2) leads to

$$\begin{aligned}
\sigma_{\text{PMT}}^2 &= \left(\frac{I_{\text{PMT}} - I_{\text{PMT,ped}}}{I_{\text{diode}} - I_{\text{diode,ped}}} \cdot \sigma_{QE_{\text{diode}}} \right)^2 \\
&+ \left(\frac{QE_{\text{diode}}}{I_{\text{diode}} - I_{\text{diode,ped}}} \cdot \sigma_{I_{\text{PMT}}} \right)^2 \\
&+ \left(-\frac{QE_{\text{diode}}(I_{\text{PMT}} - I_{\text{PMT,ped}})}{(I_{\text{diode}} - I_{\text{diode,ped}})^2} \cdot \sigma_{I_{\text{diode}}} \right)^2 \\
&+ \left(\frac{QE_{\text{diode}}}{I_{\text{diode}} - I_{\text{diode,ped}}} \cdot \sigma_{I_{\text{PMT,ped}}} \right)^2 \\
&+ \left(-\frac{QE_{\text{diode}}(I_{\text{PMT}} - I_{\text{PMT,ped}})}{(I_{\text{diode}} - I_{\text{diode,ped}})^2} \cdot \sigma_{I_{\text{diode,ped}}} \right)^2 .
\end{aligned} \tag{A.3}$$

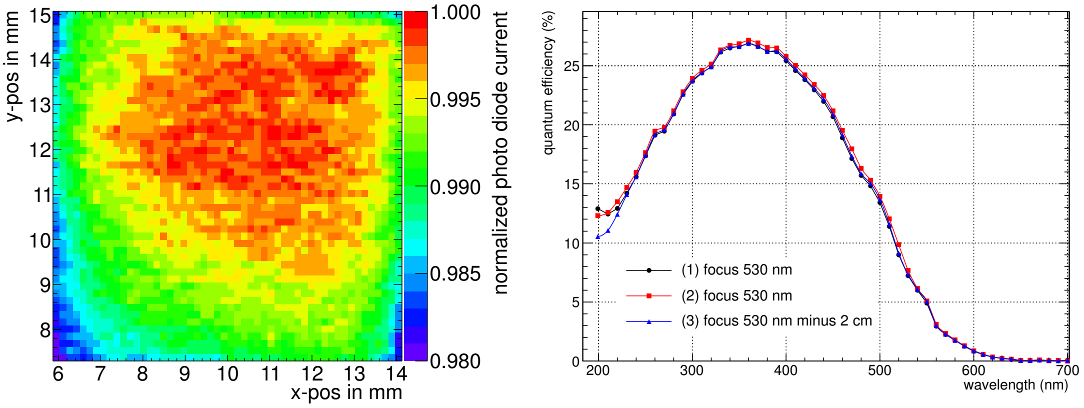

Figure A.7 – Left: Spatially resolved current measured by scanning the photodiode surface with a light spot of constant intensity. The most central 8×8 mm^2 are shown. Right: *QE* curves of a H8500-03 MAPMT. For measurements (1) and (2) the focus was adjusted on the photodiode/PMT for 530 nm. For measurement (3) the photodiode has been placed 2 cm in front of the 530 nm focus.

The contributions to the this error are

- The error of the photodiode calibration is specified to be $\sigma_{QE_{\text{diode}}} = 2$ % absolute.
- The error of the picoamperemeter is depending on the range:
  $\sigma_{I_{\text{PMT}}} = \sigma_{I_{\text{PMT,ped}}} = \sigma_{I_{\text{diode,ped}}} = 0.4$ % for $I \leq 20$ nA
  $\sigma_{I_{\text{PMT}}} = \sigma_{I_{\text{PMT,ped}}} = \sigma_{I_{\text{diode,ped}}} = 0.2$ % for $I \leq 200$ nA
  $\sigma_{I_{\text{PMT}}} = \sigma_{I_{\text{PMT,ped}}} = \sigma_{I_{\text{diode,ped}}} = 0.15$ % for $I \leq 2$ μA
  $\sigma_{I_{\text{PMT}}} = \sigma_{I_{\text{PMT,ped}}} = \sigma_{I_{\text{diode,ped}}} = 0.1$ % for $I \leq 20$ mA

  For the current of the photodiode its inhomogeneity has to be taken into account. It has been determined by scanning the surface with a beam spot of approximately 1 mm in diameter and was measured to be < 2 % (Fig. A.7 left). This value is added to the error of the picoamperemeter:

  $\sigma_{I_{\text{diode}}} = (2 + 0.4)$ % for $I \leq 20$ nA
  $\sigma_{I_{\text{diode}}} = (2 + 0.2)$ % for $I \leq 200$ nA
  $\sigma_{I_{\text{diode}}} = (2 + 0.15)$ % for $I \leq 2$ μA
  $\sigma_{I_{\text{diode}}} = (2 + 0.1)$ % for $I \leq 20$ mA
- It is important to have exactly the same amount of light on PMT and photodiode as differences are a source of errors. It was found that chromatic dispersion can lead to a major contribution to the error: Due to chromatic dispersion of the lenses the focal length is different for different wavelengths. The result is that the light spot in the UV region might reach the outer parts of the photodiode. Therefore, care has to be taken when adjusting the optics at a visible wavelength. Fig. A.7 (right) shows the *QE*-curve of three measurements. Measurement 1 and 2 are made with adjusting the optics to the focus of green light of 530 nm. For measurement 3 the photodiode has been placed 2 cm in front of the 530 nm focus. It can be seen that the adjustment for measurement 3 gives a *QE* curve without underestimating the photodiode current. The standard deviation of the measurements shown in Fig. A.7 (right) is added to $\sigma_{I_{\text{PMT}}}$.

Adding all erros described above according to equation (A.3) leads to error bars for the *QE* measurements as shown in Fig. A.8 for a MAPMT with and without WLS coating.

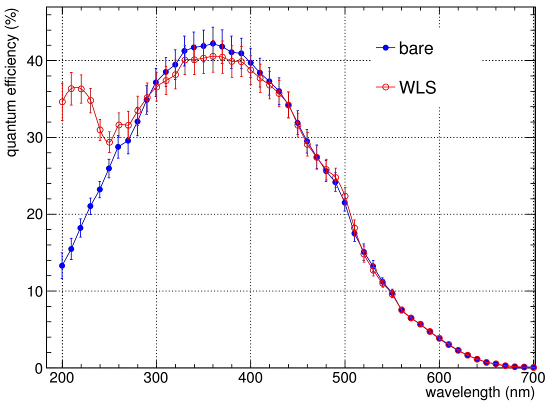

Figure A.8 – *QE* curves of a R11265-103-M16 MAPMT with error bars. Measurements with and without WLS coating are shown. It can be seen that the error bars are relatively large towards shorter wavelengths due to the lower intensity of the light source in the UV range, chromatic dispersion, and the difficult handling of invisible UV light with respect to the optical adjustment.

Appendix B

Stability of single photon counting measurements

In order to compare the relative single photon detection efficiency of different MAPMTs (cf. section 3.10), the single photon source has to be homogeneous in space and constant in time. A measurement has been performed using the setup shown in Fig. 3.7. Two MAPMTs, one H8500D-03 and one R11265-103-M16, were simultaneously illuminated by homogeneously distributed single photons of $405\,\mathrm{nm}$ wavelength. The light source was a laser diode, pulsed with a frequency of $5\,\mathrm{kHz}$. The average hit multiplicity (number of hits per light pulse) was 9.2 hits on the 2" H8500D-03 and 3.2 hits on the 1" R11265-103-M16. The integrated number of hits during the measurement time of $400\,\mathrm{s}$ was $\approx 1.4 \cdot 10^7$ for the H8500D-03 and $\approx 4.8 \cdot 10^6$ for the R11265-103-M16.

A second measurement was done after $30\,\mathrm{min}$ and with the diffuse light source slightly moved. Between the two measurements, the integrated number of hits per MAPMT varied by $0.54\,\%$ for the H8500D-03 and by $0.05\,\%$ for the R11265-103-M16.

From this measurement the conclusion can be drawn that the uncertainties in single photon counting measurements due to inhomogeneities and time stability of the light source is well below $1\,\%$.

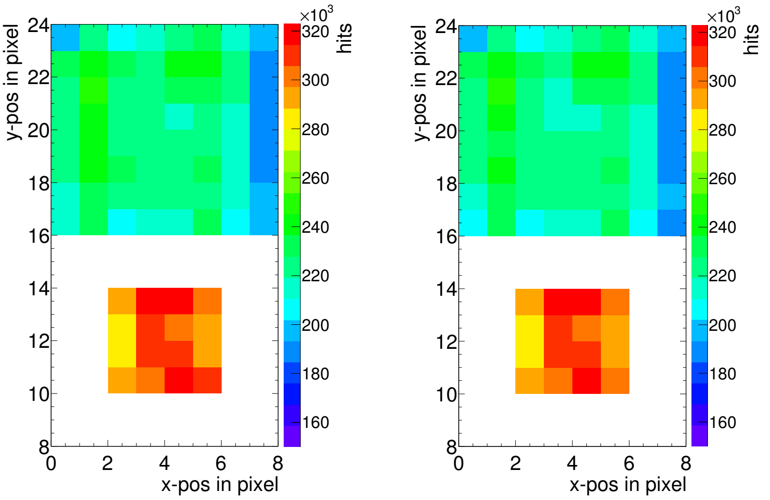

Figure B.1 – Number of hits per pixel for the determination of homogeneity and time stability of the single photon source. The upper MAPMT is a H8500D-03 (DA0140), the lower a R11265-103-M16 (ZN7033).

Appendix C

Single photoelectron spectra

By introducing well-defined charge pulses into the readout chain, the conversion factor between ADC counts and coulombs, i.e. the charge calibration, can be determined. For this purpose, a high-resistance current source is needed. Using a 10 kΩ resistor, voltage pulses from a pulse generator can be converted into charge puslses. The input impedance of the n-xyter chip is small. However, it is not known precisely and is even not necessarily constant. Thus, the fairly large 10 kΩ resistor is used and allows neglecting the n-xyter input impedance when calculating the pulse charge from amplitude and duration of the voltage pulse and the resistor. The circuit diagram of the pulse source is sketched in Fig. C.1.

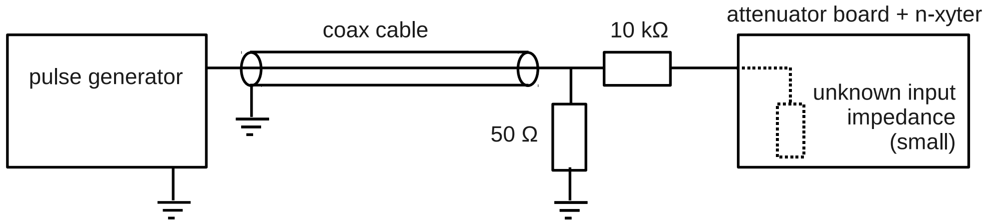

Figure C.1 – Circuit diagram of the pulse source for the calibration of the n-xyter readout chain. The voltage pulse from the pulse generator is converted into a well-defined charge pulse.

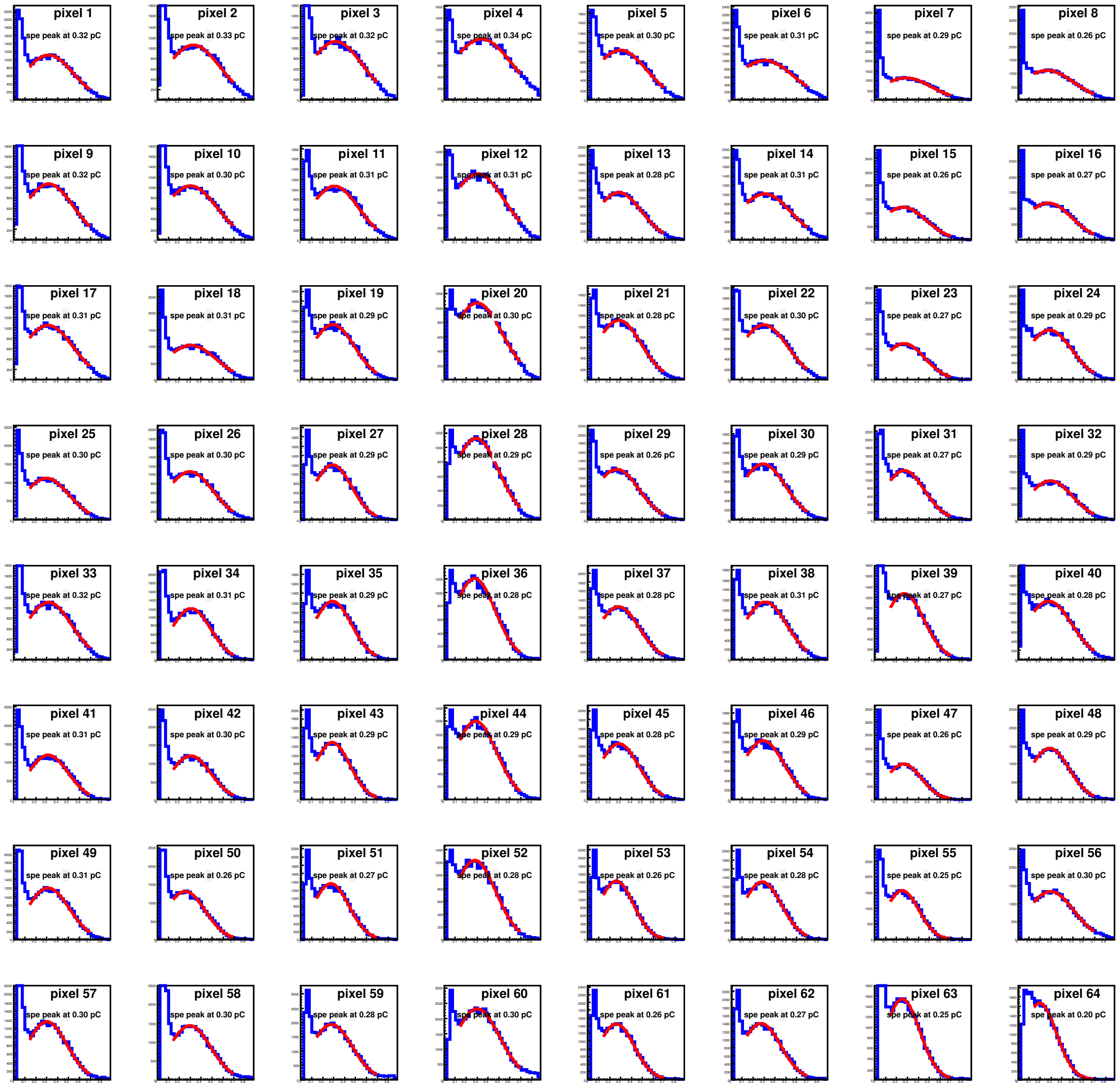

Figure C.2 – Single photoelectron spectra of a H8500D-03 (DA0150). The scale on the x-axis spreads from 0 pC to 0.9 pC.

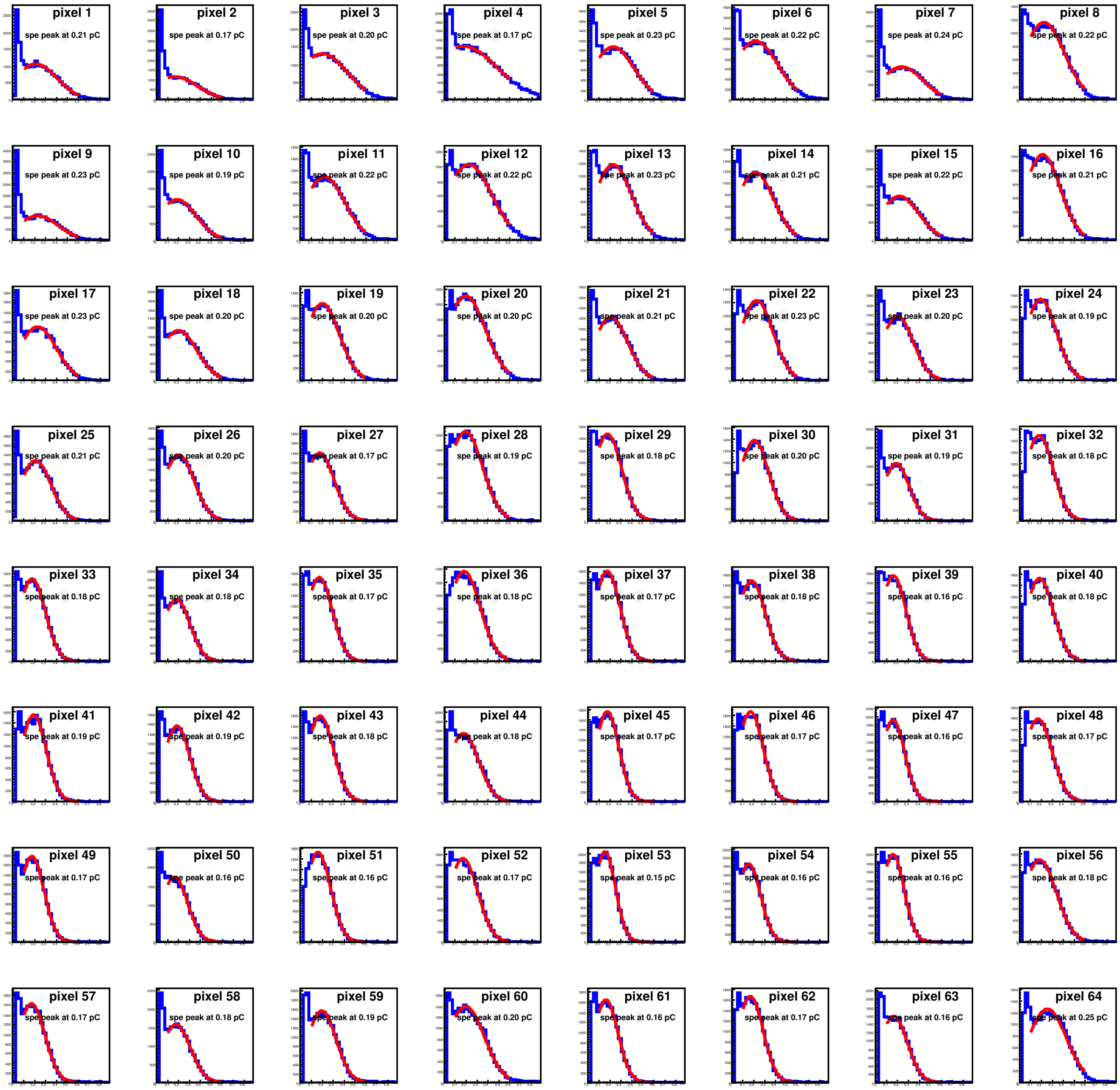

Figure C.3 – Single photoelectron spectra of a “bad” H8500D (CA5093). The scale on the x-axis spreads from 0 pC to 0.9 pC.

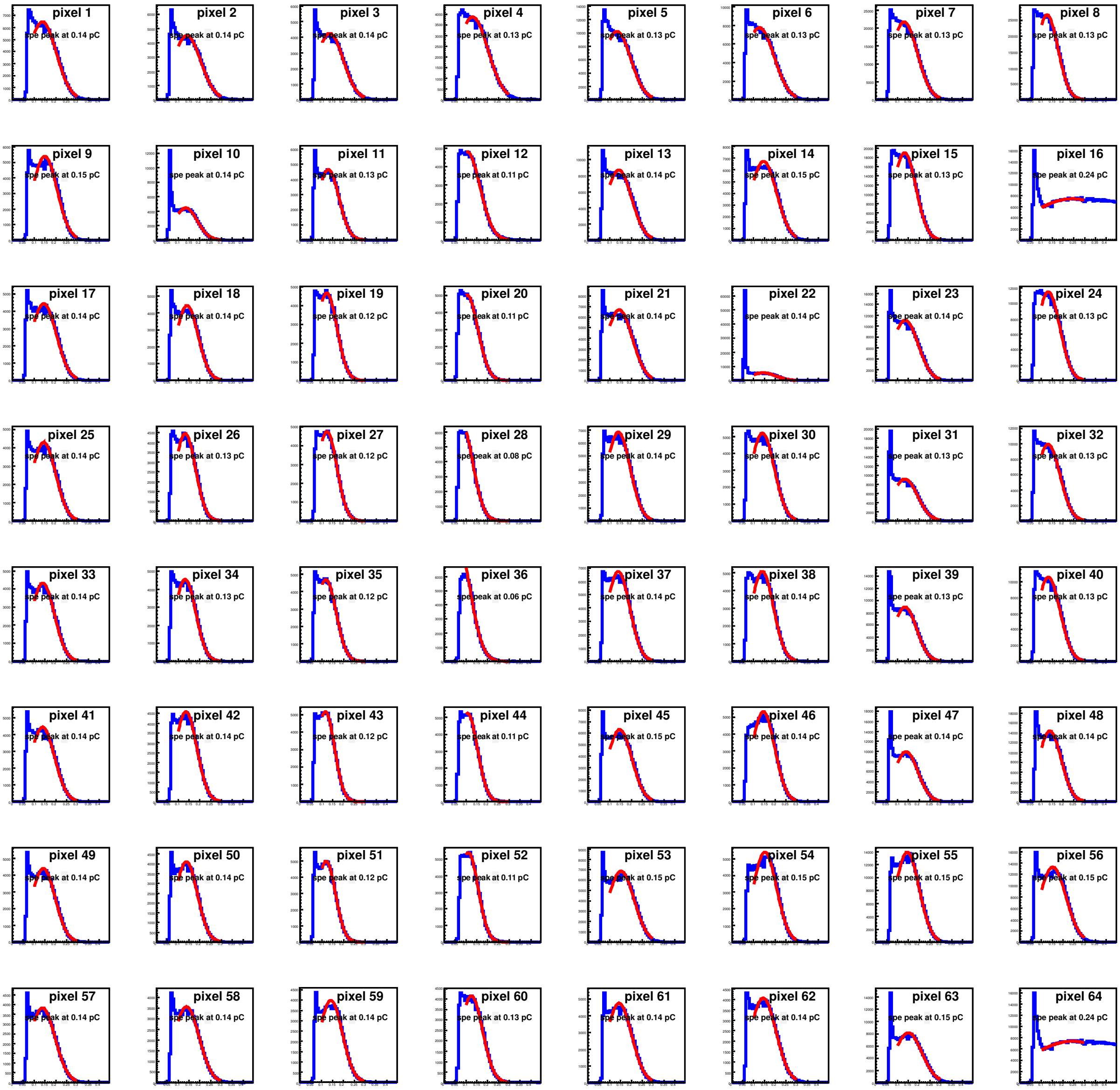

Figure C.4 – Single photoelectron spectra of a H10966A-103 (ZL0003). The scale on the x-axis spreads from 0 pC to 0.45 pC.

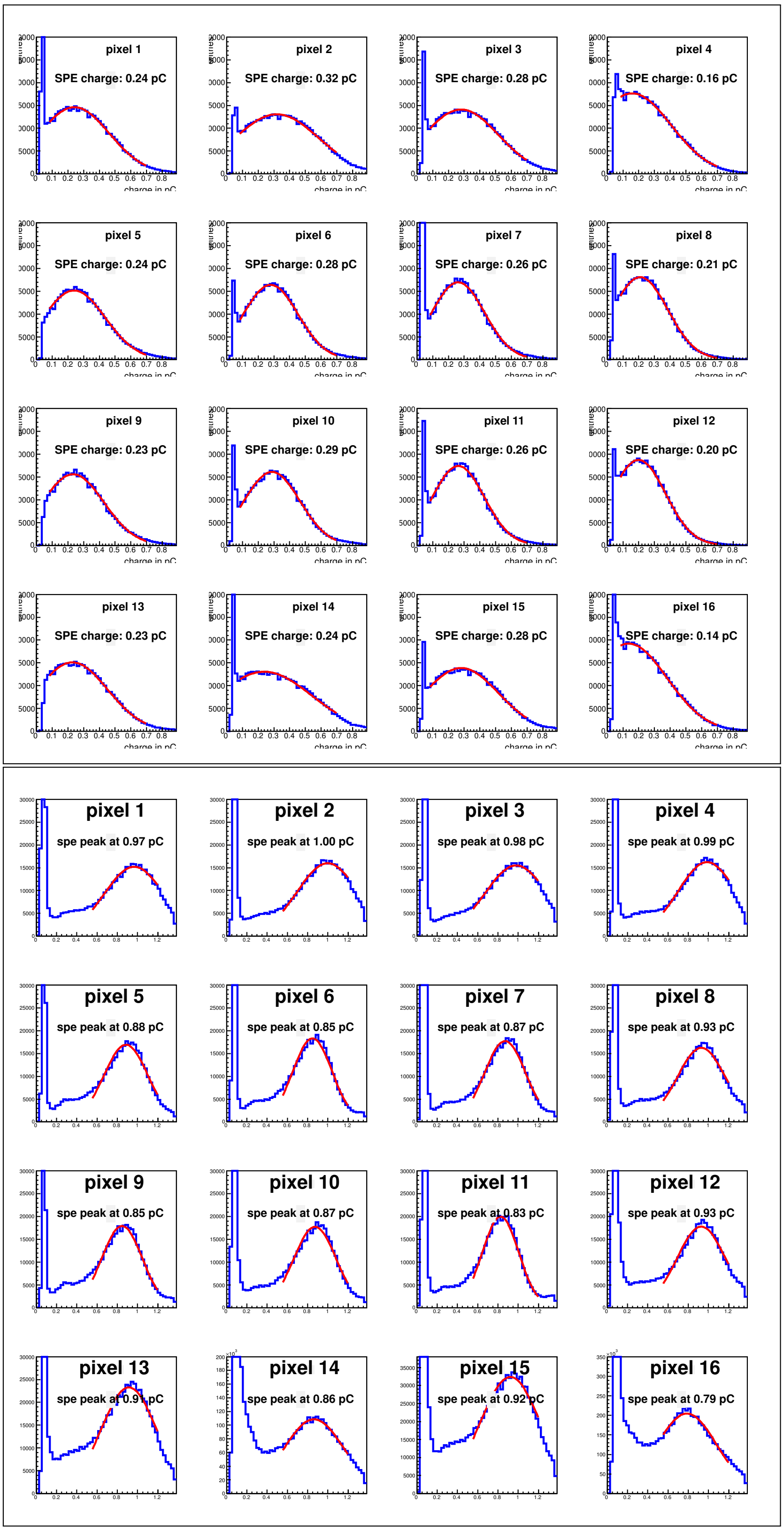

Figure C.5 – Single photoelectron spectra two R11265-103-M16. One average tube is shown on the top (ZN0733) and one with very high gain at the bottom (ZN0593). The scale on the x-axis spreads from 0 pC to 0.9 pC on top and from 0 pC to 1.4 pC at the bottom.

Appendix D

Simulation parameters

parameter name	value	description
pdg	11	particle ID, e^-
pdg	-211	particle ID, π^-
vx	gRandom->Gaus(0.,0.9)	x-coord. of vertex in cm
vy	gRandom->Gaus(0.,0.4)	y-coord. of vertex in cm
vz	-100	z-coord. of vertex in cm
minMomentum	2-10	min. momentum in GeV
maxMomentum	2-10	max. momentum in GeV
theta	TMath::Abs(gRandom->Gaus(0., 5.1e-3))	polar angle
phi	gRandom->Uniform(-1.*TMath::Pi(), TMath::Pi())	azimuthal angle

Table D.1 – Input parameters for the particle generation according to the beam characteristics at the PS/T9 beam line.

```
RICHgas_CO2_dis_Ogawa_Mehu    -2  12. 16. 6. 8.  1.977e-3  1 2
                               0  1  20.  .001
                              79
                              1.77  5000 1.0  1.000446525
                              2.0   5000 1.0  1.000448273
                              2.1   5000 1.0  1.000449086
                              2.2   5000 1.0  1.000449933
                              2.3   5000 1.0  1.000450813
                              2.4   5000 1.0  1.000451726
                              2.5   5000 1.0  1.000452675
                              2.6   5000 1.0  1.000453660
                              2.7   5000 1.0  1.000454682
                              2.8   5000 1.0  1.000455743
                              2.9   5000 1.0  1.000456843
                              3.0   5000 1.0  1.000457985
                              3.1   5000 1.0  1.000459170
                              3.2   5000 1.0  1.000460400
                              3.3   5000 1.0  1.000461676
                              3.4   5000 1.0  1.000463001
                              3.5   5000 1.0  1.000464377
                              3.6   5000 1.0  1.000465804       …
                              3.7   5000 1.0  1.000467286       6.280     4483.05   1.0  1.000529764
                              3.8   5000 1.0  1.000468825       6.357     2370.02   1.0  1.000532434
                              3.9   5000 1.0  1.000470421       6.398     1699.05   1.0  1.000533874
                              4.0   5000 1.0  1.000472079       6.429     1398.85   1.0  1.000534972
                              4.1   5000 1.0  1.000473798       6.476     961.48    1.0  1.000536650
                              4.2   5000 1.0  1.000475582       6.499     715.56    1.0  1.000537477
                              4.3   5000 1.0  1.000477431       6.554     485.13    1.0  1.000539470
                              4.4   5000 1.0  1.000479349       6.564     423.8     1.0  1.000539834
                              4.5   5000 1.0  1.000481337       6.622     241.62    1.0  1.000541964
                              4.6   5000 1.0  1.000483397       6.640     216.33    1.0  1.000542629
                              4.7   5000 1.0  1.000485529       6.689     137.81    1.0  1.000544453
                              4.8   5000 1.0  1.000487737       6.696     132.89    1.0  1.000544715
                              4.9   5000 1.0  1.000490021       6.701     128.31    1.0  1.000544902
                              5.0   5000 1.0  1.000492382       6.716     104.52    1.0  1.000545465
                              5.1   5000 1.0  1.000494822       6.768     68.53     1.0  1.000547427
                              5.2   5000 1.0  1.000497342       6.777     66.68     1.0  1.000547769
                              5.3   5000 1.0  1.000499943       6.794     48.51     1.0  1.000548415
                              5.4   5000 1.0  1.000502625       6.858     35.1      1.0  1.000550866
                              5.5   5000 1.0  1.000505389       6.929     19.79     1.0  1.000553614
                              5.6   5000 1.0  1.000508235       6.946     16.84     1.0  1.000554277
                              5.7   5000 1.0  1.000511164       6.977     12.49     1.0  1.000555490
                              5.735 5000 1.0  1.000512209       6.983     12.36     1.0  1.000555725
                              5.789 5000 1.0  1.000513841       7.005     10        1.0  1.000556590
                              5.844 5000 1.0  1.000515527       7.027     8.69      1.0  1.000557458
                              5.899 5000 1.0  1.000517238       7.050     7.75      1.0  1.000558368
                              5.956 5000 1.0  1.000519038       7.070     6.54      1.0  1.000559162
                              6.014 5000 1.0  1.000520896       7.088     5.62      1.0  1.000559878
                              6.073 5000 1.0  1.000522814       7.131     4.65      1.0  1.000561596
                              6.210 5000 1.0  1.000527376       7.149     3.95      1.0  1.000562318
                              6.225 5000 1.0  1.000527884       7.212     3.13      1.0  1.000564858
                                                         …
```

Figure D.1 – Properties of the new RICH gas medium (radiator). The absorption length of CO_2 is calculated from [107] and its refractive index taken from [68]. The first line of numbers states, from left to right, the number of components (2), the atomic weight of the components (12 for C, 16 for O), the atomic numbers of the components (6 for C, 8 for O), the mass density in g/cm^3, the weight of each component in the mixture (1× C, 2× O). The second line states a sensitivity flag, a field flag, the maximum field value in kgauss, and the boundary crossing precision (see [149] for details). The parameter in the third line gives the number of lines used to define the optical properties of the medium (79 in this case). The following lines contain the photon energy in eV ($1.77\,\text{eV} \mathrel{\widehat{=}} 699.91\,\text{nm}$, $7.212\,\text{eV} \mathrel{\widehat{=}} 171.78\,\text{nm}$) and the corresponding absorption length in cm, the detection efficiency of the radiator, and the refractive index.

```
RICHglassJLO      -2  28.09  16.  14.  8.  2.2  1.  2.
                   1  0  20.  .0001
                   63
                   1.5485 0.1572    1.0  0
                   1.5681 0.1532    1.0  0
                   1.5882 0.1522    1.0  0
                   1.6089 0.1495    1.0  0
                   1.6300 0.1476    1.0  0
                   1.6518 0.1442    1.0  0
                   1.6741 0.1375    1.0  0
                   1.6970 0.1384    1.0  0
                   1.7206 0.1371    1.0  0
                   1.7448 0.1331    1.0  0
                   1.7698 0.1314    1.0  0
                   1.7954 0.1257    1.0  0
                   1.8218 0.1228    1.0  0
                   1.8490 0.1209    1.0  0
                   1.8770 0.1310    1.0  0
                   1.9059 0.1249    1.0  0
                   1.9357 0.1220    1.0  0
                   1.9664 0.1215    1.0  0
                   1.9981 0.1226    1.0  0
                   2.0309 0.1178    1.0  0
                   2.0647 0.1191    1.0  0
                   2.0997 0.1202    1.0  0
                   2.1359 0.1208    1.0  0
                   2.1734 0.1171    1.0  0
                   2.2122 0.1194    1.0  0
                   2.2524 0.1201    1.0  0
                   2.2941 0.1138    1.0  0
                   2.3374 0.1136    1.0  0
                   2.3824 0.1153    1.0  0
                   2.4291 0.1191    1.0  0
                   2.4777 0.1211    1.0  0
                   2.5282 0.1201    1.0  0
                   2.5809 0.1219    1.0  0
                   2.6358 0.1268    1.0  0
                   2.6931 0.1262    1.0  0
                   2.7530 0.1260    1.0  0
                   2.8155 0.1282    1.0  0
                   2.8810 0.1308    1.0  0
                   2.9496 0.1318    1.0  0
                   3.0215 0.1329    1.0  0
                   3.0971 0.1346    1.0  0
                   3.1765 0.1351    1.0  0
                   3.2601 0.1367    1.0  0
                   3.3482 0.1383    1.0  0
                   3.4412 0.1396    1.0  0
                   3.5395 0.1407    1.0  0
                   3.6436 0.1420    1.0  0
                   3.7540 0.1398    1.0  0
                   3.8714 0.1409    1.0  0
                   3.9962 0.1407    1.0  0
                   4.1294 0.1403    1.0  0
                   4.2718 0.1395    1.0  0
                   4.4244 0.1387    1.0  0
                   4.5883 0.1362    1.0  0
                   4.7647 0.1376    1.0  0
                   4.9553 0.1390    1.0  0
                   5.1618 0.1396    1.0  0
                   5.3862 0.1471    1.0  0
                   5.6311 0.1590    1.0  0
                   5.8992 0.1862    1.0  0
                   6.1942 0.2253    1.0  0
                   6.5202 0.2503    1.0  0
                   6.8824 0.2603    1.0  0
```

Figure D.2 – Properties of the new RICH glass medium (mirror). The material is composed of SiO_2. The second column of the optical properties contains the absorption probability in contrast to the RICHgas which is defined by the absorption length. The absorption probability is taken from [71] and extrapolated from 200 nm to 180 nm corresponding to 6.8824 eV. The refractive index of the RICHglass is set to 0.

```
det_type == 6

fLambdaMin = 160.;
fLambdaMax = 700.;
fLambdaStep = 10.;

fEfficiency[0] = 0.0;
fEfficiency[1] = 0.0;
fEfficiency[2] = 0.0324;
fEfficiency[3] = 0.0586;
fEfficiency[4] = 0.0945;
fEfficiency[5] = 0.1061;
fEfficiency[6] = 0.1265;
fEfficiency[7] = 0.1482;
fEfficiency[8] = 0.1668;
fEfficiency[9] = 0.1887;
fEfficiency[10] = 0.2093;
fEfficiency[11] = 0.2134;
fEfficiency[12] = 0.2303;
fEfficiency[13] = 0.2482;
fEfficiency[14] = 0.2601;
fEfficiency[15] = 0.2659;
fEfficiency[16] = 0.2702;
fEfficiency[17] = 0.283;
fEfficiency[18] = 0.2863;
fEfficiency[19] = 0.2863;
fEfficiency[20] = 0.2884;
fEfficiency[21] = 0.286;
fEfficiency[22] = 0.2811;
fEfficiency[23] = 0.2802;
fEfficiency[24] = 0.272;
fEfficiency[25] = 0.2638;
fEfficiency[26] = 0.2562;
fEfficiency[27] = 0.2472;
fEfficiency[28] = 0.2368;
fEfficiency[29] = 0.2218;
fEfficiency[30] = 0.2032;
fEfficiency[31] = 0.186;
fEfficiency[32] = 0.1735;
fEfficiency[33] = 0.1661;
fEfficiency[34] = 0.1483;
fEfficiency[35] = 0.121;
fEfficiency[36] = 0.0959;
fEfficiency[37] = 0.0782;
fEfficiency[38] = 0.0647;
fEfficiency[39] = 0.0538;
fEfficiency[40] = 0.0372;
fEfficiency[41] = 0.0296;
fEfficiency[42] = 0.0237;
fEfficiency[43] = 0.0176;
fEfficiency[44] = 0.0123;
fEfficiency[45] = 0.0083;
fEfficiency[46] = 0.005;
fEfficiency[47] = 0.003;
fEfficiency[48] = 0.0017;
fEfficiency[49] = 0.0008;
fEfficiency[50] = 0.0006;
fEfficiency[51] = 0.0003;
fEfficiency[52] = 0.0003;
fEfficiency[53] = 0.0002;
fEfficiency[54] = 0.0001;
```

Figure D.3 – Numerical *QE* values for *pmtType* = 6: H8500D-03 (posF in CernOct2011 setup, DA0132, DA0136, DA0138, DA0147) as implemented in *CbmRichHitProducer.cxx* and *CbmRichProtHitProducer.cxx*.

```
det_type == 10

fLambdaMin = 180.;
fLambdaMax = 640.;
fLambdaStep = 10.;

fEfficiency[0] = 0.178;
fEfficiency[1] = 0.200;
fEfficiency[2] = 0.218;
fEfficiency[3] = 0.222;
fEfficiency[4] = 0.226;
fEfficiency[5] = 0.228;
fEfficiency[6] = 0.214;
fEfficiency[7] = 0.210;
fEfficiency[8] = 0.229;
fEfficiency[9] = 0.231;
fEfficiency[10] = 0.244;
fEfficiency[11] = 0.253;
fEfficiency[12] = 0.259;
fEfficiency[13] = 0.263;
fEfficiency[14] = 0.266;
fEfficiency[15] = 0.277;
fEfficiency[16] = 0.280;
fEfficiency[17] = 0.274;
fEfficiency[18] = 0.275;
fEfficiency[19] = 0.270;
fEfficiency[20] = 0.264;
fEfficiency[21] = 0.263;
fEfficiency[22] = 0.254;
fEfficiency[23] = 0.246;
fEfficiency[24] = 0.239;
fEfficiency[25] = 0.229;
fEfficiency[26] = 0.219;
fEfficiency[27] = 0.207;
fEfficiency[28] = 0.193;
fEfficiency[29] = 0.179;
fEfficiency[30] = 0.161;
fEfficiency[31] = 0.149;
fEfficiency[32] = 0.135;
fEfficiency[33] = 0.117;
fEfficiency[34] = 0.103;
fEfficiency[35] = 0.082;
fEfficiency[36] = 0.065;
fEfficiency[37] = 0.056;
fEfficiency[38] = 0.036;
fEfficiency[39] = 0.030;
fEfficiency[40] = 0.024;
fEfficiency[41] = 0.018;
fEfficiency[42] = 0.013;
fEfficiency[43] = 0.009;
fEfficiency[44] = 0.006;
fEfficiency[45] = 0.004;
fEfficiency[46] = 0.002;
```

Figure D.4 – Numerical *QE* values for *pmtType* $= 10$: H8500D-03 (posH in CernOct2011 setup, DA0140, DA0141, DA0142, DA0154) with dip-coated WLS films as implemented in *CbmRichHitProducer.cxx* and *CbmRichProtHitProducer.cxx*.

```
det_type == 13

fLambdaMin = 180.;
fLambdaMax = 640.;
fLambdaStep = 10.;

fEfficiency[0] = 0.043;
fEfficiency[1] = 0.078;
fEfficiency[2] = 0.123;
fEfficiency[3] = 0.146;
fEfficiency[4] = 0.173;
fEfficiency[5] = 0.202;
fEfficiency[6] = 0.225;
fEfficiency[7] = 0.253;
fEfficiency[8] = 0.281;
fEfficiency[9] = 0.290;
fEfficiency[10] = 0.315;
fEfficiency[11] = 0.344;
fEfficiency[12] = 0.366;
fEfficiency[13] = 0.378;
fEfficiency[14] = 0.384;
fEfficiency[15] = 0.400;
fEfficiency[16] = 0.403;
fEfficiency[17] = 0.404;
fEfficiency[18] = 0.407;
fEfficiency[19] = 0.403;
fEfficiency[20] = 0.396;
fEfficiency[21] = 0.395;
fEfficiency[22] = 0.383;
fEfficiency[23] = 0.370;
fEfficiency[24] = 0.359;
fEfficiency[25] = 0.347;
fEfficiency[26] = 0.331;
fEfficiency[27] = 0.310;
fEfficiency[28] = 0.285;
fEfficiency[29] = 0.263;
fEfficiency[30] = 0.244;
fEfficiency[31] = 0.232;
fEfficiency[32] = 0.213;
fEfficiency[33] = 0.182;
fEfficiency[34] = 0.151;
fEfficiency[35] = 0.126;
fEfficiency[36] = 0.106;
fEfficiency[37] = 0.092;
fEfficiency[38] = 0.069;
fEfficiency[39] = 0.060;
fEfficiency[40] = 0.051;
fEfficiency[41] = 0.042;
fEfficiency[42] = 0.034;
fEfficiency[43] = 0.026;
fEfficiency[44] = 0.019;
fEfficiency[45] = 0.014;
fEfficiency[46] = 0.009;
```

Figure D.5 – Numerical *QE* values for *pmtType* $= 13$: R11265-103-M16 (ZN0590, ZN0593, ZN0731, ZN0733) as implemented in *CbmRichHitProducer.cxx* and *CbmRichProtHitProducer.cxx*.

```
det_type == 14

fLambdaMin = 180.;
fLambdaMax = 640.;
fLambdaStep = 10.;

fEfficiency[0] = 0.239;
fEfficiency[1] = 0.294;
fEfficiency[2] = 0.332;
fEfficiency[3] = 0.351;
fEfficiency[4] = 0.352;
fEfficiency[5] = 0.338;
fEfficiency[6] = 0.303;
fEfficiency[7] = 0.286;
fEfficiency[8] = 0.307;
fEfficiency[9] = 0.307;
fEfficiency[10] = 0.324;
fEfficiency[11] = 0.340;
fEfficiency[12] = 0.354;
fEfficiency[13] = 0.364;
fEfficiency[14] = 0.371;
fEfficiency[15] = 0.390;
fEfficiency[16] = 0.389;
fEfficiency[17] = 0.392;
fEfficiency[18] = 0.395;
fEfficiency[19] = 0.393;
fEfficiency[20] = 0.388;
fEfficiency[21] = 0.388;
fEfficiency[22] = 0.378;
fEfficiency[23] = 0.367;
fEfficiency[24] = 0.358;
fEfficiency[25] = 0.347;
fEfficiency[26] = 0.333;
fEfficiency[27] = 0.310;
fEfficiency[28] = 0.384;
fEfficiency[29] = 0.265;
fEfficiency[30] = 0.248;
fEfficiency[31] = 0.238;
fEfficiency[32] = 0.220;
fEfficiency[33] = 0.188;
fEfficiency[34] = 0.150;
fEfficiency[35] = 0.123;
fEfficiency[36] = 0.104;
fEfficiency[37] = 0.089;
fEfficiency[38] = 0.068;
fEfficiency[39] = 0.058;
fEfficiency[40] = 0.050;
fEfficiency[41] = 0.041;
fEfficiency[42] = 0.033;
fEfficiency[43] = 0.025;
fEfficiency[44] = 0.018;
fEfficiency[45] = 0.013;
fEfficiency[46] = 0.008;
```

Figure D.6 – Numerical *QE* values for *pmtType* $= 14$: R11265-103-M16 (ZN0590, ZN0593, ZN0731, ZN0733) with di-coated WLS films as implemented in *CbmRichHitProducer.cxx* and *CbmRichProtHitProducer.cxx*.

```
det_type == 15

fLambdaMin = 180.;
fLambdaMax = 640.;
fLambdaStep = 10.;

fEfficiency[0] = 0.037;
fEfficiency[1] = 0.063;
fEfficiency[2] = 0.103;
fEfficiency[3] = 0.110;
fEfficiency[4] = 0.131;
fEfficiency[5] = 0.153;
fEfficiency[6] = 0.172;
fEfficiency[7] = 0.195;
fEfficiency[8] = 0.215;
fEfficiency[9] = 0.217;
fEfficiency[10] = 0.232;
fEfficiency[11] = 0.249;
fEfficiency[12] = 0.261;
fEfficiency[13] = 0.267;
fEfficiency[14] = 0.271;
fEfficiency[15] = 0.285;
fEfficiency[16] = 0.286;
fEfficiency[17] = 0.285;
fEfficiency[18] = 0.287;
fEfficiency[19] = 0.285;
fEfficiency[20] = 0.280;
fEfficiency[21] = 0.279;
fEfficiency[22] = 0.272;
fEfficiency[23] = 0.264;
fEfficiency[24] = 0.256;
fEfficiency[25] = 0.248;
fEfficiency[26] = 0.239;
fEfficiency[27] = 0.223;
fEfficiency[28] = 0.204;
fEfficiency[29] = 0.189;
fEfficiency[30] = 0.177;
fEfficiency[31] = 0.170;
fEfficiency[32] = 0.155;
fEfficiency[33] = 0.130;
fEfficiency[34] = 0.105;
fEfficiency[35] = 0.087;
fEfficiency[36] = 0.073;
fEfficiency[37] = 0.060;
fEfficiency[38] = 0.041;
fEfficiency[39] = 0.033;
fEfficiency[40] = 0.027;
fEfficiency[41] = 0.020;
fEfficiency[42] = 0.015;
fEfficiency[43] = 0.010;
fEfficiency[44] = 0.006;
fEfficiency[45] = 0.004;
fEfficiency[46] = 0.003;
```

Figure D.7 – Numerical *QE* values for *pmtType* $= 15$: H8500D-03 (posC in CernOct2012 setup, DA0141 ,DA0142, DA0147, DA0154) as implemented in *CbmRichHitProducer.cxx* and *CbmRichProtHitProducer.cxx*.

```
det_type == 16

fLambdaMin = 180.;
fLambdaMax = 640.;
fLambdaStep = 10.;

fEfficiency[0] = 0.202;
fEfficiency[1] = 0.240;
fEfficiency[2] = 0.269;
fEfficiency[3] = 0.277;
fEfficiency[4] = 0.279;
fEfficiency[5] = 0.273;
fEfficiency[6] = 0.245;
fEfficiency[7] = 0.228;
fEfficiency[8] = 0.243;
fEfficiency[9] = 0.243;
fEfficiency[10] = 0.253;
fEfficiency[11] = 0.259;
fEfficiency[12] = 0.262;
fEfficiency[13] = 0.263;
fEfficiency[14] = 0.265;
fEfficiency[15] = 0.278;
fEfficiency[16] = 0.279;
fEfficiency[17] = 0.281;
fEfficiency[18] = 0.283;
fEfficiency[19] = 0.281;
fEfficiency[20] = 0.277;
fEfficiency[21] = 0.275;
fEfficiency[22] = 0.267;
fEfficiency[23] = 0.260;
fEfficiency[24] = 0.253;
fEfficiency[25] = 0.245;
fEfficiency[26] = 0.234;
fEfficiency[27] = 0.219;
fEfficiency[28] = 0.201;
fEfficiency[29] = 0.187;
fEfficiency[30] = 0.175;
fEfficiency[31] = 0.167;
fEfficiency[32] = 0.150;
fEfficiency[33] = 0.124;
fEfficiency[34] = 0.098;
fEfficiency[35] = 0.080;
fEfficiency[36] = 0.066;
fEfficiency[37] = 0.055;
fEfficiency[38] = 0.040;
fEfficiency[39] = 0.033;
fEfficiency[40] = 0.026;
fEfficiency[41] = 0.020;
fEfficiency[42] = 0.014;
fEfficiency[43] = 0.010;
fEfficiency[44] = 0.006;
fEfficiency[45] = 0.004;
fEfficiency[46] = 0.002;
```

Figure D.8 – Numerical *QE* values for *pmtType* $= 16$: H8500D-03 (posC in CernOct2012 setup, DA0141 ,DA0142, DA0147, DA0154) with dip-coated WLS films as implemented in *CbmRichHitProducer.cxx* and *CbmRichProtHitProducer.cxx*.

```
det_type == 17

fLambdaMin = 180.;
fLambdaMax = 640.;
fLambdaStep = 10.;

fEfficiency[0] = 0.007;
fEfficiency[1] = 0.040;
fEfficiency[2] = 0.085;
fEfficiency[3] = 0.103;
fEfficiency[4] = 0.130;
fEfficiency[5] = 0.160;
fEfficiency[6] = 0.186;
fEfficiency[7] = 0.215;
fEfficiency[8] = 0.244;
fEfficiency[9] = 0.256;
fEfficiency[10] = 0.281;
fEfficiency[11] = 0.310;
fEfficiency[12] = 0.332;
fEfficiency[13] = 0.344;
fEfficiency[14] = 0.355;
fEfficiency[15] = 0.376;
fEfficiency[16] = 0.382;
fEfficiency[17] = 0.386;
fEfficiency[18] = 0.390;
fEfficiency[19] = 0.390;
fEfficiency[20] = 0.387;
fEfficiency[21] = 0.386;
fEfficiency[22] = 0.376;
fEfficiency[23] = 0.365;
fEfficiency[24] = 0.356;
fEfficiency[25] = 0.345;
fEfficiency[26] = 0.328;
fEfficiency[27] = 0.302;
fEfficiency[28] = 0.278;
fEfficiency[29] = 0.257;
fEfficiency[30] = 0.241;
fEfficiency[31] = 0.227;
fEfficiency[32] = 0.191;
fEfficiency[33] = 0.153;
fEfficiency[34] = 0.128;
fEfficiency[35] = 0.112;
fEfficiency[36] = 0.098;
fEfficiency[37] = 0.085;
fEfficiency[38] = 0.064;
fEfficiency[39] = 0.055;
fEfficiency[40] = 0.047;
fEfficiency[41] = 0.039;
fEfficiency[42] = 0.030;
fEfficiency[43] = 0.023;
fEfficiency[44] = 0.017;
fEfficiency[45] = 0.011;
fEfficiency[46] = 0.007;
```

Figure D.9 – Numerical *QE* values for *pmtType* $= 17$: H10966A-103 (posE in CernOct2012 setup, ZL0003) as implemented in *CbmRichHitProducer.cxx* and *CbmRichProtHitProducer.cxx*.

```
det_type == 18

fLambdaMin = 180.;
fLambdaMax = 640.;
fLambdaStep = 10.;

fEfficiency[0] = 0.241;
fEfficiency[1] = 0.304;
fEfficiency[2] = 0.351;
fEfficiency[3] = 0.364;
fEfficiency[4] = 0.368;
fEfficiency[5] = 0.357;
fEfficiency[6] = 0.311;
fEfficiency[7] = 0.279;
fEfficiency[8] = 0.299;
fEfficiency[9] = 0.304;
fEfficiency[10] = 0.321;
fEfficiency[11] = 0.329;
fEfficiency[12] = 0.336;
fEfficiency[13] = 0.342;
fEfficiency[14] = 0.350;
fEfficiency[15] = 0.370;
fEfficiency[16] = 0.374;
fEfficiency[17] = 0.379;
fEfficiency[18] = 0.383;
fEfficiency[19] = 0.384;
fEfficiency[20] = 0.381;
fEfficiency[21] = 0.382;
fEfficiency[22] = 0.372;
fEfficiency[23] = 0.362;
fEfficiency[24] = 0.354;
fEfficiency[25] = 0.344;
fEfficiency[26] = 0.327;
fEfficiency[27] = 0.300;
fEfficiency[28] = 0.275;
fEfficiency[29] = 0.259;
fEfficiency[30] = 0.244;
fEfficiency[31] = 0.231;
fEfficiency[32] = 0.195;
fEfficiency[33] = 0.155;
fEfficiency[34] = 0.130;
fEfficiency[35] = 0.113;
fEfficiency[36] = 0.097;
fEfficiency[37] = 0.083;
fEfficiency[38] = 0.065;
fEfficiency[39] = 0.055;
fEfficiency[40] = 0.046;
fEfficiency[41] = 0.038;
fEfficiency[42] = 0.030;
fEfficiency[43] = 0.022;
fEfficiency[44] = 0.016;
fEfficiency[45] = 0.011;
fEfficiency[46] = 0.007;
```

Figure D.10 – Numerical *QE* values for *pmtType* = 18: H10966A-103 (posE in CernOct2012 setup, ZL0003) with dip-coated WLS film as implemented in *CbmRichHitProducer.cxx* and *CbmRichProtHitProducer.cxx*.

Appendix E

List of symbols and abbreviations

α	Fine-structure constant
$\beta = v/c$	Velocity in units of the speed of light
λ	Wavelength
μ_B	Baryon chemical potential
π_{suppr}	Pion suppression factor
ρ_B	Net baryon density
σ_r	Width of a gaussian fit to the ring radius distribution
τ	Lifetime
θ	Cherenkov angle
B	Magnetic field strength
c	Speed of light in the vacuum
E	Energy
f	Focal length
I	Electric current
h	Planck constant
L	Radiator length
n	Refractive index
N	Number of emitted Cherenkov photons
N_{det}	Number of detected Cherenkov photons (hit multiplicity)
m_{ee}	Invariant mass of an $e^{\pm}$ pair
p	Momentum; pressure
p_t	Transverse momentum
Q	Electric charge
QE	Quantum efficiency
r	Ring radius
R	Mirror radius of curvature
T	Temperature
T_C	Critical temperature
v	Velocity
y	Rapidity

ADC	Analog-to-digital converter
BA	Bialkali
CERN	European Organization for Nuclear Research
CBM	Compressed Baryonic Matter
ECAL	Electromagnetic calorimeter
FAIR	Facility for Antiproton and Ion Research
FPGA	Field-programmable gate array
GSI	Helmholtzzentrum für Schwerionenforschung
HV	High voltage
LHC	Large Hadron Collider
MCP	Micro Channel Plate photomultiplier tube
MAPMT	Multianode photomultiplier tube
MUCH	Muon Detection System
MVD	Micro-Vertex Detector
NICA	Nuclotron-based Ion Collider Facility
PMT	Photomultiplier tube
PS	Proton Synchrotron
PSD	Projectile Spectator Detector
PT	p-Terphenyl
RICH	Ring Imaging Cherenkov detector
RHIC	Relativistic Heavy Ion Collider
SBA	Super bialkali
SIS	Schwerionensynchrotron at GSI
STS	Silicon Tracking System
TOF	Time-of-flight detector
TRD	Transition Radiation Detector
SBA	Super bialkali
TPB	Tetraphenyl-butadiene
UV	Ultraviolet
WLS	Wavelength shifting

References

[1] The ATLAS Collaboration, *Observation of a new particle in the search for the Standard Model Higgs boson with the ATLAS detector at the LHC*, Phys. Lett. B 716 (2012), p. 1.

[2] The CMS Collaboration, *Observation of a new boson at a mass of 125 GeV with the CMS experiment at the LHC*, Phys. Lett. B 716 (2012), p. 30.

[3] *Birth of a Higgs boson*, Cern Courier (April 2013), URL: http://cerncourier.com/cws/article/cern/53086.

[4] P.A.R. Ade et al. (Planck Collaboration), *Planck 2013 results. I. Overview of products and scientific results*, arXiv:1303.5062v1 (2013), URL: http://arxiv.org/abs/1303.5062.

[5] P. Senger, *Status of the CBM experiment*, 22nd CBM Collaboration Meeting, Dubna, 2013, URL: https://indico.gsi.de/conferenceOtherViews.py?view=standard&confId=2054.

[6] CBM Collaboration, *Technical Design Report for the CBM Ring Imaging Cherenkov (RICH) Detector*, 2013, URL: http://repository.gsi.de/record/65526.

[7] *FAIR Green Paper - The Modularized Start Version*, Darmstadt 2009, URL: http://www.gsi.de/documents/DOC-2009-Nov-124-1.pdf.

[8] Y. Aoki et al., *The order of the quantum chromodynamics transition predicted by the standard model of particle physics*, Nature 443 (2006), p. 675.

[9] S. Borsanyi et al., *Is there still any T_c mystery in lattice QCD? Results with physical masses in the continuum limit III*, JHEP 1009 (2010), p. 073.

[10] A. Basavov et al., *The chiral and deconfinement aspects of the QCD transition*, arXiv:1111.1710v1 (2011), URL: http://arxiv.org/abs/1111.1710.

[11] Z. Fodor and S.D. Katz, *Critical point of QCD at finite T and mu, lattice results for physical quark masses*, JHEP 0404 (2004), p. 050.

[12] A. Andronic et al., *Hadron production in ultra-relativistic nuclear collisions: Quarkyonic matter and a triple point in the phase diagram of QCD*, Nucl. Phys. A 837 (2010), p. 65.

[13] K. Fukushima and C. Sasaki, *The phase diagram of nuclear and quark matter at high baryon density*, arXiv:1301.6377v3 (2013), URL: http://arxiv.org/abs/1301.6377.

[14] B. Friman et al. (Eds.), *The CBM Physics Book*, ed. by Springer, 2011.

[15] B. Schenke, *Hydrodynamics and transport*, Student day of the Quark Matter 2012 International Conference, 2012, URL: https://indico.cern.ch/getFile.py/access?contribId=688&sessionId=64&resId=0&materialId=slides&confId=181055.

[16] C. Höhne, *Physics of compressed baryonic matter*, J. Phys.: Conf. Ser. 420 (2013), p. 012016.

[17] A. Andronic, P. Braun-Munzinger, and J. Stachel, *Thermal hadron production in relativistic nuclear collisions: The hadron mass spectrum, the horn, and the QCD phase transition*, Phys. Lett. B 673 (2009), p. 142.

[18] T. Ullrich, B. Wysłouch, and J. Harris (Eds.), Nucl. Phys. A 904-905 (Proceedings of the 23rd Internatinal Conference on Ultrarelativistic Nucleus-Nucleus Collisions, Quark Matter 2012), 2013.

[19] J. Randrup and J. Cleymans, *Maximum freeze-out baryon density in nuclear collisions*, Phys. Rev. C 74 (2006), p. 047901.

[20] L. Kumar, Nucl. Phys. A 904-905 (2013), p. 256.

[21] E. O'Brian, *Recent PHENIX Results from the RHIC Energy Scan*, Nucl. Phys. A 904-905 (2013), p. 264.

[22] A. Schmah, *Highlights of the Beam Energy Scan from STAR*, arXiv:1202.2389v1 (2012), URL: http://arxiv.org/abs/1202.2389.

[23] A. Aduszkiewicz et al. (NA61 Collaboration), *NA61/SHINE at the CERN SPS: Plans, status and first results*, Acta Physica Polonica B43 (2012), p. 635.

[24] *NICA White Paper*, 2011, URL: http://nica.jinr.ru/files/WhitePaper.pdf.

[25] W. Ehehalt and W. Cassing, *Relativistic transport approach for nucleus-nucleus collisions from SIS to SPS*, Nucl. Phys. A 602 (1996), p. 449.

[26] Yu.B. Ivanov, V.N. Russkikh, and V.D. Toneev, *Relativistic heavy-ion collisions within three-fluid hydrodynamics: Hadronic scenario*, Phys. Rev. C 73 (2006), p. 044904.

[27] S.A. Bass et al., *Microscopic Models for Ultrarelativistic Heavy Ion Collisions*, Prog. Part. Nucl. Phys. 41 (1998), p. 225.

[28] M. Bleicher et al., *Relativistic hadron-hadron collisions in the ultra-relativistic quantum molecular dynamics model*, J. Phys. G: Nucl. Part. Phys. 25 (1999), p. 1859.

[29] W. Cassing, E.L. Bratkovskaya, and A. Sibirtsev, *Open charm production in relativistic nucleus-nucleus collisions*, Nucl. Phys. A 691 (2001), p. 753.

[30] A. Andronic, P. Braun-Munzinger, and J. Stachel, *Hadron production in central nucleus-nucleus collisions at chemical freeze-out*, Nucl. Phys. A 772 (2006), p. 167.

[31] J. Heuser, *The Compressed Baryonic Matter Experiment at FAIR*, Nucl. Phys. A 904-905 (2013), p. 941.

[32] The CBM collaboration, *Nuclear matter physics at SIS-100*, Darmstadt 2012, URL: https://www.gsi.de/documents/DOC-2011-Aug-29-1.pdf.

[33] G. Agakishiev et al. (HADES Collaboration), *Deep Subthreshold Ξ-Production in Ar+KCl Reactions at* 1.76 AGeV, Phys. Rev. Lett. 103 (2009), p. 132301.

[34] C. Blume, *Energy dependence of hadronic observables*, J. Phys. G 31 (2005), S57.

[35] S. Voloshin and Y. Zhang, *Flow Study in Relativistic Nuclear Collisions by Fourier Expansion of Azimuthal Particle Distributions*, Z. Phys. C 70 (1996), p. 665.

[36] H. Stöcker, *Collapse of Flow: Probing the Order of the Phase Transition*, arXiv:0710.5089v1 (2007), URL: http://arxiv.org/abs/0710.5089.

[37] R. Pisarski, *Phenomenology of the chiral phase transition*, Phys. Lett. B 110 (1982), p. 155.

[38] A. Andronic et al., *Charmonium and open charm production in nuclear collisions at SPS/FAIR energies and the possible influence of a hot hadronic medium*, Phys. Lett. B 659 (2008), p. 149.

[39] O. Linnik, E.L. Bratkovskaya, and W. Cassing, *Open and hidden charm in proton-nucleus and heavy-ion collisions*, Int. J. Mod. Phys. E 17 (2008), p. 1367.

[40] T. Matsui and H. Satz, *J/ψ-Suppression by Quark-Gluon Plasma Formation*, Phys. Lett. B 178 (1986), p. 416.

[41] NA50 Collaboration, *A new measurement of J/ψ suppression in Pb-Pb collisions at* 158 GeV *per nucleon*, Eur. Phys. J. C 39 (2005), p. 335.

[42] R. Arnaldi et al. (NA60 Collaboration), *J/ψ production in p-A and A-A collisions at fixed target experiments*, Nucl. Phys. A 830 (2009), p. 345c.

[43] A. Andronic et al., *Production of light nuclei, hypernuclei and their antiparticles in relativistic nuclear collisions*, Phys. Lett. B 697 (2011), p. 203.

[44] E.V. Shuryak, *Quark-gluon plasma and hadronic production of leptons, photons and psions*, Phys. Lett. B 78 (1987), p. 150.

[45] R. Porter et al. (DLS Collaboration), *Dielectron Cross Section Measurements in Nucleus-Nucleus Reactions at* 1.0 AGeV, Phys. Rev. Lett. 79 (1997), p. 1229.

[46] G. Agakishiev et al. (HADES Collaboration), *Study of dielectron production in C+C collisions at* 1 AGeV, Phys. Lett. B 663 (2008), p. 43.

[47] Y. Pachmayer, *Dielectron Production in $^{12}C + ^{12}C$ Collisions at* 1 GeV/u *and the Solution to the DLS Puzzle*, arXiv:0804.3993v1 (2008), URL: http://arxiv.org/abs/0804.3993.

[48] D. Adamova et al. (CERES Collaboration), *Modification of the ρ meson detected by low-mass electron-positron pairs in central Pb-Au collisions at* 158 AGeV/c, Phys. Lett. B 666 (2008), p. 425.

[49] S. Damjanovic (NA60 Collaboration), *First measurement of the ρ spectral function in nuclear collisions*, Nucl. Phys. A 774 (2006), p. 715.

[50] G. Agakishiev et al. (HADES Collaboration), *Dielectron production in Ar+KCl collisions at* 1.76 AGeV, Phys. Rev. C 84 (2011), p. 014902.

[51] I. Frölich et al., *Pluto: A Monte Carlo Simulation Tool for Hadronic Physics*, arXiv:0708.2382 (2008), URL: http://arxiv.org/abs/0708.2382.

[52] J. Heuser et al., *Technical Design Report for the CBM Silicon Tracking System (STS)*, GSI Report 2013-4, URL: http://repository.gsi.de/record/54798.

[53] I. Kisel, *Event reconstruction in the CBM experiment*, Nucl. Instrum. Meth. Vol. A 566 (2006), p. 85.

[54] S. Gorbunov et al., *Fast SIMDized Kalman filter based track fit*, Comp. Phys. Comm. 178 (2008), p. 374.

[55] V. Friese, *Computational Challenges for the CBM Experiment*, Lecture Notes in Computer Science 7125 (Proceedings of MMCP 2011), 2012, p. 17.

[56] P.A. Cherenkov, *Visible Radiation Produced by Electrons Moving in a Medium with Velocities Exceeding that of Light*, Phys. Rev. 52 (1937), p. 378.

[57] L. Mallet, Compte Rendu 183 (1926), p. 274.

[58] L. Mallet, Compte Rendu 187 (1928), p. 222.

[59] L. Mallet, Compte Rendu 188 (1929), p. 445.

[60] T. Ypsilantis and J. Seguinot, *Theory of ring imaging Cherenkov counters*, Nucl. Instrum. Meth. Vol. A 343 (1994), p. 30.

[61] I. Frank and I. Tamm, *Coherent visible radiation of fast electrons passing through matter*, C. R. Acad. Sci. URSS 14 (1937), p. 109.

[62] J. Seguinot and T. Ypsilantis, *Photoionization and Cherenkov ring imaging*, Nucl. Instrum. Meth. 142 (1977), p. 377.

[63] I. Adam et al., *The DIRC Particle Identification System for the BABAR Experiment*, Nucl. Instrum. Meth. Vol. A 538 (2005), p. 281.

[64] C. Schwarz, *Development of the PANDA barrel DIRC*, JINST 4 (2009), P12016.

[65] M. Buenerd, *The RICH counter of the AMS experiment*, Nucl. Instrum. Meth. Vol. A 502 (2003), p. 158.

[66] J. Engelfried, *Cherenkov light imaging - Fundamentals and recent developments*, Nucl. Instrum. Meth. Vol. A 639 (2011), p. 1.

[67] J. Engelfried, *Summary of the workshop*, 8th International Workshop on Ring Imaging Cherenkov Detectors (RICH2013), Hayama, Kanagawa, Japan, 2013.

[68] A. Bideau-Mehu et al., *Interferometric determination of the refractive index of carbon dioxide in the ultraviolet region*, Opt. Commun. 9 (1973), p. 432.

[69] H. Morii et al., *Quenching effects in nitrogen gas scintillation*, Nucl. Instrum. Meth. Vol. A 526 (2004), p. 399.

[70] E. Lebedeva et al., *Measurements of the surface homogeneity for the prototype mirrors of the CBM-RICH detector*, CBM Progress Report 2011 (2012).

[71] S. Reinecke, *Charakterisierung von Spiegeln für den RICH-Detektor von CBM*, Diploma thesis, Bergische Universtät Wuppertal, 2011.

[72] P. Glässel, *The Limits of ring image Cherenkov technique*, Nucl. Instrum. Meth. Vol. A 433 (1999), p. 17.

[73] J. Schwiening, *Private communication*, GSI Darmstadt, 2013.

[74] *CbmRoot*, URL: http://fairroot.gsi.de.

[75] S. Lebedev, *Private communication*, Justus-Liebig-Universität Gießen, 2013.

[76] P.V.C. Hough, *A Method and Means for Recognizing Complex Patterns*, US Patent : 3, 069, 654 (1962).

[77] S. Lebedev et al., *Ring Recognition and Electron Identification in the RICH detector of the CBM Experiment at FAIR*, JINST 219 (2010), p. 032015.

[78] G. Ososkov N. Chernov, Comp. Phys. Comm. 33 (1984), p. 329.

[79] N. Chernov, *On the Convergence of Fitting Algorithms in Computer Vision*, J Math Im Vi 27 (2007), p. 231.

[80] T. Galatyuk, C. Höhne, and J. Stroth, *Di-electron reconstruction with CBM*, CBM Progress Report 2009 (2010).

[81] E. Lebedeva and C. Höhne, *Status of low-mass di-electron simulations in the CBM experiment*, CBM Progress Report 2012 (2013).

[82] C. Höhne et al., *Development of a RICH detector for electron identification in CBM*, Nucl. Instrum. Meth. Vol. A 595 (2008), p. 187.

[83] J. Abraham et al. (Pierre Auger Collaboration), *The Fluorescence Detector of the Pierre Auger Observatory*, Nucl. Instrum. Meth. Vol. A 620 (2010), p. 227.

[84] A. Ostankov (MAGIC Collaboration), *The image camera of the 17 m diameter air Cherenkov telescope MAGIC*, Nucl. Instrum. Meth. Vol. A 471 (2001), p. 188.

[85] A. Kohnle, *Photodetectors for HESS*, Nucl. Instrum. Meth. Vol. A 442 (2000), p. 322.

[86] F. Halzen, *Astroparticle Physics with High Energy Neutrinos: from AMANDA to IceCube*, Eur. Phys. J. C 46 (2006), p. 669.

[87] Hamamatsu Photonis K.K., *Photomultiplier Tubes, Basics and Applications*, ed. by World Technical Writing Inc., 2007.

[88] Photonis, *Photomultiplier Tubes, Principles & Applications*, ed. by S-O Flyckt and Carole Mamonier, 2002.

[89] Electron Tube Division Hamamatsu Photonics K.K., *Hamamatsu H8500 Series / H10966 Series data sheet*, 2011.

[90] S. Reinecke et al., *Overview of the RICH-prototype beam test 2012 at the CERN-PS*, CBM Progress Report 2012 (2013).

[91] D. Ryckbosch., *The HERMES RICH detector*, Nucl. Instrum. Meth. Vol. A 433 (1999), p. 98.

[92] S. Korpar et al., *The HERA-B RICH*, Nucl. Instrum. Meth. Vol. A 433 (1999), p. 128.

[93] P. Abbon et al., *15*, Nucl. Instrum. Meth. Vol. A 639 (2011).

[94] The LHCb Collaboration, *Framework Technical Design Report for the LHCb upgrade*, CERN-LHCC-2012-007 (2012).

[95] R.A. Montgomery, *A ring imaging Cherenkov detector for CLAS12*, Nucl. Instrum. Meth. Vol. A 732 (2013), p. 366.

[96] M.K. Daniel et al., *A Compact High Energy Camera for the Cherenkov Telescope Array*, arXiv:1307.2807v1, Proceedings of the 33rd International Cosmic Ray Conference (ICRC2013), Rio de Janeiro (Brazil) (2013), URL: http://arxiv.org/abs/1307.2807.

[97] M. Casolino (JEM-EUSO Collaboration)., *Detecting ultra-high energy cosmic rays from space with unprecedented acceptance: objectives and design of the JEM-EUSO mission*, Astrophys. Space Sci. Trans. 7 (2011), p. 477.

[98] Electron Tube Division Hamamatsu Photonics K.K., *Hamamatsu R11265-100-M16 tentative data sheet*, 2011.

[99] Y. Hotta and K. Nagura, *Private communication*, Hamamatsu Photonics K.K., Electron Tube Division, 2012.

[100] M. Alemi et al., *First operation of a hybrid photon detector prototype with electrostatic cross-focussing and integrated silicon pixel readout*, Nucl. Instrum. Meth. Vol. A 449 (2000), p. 48.

[101] Y. Musienko, *State of the art in SiPM's*, SiPM workshop, Cern, 2011, URL: http://indico.cern.ch/conferenceProgram.py?confId=117424.

[102] J. Schwiening, *The barrel DIRC detector for the PANDA experiment at FAIR*, Nucl. Instrum. Meth. Vol. A 639 (2011), p. 315.

[103] J. Adamczewski-Musch and S. Linev, *A Go4-based online-analysis framework for CBM tests*, CBM Progress Report 2011 (2012).

[104] R. Brun and F. Rademakers, *ROOT - An Object Oriented Data Analysis Framework*, Nucl. Instrum. Meth. Vol. A 389 (1997), p. 81, URL: http://root.cern.ch/.

[105] I. Sorokin et al., *Transconductance calibration of n-XYTER 1.0 readout ASIC*, Nucl. Instrum. Meth. Vol. A 714 (2013), p. 136.

[106] Photonis USA Pennsylvania Inc., *Planacon XP85012 MCP-PMT data sheet*, 2013.

[107] M. Ogawa, *Absorption Cross Sections of* O_2 *and* CO_2 *Continua in the Schumann and far-uv Regions*, J. Chem. Phys. 54 (1971), p. 2550.

[108] J. Eschke et al., *Investigation of crosstalk in multi-anode photomultipliers for the CBM-RICH photodetector*, CBM Progress Report 2010 (2011).

[109] S. Reinecke, *Tests and comparison of various photon detection devices for the CBM-RICH*, Workshop on fast Cherenkov detectors (DIRC2013), 2013, URL: https://indico.gsi.de/conferenceTimeTable.py?confId=2099#all.

[110] S. Querchfeld, *Test neuer Photomultiplier für die Entwicklung einer Auger-Nord Fluoreszenz Kamera*, Diploma thesis, Bergische Universtät Wuppertal, 2010.

[111] A. Schmidt et al., *Prototyping the WASA DIRC*, JINST 6 (2011), p. C10005.

[112] Y. Hotta and K. Nagura, *Private communication*, Hamamatsu Photonics K.K., Electron Tube Division, 2013.

[113] E.L. Garwin et al., *Method for elimination of quartz-face phototubes in Cherenkov counters by use of wavelength-shifter*, Nucl. Instrum. Meth. 107 (1973), p. 365.

[114] P. Baillon et al., *Ultraviolet Cherenkov light detector*, Nucl. Instrum. Meth. 126 (1975), p. 13.

[115] M.A.F. Alves, M.C.M. Dos Santos, and A.J.P.L. Policarpo, *Wavelength shifters for xenon proportional scintillation counters*, Nucl. Instrum. Meth. 119 (1974), p. 485.

[116] A.M. Gorin et al., *On the increase of ultraviolet radiation detection efficiency in nuclear particle detectors with the help of transparent wavelength shifter films*, Nucl. Instrum. Meth. Vol. A 251 (1986), p. 461.

[117] G. Eigen and E. Lorenz, *A method of coating photomultipliers with wavelength shifters*, Nucl. Instrum. Meth. 166 (1979), p. 165.

[118] J.A.R. Samson, *Techniques of vacuum ultraviolet spectroscopy*, ed. by J. Wiley Inc., 1967.

[119] R. Allison et al., *Absolute Fluorescent Quantum Efficiency of Sodium Salicylate*, J. Opt. Soc. Am. 54 (1964), p. 747.

[120] C. Höhne et al., *Development of a RICH detector for CBM: simulations and experimental tests*, Nucl. Instrum. Meth. Vol. A 639 (2011), p. 294.

[121] *Wikipedia*, 28 February 2013, URL: http://en.wikipedia.org/wiki/Terphenyl.

[122] P. Koczon et al., *Materials' properties of wavelength shifting films for the CBM-RICH detector - thickness dependence and efficiency*, CBM Progress Report 2009 (2010).

[123] *Wikipedia*, 4 March 2013, URL: http://de.wikipedia.org/wiki/Chemical_Solution_Deposition.

[124] M. Dürr, *Private communication*, Justus-Liebig-Universität Gießen, 2013.

[125] I. Galm et al., *Wavelength-shifting films for use on MAPMTs with UV-extended windows*, CBM Progress Report 2011 (2012).

[126] M. Dürr et al., *Status report on WLS films for PMTs with UV-window*, 19th CBM Collaboration Meeting, Darmstadt, 2012, URL: https://indico.gsi.de/getFile.py/access?contribId=86&sessionId=8&resId=0&materialId=slides&confId=1368.

[127] D. Paneque et al., *A method to enhance the sensitivity of photomultipliers for Air Cherenkov Telescopes by applying a lacquer that scatters light*, Nucl. Instrum. Meth. Vol. A 518 (2004), p. 619.

[128] V. Körstgens et al., *Improvement of quantum efficiency of photomultiplier tubes by humidity controlled coatings based on porous polymer structures*, Appl. Phys. Lett. 93 (2008), p. 041916.

[129] E.G. Bamberg, *Optical Factors in the Photoemission of Thin Films*, Appl. Opt. 6 (1967), p. 2163.

[130] D. Paneque, *The MAGIC Telescope: development of new technologies and first observations*, Ph.D. thesis, Technische Universität München, 2004.

[131] *Schott 8337B data sheet*, March 2012, URL: http://www.us.schott.com/tubing/english/product_selector/index.html?glassid=8337B.

[132] *Refrective Index Database*, URL: http://refractiveindex.info/?group=GASES&material=Air.

[133] A. Montesdeoca-Santana et al., *XPS characterization of different thermal treatments in the ITO-Si interface of a carbonate-textured monocrystalline silicon solar cell*, Nucl. Instrum. Meth. Vol. B 268 (2010), p. 374.

[134] Electron Tube Division Hamamatsu Photonics K.K., *Information sheet on cross-talk change for H8500*, 2007.

[135] L. Kotchenda et al., *STAR TPC gas system*, Nucl. Instrum. Meth. Vol. A 499 (2003), p. 703.

[136] L. Kotchenda et al., *PHENIX Muon Tracking Detector Gas System*, Nucl. Instrum. Meth. Vol. A 578 (2007), p. 172.

[137] C. Pauly et al., *The photon detection system of the CBM-RICH prototype detector*, CBM Progress Report 2011 (2012).

[138] A.S. Brogna et al., *N-XYTER, a CMOS read-out ASIC for high resolution time and amplitude measurements on high rate multi-channel counting mode neutron detectors*, Nucl. Instrum. Meth. Vol. A 568 (2006), p. 301.

[139] N. Abel et al., *Development of the Read Out Controller for the nXYTER Freont End Board*, CBM Progress Report 2007 (2008).

[140] S. Manz et al., *An universal read-out controller*, JINST 10 (2008), p. C11017.

[141] L. Durieu et al., *Optics studies for the T9 beam line in the CERN PS east area secondary beam facility*, Proceedings of the 2011 Particle Accelerator Conference, Chicago, 2001, p. 1547, URL: http://sba.web.cern.ch/sba/Documentations/Eastdocs/docs/T9Note.pdf.

[142] C. Pauly et al., *Fiber hodoscopes for beam diagnostic and particle tracking*, CBM Progress Report 2011 (2012).

[143] J. Adamczewski-Musch et al., *Data Acquisition Backbone Core DABC*, J. Phys.: Conf. Ser. 119 (2008), p. 022002.

[144] J. Adamczewski-Musch et al., *Data acquisition and online monitoring software for CBM test beams*, J. Phys.: Conf. Ser. 396 (2012), p. 012001.

[145] J. Adamczewski-Musch et al., *Online Object Monitoring With Go4 V4.4*, IEEE Trans. Nuclear Sciences 58-4 (2011), p. 1477.

[146] L. Kotchenda et al., *Beamtest results of the RICH prototype gas system*, CBM Progress Report 2011 (2012).

[147] L. Kotchenda et al., *Results of the RICH prototype gas system during the 2012 beam test*, CBM Progress Report 2012 (2013).

[148] N. Metroplis, *The beginning of the Monte Carlo method*, Los Alamos Science, Special Issue (1987), p. 125.

[149] CERN Program Library Long Write-up W5013, *GEANT - Detector description and simulation tool*, 1993, URL: http://wwwasdoc.web.cern.ch/wwwasdoc/geant_html3/geantall.html.

[150] S. Reinecke, *Characterization of different multianode photon detectors in the CBM-RICH beamtime 2012*, 21st CBM Collaboration Meeting, Darmstadt, 2013, URL: https://indico.gsi.de/getFile.py/access?contribId=78&sessionId=14&resId=0&materialId=slides&confId=1912.

[151] S. Schmid, *Private communication*, Hamamatsu Photonics Deutschland GmbH, 2013.

Acknowledgement

This work would not have been possible without the contribution of many people who I am deeply indebted to.

I am very grateful to Prof. Karl-Heinz Kampert for giving me the opportunity to be part of his working group and the CBM-RICH project. I appreciate his continuous support, his advices, and the pleasant way of supervision and leadership.

My gratitude goes to Prof. Claudia Höhne for reviewing this thesis and for initiating and pushing forward the CBM-RICH project for all the years, allowing me to join during the fascinating phase of prototyping. I am also deeply grateful for frequent discussions and many valuable suggestions regarding data analysis.

The successful completion of this thesis is due to the competent guidance from the beginning and the support from Dr. Christian Pauly. I am deeply thankful to Christian for coming up with so many ideas that i could follow up and being such enjoyable colleague in the office, the lab, and on business trips. The same holds true for Dr. Tariq Mahmoud, who, in addition, I want to thank for sharing with me his knowledge about heavy ion physics and for many discussions.

The study of wavelength shifting films was only possible thanks to the expertise of Prof. Michael Dürr and his group and the good cooperation between Esslingen and Wuppertal. I am grateful for the opportunity to get an insight into this exciting technique.

I want to thank Prof. Zoltán Fodor for being part of my PhD Committee and participating in the regular and fruitful meetings.

The help of Jahan Pouryamout and Uwe Naumann in solving mechanical and electrical issues was crucial for the installation of the PMT test stand in the lab. The successful beam test campains at CERN are based on the joint effort and the commitment of the whole collaboration and people from the cooperating institutes at Darmstadt, Esslingen, Gießen, Wuppertal, Dubna, Moscow, Saint Petersburg, and Pusan. In particular, I want to express my appreciation to Dr. Jörn Adamczewski-Musch, Dr. Christina Dritsa, Dr. Jürgen Eschke, Yoonsung John, Dr. Leonid Kochenda, Dr. Peter Kravtsov, Dr. Sergey Linev, Dr. Jan Michel, Yongho Nam, Egor Ovcharenko, Dr. Yuriy Ryabov, Jihye Song, Jungyu Yi, and all the others who are already mentioned elsewhere on this page.

I am indepted to Dr. Semen Lebedev and Elena Lebedeva for their help and cooperation with respect to simulations and to Dr. Dmytro Kresan for helping me getting started on CbmRoot.

My gratitude is also due to Dr. Razmik Mirzoyan from MPI für Physik and Dr. Dietmar Borchert from Fraunhofer ISE for the possibility of calibration and cross-checking measurements.

I thank Dr. Julian Rautenberg and Sascha Reinecke for our discussions on measurements and data analysis and their help concerning all my problems with soft and hardware. I owe Sven Querchfeld a dept of gratitude for sharing his knowledge about PMTs and for his hands-on attitude which was very helpful for improving the measurement setups.

All my colleagues from the astroparticle physics group in Wuppertal should be acknowledged for creating such nice atmosphere which was a pleasure to work in. Many thanks go to Ahmad, Alex, Anna, Andreas, Andreas, Benjamin, Biswajit, Carla, Christian, Daniel, Daniel, Daniel, Daniel, David, Dennis, Franziska, Ingolf, Jahan, Jan, Jens, Jörg, Johannes, Jonas, Julian, Karl-Heinz, Klaus, Lu, Lukas, Nicole, Marcelo, Maria, Oana, Philipp, Pietro, Ruth, Sascha, Sebastian, Sven, Timo, Tobias, and Uwe. In addition, I am thankful to Ingrid Schaarwächter for solving all administrative issues and making everything easy by being so organised.

I appreciate the possibility to participate in the Helmholtz Graduate School for Heavy Ion Research and to attend many valuable courses, lecture and power weeks. I am grateful for financial help from HGS-HIRe and DAAD for presenting results abroad.

Finally, I want to thank my friends and my family who are a constant source of support and who are always there for me. And of course, I thank Amada for her support and love. There are no words strong enough to express how well I feel at your side.